



Durham E-Theses

New Models to Analyse the Performance of Magnetic Cores in Electromagnetic Machines for Renewable Energy Systems

ZHANG, ZHI

How to cite:

ZHANG, ZHI (2023) *New Models to Analyse the Performance of Magnetic Cores in Electromagnetic Machines for Renewable Energy Systems*, Durham theses, Durham University. Available at Durham E-Theses Online: <http://etheses.dur.ac.uk/15090/>

Use policy

The full-text may be used and/or reproduced, and given to third parties in any format or medium, without prior permission or charge, for personal research or study, educational, or not-for-profit purposes provided that:

- a full bibliographic reference is made to the original source
- a [link](#) is made to the metadata record in Durham E-Theses
- the full-text is not changed in any way

The full-text must not be sold in any format or medium without the formal permission of the copyright holders.

Please consult the [full Durham E-Theses policy](#) for further details.

New Models to Analyse the Performance of Magnetic Cores in Electromagnetic Machines for Renewable Energy Systems



Author: Zhi Zhang

Supervisor: Dr. Hamed Hamzehbahmani

Prof. Philip H. Gaskell

Department of Engineering, University of Durham

This thesis is submitted for the degree of *Doctor of Philosophy*.

Collingwood College

March 2023

I wish to dedicate this thesis to all the researchers who have contributed, are contributing and will contribute to the field of electromagnetics . . .

Declaration

I declare that except where explicit references are made to the work of others, the contents of this thesis are the result of my independent work/investigation and have not been submitted in whole or in part for consideration for any other degree or qualification in this, or any other university. This thesis contains nothing about the outcome of work in collaboration with others except as specified in the text and Acknowledgements. The thesis includes fewer than 60,000 words, including appendices, bibliography, footnotes, tables, and equations and has fewer than 150 figures. This thesis is submitted in partial fulfilment of the requirements for the degree of Doctor of Philosophy. I hereby give consent for my thesis, if accepted, to be available for photocopying and for inter-library loan and for the title and summary to be made available to outside organisations.

Author: Zhi Zhang

March 2023

Acknowledgements

The research presented in this thesis was undertaken in Durham University's Engineering Department. My appreciation to the organisation for providing the resources needed to complete this project is beyond my expression. I would also like to show my gratefulness to those below.

I wish to express my deepest gratitude to my primary supervisor Dr Hamed Hamzehbahmani, for his guidance and inspiration. He always encouraged me with an enlightened view, and his insight and enthusiasm boosted me to improve this work continually.

I am very grateful to my second supervisor Professor Philip H. Gaskell, for the presentation review, paper review, thesis review, and Latex introduction. His invaluable comments contributed significantly to this project. His enlightenment makes me achieve perfection in my work.

I would also like to thank the staff and students at the Engineering Department and the IT service staff; their help and suggestions are deeply appreciated.

My gratitude is extended to Cogent Power Ltd. for providing sample electrical steel sheets, without which it would not have been possible to conduct relevant experiments. Furthermore, without the help of Dr Hamed Hamzehbahmani for the experiment instruction, it would have been impossible to complete this project and make a remarkable achievement.

My appreciation extends to the National Physical Laboratory (NPL) who provided access essential experiment equipment. Mainly, I would like to express my gratitude to Dr Graeme Finch and Dr Daniel Brunt for their kindness in helping me in conducting experiments.

I wish to express my indebtedness to my family for all they have done to support my career. My parents and my sister are incredibly supportive of me pursuing my academic achievements.

Finally, I am greatly indebted to my wife, Hong, for the love, encouragement, support, and patience she always has for me. I wish to extend special gratitude to my lovable girls for their laughter accompanying my thesis writing.

Abstract

The magnetic core made, from electrical steels, is an essential part of an electromagnetic machine to link primary and secondary windings with a low reluctance path of magnetic flux to transfer electrical energy between windings. Despite this, the inevitable core loss remains a long-standing troublesome problem hindering the design of efficient and reliable machines. Therefore, it is indispensable to fully understand the magnetic characteristics of electrical steels under magnetic excitation to predict the magnetic core performance when an electromagnetic machine is in service within a power system.

The best way to investigate the magnetic characteristics of electrical steels is to model the magnetic hysteresis and calculate the energy losses under sinusoidal and non-sinusoidal excitation for a wide range of frequencies and peak flux densities. There are numerous excellent models to trace hysteresis loops at low frequencies. However, no models have been developed for simulating the hysteresis loops at high frequencies due to the distortion and irregularity of the curves caused by the complexity of the physical mechanism at high frequencies. To investigate the performance of electrical steels as a magnetic core, this study proposes a novel single equation model derived from the analysis of magnetic domain patterns in ferromagnetic materials to trace hysteresis loops and calculate the energy losses for both low and high frequencies, including both major and minor hysteresis loops.

The magnetic domain patterns in electrical steels consist of two categories, anisotropic domain and isotropic domain; these domain patterns exist in both grain-oriented electrical steels (GOESs) and non-oriented electrical steels (NOESs), but the domain shape and size are somewhat different. The magnetic properties are dominated by the proportion of domain pattern components in the electrical steels. The GOESs are characterised mainly by the anisotropic domain component, and the NOESs are determined mainly by the isotropic domain component. So, it is reasonable for the proposed single equation model containing two items representing anisotropic and isotropic domains to be applied for both GOESs and NOESs.

The energy losses of the magnetic core are the primary concern of power system companies considering the operation cost and climate protection. Typically, the prediction of energy losses is made to evaluate the area of the hysteresis loops. It is difficult for some models to calculate the hysteresis loop area, so finite element computational methods are used to calculate the losses. The calculation of energy losses using the single equation model is advantageous for predicting energy losses because it is made to integrate the equation over the excitation field range.

The physical mechanism of energy loss separation is analysed to propose a novel theory of ferromagnetism to provide the proposed model with the necessary physical grounding. The new separation principle of energy loss is investigated according to the microstructure variation of the ferromagnetic material under an external field. Accordingly, the energy loss of the magnetic core includes three components, hysteresis loss, eddy current loss, and magnetisation loss. The components are calculated to fit the relevant measurement data.

List of Abbreviations and Nomenclature

Abbreviations

AC	Alternating Current
BS	British standard
DC	Direct Current
ELSM	Energy loss separation model
Fe	Iron
FE	Finite Element
GOES	Grain Oriented Electrical Steel
IEEE	Institute of Electrical and Electronics Engineers
IET	Institution of Engineering and Technology
J-A	Jiles–Atherton
NOES	Non-Oriented Electrical Steel
PID	Proportional–integral–derivative
Si	Silicon
SST	Single Strip Tester
WMF	Weiss mean field

Nomenclature

B	Magnetic Flux Density
B_{pk}	Peak flux density
B_s	Magnetic flux density at saturation magnetisation
d	Thickness of steel sheet
f	Frequency
h	Excitation Field
H	Magnetic Field
H_c	Coercivity
H_{hyst}	Static Hysteresis field
H_{clas}	Classical eddy current field
H_{exce}	Excess field
H_h	Hysteresis field
H_e	Eddy current counter field
H_m	Magnetisation field
H_w	Weiss Mean field
i	Excitation current
J	Magnetic polarisation
k_B	Boltzmann constant
k_e	Eddy current loss coefficient
k_{ex}	Excess loss coefficient
k_h	Hysteresis loss coefficient
m_a	Anisotropic domain unit volume magnetic moment
m_i	Isotropic domain unit volume magnetic moment
M	Magnetisation
M_{an}	Anhysteretic Magnetisation
M_s	Saturation magnetisation
N	Number of turns of excitation winding

T	Tesla
T	Temperature
V	Volume of substance
W	Core loss
W_{clas}	Classical eddy current loss
W_{exce}	Excess loss
W_h	Hysteresis loss
W_m	Magnetisation loss
W_{tot}	Total core loss
α	Weiss mean field constant
σ	Electrical conductivity
δ	Skin depth
\mathcal{L}	Langevin equation
ρ	Electrical resistivity
μ_0	Permeability of vacuum
μ	Permeability of substance
μ_r	Relative permeability

Contents

Declaration.....	3
Acknowledgements.....	4
Abstract.....	5
List of Abbreviations and Nomenclature	7
Abbreviations.....	7
Nomenclature	8
List of Figure Captions	13
List of Table Captions.....	21
Chapter 1 Introduction	22
1.1 Background	22
1.2 Research Objectives.....	23
1.3 Fundamental Magnetism.....	25
1.3.1 Magnetic Field	25
1.3.2 Magnetic Induction.....	25
1.3.3 Magnetisation.....	26
1.3.4 Magnetic Polarisation	26
1.3.5 Relationship Between H , M and B	27
1.3.6 Zeeman Energy	28
1.3.7 Magnetic Hysteresis Loop.....	28
1.4 Domain Theory	29
1.4.1 Weiss mean field.....	31
1.4.2 Domain structures	31
1.5 Electrical Steels	33
1.5.1 Magnetic properties in GOESs and NOESs	34
1.5.2 Microstructures in GOES and NOES.....	35
1.6 Summary	37
Chapter 2 Previous Related Work.....	38
2.1 Introduction	38
2.2 Static and dynamic hysteresis model	39

2.3 Magnetic loss evaluation model	46
2.4 Jiles–Atherton model.....	53
2.4.1 Anhyseteric Magnetisation	53
2.4.2 Hysteresis Modelling	56
2.5 Preisach model.....	65
2.5.1 Hybrid model combining J-A and Preisach models	68
2.6 Summary	70
Chapter 3 Magnetisation and Measurement Systems	72
3.1 Single Sheet Tester	72
3.2 Epstein Frame	75
3.3 Comparison of SST and Epstein Frame	79
3.4 Research on Accurate Measurements.....	83
Chapter 4 Novel magnetisation theory of ferromagnetic materials	85
4.1 Introduction	85
4.2 Measurement System and Hysteresis Mechanism	89
4.3 Separation of the Magnetic Field	92
4.4 Coercive Force and Coercivity	97
4.5 Analysis on Hysteresis Loops of GOES and NOES	99
4.6 Conclusions	103
Chapter 5 A novel hysteresis model of ferromagnetism based on domain theory.....	105
5.1 Introduction	105
5.2 Domain Patterns	108
5.3 Model Derivation	110
5.4 Hysteresis Removal Procedure	114
5.5 Conclusions	118
Chapter 6 Dynamic Modelling of Grain-Oriented Electrical Steels.....	119
6.1 Fitting the Model to the Measurement Data of GOESs	119
6.2 Evaluation of Energy Losses Using the Novel Model.....	127
6.3 Investigation of Non-sinusoidal Excitation for GOESs	129
6.3.1 Motivation based on emerging renewable energy	129

6.3.2 Fitting the Model to the Measurement Data of GOESs Under Non-sinusoidal Excitation	130
6.4 Conclusions	136
Chapter 7 Dynamic Modelling of Non-Oriented Electrical Steels.....	138
7.1 Fitting the Model to the Measurement Data of NOESs collected using an SST	138
7.1.1 Modelling Results of NOESs for measurement data collected using an SST..	139
7.1.2 Energy Losses Evaluation of NOESs	144
7.2 Fitting the Model to the Measurement Data of NOESs collected using an Epstein Frame	145
7.2.1 Modelling Results of NOESs for measurement data collected using an Epstein Frame	146
7.2.2 Energy Losses Evaluation of NOESs	151
7.3 Conclusions	152
Chapter 8 A novel energy loss separation model of ferromagnetism	153
8.1 New Energy loss Separation Model derivation	153
8.2 Energy loss modelling for GOESs	159
8.3 Energy loss modelling for NOESs	164
8.4 Summary	171
Chapter 9 Summary and Conclusion.....	172
9.1 Summary.....	172
9.2 Conclusion and future work	173
References	176
Appendix I – Research Outcomes	184
Appendix II – Journal Paper	185
Appendix III – Conference Posters.....	204

List of Figure Captions

Fig. 1.1 Schematic of a narrow transverse cavity of free space within a ferromagnetic lamination.....	27
Fig. 1.2 Typical hysteresis loops of a NOES.....	29
Fig. 1.3 Example of a grain-oriented electrical steel surface’s microstructure, based in a 30x30mmx0.27mm sample [12].....	30
Fig. 1.4 Schematic of a Bloch wall separating two domains, leading to a 180° angular displacement [14].	30
Fig. 1.5 Schematic anisotropic domain structures in a single crystal iron.	32
Fig. 1.6 Schematic isotropic domain structures in a single crystal iron.	32
Fig. 1.7 Magnetisation curves of a typical GOES measured for different orientation angles [16].....	34
Fig. 1.8 Magnetisation curves of typical NOESs measured for different orientation angles [16].....	35
Fig. 1.9 Hysteresis loop for GOES and NOES at 50Hz.	36
Fig. 1.10 Cube and Goss texture with crystallographic grain orientation [17].....	36
Fig. 1.11 A schematic of the different microstructures found in GOES and NOES [17].	37
Fig. 2.1 Single steel sheet under magnetisation test.....	39
Fig. 2.2 Static and dynamic hysteresis loops for GOESs measured with an Epstein frame at controlled sinusoidal induction for $f = 50$ Hz and $B_{pk} = 1.7$ T [1].....	42
Fig. 2.3 Comparison of measured and calculated hysteresis loops of GOESs for $g(B) = \text{constant}$ [1].....	43
Fig. 2.4 Comparison of measured and calculated hysteresis loops of GOESs for $g(B) = \text{variable}$ where $G_m = 0.38 (A/m) \cdot (s/T)^{0.5}$ and $k_1 = 0.576 1/T^2$ [1].....	44
Fig. 2.5 Comparison of measured hysteresis loops of GOESs with dynamic loops calculated with two components [1].	45
Fig. 2.6 Loop of B vs H_{clas} for GOESs at frequency 60 Hz and peak flux density 1.5 T [48].....	50
Fig. 2.7 Loop of B vs H_{clas} for NOESs at frequency 60 Hz and peak flux density 1.5 T [48].....	50
Fig. 2.8 Loss separation for NOESs at magnetisation frequency 60 Hz and peak flux density 1.5 T with final grain size 11 μm [48].....	51
Fig. 2.9 Loss separation for NOESs at magnetisation frequency 60 Hz and peak flux density 1.5 T with final grain size 58 μm [48].....	51
Fig. 2.10 Loss separation for NOESs at magnetisation frequency 60 Hz and peak flux density 1.5 T with final grain size 62 μm [48].....	52

Fig. 2.11 Loss separation for GOESs at magnetisation frequency 60 Hz and peak flux density 1.5 T [48].	52
Fig. 2.12 Loss separation for GOESs at magnetisation frequency 100 Hz and peak flux density 1.5 T [48].	53
Fig. 2.13 Measurement of Initial magnetisation curve, Hysteresis curve and An hysteretic magnetisation curve for isotropic soft magnetic material [53].	54
Fig. 2.14 (a) A magnetic moment m in the spherical coordinate system, angles θ and φ are polar coordinates. (b) Anisotropic orientations for specific cases: 1D, 2D and 3D, the magnetic field H is applied along Z direction; K_u is anisotropy constant and γ is the direction of anisotropy [54].	54
Fig. 2.15 An hysteretic magnetisation curves calculated for various values of anisotropy constants and in different anisotropic directions [54].	56
Fig. 2.16 The hysteresis loop calculated from solution of the J-A model equations with $M_s = 1.7 \times 10^6$ A/m, $a = 1000$ A/m, $k = 500$ A/m, $\alpha = 0.001$, $c = 0.1$ [57].	58
Fig. 2.17 The hysteresis loop calculated from solution of the J-A model equations with $M_s = 1.7 \times 10^6$ A/m, $a = 1000$ A/m, $k = 2000$ A/m, $\alpha = 0.001$, $c = 0.1$ [57].	58
Fig. 2.18 The hysteresis loop calculated from solution of the J-A model equations with $M_s = 1.7 \times 10^6$ A/m, $a = 1000$ A/m, $k = 2000$ A/m, $\alpha = 0.0017$, $c = 0.1$ [57].	59
Fig. 2.19 The hysteresis loop calculated from solution of the J-A model equations with $M_s = 1.2 \times 10^6$ A/m, $a = 1.2 \times 10^5$ A/m, $k = 5 \times 10^5$ A/m, $\alpha = 0.5$, $c = 0.05$ [57].	59
Fig. 2.20 The AM curve and hysteresis loops of the anisotropic magnetic material calculated with the J - A model's parameters: $M_s = 1.3 \times 10^6$ A/m, $a = 1000$ A/m, $k = 5000$ A/m, $\alpha = 0.001$. $c = 0.05$. The magnetisation is parallel to the easy axis ($\psi = 0$) [59].	62
Fig. 2.21 The AM curve and hysteresis loops of the anisotropic magnetic material calculated with the J-A model's parameters: $M_s = 1.3 \times 10^6$ A/m, $a = 1000$ A/m, $k = 5000$ A/m, $\alpha = 0.001$. $c = 0.05$. The magnetisation is parallel to the easy axis ($\psi = 90^\circ$) [59].	63
Fig. 2.22 Comparison of hysteresis loops between measured (points), calculated with improved J-A model (solid line) and original J-A model (dashed line) [60].	64
Fig. 2.23 Comparison of hysteresis loops between measured, calculated with improved arctangent model and original J-A model [61].	64
Fig. 2.24 Comparison of hysteresis loops between measured, calculated with modified and original J-A model [62].	65
Fig. 2.25 Comparison of hysteresis loops between measured and calculated hysteresis loops using the improved J-A model [63].	65
Fig. 2.26 Preisach relay operator [65].	66
Fig. 2.27 Preisach model block diagram [66].	67
Fig. 2.28 Hysteresis curves generated using Preisach model with different numbers of hysterons [67].	68
Fig. 2.29 Hybrid hysteresis model construction [69].	69

Fig. 2.30 Comparison of calculated and measured $B - H$ loops of GOES at excitation frequency $f = 50$ Hz [69].	69
Fig. 2.31 Comparison of calculated and measured $B - H$ loops of NOES at excitation frequency $f = 50$ Hz [69].	70
Fig. 3.1 SST with double yoke measuring coil system.	72
Fig. 3.2 Schematic of Single sheet tester with sample.	73
Fig. 3.3 Circuit for determining the total loss and magnetic flux density [71].	74
Fig. 3.4 Circuit for measuring the excitation current and magnetic field strength [71].	74
Fig. 3.5 Schematic diagram of computer - controlled SST measurement system.	75
Fig. 3.6 Epstein Frame with squared coil arrangement.	76
Fig. 3.7 Schematic of an Epstein frame and samples.	76
Fig. 3.8 Circuit for the core loss measurement [73].	77
Fig. 3.9 Circuit for measuring the magnetising current and peak magnetic field strength using a voltmeter [73].	78
Fig. 3.10 Computer-controlled measurement system of Epstein frame [74].	78
Fig. 3.11 Hysteresis loops for NOESs at 50 Hz and 1.3 T measured using SST and Epstein Frame.	79
Fig. 3.12 Hysteresis loops for NOESs at 100 Hz and 1.3 T measured using SST and Epstein Frame.	80
Fig. 3.13 Hysteresis loops for NOESs at 200 Hz and 1.3 T measured using SST and Epstein Frame.	80
Fig. 3.14 Hysteresis loops for NOESs at 400 Hz and 1.3 T measured using SST and Epstein Frame.	81
Fig. 3.15 Hysteresis loops for NOESs at 800 Hz and 1.3 T measured using SST and Epstein Frame.	81
Fig. 3.16 Energy losses per cycle for NOESs at 50 - 800 Hz and 1.3 T measured using SST and Epstein Frame.	82
Fig. 4.1 Domain variations in NOES during the magnetisation procedure.	87
Fig. 4.2 Domain variations in GOES during the magnetisation procedure.	88
Fig. 4.3 Control loop of the measurement system with field separation components.	90
Fig. 4.4 Waveforms of magnetic field and magnetic flux density.	90
Fig. 4.5 Magnetic field, hysteresis field and excitation field in a spiral up magnetisation process.	93
Fig. 4.6 Corresponding hysteresis field of magnetisation processes.	93
Fig. 4.7 Magnetic field, excitation field, and magnetic flux density for NOES at 50 Hz and 1.4 T.	100
Fig. 4.8 Hysteresis loop and single curves for NO steel at 50 Hz and 1.4 T.	101

Fig. 4.9 Magnetic field, excitation field, and magnetic flux density for GOESs at 50 Hz and 1.7 T.	101
Fig. 4.10 Hysteresis loop and single curves for GOESs at 50 Hz and 1.7 T.	101
Fig. 5.1 Typical domain patterns for ferromagnetic materials. Top row anisotropic case: (a) demagnetised state; (b) in the presence of an excitation field. Bottom row isotropic case: (c) demagnetised state; (d) in the presence of an excitation field.	108
Fig. 5.2 Flowchart of hysteresis modelling using new hysteresis model.	115
Fig. 5.3 Measured hysteresis loop for GOES at a magnetisation frequency of 50 Hz and peak flux density of 1.7 T.	115
Fig. 5.4 Single curves for GOES at a frequency of 50 Hz and peak flux density of 1.7 T, obtained by displacing the measured ascending and descending curve of the hysteresis loop in Fig 5.3. an amount H_c to the left and right, respectively.	116
Fig. 5.5 Overlapping single curves for GOES at a frequency of 50 Hz and peak flux density of 1.7 T, obtained by rotating the ascending curve through 180° about both the B and h axis.	116
Fig. 5.6 Superimposed modelled and obtained single curves for GOES at a frequency of 50 Hz and peak flux density of 1.7 T.	117
Fig. 5.7 Measured and modelled hysteresis loop for GOES at a frequency of 50 Hz and peak flux density of 1.7 T superimposed against the corresponding measured data.	118
Fig. 6.1 Single curves of GOESs derived from the loops measured at a frequency of 50 Hz and peak flux densities ranging from 1.0 to 1.7 T under sinusoidal flux density.	120
Fig. 6.2 Single curves of GOESs derived from the loops measured at a frequency of 100 Hz and peak flux densities ranging from 1.0 to 1.7 T under sinusoidal flux density.	120
Fig. 6.3 Single curves of GOESs derived from the loops measured at a frequency of 200 Hz and peak flux densities ranging from 1.0 to 1.7 T under sinusoidal flux density.	122
Fig. 6.4 Single curves of GOESs derived from the loops measured at a frequency of 400 Hz and peak flux densities ranging from 1.0 to 1.7 T under sinusoidal flux density.	122
Fig. 6.5 Single curves of GOESs derived from the loops measured at a frequency of 800 Hz and peak flux densities ranging from 1.0 to 1.7 T under sinusoidal flux density.	123
Fig. 6.6 Single curves of GOESs derived from the loops measured at a frequency of 1000 Hz and peak flux densities ranging from 1.0 to 1.7 T under sinusoidal flux density.	123
Fig. 6.7 Modelled contiguous curve sections, 6 in total, superimposed on the corresponding measured single curve for GOESs measured at a frequency of 800 Hz and peak flux density of 1.7 T under sinusoidal flux density.	124
Fig. 6.8 Comparison between modelled and measured hysteresis loops for GOESs at 50 Hz and peak flux densities ranging from 1.0 T to 1.7 T under sinusoidal flux density.	125

Fig. 6.9 Comparison between modelled and measured hysteresis loops for GOESs at 100 Hz and peak flux densities ranging from 1.0 T to 1.7 T under sinusoidal flux density. ...	125
Fig. 6.10 Comparison between modelled and measured hysteresis loops for GOESs at 200 Hz and peak flux densities ranging from 1.0 T to 1.7 T under sinusoidal flux density. ...	125
Fig. 6.11 Comparison between modelled and measured hysteresis loops for GOESs at 400 Hz and peak flux densities ranging from 1.0 T to 1.7 T under sinusoidal flux density. ...	126
Fig. 6.12 Comparison between modelled and measured hysteresis loops for GOESs at 800 Hz and peak flux densities ranging from 1.0 T to 1.7 T under sinusoidal flux density. ...	126
Fig. 6.13 Comparison between modelled and measured hysteresis loops for GOESs at 1000 Hz and peak flux densities ranging from 1.0 T to 1.7 T under sinusoidal flux density.	126
Fig. 6.14 Comparison between calculated and measured energy losses per cycle for GOESs at frequencies from 50 Hz to 1000 Hz and peak flux densities from 1.0 T to 1.7 T.	128
Fig. 6.15 Energy loss errors between the modelled and measured energy losses for GOESs at frequencies from 50 Hz to 1000 Hz and peak flux densities from 1.0 T to 1.7 T.	128
Fig. 6.16 Single Curves for GOESs under non-sinusoidal excitation at a frequency of 50 Hz and peak flux density of 1.0 T with 3 rd , 7 th , and 11 th harmonics.	132
Fig. 6.17 Single Curves for GOESs under non-sinusoidal excitation at a frequency of 50 Hz and peak flux density of 1.1 T with 3 rd , 7 th , and 11 th harmonics.	132
Fig. 6.18 Single Curves for GOESs under non-sinusoidal excitation at a frequency of 50 Hz and peak flux density of 1.3 T with 3 rd , 7 th , and 11 th harmonics.	133
Fig. 6.19 Single Curves for GOESs under non-sinusoidal excitation at a frequency of 50 Hz and peak flux density of 1.5 T with 3 rd , 7 th , and 11 th harmonics.	133
Fig. 6.20 Single Curves for GOESs under non-sinusoidal excitation at a frequency of 50 Hz and peak flux density of 1.7 T with 3 rd , 7 th , and 11 th harmonics.	134
Fig. 6.21 Comparison of hysteresis loops for GOESs under non-sinusoidal excitation at a frequency of 50 Hz and peak flux density of 1.0 T with 3 rd , 7 th , and 11 th harmonics.....	134
Fig. 6.22 Comparison of hysteresis loops for GOESs under non-sinusoidal excitation at a frequency of 50 Hz and peak flux density of 1.1 T with 3 rd , 7 th , and 11 th harmonics.....	135
Fig. 6.23 Comparison of hysteresis loops for GOESs under non-sinusoidal excitation at a frequency of 50 Hz and peak flux density of 1.3 T with 3 rd , 7 th , and 11 th harmonics.....	135
Fig. 6.24 Comparison of hysteresis loops for GOESs under non-sinusoidal excitation at a frequency of 50 Hz and peak flux density of 1.5 T with 3 rd , 7 th , and 11 th harmonics.....	136
Fig. 6.25 Comparison of hysteresis loops for GOESs under non-sinusoidal excitation at a frequency of 50 Hz and peak flux density of 1.7 T with 3 rd , 7 th , and 11 th harmonics.....	136
Fig. 7.1 Single Curves for NOESs under sinusoidal excitation at a frequency of 50 Hz and peak flux densities ranging from 1.0 T to 1.4 T.	139

Fig. 7.2 Single Curves for NOESs under sinusoidal excitation at a frequency of 100 Hz and peak flux densities ranging from 1.0 T to 1.4 T.	140
Fig. 7.3 Single Curves for NOESs under sinusoidal excitation at a frequency of 200 Hz and peak flux densities ranging from 1.0 T to 1.4 T.	140
Fig. 7.4 Single Curves for NOESs under sinusoidal excitation at a frequency of 400 Hz and peak flux densities ranging from 1.0 T to 1.4 T.	141
Fig. 7.5 Single Curves for NO steel under sinusoidal excitation at a frequency of 800 Hz and peak flux densities ranging from 1.0 T to 1.4 T.	141
Fig. 7.6 Comparison of hysteresis loops for NOESs under sinusoidal excitation at 50 Hz and peak flux densities ranging from 1.0 T to 1.4 T.	142
Fig. 7.7 Comparison of hysteresis loops for NOESs under sinusoidal excitation at 100 Hz and peak flux densities ranging from 1.0 T to 1.4 T.	142
Fig. 7.8 Comparison of hysteresis loops for NOESs under sinusoidal excitation at 200 Hz and peak flux densities ranging from 1.0 T to 1.4 T.	143
Fig. 7.9 Comparison of hysteresis loops for NOESs under sinusoidal excitation at 400 Hz and peak flux densities ranging from 1.0 T to 1.4 T.	143
Fig. 7.10 Comparison of hysteresis loops for NOESs under sinusoidal excitation at 800 Hz and peak flux densities ranging from 1.0 T to 1.4 T.	144
Fig. 7.11 Comparison between the calculated and measured energy losses per cycle for NOESs at frequencies from 50 Hz to 800 Hz and peak flux densities from 1.0 T to 1.4 T.	144
Fig. 7.12 Energy loss errors for NOESs under sinusoidal excitation at frequencies from 50 Hz to 800 Hz and peak flux densities from 1.0 T to 1.4 T.	145
Fig. 7.13 Single Curves for NOESs under sinusoidal excitation at a frequency of 50 Hz and peak flux densities ranging from 1.0 T to 1.5 T.	146
Fig. 7.14 Single Curves for NOESs under sinusoidal excitation at a frequency of 100 Hz and peak flux densities ranging from 1.0 T to 1.5 T.	147
Fig. 7.15 Single Curves for NOESs under sinusoidal excitation at a frequency of 200 Hz and peak flux densities ranging from 1.0 T to 1.5 T.	147
Fig. 7.16 Single Curves for NOESs under sinusoidal excitation at a frequency of 400 Hz and peak flux densities ranging from 1.0 T to 1.5 T.	148
Fig. 7.17 Single Curves for NOESs under sinusoidal excitation at a frequency of 800 Hz and peak flux densities ranging from 1.0 T to 1.5 T.	148
Fig. 7.18 Comparison of hysteresis loops for NOESs under sinusoidal excitation at 50 Hz and peak flux densities ranging from 1.0 T to 1.5 T.	149
Fig. 7.19 Comparison of hysteresis loops for NOESs under sinusoidal excitation at 100 Hz and peak flux densities ranging from 1.0 T to 1.5 T.	149
Fig. 7.20 Comparison of hysteresis loops for NOESs under sinusoidal excitation at 200 Hz and peak flux densities ranging from 1.0 T to 1.5 T.	150

Fig. 7.21 Comparison of hysteresis loops for NOESs under sinusoidal excitation at 400 Hz and peak flux densities ranging from 1.0 T to 1.5 T.	150
Fig. 7.22 Comparison of hysteresis loops for NOESs under sinusoidal excitation at 800 Hz and peak flux densities ranging from 1.0 T to 1.5 T.	151
Fig. 7.23 Comparison between calculated and measured energy losses per cycle for NOESs under sinusoidal excitation at frequencies of 50 Hz to 800 Hz and peak flux densities ranging from 1.0 T to 1.5 T.	151
Fig. 7.24 Energy loss errors for NOESs under sinusoidal excitation at frequencies of 50 Hz to 800 Hz and peak flux densities ranging from 1.0 T to 1.5 T.	152

Fig. 8.1 The magnetisation of GOES.	154
Fig. 8.2 The magnetisation of NOES.	154
Fig. 8.3 Magnetisation process intertwined with the magnetic field, hysteresis field, magnetisation field and eddy current field.	156
Fig. 8.4 Eddy current and related field.	157
Fig. 8.5 Magnetic field components calculated for a GOES magnetised at a frequency of 50 Hz and peak flux density of 1.7 T.	160
Fig. 8.6 Hysteresis loops based on magnetic field components calculated for a GOES at a frequency 50 Hz and peak flux density of 1.7 T.	160
Fig. 8.7 Energy loss components per cycle calculated for GOESs magnetised at frequency 50 Hz and peak flux densities from 1.0 T to 1.7 T.	161
Fig. 8.8 Energy loss component per cycle proportions calculated for GOESs magnetised at frequency 50 Hz and peak flux densities from 1.0 T to 1.7 T.	161
Fig. 8.9 Magnetic field components calculated for GOESs magnetised at frequency 100 Hz and peak flux density 1.7 T.	162
Fig. 8.10 Hysteresis loops based on magnetic field components calculated for GOESs at frequency 100 Hz and peak flux density 1.7 T.	163
Fig. 8.11 Energy loss components per cycle calculated for GOESs magnetised at frequency 100 Hz and peak flux densities from 1.0 T to 1.7 T.	163
Fig. 8.12 Energy loss component proportions per cycle calculated for GOESs magnetised at frequency 100 Hz and peak flux densities from 1.0 T to 1.7 T.	164
Fig. 8.13 Magnetic field components calculated for NOESs magnetised at frequency 50 Hz and a peak flux density of 1.4 T.	165
Fig. 8.14 Hysteresis loops based on magnetic field components calculated for NOESs at frequency 50 Hz and a peak flux density of 1.4 T.	166
Fig. 8.15 Energy loss components per cycle calculated for NOESs magnetised at frequency 50 Hz and peak flux densities from 1.0 T to 1.4 T.	166
Fig. 8.16 Energy loss component per cycle proportions calculated for NOESs magnetised at frequency 50 Hz and peak flux densities from 1.0 T to 1.4 T.	167

Fig. 8.17 Magnetic field components calculated for NOESs magnetised at frequency 100 Hz and peak flux density 1.4 T.168

Fig. 8.18 Hysteresis loops based on magnetic field components calculated for NOESs at frequency 100 Hz and peak flux density 1.4 T.168

Fig. 8.19 Energy loss components per cycle calculated for NOESs magnetised at frequency 100 Hz and peak flux densities from 1.0 T to 1.4 T.169

Fig. 8.20 Energy loss component per cycle expressed as a percentage for NOESs magnetised at frequency 100 Hz and peak flux densities from 1.0 T to 1.4 T.170

List of Table Captions

Table 2.1 Parameters in the J-A model.....	61
Table 2.2 Parameters in the J-A model extension.....	61
Table 3.1 Energy losses for NOESs at 50 - 800 Hz and 1.3 T measured using SST and Epstein Frame.....	82
Table 4.1 Comparison of WMF Feedback effects and PID controller outputs.....	91
Table 5.1 Parameters associated with equation (5.28) for obtaining the magnetising and demagnetising curve sections of Fig. 5.5 for GOES magnetised at a frequency of 50 Hz and peak flux density of 1.7 T.....	117
Table 6.1 Parameters associated with equation (5.30) used to obtain the contiguous magnetisation and demagnetisation curve sections, 6 in total, of Fig. 6.7 magnetised for GOES at a frequency of 800 Hz and peak flux density of 1.7 T.	124
Table 8.1 Energy loss components per cycle calculated for GOESs magnetised at frequency 50 Hz and peak flux densities from 1.0 T to 1.7 T.	162
Table 8.2 Energy loss components per cycle calculated for GOESs magnetised at frequency 100 Hz and peak flux densities from 1.0 T to 1.7 T.	164
Table 8.3 Energy loss components per cycle calculated for NOESs magnetised at frequency 50 Hz and peak flux densities from 1.0 T to 1.4 T.	167
Table 8.4 Energy loss components per cycle calculated for NOESs magnetised at frequency 100 Hz and peak flux densities from 1.0 T to 1.4 T.	170

Chapter 1 Introduction

1.1 Background

Ferromagnetic materials, such as grain-oriented electrical steels (GOESs) and non-oriented electrical steels (NOESs), are the crucial components of electromagnetic devices. According to [1], more than 90% of transformer cores are assembled using GOESs, while for large transformers (> 10 KVa) a vast number are constructed using magnetic cores that are fully processed or semi-processed NOESs. NOESs are widely used in industry, from large motors and generators that require good isotropic magnetic properties to EI laminates for small transformers. Power networks and their efficiency have been ameliorated significantly in recent years due to usage of advanced electrical steels, the demand for which is increasing in tandem with the growth of electrical power infrastructure and the rapid spread in the move to renewable energy sources, a trend resulting from the installation of more wind turbines and power transformers in urban areas and offshore regions.

The modelling of the transient response of an electromagnetic machine within a power system is vital for determining the resilience and stability of a power grid. For this purpose, it is desirable to be able to generate, via simulation, the magnetic hysteresis loops of the core material during regular operation, short-circuit current and peak load shaving. An accurate interpretation of the magnetisation processes in GOESs and NOESs is essential to take full advantage of the power transformers, motors, converters, and generators in a power system. The capability to embed hysteretic models in the equivalent circuits is also critical, so that modelling of electromagnetic machines can be explored under unexpected conditions. Despite this, a general physical model which satisfactorily describes the magnetisation processes in GOESs and NOESs remains an unresolved conundrum for physicists and engineers alike.

Predicting the energy loss associated with GOESs and NOESs under sinusoidal waveform excitations is essential to facilitate the design, application, and maintenance of electromagnetic devices. It is especially critical when magnetic cores are operated under high voltage and current excitations in the case of power transformers used in high voltage transmission systems. It is a long-established fact that both high frequency and high peak flux density affect and significantly exacerbate the core loss, making the prediction of energy loss difficult using conventional models and standardised experimental setups. Accordingly, the modelling of magnetisation processes at high frequencies has remained an unsolved problem, with few references to be found in the literature that have addressed this problem.

Conventional hysteresis models, such as those of Jiles-Atherton (J-A) [2, 3] or Preisach models [4], are widely used for interpreting the hysteretic behaviour of soft magnetic materials. Nevertheless, the accuracy needed to address hysteresis effects in GOESs and NOESs has remained a hindrance to their applications. In order to accurately describe the magnetic properties and predict the energy loss associated with GOESs and NOESs under arbitrary excitation waveforms for renewable energy systems, it is necessary to apply a hysteresis model directly that is able to reproduce the measured hysteresis loops for the electrical steel sheets. The thrust of the research reported in this thesis is the formation of an accurate model for interpreting magnetic hysteresis and calculating magnetic core losses by analysing related experimental data and using the model to track hysteresis loops.

1.2 Research Objectives

The modelling of magnetic hysteresis has been of great interest to scientists and engineers for more than a century as a means of interpreting the process of magnetisation and for improving the application of magnetic materials. As a result, research has been conducted involving intensive systematic investigation, with remarkable achievements having been made that have boosted the prosperity of the electrical power industries. So far, The J-A [2, 3] and Preisach [4] models have proved the most popular; many of the other models available are essentially derivatives of these two based on similar approaches and theories.

Magnetic hysteresis is the phenomenon of magnetic flux density lagging the magnetic field, so these two variables are the primary target of measurements using standardised experimental approaches. Some researchers ascribed the magnetic hysteresis phenomenology to the domain wall pinning sites that generate the friction forces opposing the domain wall motion [2, 3]. This assertion has been instrumental in understanding hysteretic phenomena caused by force holding back the magnetisation processes. However, this explanation is questionable because the pinning sites are caused by the impurity of silicon content. This implies the greater the silicon contents, the more hysteresis force is caused by the pinning sites, leading to more hysteresis loss during magnetisation processes. This, in turn, contradicts the fact that a greater silicon content results in less energy loss in magnetic materials. Therefore, the physical mechanism of the authentic hysteretic force is worth exploring. Meanwhile, the effects of the domain wall pinning sites also occur in initial magnetisation processes, but the initial magnetisation curves show no evidence of hysteresis. Hysteresis occurs when the directions of the magnetic field and magnetic flux density are changed.

In 1906, Pierre Weiss [5] proposed his famous hypothesis of the molecular field, resulting in his well-known domain theory, which had been instrumental in understanding

ferromagnetic features in magnetisation processes. In 1958, Pry and Bean [6] presented their PB model enabling the loss calculation of ferromagnetic materials according to the analysis of the motion of rigid domain walls normal to the sheet surfaces. In 1988, Bertotti [7] asserted that energy loss prediction based on domain wall motion of regular domain structures are of limited validity due to their oversimplified nature. Since then, attempts to establish a magnetisation model adopting a domain concept were discarded, with researchers turning to other theories to build an entirely new model to describe the magnetic properties, for which it is vital to understand clearly the physical mechanism underpinning the magnetisation processes.

The best approach for developing a novel model is to conduct a combined theoretical and experimental investigation. To realise this goal the following research objectives were followed in the work reported here:

1. To develop new analytical and experimental approaches to evaluate the performance of GOESs and NOESs under sinusoidal and non-sinusoidal excitation, in accordance with the relevant British Standards.

2. To collect corresponding data associated with the electrical and magnetic quantities of electrical machines and transformers, including power loss, magnetic flux density, and magnetic hysteresis loop under sinusoidal and non-sinusoidal excitation using a standardised experimental setup.

3. To explore the physical mechanism underpinning the magnetisation processes of ferromagnetism by considering classical magnetics, electromagnetics and micromagnetics.

4. To investigate the ability of existing models to simulate measurement data and choose the best approaches to undertake the research.

5. To derive novel models based on a theoretical analysis to describe the magnetisation processes, generate magnetic hysteresis loops, and to verify the same model using corresponding measurement data.

The measurement data was processed using MATLAB code to evaluate existing and new models. Finally, a comparison between the modelling predictions and measured values was made to ascertain the efficacy of the project.

The primary purpose of the research project to facilitate the understanding of the physical mechanisms associated with electrical steel, has been achieved through a combined analytical, experimental, and theoretical approach. The novel theoretical development has led to the derivation of an accurate mathematical model for explaining the magnetisation processes and predicting the core loss associated with electrical steels.

This general physical model and new energy loss separation model (ELSM) have been employed for GOESs and NOESs and verified against corresponding experimental data collected in tandem, shedding new light on understanding the mechanism of magnetisation.

1.3 Fundamental Magnetism

This section introduces the fundamental theory of magnetism and reviews the basic concepts of magnetics, essential to the comprehension of electromagnetics that form the basis of the work reported in this thesis. It concludes with a discussion of the magnetisation characteristics of soft magnetic materials to fully understand the physical underpinnings of ferromagnetism.

1.3.1 Magnetic Field

A magnetic field is caused by electrical charge motion. The magnetic force forms an energy field that can accelerate an electrical charge moving in the field, push or pull a current-carrying conductor, and exert torque on a magnetic dipole such as a compass needle. The magnetic field even reorientates the spinning and affects the motion of electrons within certain types of atoms.

The SI (International System) unit of magnetic field strength H is amperes per metre (A/m) under the excitation current. There are two definitions of amperes per meter. The first is for H generated by an unlimited long solenoid, with n coil turns per metre, and the current is $1/n$ amperes. The second definition is for the case of an H of $1/4n$ amperes per meter produced by a 1-meter-long straight conductor at a radial distance of 1 meter with a current of 1 ampere [8].

H generated by an electrical current is described according to Ampere's law [8], which is expressed mathematically as:

$$Ni = \int_s Hdl, \quad (1.1)$$

where N is the coil number of the current-carrying solenoid, each carrying a steady current i . The magnetic field H is excited by the current passing through the solenoid. l is the unit vector normal to the surface. The total Ampere-turn equals the line integral of H around a closed surface surrounded by the current.

1.3.2 Magnetic Induction

Magnetic induction B , i.e., the magnetic flux density, is the response of a medium to an external H generated by a current or voltage source. The unit of B is Tesla (T), which is equivalent to one weber per meter squared (1 Wb/m^2). One Tesla represents one kilogram per second squared per ampere ($\text{kg/s}^2/\text{A}$).

In many substances, such as diamagnetism and paramagnetism, B is a linear function of H . In free space, B is given [8] by:

$$B = \mu_0 H, \quad (1.2)$$

where μ_0 is the permeability of free space, which is a universal constant. The unit of μ_0 is expressed as (volt second)/ (amp metre), also known as Henries/metre. The value in SI units is given as $\mu_0 = 1.25663706212 \times 10^{-6}$ H/m [9, 10].

In other substances, such as ferromagnetism, antiferromagnetism and ferrimagnetism, B is not a linear function of H , the response being more complicated. The mapping from B to H is a functional relationship of one-to-two (One magnetic field value corresponds to two magnetic flux density values in the hysteresis loop and B is expressed [8] as:

$$B = \mu H, \quad (1.3)$$

where μ is the permeability of the substance, which varies with H and expressed as:

$$\mu = \mu_0 \mu_r, \quad (1.4)$$

where μ_r is the relative permeability and is the ratio of the permeability of a specific medium to the permeability of free space μ_0 .

1.3.3 Magnetisation

Magnetisation M is defined as the magnetic moment per unit volume of a solid substance. In SI units M is measured in ampere per metre and expressed [8] as:

$$M = \frac{\sum m_i}{V}, \quad (1.5)$$

where $\sum m_i$ is the vector sum of all individual magnetic moments and V is the whole volume; in other words, M is the average distribution of magnetic moments in the material.

The concept of a magnetic moment is essential to analyse the magnetic properties of magnetic materials because electron motion and self-spinning in an atom generate a current that produces a magnetic moment. The sum of the magnetic moments in the substance contribute to the magnetic characteristics.

1.3.4 Magnetic Polarisation

The magnetic polarisation J is the value that quantifies the response of a magnetic material to an external magnetic field. The response arises through domain rearrangement leading to the realignment of internal magnetic dipole moments. Polarisation represents the same quantity as M but scaled by μ_0 . The unit of polarisation is T, the same as B , and is expressed [8] as:

$$J = \mu_0 M. \quad (1.6)$$

It is worth noting that M (A/m) and J (T) represent averaged quantities. Their values are calculated over the whole material spanning many individual magnetic domains and the vector sum of all magnetic moments.

1.3.5 Relationship Between H , M and B

B consists of two components; one is from H ; other one is from M . H is produced either by an exciting current or voltage source outside the material via a solenoid or electromagnet or by a permanent magnet. M results from the vector sum of the spinning magnetic moment and orbital angular momentum of electrons in the atoms within the substance.

B can be observed from the cross-section AA' by considering a very narrow transverse cavity of free space with a south pole and a north pole existing inside a ferromagnetic lamination, as shown in Fig. 1.1.

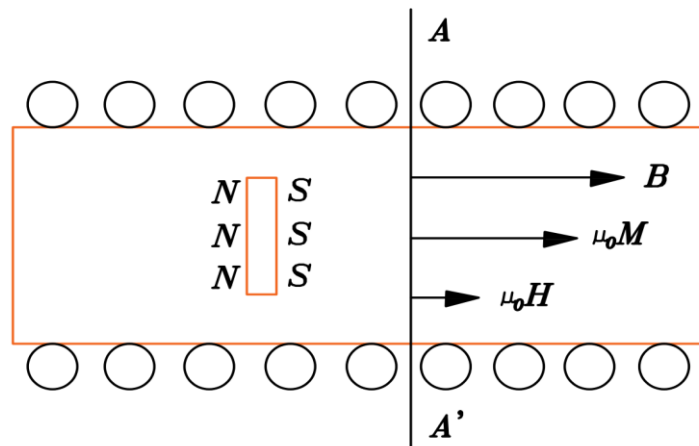


Fig. 1.1 Schematic of a narrow transverse cavity of free space within a ferromagnetic lamination.

H excited by the current in the magnetising winding, see equation (1.1), crosses this gap, and contributes a portion of B equal to $\mu_0 H$. This magnetic flux density component is the same regardless of whether there is any material or not in the lamination.

In addition, H , acting from left to right, magnetises the material to produce M on the surface of the cavity, just like a magnetic pole is produced on the ends of a magnetised bar. The contribution to the induction from M is $\mu_0 M$, such that B is simply the vector sum of these two components [8]:

$$B = \mu_0(H + M). \quad (1.7)$$

Equation (1.7) reveals the relationship between these three fundamental magnetic quantities and is valid for all substances.

1.3.6 Zeeman Energy

The energy of B in the presence of H is calculated in terms of Zeeman Energy and expressed as [8]:

$$W = -H \cdot B. \quad (1.8)$$

The energy of the magnetic moment at the microscale is a basic definition for understanding the classical theory of magnetism, and the new model proposed in this thesis is derived by analysing the energy of the magnetic moment for the different domain patterns in magnetic materials.

The Zeeman energy is the energy that aligns the magnetic dipoles in a steel sheet with an external excitation field. So, the Zeeman energy is the fundamental causation of magnetic domain reconfiguration under the external H .

1.3.7 Magnetic Hysteresis Loop

The hysteresis loop is a four-quadrant $B - H$ plot representing the bulk magnetic properties of a ferromagnetic material. Alternatively, a plot of M vs H is used to describe the magnetisation processes, but these two plots contain slightly different information. The major and minor $B - H$ hysteresis loops of a typical NOES steel are shown in Fig. 1.2, this figure is created using the measurement data measured at 50 Hz and peak flux densities ranging from 1.0 T to 1.4 T.

The initial magnetisation curve connecting the origin to the major loop tip B_s represents the magnetisation process increasing H from 0 (under the demagnetised condition) until the M_s is reached for the first time. However, it should be noted that the magnetisation curve is irreversible, which means if H is decreased after saturation has been reached in the positive direction, the magnetisation curve will not follow the previous route.

When H is decreased to zero, the magnetic induction in the material will arrive at B_r , which is called the remanence or remanent induction. If the direction of H is then reversed by reversing the magnetising current in the winding, B will be reduced to zero when H equals the coercivity $-H_c$.

If H is further increased in the reverse direction, negative saturation will be reached at $-B_s$. If the field is turned to the initial direction and reduced to zero, B will arrive at $-B_r$. Then, when the magnetic field is increased to the coercivity H_c , the magnetic flux density reaches zero. Finally, if the magnetic field continues to increase, positive saturation will again be obtained.

The diagram forms a loop enclosed by the increasing curve (from $-B_s$ to B_s via $-B_r$) and decreasing curve (from B_s to $-B_s$ via B_r). This sigmoidal loop depicted is known as the major hysteresis loop, and the peak flux densities at both tips represent saturation flux densities. If the initial magnetisation process is interrupted at some intermediate point less than B_s and the magnetic field is reduced and further reversed, the magnetic flux density will travel around the minor hysteresis loop, which is produced when one or both extreme tips defining the loop is not $\pm B_s$. The increasing curve is symmetrical to the decreasing curve about the origin as a point of inversion, i.e., if the increasing curve is rotated 180 degrees about the origin, it will be the mirror image of the decreasing curve.

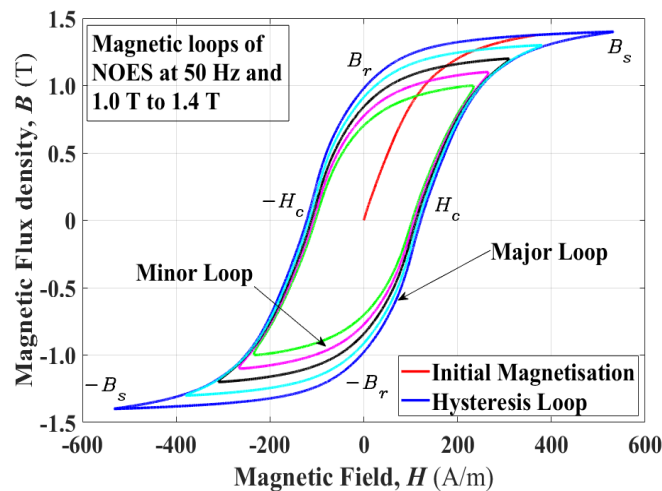


Fig. 1.2 Typical hysteresis loops of a NOES.

1.4 Domain Theory

In his famous papers, Pierre Weiss developed the domain theory of ferromagnetism [5, 11]. He asserted that magnetic domains existed in ferromagnetic materials which were cooled below the Curie temperature. Magnetic domains are small regions in a magnetic material, and in which the individual magnetic moments of the atoms are oriented spontaneously in a unitary direction. Typically, in such a domain, there are around 10^{12} to 10^{14} atomic magnetic moments aligned parallel so that the magnetisation of the domain reaches near saturation. Because the domains' moments are oriented randomly, all the magnetisations of the domains cancel out each other. So, the magnetic materials manifest no net magnetisation under no external magnetic field.

Magnetic domains universally exist in ferromagnetic, ferrimagnetic and antiferromagnetic materials. In paramagnetic and diamagnetic materials, the atomic dipoles orientate in response to an external magnetic field without spontaneous alignment, so these materials do not have magnetic domains. On the other hand, magnetic domain structure affects the magnetic properties of ferromagnetic materials, such as iron, nickel, cobalt, and their alloys dramatically. The subject of magnetic domains

is called micromagnetics, and the associated domain microstructure is as shown in Fig. 1.3 [12].

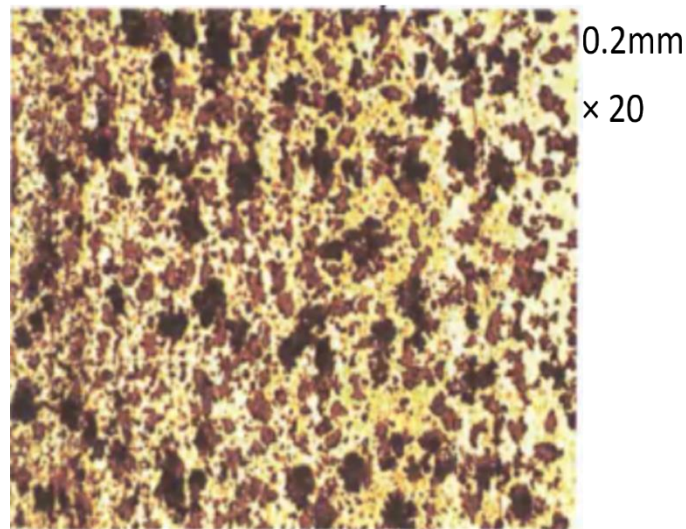


Fig. 1.3 Example of a grain-oriented electrical steel surface's microstructure, based in a 30x30mmx0.27mm sample [12].

The transition regions between magnetic domains are named domain walls. The domain walls in ferromagnetic materials are usually referred to as Bloch walls, suggested by Bloch in 1932 [13]. In these transition regions, the magnetic moments realign between adjacent domains magnetised in different directions and therefore belong to neither domain. The Bloch wall is visualised in Fig. 1.4 [14]. The total angular displacement across adjacent domain walls is usually 180° or 90° , especially in cubic materials, because of the anisotropy. The change in the direction of the magnetic moment gradually occurs on many atomic planes.

Magnetisation processes are completely dominated by the domain processes under an applied external field, including domain wall motion, domain rotation, domain annihilation, and domain nucleation.

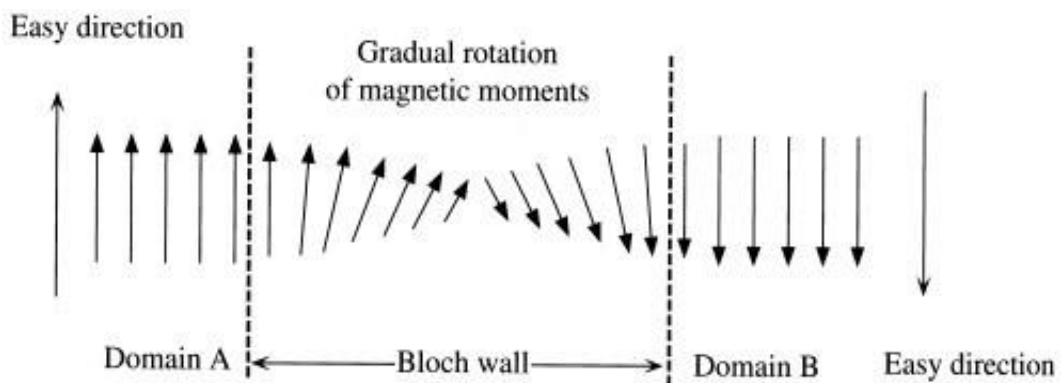


Fig. 1.4 Schematic of a Bloch wall separating two domains, leading to a 180° angular displacement [14].

1.4.1 Weiss mean field

The Weiss mean field (WMF) was proposed by Pierre Weiss according to Langevin's function of paramagnetism with an additional term. The mean field is caused by interatomic interaction, which gives rise to a specific alignment of neighbouring atomic magnetic moments due to the lowest energy caused in this configuration. In the original Weiss theory, the mean field, H_w , is expressed as being proportional to the bulk M [8]:

$$H_w = \alpha M, \quad (1.9)$$

where α is the mean field constant. In a domain of ferromagnetic materials, magnetisation and saturation occur simultaneously. So, the mean field of the atomic interaction which is responsible for the orientation of atomic moments within the domain can be expressed as:

$$H_w = \alpha M_s. \quad (1.10)$$

It should be noted that several different types of magnetic materials are determined by the ordering of the atomic interaction. When the parameter $\alpha > 0$, the ordering of neighbouring atoms is parallel, which leads to ferromagnetism. When $\alpha < 0$, the ordering is antiparallel, which leads to simple antiferromagnetism. When the ordered state is antiparallel with different magnitudes of the adjacent atomic moments so there is a local net magnetisation, materials composed of such ordering domains are termed ferrimagnetism.

1.4.2 Domain structures

There are tens or hundreds of domains in a square centimetre iron crystal, but it comprises two types of domain structures, i.e., anisotropic and isotropic domain structures. The minimum information required to describe a crystal structure consists of the unit cell type and the coordinates of an atom located at a cell corner, which are represented as (0, 0, 0). Atoms positioned along the cell edges are designated by coordinates such as (0, 0, 1), (0, 1, 0), or (1, 0, 0) [15]. As shown in Fig. 1.5a, the domains in demagnetised conditions are spontaneously magnetised to saturation in directions of the easy axes: [010], [100], [0 $\bar{1}$ 0], and [$\bar{1}$ 00]. This anisotropic domain structure has strong magnetic properties of preferred orientation, which is the main contribution of inhomogeneous magnetic materials. For example, if the sample is magnetised along the [010] direction with an H , the [010] domain will grow in volume at the expense of other domains by the mechanism of domain-wall motion, as illustrated in Fig. 1.5b.

This domain wall motion minimises the magnetic potential energy of the crystal during the magnetisation process. According to equation (1.8), the energy of a [010] domain in

the field is calculated to be $-M_s H$ per unit volume, that of the $[010]$ domain is $M_s H$, and that of the $[100]$ or $[100]$ domain is zero, respectively. Increasing the field to a certain value will eliminate all other domains except for the $[010]$ domain, and finally, the crystal is now a saturated single domain as shown in Fig. 1.5c. This result is achieved by applying a low H needed for pushing the domain wall motion.

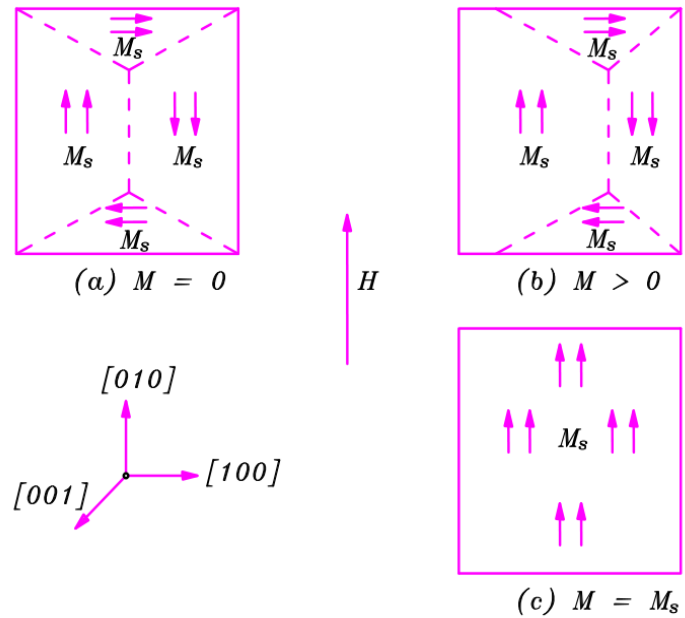


Fig. 1.5 Schematic anisotropic domain structures in a single crystal iron.

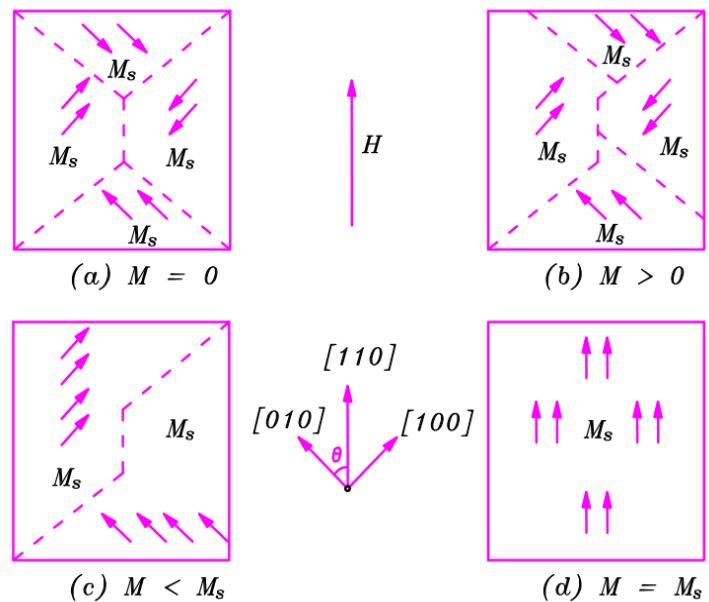


Fig. 1.6 Schematic isotropic domain structures in a single crystal iron.

Isotropic domain structure is shown in Fig. 1.6a, where the domains in demagnetised conditions are also spontaneously magnetised to saturation in directions of the easy axes: $[010]$, $[100]$, $[010]$, and $[100]$. Nevertheless, the H is in an arbitrary direction, which means that higher H , of the order of several hundred amperes per meter, are needed to saturate

iron in an arbitrary direction. It can be imagined that there are hundreds of thousands of domains in a magnetic material. If the isotropic domain structures dominate the magnetic material, these domains are oriented randomly so that this arbitrary magnetic direction will lead to a homogeneous structure; then isotropy is observed.

In this case, the H points in the $[110]$ direction, which has an arbitrary angle with the $[010]$ direction. For this H orientation, the alteration of domain structures during magnetisation is shown in Fig. 1.6. Domain wall motion happens continually until only two domains are left as shown in Fig. 1.6c, each with the same potential energy. The further increase of H can rotate the M_s vector of each domain until it is parallel with H , where the bulk M reaches its maximum value. This process is called domain rotation, which usually occurs only in a high H . To rotate the domain to the magnetic direction, the H needs to overcome the force of crystal anisotropy, which is usually quite strong. Crystal anisotropy is deemed a force that tends to hold the atomic magnetic moments in certain crystallographic directions in a crystal. When the rotation process is complete, the domain wall disappears, and the crystal is saturated in the H direction.

1.5 Electrical Steels

Electrical steels are Fe-Si alloys as Si is the primary alloying element added to steels to influence their physical properties positively. High-silicon alloys are used for special electrical steels because of their ability to decrease hysteresis losses, enlarge permeability, and increase electrical resistivity. However, it has some unfavourable consequences, including a decrease in the Curie temperature, reduction in saturation magnetization, and embrittlement of the alloy. These adverse effects become prominent when the silicon additions exceed approximately 2 wt.%. Despite these disadvantages, their enhanced magnetic properties have made silicon steel a superior choice for making the magnetic cores of transformers, motors, generators, and reactors. It is worth noting that almost 80% of the market is occupied by Fe-Si electrical steels, considering the proportion of various groups of soft magnetic materials [16].

Different magnetic properties are required depending on the type of application. In the case of electrical power and distribution transformers, the most important factors are low power loss and high saturation magnetisation. In the electrical power industry, the frequency of AC in the power grid is generally at relatively low rates, namely, 50-60 Hz. Electrical eddy currents are induced in the magnetic core under normal operations at these frequencies. Alloying the Fe with Si has a sizeable notable effect on the electric and magnetic properties of the material. With an increased factor of Silicon, electric resistivity increases dramatically to almost sevenfold at 6.5% content of Si. Meanwhile, the Silicon ingredient also reduces the Saturation polarisation, magnetostriction and Curie temperature.

1.5.1 Magnetic properties in GOESs and NOESs

Electrical steels are categorised into GOESs and NOESs. For both, the magnetic properties often differ with magnetisation orientation in a single crystal. Nonetheless, bulk solid samples reveal different magnetic properties due to different crystallographic orientations. In GOESs, the grains are aligned along the rolling direction, so the characteristics of anisotropy are strengthened. Then, the magnetic properties of GOESs are directionally dependent. The magnetisation curves of a typical GOES measured for various angles of magnetisation, are shown in Fig. 1.7 [16]. It is evident that the best result is obtained by magnetising along the rolling direction, and magnetisation around 45° leads to the worst performance.

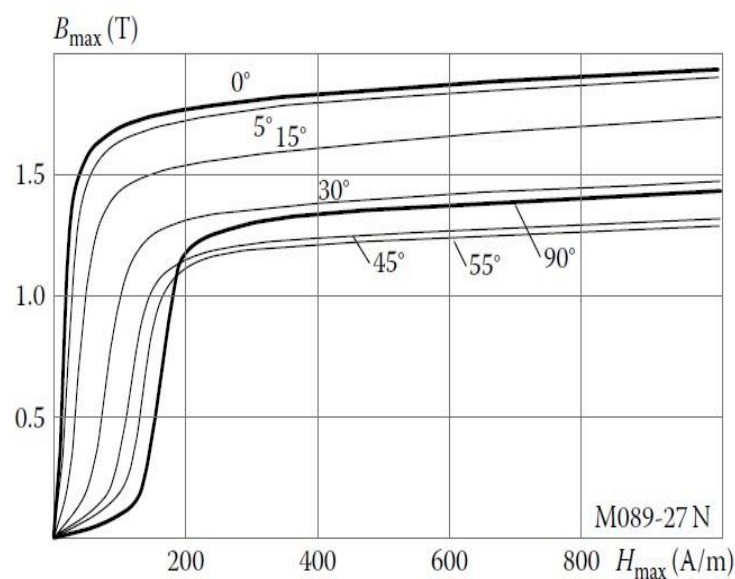


Fig. 1.7 Magnetisation curves of a typical GOES measured for different orientation angles [16].

As presented in Fig. 1.7, GOES is strongly anisotropic, so the magnetic properties other than in the rolling direction are poor. This anisotropy should be fully taken advantage of in the design of electromagnetic devices. The magnetisation needs to be parallel to the rolling direction. As the magnetic core in power transformers, the alternating magnetic flux lies in the rolling direction of the Fe-Si steel sheets. Therefore, suppose the direction of magnetic flux is not along with the rolling direction, such as applications in rotating machines, GOESs will give the worst performance of the designed electromagnetic machines.

In NOESs, the enormous number of crystals present are oriented randomly so that all the anisotropy of the single crystal counteracts each other resulting in no anisotropic behaviour. Fig. 1.8 shows the magnetisation curves of typical NOESs determined for various angles of magnetisation [16]. It should be noted that this material is not purely isotropic, but compared with a typical GOES, the disparity of properties with the change

of magnetisation direction are acceptably small. That is why the NOESs are often used in preference to GOESs in rotating machines. Although NOESs generally exhibit lower quality than GOESs, such poor properties are acceptable in many devices. Therefore, it is mainly considered from an economic point of view. Moreover, because this SiFe steel contains less silicon (0%–3%), it is more ductile, making the material more workable during manufacturing processes.

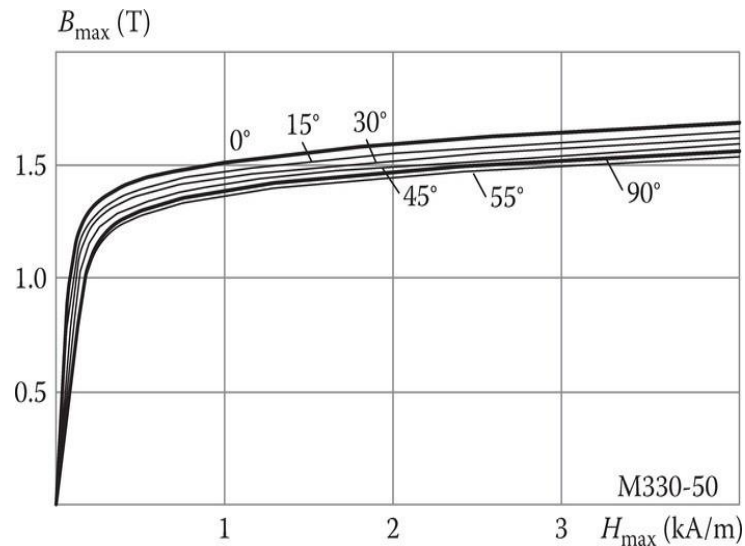


Fig. 1.8 Magnetisation curves of typical NOESs measured for different orientation angles [16].

1.5.2 Microstructures in GOES and NOES

Shown in Fig. 1.9 is the major hysteresis loops created from the measurement data for GOES and NOES magnetised at 50Hz, and peak flux densities 1.7 T and 1.4 T, respectively. Both groups of data are measured along with the rolling directions. It is evident that the coercivity values for NOES are 5 or 6 times greater than the coercivities of GOES; no wonder GOESs provide far smaller core loss than NOESs. So, NOES can be deemed harder magnetically than GOES. Meanwhile, GOES has higher saturation magnetisation, resulting in a narrow S-shape hysteresis loop. The hysteresis loop of the NOES looks more like a loop with two regular sigmoidal curves.

The magnetic properties of electrical steels are determined by the microstructures. As shown in Fig. 1.10(a), the ideal texture of NOESs would be a cube grain texture. The favourable texture is with its (001) or (110) planes parallel to the plane of the sheet, and [100] axes distributed uniformly in the material [17]. As shown in Fig. 1.11, the grains of NOESs are oriented randomly, which means that the grain structure can be observed on different surfaces in terms of the plane of the sheet. The magnetic domains in the grain will conform to the grain structure. Therefore, the magnetic properties of electrical steels are almost the same in any direction of magnetisation in the plane of the sample. Then, NOESs have no preferred crystallographic texture produced due to abnormal grain

growth, but it still has procedures to change grain sizes to achieve desirable magnetic properties. So, NOESs are the most economical material used in rotating electrical machines, as in motors and generators. Sometimes, fully processed and semi-processed NOESs can also be used in large and small transformers due to cost considerations.

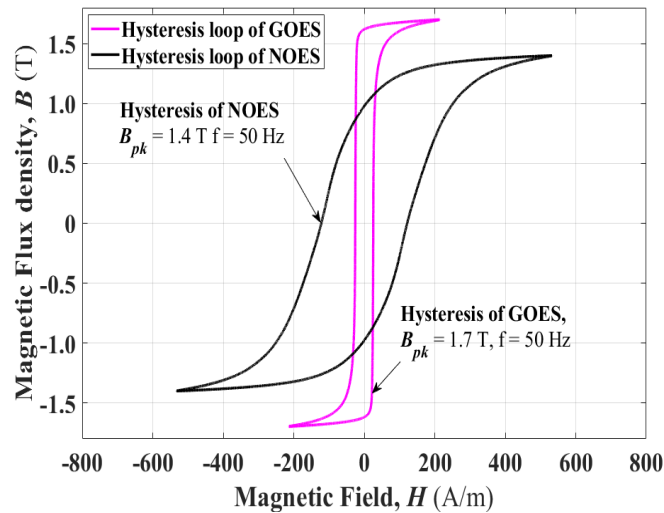


Fig. 1.9 Hysteresis loop for GOES and NOES at 50Hz.

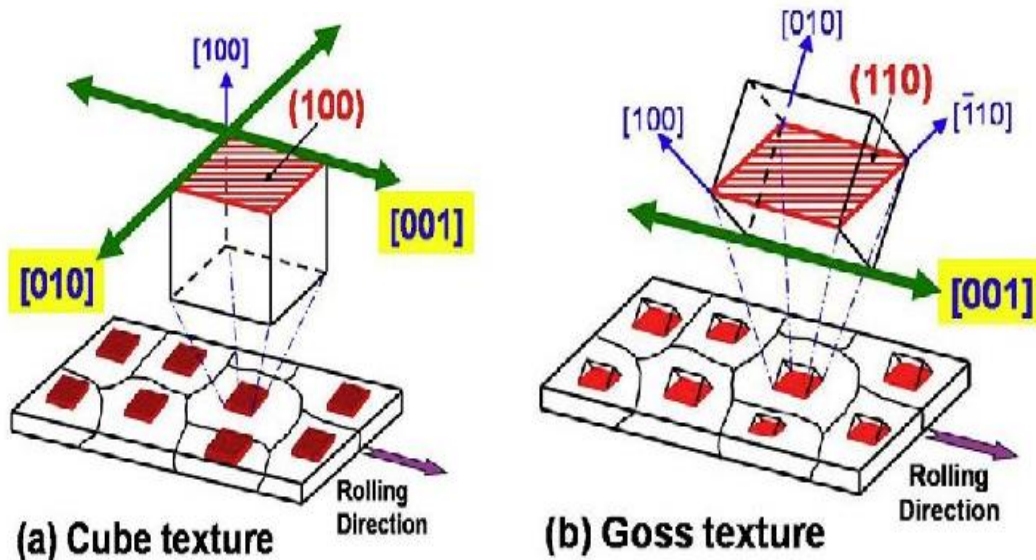


Fig. 1.10 Cube and Goss texture with crystallographic grain orientation [17].

The name NOES was created in the 1930s to distinguish it from the newly invented GOES. GOESs are soft magnetic polycrystalline metallic alloys used as magnetic core materials in electrical power transformers and motors. For transformer applications, the flux is mainly in the length of the laminations, and therefore it is desirable to increase permeability in the rolling direction. This is achieved by a suitable combination of annealing, hot rolling, and cold rolling to produce textured sheets, known as Goss texture, shown in Fig. 1.10(b) [17]. The texture is developed with the [001] direction in the lamination length, which is in the rolling direction. Meanwhile, the (110) plane close to

the sheet plane has the privilege of growth. Therefore, electrical steels are characterised by the Goss texture, i.e., a (110) <001> preferred crystal orientation shown in Fig. 1.11 [17]. The <001> type crystallographic directions are the easy magnetisation directions; hence the permeability is greater in the rolling direction.

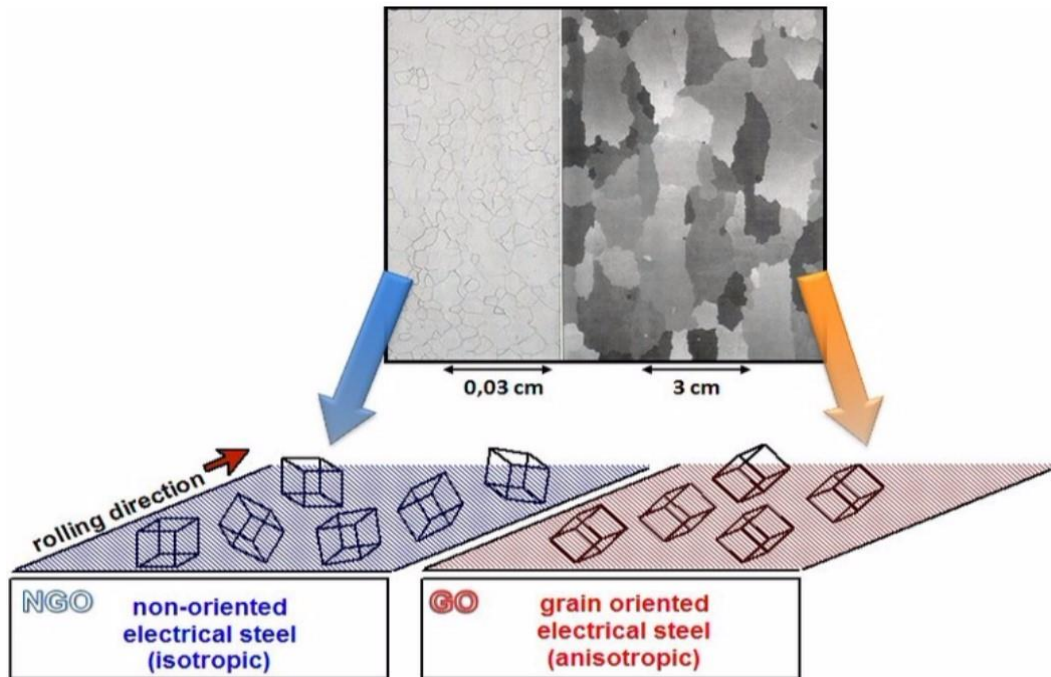


Fig. 1.11 A schematic of the different microstructures found in GOES and NOES [17].

1.6 Summary

This chapter has presented the concepts of fundamental magnetism, domain theory, and electrical steels, establishing the basis for investigating the magnetic properties of electrical steels. This thesis focusses on studying the magnetisation processes of electrical steels concerning hysteresis modelling and energy loss evaluation. These issues will be addressed using domain theory through analysing the domain structure variations under external excitation. However, each issue is concerned with a different physical mechanism that have been investigated in detail in the pertinent research.

Chapter 2 Previous Related Work

This chapter reviews the articles that have appeared concerning prediction of core losses and interpretation of the magnetic behaviour of electrical steel laminations under sinusoidal excitation waveforms, including hysteresis and energy loss separation modelling. The advanced hysteresis models are investigated, and energy loss separation model (ELSM) involving eddy current model coupling with hysteresis models are applied to electrical steels. Hysteresis and eddy-current are linked to the magnetisation processes, so a comprehensive understanding of their relationships is essential to achieving the goals of this thesis.

2.1 Introduction

Energy dissipation happens in a ferromagnetic material excited under a time varying magnetic field, a phenomenon traditionally called iron loss, which has been observed since the 18th century [18]. Steinmetz proposed an empirical equation in 1890 [19] to calculate the iron loss per unit volume in magnetic materials when subjected to an external sinusoidally varying magnetic flux. Although subsequently attempts have been made to provide a clear explanation of the unique physical mechanism of iron loss, the precise procedure for determining iron loss has not yet been established. Moreover, the complexity of the magnetisation processes makes the energy loss mechanism difficult to comprehend.

The inherent complexity of the magnetisation process is a crucial factor influencing the establishment and development of appropriate models. The assumption that the magnetic material is subdivided into magnetic domains interfaced through the domain wall boundary successfully describes the magnetisation processes. These domains have been observed experimentally but finding a clear explanation of the mechanism responsible for the observed iron loss is still challenging. Meanwhile, although researchers made tremendous efforts to establish a model to predict the iron loss or describe hysteresis in accordance with domain theory, satisfactory results have yet to be found [20].

When a material is magnetised by a magnetic field, its state remains at the local minimum of free energy, and thermodynamic equilibrium cannot be reached, giving rise to the hysteresis phenomenon, with the observed hysteresis loop being a unique fingerprint that characterises the magnetic materials [21]. The lagging behind of the applied magnetic field H with respect to the magnetic flux density B appears because of ferromagnetic hysteresis. For more than a century, engineers and scientists have been conducting experimental and research work to explain this phenomenon. At the same

time, hysteresis models based on knowledge of physical or mathematical properties in specific target systems have been developed.

Since ferromagnetic materials are electrically conductive, eddy currents are generated wherever the magnetic flux changes. Therefore, to accurately predict the iron loss and magnetisation behaviour of electromagnetic steel sheets under a sinusoidal excitation waveform, a hysteresis model directly coupled to the eddy current model should be developed [22].

The aim of this chapter is to present a direct comparative analysis of most of the well-known static hysteresis models in combination with the dynamic model for the prediction of magnetisation processes and energy losses under sinusoidal excitation. The new models in this study are developed based on an in-depth analysis of magnetic theory and previous models.

2.2 Static and dynamic hysteresis model

The macroscopic static and dynamic behaviour of electrical steel laminations operating under sinusoidal flux waveforms results from several intertwined microstructural configurations, atomic dipole, eddy current, micro eddy current, domain variation, and domain wall movement. The magnetic properties and core losses are significantly affected by grain textures and domain patterns. In addition, the performance analysis of a magnetic core in electromagnetic devices should be considered under different operational conditions, such as energy loss prediction with varied frequencies and peak flux densities.

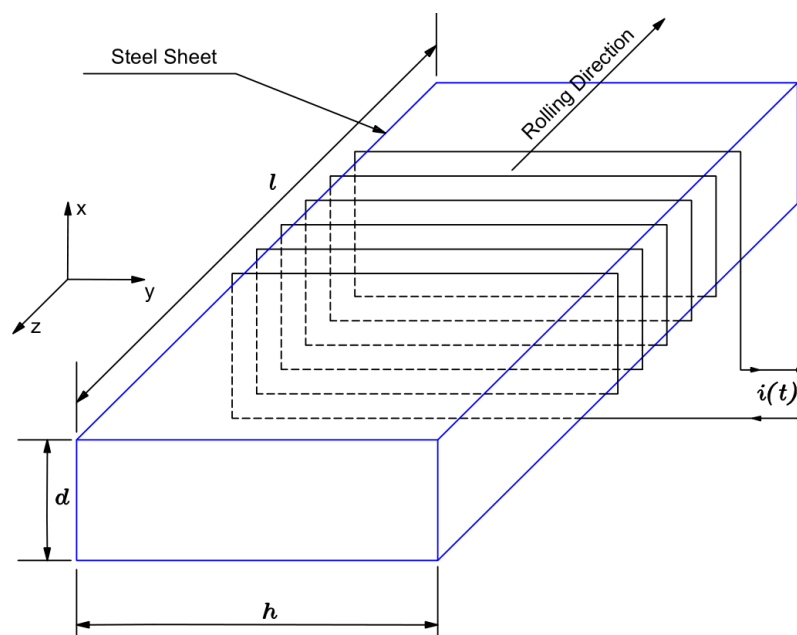


Fig. 2.1 Single steel sheet under magnetisation test.

Conventionally, the quantitative description of the magnetisation process in an electrical steel sheet shown in Fig. 2.1 is expressed as a one-dimensional diffusion (penetration) equation [1, 22], namely:

$$\frac{\partial^2 H}{\partial x^2} = \sigma \frac{\partial B}{\partial t}. \quad (2.1)$$

Equation (2.1) links the magnetic field strength H and the magnetic flux density B through the ferromagnetic material conductivity σ . This well-known 1-D penetration equation was derived from the Ampere–Maxwell law and Faraday’s law [21]; it can be used to model homogeneous materials in which grains and domains are arbitrarily oriented. When formulating the boundary value problem (BVP), it is important to consider that the corresponding numerical scheme is utilized in a transient simulator. In this simulator, the Maxwell equations are solved alongside the ordinary differential equations (ODEs) that describe the lumped elements of an electrical circuit. To establish the coupling between these two components, the magnetic circuit described by the BVP is treated as a two-pole element. Across the terminals of this element, an arbitrary time-varying voltage is applied. The specific value of this voltage is not known in advance and needs to be determined during the solution of the BVP using the Neumann boundary conditions (BCs) [115].

Generally, the modelling methods of GOESs and NOESs are different due to the micromagnetic structure differences. However, the magnetic characteristics of NOESs are deemed homogeneous because the grains are oriented randomly so that the isotropic magnetic domain patterns dominate the magnetic properties. In this case, (2.1) coupled with a static hysteresis model can be used to describe the hysteresis and evaluate the iron loss with sufficient accuracy [20]. Therefore, the magnetisation dynamics can be determined, and the shape of the hysteresis loop can be modelled.

Magnetic core loss is linked to three effects: static hysteresis, classical eddy current, and excess loss [1, 7, 23, 24]. Seminal contributions for predicting power losses and describing magnetic hysteresis were made by Bertotti [7] and Zirka [1]; they investigated the power loss separation principle, which can be expressed simply as:

$$W_{tot} = W_{hyst} + W_{clas} + W_{exce}, \quad (2.2)$$

where W_{hyst} is the static hysteresis component obtained by calculating the area of the quasi-static hysteresis loop [25]. The Steinmetz empirical equation is still used to calculate the static hysteresis losses [26]. W_{clas} is evaluated by (2.1) in the case of low frequencies, where the skin effect is negligible. In the case of high frequency, the skin effect in NOESs is significant and must be considered [27]. Bertotti [7] asserted that the excess loss of magnetic materials is caused by competition between the external magnetic field and the counter field generated by the eddy currents and domain configurations. The

corresponding component was derived as a function of magnetisation frequency and peak flux density. So that the total power losses can be approximated in terms of a function of magnetisation frequency and peak flux density [28].

The static hysteresis loss is measured via an Epstein frame under a magnetisation frequency close to 0 Hz [1, 29]. The eddy current loss is caused by the current generated within the core materials subjected to a varying magnetic flux density. The modelling result of (2.1) can be used to evaluate the eddy current loss [1]. So, the complicated issue of the interaction between hysteresis and eddy current in homogeneous materials can be addressed using (2.1) coupled with a static hysteresis model.

Conventional hysteresis models such as those of Preisach [4] or J-A models [2, 3] can trace the hysteresis loop without considering the eddy current effect. However, both models can be used to model the static hysteresis loop, with the J-A model being the most popular and helpful model to simulate the static hysteresis loops by substituting the measured loop obtained using the Epstein frame.

Bertotti [21] developed the separation scheme of the magnetic field at the sheet surface. According to the power loss separation principle, the magnetic field is divided into a static hysteresis field, classical eddy current field, and excess field corresponding to the power loss separation, and is expressed as:

$$H(t) = H_{hyst} + H_{clas} + H_{exce}. \quad (2.3)$$

The separation fields are expressed in terms of magnetic flux density, which facilitates the creation of hysteresis loops and the calculation of power losses [1],

$$H(t) = H_{hyst}(B) + \frac{d^2}{12\rho} \frac{dB}{dt} + g(B)\delta \left| \frac{dB}{dt} \right|^{\frac{1}{2}}, \quad (2.4)$$

where $H_{hyst}(B)$ is the hysteresis field measured or calculated by means of the static hysteresis model (SHM), $g(B)$ is an empirical function coefficient of excess field, and can be either constant [30] or a function of B [21], δ is a direction parameter, and takes the value +1 for ascending ($dH/dt > 0$) and -1 for descending ($dH/dt < 0$) hysteresis branches, respectively. The second term on the right-hand side of (2.4) represents the eddy current field calculated with (2.1) for a thin ferromagnetic sheet of a linear ferromagnetic material at a sufficiently low frequency so that the skin effect can be ignored [1].

The magnetic characteristics of GOESs are deemed inhomogeneous because the grains in GOESs are oriented mainly in the rolling direction so that the anisotropic magnetic domain patterns dominate the magnetic properties. The modelling results are different in anisotropic GOES sheets, which are used mainly for the magnetic core of power transformers, reactors, and other devices in which the magnetic flux is in line with the rolling direction. Shortly after being invented by Goss [31] in 1934 and industrialised by

ARMCO in the 1940s, it was realised that the total loss in this material is anomalously higher than the calculated loss using (2.1), even when using an accurate static hysteresis model to link the magnetic field H and magnetic flux density B when solving the appropriate Maxwell's equations [1].

It is realised that the magnetisation properties and core losses in GOESs and NOESs differ considerably due to different microstructures, such as domain patterns, grain sizes, and grain orientation preferences. At the power frequency, using the 1-D diffusion equation (2.1) to evaluate the energy loss for the NOESs, the difference between the measured loss and the calculated loss, the so-called anomalous or excess loss, may not be significant, but if the classical equation is used to evaluate the GOESs, the excess loss can reach around 40% of the total loss [1].

The static and dynamic hysteresis loops shown in Fig. 2.2 were made [1] for GOESs with parameters, $d = 0.27\text{mm}$ and $\rho = 0.48 \times 10^6\text{Ohm}\cdot\text{m}$. The steady-state hysteresis loop 3) was measured using an Epstein frame by means of digital feedback to achieve a controlled sinusoidal magnetic flux density at 50 Hz and 1.7 T. The area of the hysteresis loop 3) is equal to the total energy loss $W_{tot} (\text{J}/\text{m}^3)$, dissipated in the unit volume of the steel sheet per cycle [1].

Modelling the static hysteresis loop is perhaps the most challenging part of the modelling of the three-separation scheme to understand the magnetisation process of a ferromagnetic material. Therefore, the development of a quasi-static model is of fundamental importance. It should be able to predict the magnetic properties of ferromagnetic materials, i.e., the B corresponding to the changes of the magnetic field H . This behaviour is determined by the entire magnetisation process.

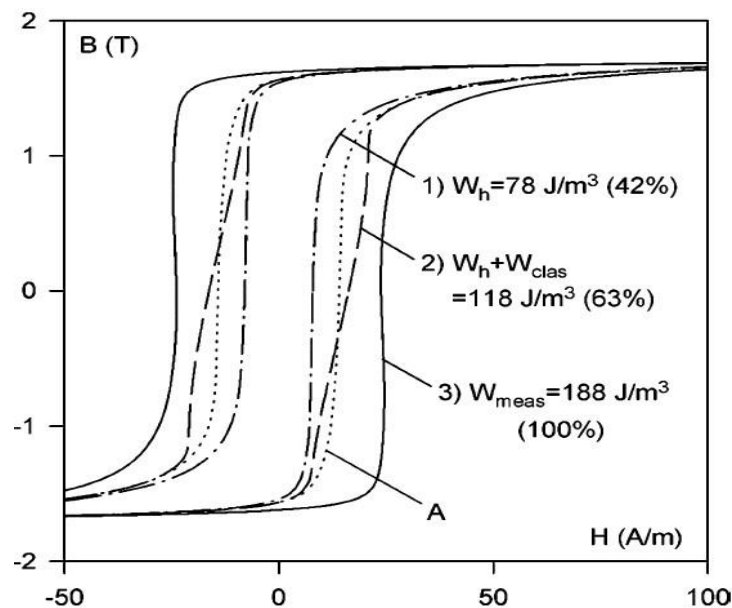


Fig. 2.2 Static and dynamic hysteresis loops for GOESs measured with an Epstein frame at controlled sinusoidal induction for $f = 50\text{ Hz}$ and $B_{pk} = 1.7\text{ T}$ [1].

In Fig 2.2, the quasi-static hysteresis loop 1) was taken from the same Epstein frame used to measure the steady-state hysteresis loop, connected to a permeameter with the period of sinusoidal induction of the order of 300s. The static hysteresis loss measured is equal to 42% of the total loss measured at 50 Hz and 1.7 T [1].

The area of the dynamic loop obtained from loop 2) is the sum of hysteresis and classical eddy-current losses ($W_{cal} = W_h + W_{clas}$), whereas the classical eddy current component was calculated from (2.1) using a finite-difference scheme [32]. It can be seen from Fig. 2.2, the calculated W_{cal} equals $118 J/m^3$. The measure total energy loss W_{tot} , is the area of measured loop 3), then, the W_{exce} accounts for 37% of the W_{tot} [1].

Loop A was calculated as the sum of the two terms on the righthand side of (2.4), representing the sum of quasi-static hysteresis and classical eddy-current components in the separation principle. The classical eddy-current component, generated using the middle term of equation (2.4), forms an elliptic loop in the eddy current field as a function of magnetic flux density. On the other hand, the quasi-static hysteresis component corresponds to a measured hysteresis loop. The classical loss per cycle is equal to $40 J/m^3$ and is obtained from the area between loops 1) and 2), whereas the excess loss is calculated from the area between loops 2) and 3) to be equal to $70 J/m^3$. Then, for this typical GOESs, the percentages of quasi-static hysteresis, classical eddy-current, and excess losses are 42%, 21%, and 37%, respectively [1].

Evidently, the solution of the finite-difference scheme of (2.1) is not sufficient for modelling GOESs, the use of (2.4) may be regarded as an acceptable way. The sum of the first two items in (2.4) shown in Fig. 2.2 is indicated by the dotted line loop A, and its shape and area ($111 J/m^3$) are different from loop 2) found numerically.

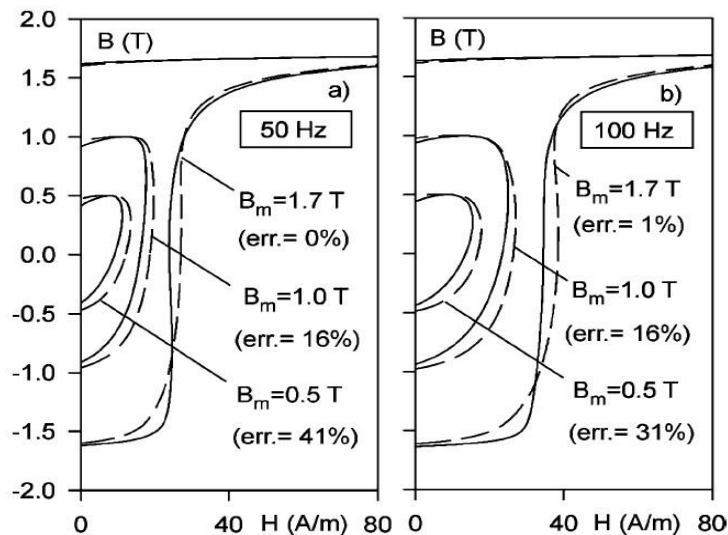


Fig. 2.3 Comparison of measured and calculated hysteresis loops of GOESs for $g(B) = \text{constant}$ [1].

For modelling GOESs sheet, the $g(B)$ in the third item of the righthand side of (2.4) is vital to create an accurate loop and reproduce the excess loss. A simple way is to treat the $g(B)$ as a constant [30]; the results are shown in Fig. 2.3. The dynamic loop shown as a solid line in a) and b) was measured with a sinusoidal flux density at 50 Hz and 100 Hz, respectively. The calculated loop shown as a dashed line was calculated choosing $g(B) = 0.5565$ to make the loop calculation equal in area to the measured loop at 1.7 T, 1.0 T and 0.5 T, and 50 Hz and 100 Hz. It can be seen from Fig. 2.3 that the areas of all the calculated loops are significantly larger than the corresponding measured loop area; the percentage errors are listed in Fig. 2.3[1].

Since the waists of all the loops calculated at $g(B) = \text{constant}$ is widened, $g(B)$ should be minimum at low $|B|$ and should be increased when $|B|$ increases. The calculated loops shown in Fig. 2.4 were obtained by expressing $g(B)$ as a variable [1] of the form:

$$g(B) = G_m (1 + k_1 B^2). \quad (2.5)$$

These coefficients provide zero error in the loop area only at 50 Hz and 1.7 T. All other calculated loop shapes shown in Fig. 2.4 as dashed lines are closer to the shapes of the measured loop, and the average errors are three times lower than those in Fig. 2.3 [1].

In addition, equation (2.4) together with function (2.5) enables modelling the dynamic hysteresis loop, so when the sinusoidal magnetic induction frequency reaches 200 Hz (at 1.7 T), the loss can be accurately predicted. At lower magnetic flux density, for example at 1 T, especially at 0.5 T, the model still has excellent predictive capability at frequencies up to 400 Hz [1].

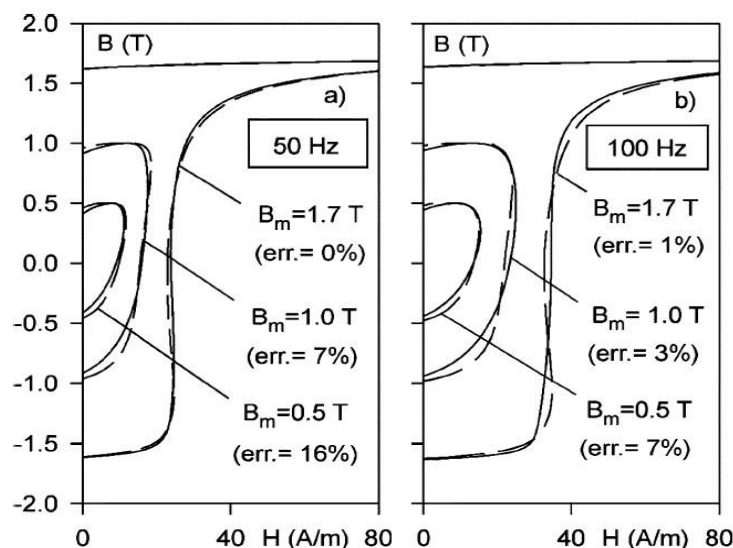


Fig. 2.4 Comparison of measured and calculated hysteresis loops of GOESs for $g(B) = \text{variable}$ where $G_m = 0.38 \text{ (A/m)} \cdot (\text{s/T})^{0.5}$ and $k_1 = 0.576 \text{ 1/T}^2$ [1].

The solution of (2.1) is not sufficient for modelling GOESs, but the use of (2.4) may be regarded as an acceptable way. For modelling GOESs, the $g(B)$ in the third item of the righthand side of (2.4) is vital to create accurate loops and reproduce the excess loss. When modelling with low harmonic content magnetic induction, the third term in (2.4) can be abandoned and the second term can be multiplied by the coefficient k_2 [33] to compensate for the resulting loss deficiency, and equation (2.4) can be rewritten as:

$$H(t) = H_h(B) + k_2 \frac{d^2}{12\rho} \frac{dB}{dt}. \quad (2.6)$$

The core loss calculated using (2.6) mainly considers two effects: magnetic hysteresis and eddy current in conductive materials. The eddy currents consume energy from the magnetic field source and dissipate it as heat in the magnetic material.

The contribution of (2.6) is to help understand the magnetic losses in soft ferromagnetic materials, which may be helpful for fundamental physicists interested in microscopic magnetisation processes and engineers interested in applying electrical technology in electrical steel. Equation (2.6) delivers essential enlightenment regarding the dependence of power loss on the magnetisation frequency f and peak flux density B . Further work is to clarify how this dependence is related to the parameters, such as grain size, which define the microstructure of a given material, and features like magnetic domain size, which can characterise its magnetic domain structure [34, 35].

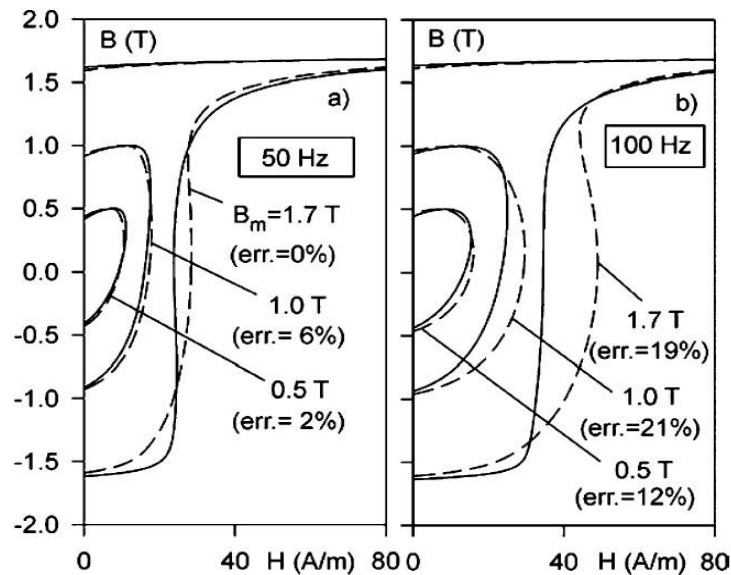


Fig. 2.5 Comparison of measured hysteresis loops of GOESs with dynamic loops calculated with two components [1].

It has been found numerically that if $k_2 = 3.306$ is used, the loop calculated using (2.6) has the same area as the corresponding one measured at 50 Hz and 1.7 T. It can be seen from Fig. 2.5a) that almost all loops constructed by the two-component model (2.6) are

close enough to the measured loop at the fitting frequency 50 Hz. However, it can be seen in Fig.2.5b) that the use of (2.6) is no longer acceptable even at as low as 100 Hz [1].

In this situation, the use of the phenomenological three-component model of the ferromagnetic branch becomes almost the only reliable method of accounting for dynamic processes in GOESs [1].

So far, this phenomenological three-component model has been reviewed and analysed and is deemed to be the only reliable method to solve the dynamic process in GOESs due to the lack of a general physical model [1].

2.3 Magnetic loss evaluation model

The first empirical equation used to calculate the power core loss was proposed by Charles Steinmetz in 1892 [19]. Steinmetz's equation, sometimes also called the power equation, is used to calculate the power loss per unit volume when the magnetic core is subjected to a sinusoidal excitation. The equation is expressed as:

$$W = kf^a B_{pk}^n, \quad (2.7)$$

where W is the time-average power loss per unit volume, f is the magnetisation frequency, and B_{pk} is the peak magnetic flux density; k , a , and n , called the Steinmetz coefficient, are material parameters generally obtained empirically from the material's $B - H$ hysteresis loop by curve fitting. In a typical magnetic material, the Steinmetz coefficients vary with temperature.

Eddy current loss was introduced in [36, 37]. According to this contribution, the average power loss per unit volume W of any magnetic material is decomposed into the sum of hysteresis and a dynamic effect. This loss separation has been used for a long time in the study of core losses and is expressed in the following way:

$$W = W_{hyst} + W_{clas}, \quad (2.8)$$

where W_{hyst} is the static hysteresis component equal to the area of the quasi-static hysteresis loop [38], and W_{clas} is evaluated by solving the classical Maxwell penetration equation in the case of low frequencies [39]. In the case of the range of magnetisation frequencies where the skin effect is negligible, the eddy current loss is predicted using the following equation [21]:

$$W_{clas} = \frac{\pi^2 d^2 \sigma}{6} f B_{pk}^2, \quad (2.9)$$

Where d is the thickness of the steel sheet, σ is the electrical conductivity of the material, and B_{pk} is the peak flux density. Equation (2.9) is only valid under so-called quasi-static conditions, where magnetisation frequency does not cause a skin effect. In other words, the electromagnetic wave completely penetrates the material.

Due to domain effects, it is usually found that the dynamic loss W_{dyna} is greater than W_{clas} . The difference between them is called excess loss W_{exce} . In many cases, W_{exce} is greater than W_{clas} . Then, the three-component method of the statistical loss theory separates the core loss into static hysteresis loss, classical eddy current loss, and excess loss. So, the magnetic core loss is due theoretically to three effects: hysteresis, classical eddy current, and anomalous or excess loss. Bertotti [7] and Zirka [1] investigated the power loss separation principle expressed simply as (2.2).

The Steinmetz empirical equation can be used to calculate the static hysteresis losses in [7]. The P_{clas} is evaluated using equation (2.9). In the case of high frequency, the skin effect in NOESs is significant and must be considered [27]. Bertotti asserted that the basic physical mechanism of excess loss in soft magnetic materials is due to the competition between the external magnetic field applied uniformly in the sample, and the highly inhomogeneous local counter fields resulting from the interaction of eddy currents and microstructures [41 - 43].

In 1984, Bertotti [39] proposed a statistical model of energy loss. He hypothesised that the domain walls pass through pinning centres (material impurities, dislocations, etc.) in a random sequence when domain walls move during magnetisation. Therefore, the magnetisation process should be regarded as a random spatiotemporal correlation process, and the fundamental change of magnetisation is related to the Barkhausen transition. Each Barkhausen jumping into the external magnetic field will generate micro eddy currents, which result in excess losses.

Bertotti [7] assumed that the domain structure should be considered as \tilde{n} statistically independent magnetic objects (MOs). For GOES, a single Bloch wall can be regarded as a magnetic object. While for the microcrystalline materials, the MO is the entire domain structure within a single grain [40, 41]. This method reduces the problem of excess losses by determining the physical properties of MOs based on frequency, peak flux density, and material microstructure. Bertotti described the excess loss by the following equation [7]:

$$W_{exce} = 8\sqrt{\sigma G^{(w)} S V_0} f^{1.5} B_{pk}^{1.5}, \quad (2.10)$$

where V_0 is an intrinsic parameter bounded by a material microstructure; the value of the dimensionless coefficient $G^{(w)}$ is determined by [7]:

$$G^{(w)} = \frac{4}{\pi^3} \sum_k \frac{1}{(2k+1)^3} = 0.1356. \quad (2.11)$$

Next, the corresponding components of the three-separation principle were defined in a function of magnetisation frequency and peak flux densities [7] so that the total power losses can be approximated by the following equation:

$$W_{tot} = k_h f B_{pk}^n + k_e f^2 B_{pk}^2 + k_{ex} f^{1.5} B_{pk}^{1.5}, \quad (2.12)$$

where the k_h , k_e , and k_{ex} are unknown coefficients representing static hysteresis, classical eddy current and excess losses, and n is a material parameter determined by material microstructures. These four fitting parameters are calculated using the power losses measured or found empirically from the material's magnetic hysteresis loop by curve fitting.

It is a common practice to use the two-component method and three-component method to predict iron loss of electromagnetic devices under alternating excitation. However, the classical eddy current term of (2.12) is derived from Maxwell equations assuming a perfectly homogenous sample with a uniform flux distribution over the sheet and is applicable only for low frequencies or low conductivities [7]. The static hysteresis loss P_{hyst} can also be obtained experimentally or estimated using a static hysteresis model, such as the J - A model.

The energy loss separation principle provides an important approach to studying the magnetic properties of electrical steel and subdividing the total loss into three components. It is intricate to verify the separation model because the fact is that there are no technologies to measure these components individually at a given frequency and peak flux density. Their values and proportionalities are analysed using (2.12) or improved expressions based on (2.12). For instance, the classical eddy current loss W_{clas} under a sinusoidal flux density of peak value B_{pk} can be calculated using (2.9). The W_{hyst} is measured under almost static conditions at nearly close to zero frequency. Then the W_{exce} can be calculated using (2.2) by deducing W_{hyst} and W_{clas} from measured W_{tot} .

One of the concerns is that (2.9) was derived for a ferromagnetic material with a linear characteristic of B vs H , and (2.9) is valid only for low frequencies where skin effect is insignificant and can be negligible [44]. To increase the accuracy of W_{clas} at higher frequencies, the skin effect must be considered. Then, the following equation is adopted [29]:

$$W_{clas}^{skin} = \frac{\pi^2 d^2 \sigma}{6} f B_{pk}^2 \times F(\gamma), \quad (2.13)$$

where the skin-effect function is expressed as:

$$F(\gamma) = \frac{3(sh\gamma - sin\gamma)}{\gamma(ch\gamma - cos\gamma)}, \quad (2.14)$$

and:

$$\gamma = d\sqrt{\pi f \mu_0 \mu / \rho}, \quad (2.15)$$

where μ_0 is the free space permeability and μ is the relative magnetic permeability.

One should be careful when calculating the W_{clas} using (2.13); the insufficiency may be caused because (2.14) was derived assuming that μ is a constant value. So, it is clear that (2.13) is inapplicable to nonlinear magnetic material during the analysis of W_{clas} [29]. The best way to evaluate W_{clas} is to use a dynamic hysteresis model to solve (2.1).

The dynamic behaviour of a ferromagnetic core excited under a sinusoidal flux waveform result from several intertwining phenomena: eddy current, skin effect, saturation, and domain variation. Conventionally, the substantial interaction between static hysteresis and eddy current is solved using a robust coupling model. Ignoring the skin effect of low-frequency excitation, the quantitative description of the magnetisation process in the long thin sheet is reduced to the integration of the one-dimensional penetration equation (2.1). However, solving penetration equations cannot be done directly. It is complicated and limited to specific hysteresis models and requires numerically intensive solution methods (e.g., finite-difference (FD) and finite-element (FE) methods) [45].

Other numerical techniques have been introduced in the study of the eddy current effect to investigate equation (2.1). An equivalent magnetic circuit (MEC) model was proposed to analyse the eddy currents induced inside a ferromagnetic core based on the coupling equations between the electromotive force and magnetomotive force [46]. The parametric magneto dynamic (PMD) model is used to tackle (2.1). It discretised the magnetic field distribution uniformly across a soft magnetic sheets' thickness and expressed in a simple ordinary differential equation (ODE) [47]. It is worth noting that both the MEC and the PMD model are used for coupling a static hysteresis model [47].

The behaviours of the three energy loss components are visualised for GOESs and NOESs in [48]. In this study, the classical eddy current field was investigated using Bertotti's eddy current model [21]. The classical eddy current field is expressed [21, 48] as:

$$H_{\text{clas}} = \frac{d^2}{12\rho} \frac{dB}{dt}. \quad (2.16)$$

Under a controlled external magnetic field, the magnetic flux density was obtained and expressed as a sinusoidal function of the time [48]:

$$B(t) = B_{pk} \cos(\omega t). \quad (2.17)$$

Then, dB/dt can be derived and expressed as:

$$\frac{dB}{dt} = -2\pi f B_{pk} \sin(\omega t). \quad (2.18)$$

Thus, the H_{clas} can be calculated. The loops of B vs H_{clas} for GOESs and NOESs at a frequency of 60 Hz and peak flux density of 1.5 T are demonstrated in Fig. 2.6 and Fig. 2.7, respectively. It is evident that the loops of B vs H_{clas} are described as a closed ellipse [48].

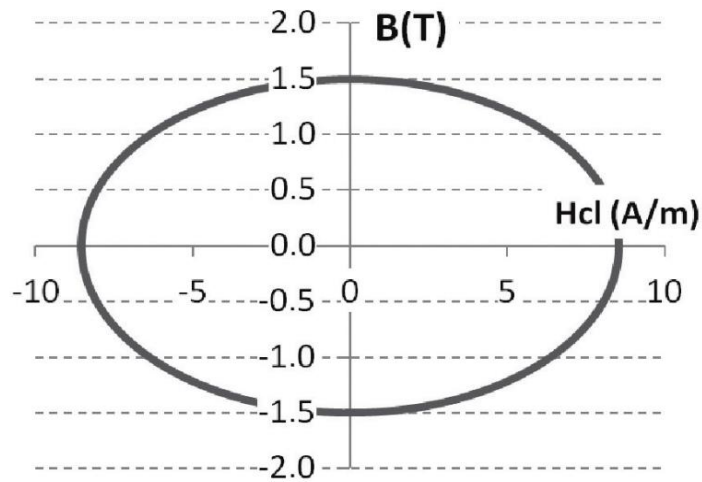


Fig. 2.6 Loop of B vs H_{clas} for GOESs at frequency 60 Hz and peak flux density 1.5 T [48].

In this work, the major hysteresis loop and static hysteresis loop were measured and obtained using an Epstein frame. The major loop and total loss were measured at frequencies of 60 Hz & 100Hz and peak flux density of 1.5 T for GOESs, and frequency of 60 Hz and peak flux density of 1.5 T for NOESs. The static hysteresis losses were made at a frequency of 0.005 Hz and a peak flux density of 1.5 T for both types of steel [48].

The excess field was calculated using (2.3), which can be done by subtracting the static hysteresis field and classical eddy current field from the magnetic field at each magnetic flux density level [48].

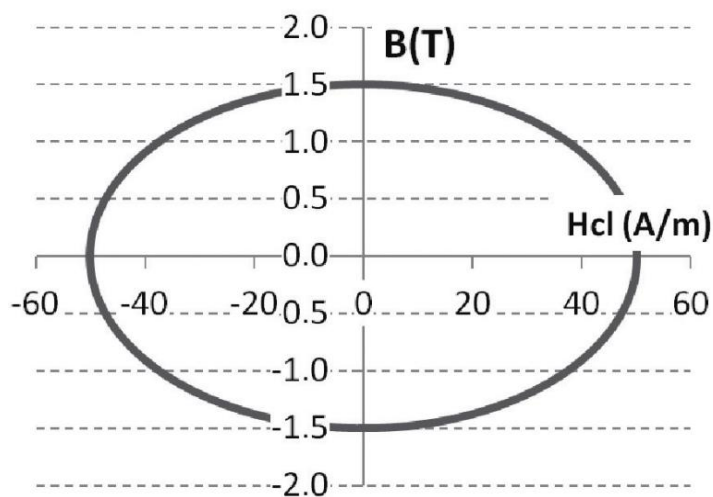


Fig. 2.7 Loop of B vs H_{clas} for NOESs at frequency 60 Hz and peak flux density 1.5 T [48].

It is known that ferromagnetic materials' magnetic properties are affected by microstructures, such as grain size and domain pattern. The hysteresis loops for total loss and its components are demonstrated in Fig. 2.8, 2.9 and 2.10 for NOESs magnetised at a frequency of 60 Hz and peak flux density of 1.5 T with grain sizes 11, 58 and 62 μm , respectively. The bigger grain size encounters fewer energy losses, which can be explained using domain theory [49].

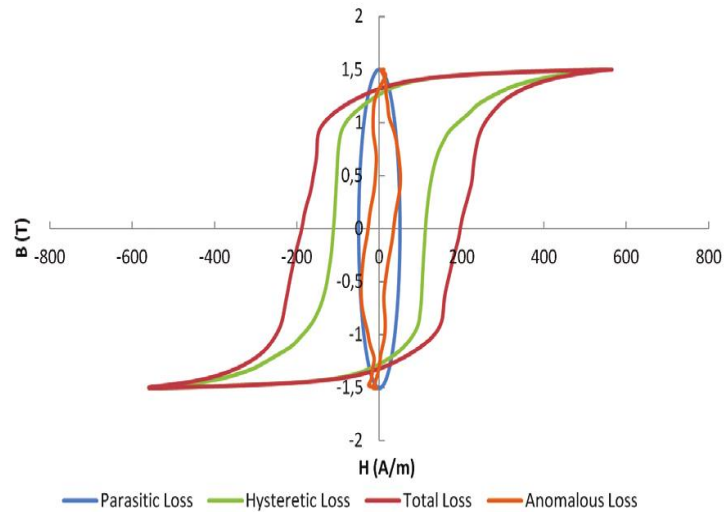


Fig. 2.8 Loss separation for NOESs at magnetisation frequency 60 Hz and peak flux density 1.5 T with final grain size 11 μm [48].

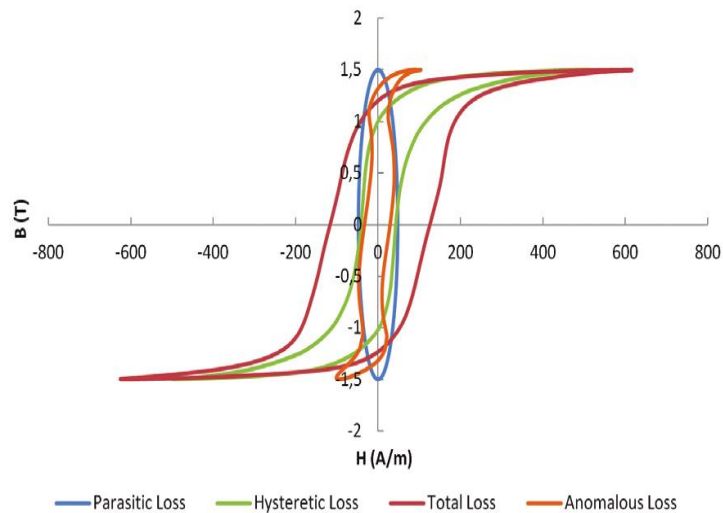


Fig. 2.9 Loss separation for NOESs at magnetisation frequency 60 Hz and peak flux density 1.5 T with final grain size 58 μm [48].

The hysteresis loops for total loss and its components are demonstrated in Fig. 2.11 and 2.12 for GOESs magnetised at peak flux density 1.5 T and frequency 60 Hz and 100 Hz, respectively. Apparently, the excess losses for GOESs account for significant proportions compared to NOESs due to the complicated microstructures and strong anisotropic grain orientations [48]. This different behaviour between GOESs and NOESs can be associated

with magnetic domain structure. In NOESs, the magnetic properties are determined by the different grain orientations. On the other hand, in GOESs, the grains are oriented mainly in the rolling direction. So, the excess losses increase due to the domain wall movement, domain rotation, domain annihilation and nucleation [6, 50 - 52].

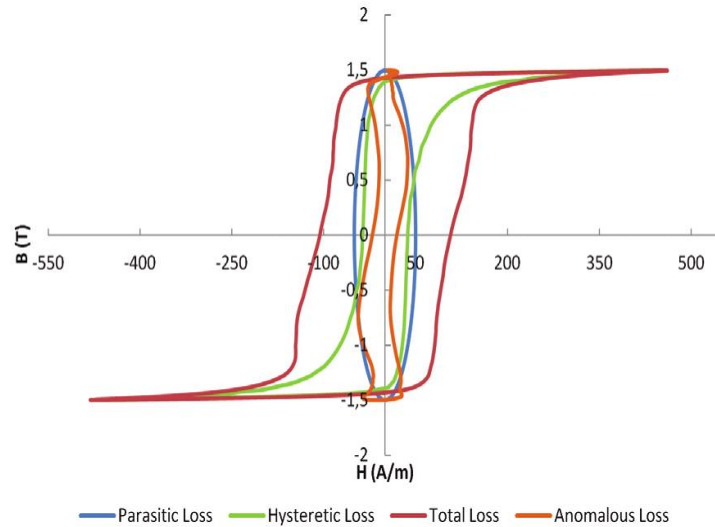


Fig. 2.10 Loss separation for NOESs at magnetisation frequency 60 Hz and peak flux density 1.5 T with final grain size 62 μm [48].

The energy loss separation components demonstrated in the above figures exhibit that the excess losses of GOESs and NOESs have different properties during the magnetisation processes. In NOESs, the excess loss is concentrated in the low magnetic flux density region. On the other hand, in GOESs, the results indicate a remarkable proportion of excess loss in the high magnetic flux density region [48]. From the above analysis, ELSMs have been developed for decades, and their importance to industry is fully appreciated.

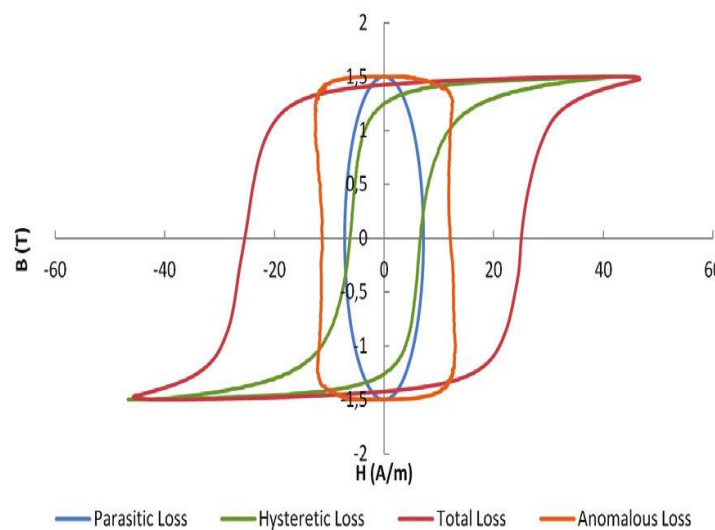


Fig. 2.11 Loss separation for GOESs at magnetisation frequency 60 Hz and peak flux density 1.5 T [48].

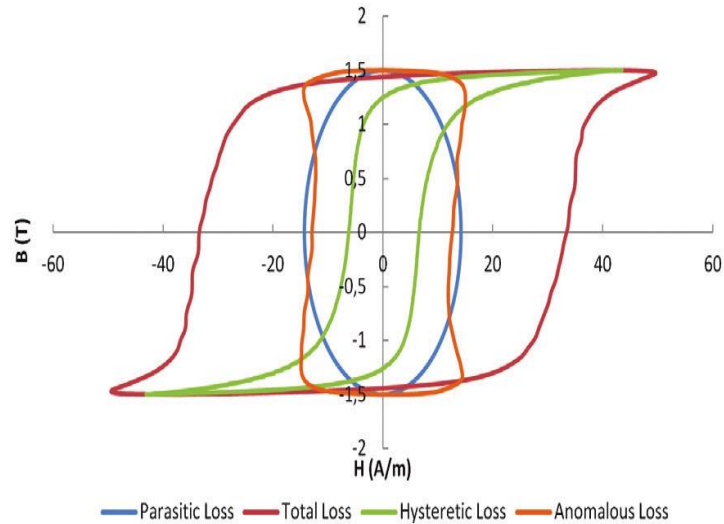


Fig. 2.12 Loss separation for GOESs at magnetisation frequency 100 Hz and peak flux density 1.5 T [48].

2.4 Jiles–Atherton model

David Jiles and D.L. Atherton [2] proposed one of the most popular models of magnetic hysteresis in 1984. The J-A model can be used to address the hysteresis effect independently without considering the eddy current effect. It can also be used to couple the relevant models solving the 1-D diffusion equation (2.1). Its main advantage is that the model can be linked to the physical parameters of magnetic materials obtained from the data sheet of manufacturers.

The interdomain coupling and anhysteretic curve are essential to derive the J-A model. Within a ferromagnetic material sample, there will be coupling between domains, expressed as a coupling with bulk magnetisation M . Then, the effective magnetic field H_{ef} influencing domain magnetic moments within the material, can be calculated using the following equation:

$$H_{ef} = H + \alpha M, \quad (2.19)$$

where α is a mean field parameter representing the inter-domain coupling, which can be determined by experiment. The effective magnetic field is analogous to the Weiss mean field acting on the individual magnetic moments within a magnetic domain [2].

2.4.1 Anhysteretic Magnetisation

The Anhysteretic Magnetisation (AM) curve is widely used to characterise ferromagnetic materials. The AM curve shown in Fig. 2.13 is S-shaped in terms of magnetisation vs magnetic field [53]. The AM curve has no hysteresis and is completely

reversible regarding an ideal magnetic material free from imperfection [8]. The AM curve is deemed one of the last problems raised to model magnetic hysteresis loops from the macroscopic viewpoint. It is widely used in the modelling of soft magnetic materials and is the basis of the J-A model [2, 3].

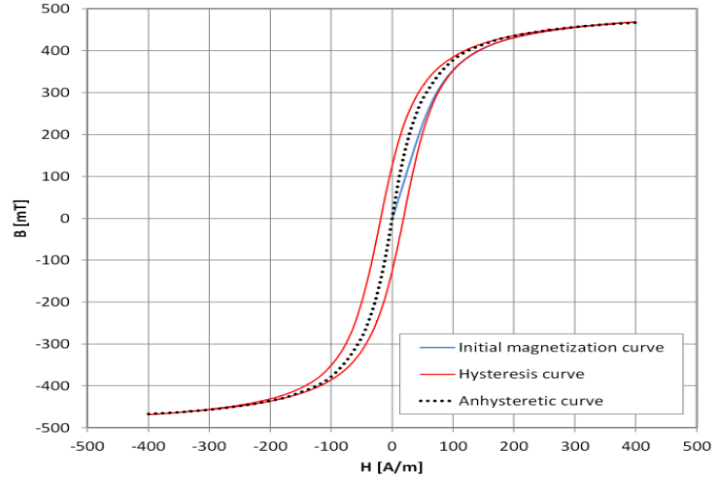


Fig. 2.13 Measurement of Initial magnetisation curve, Hysteresis curve and Anhysteretic magnetisation curve for isotropic soft magnetic material [53].

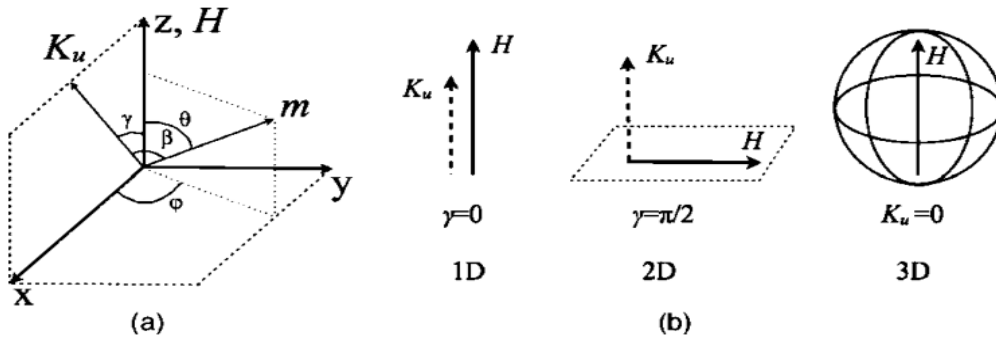


Fig. 2.14 (a) A magnetic moment m in the spherical coordinate system, angles θ and φ are polar coordinates. (b) Anisotropic orientations for specific cases: 1D, 2D and 3D, the magnetic field H is applied along Z direction; K_u is anisotropy constant and γ is the direction of anisotropy [54].

A generalised AM function for the J-A model has been developed in [54]. For a magnetic moment in the spherical coordinate system with an anisotropy shown in Fig. 2.14, when the magnetic field H is applied along Z direction, the AM function is expressed as [54]:

$$M_{an} = M_s \frac{\int_0^{2\pi} \int_0^\pi \exp(h_e \cos\theta - k_e \sin^2\beta) \sin\theta \cos\theta d\theta d\varphi}{\int_0^{2\pi} \int_0^\pi \exp(h_e \cos\theta - k_e \sin^2\beta) \sin\theta d\theta d\varphi}, \quad (2.20)$$

where

$$h_e = H_{ef} \frac{m\mu_0}{k_B T}, \quad (2.21)$$

and

$$k_e = \frac{k_u}{k_B T}, \quad (2.22)$$

and

$$\cos\beta = \sin\gamma \sin\theta \cos\varphi + \cos\gamma \cos\theta. \quad (2.23)$$

M_s is the saturation magnetisation, k_B is the Boltzmann constant, T is the temperature, and m is the magnetic moment of a magnetic domain. h_e and k_e are energy ratios for the effective field and anisotropy, respectively. k_u is the anisotropy constant, and γ is the angle between the anisotropy and Z directions [54].

When the anisotropy is positive and $\gamma = 0$ it means that the anisotropic easy direction is parallel to the magnetic field. The anisotropy is extremely high, then, the AM function can be reduced to a 1D problem and expressed as [54]:

$$M_{an} = M_s \tanh(h_e). \quad (2.24)$$

When the anisotropy is negative and $\gamma = \pi/2$, the magnetic field is perpendicular to the anisotropy direction. As shown in Fig. 2.13b, the anisotropic direction is a plane. Then, the AM function can be reduced to a 2D problem with extremely high negative anisotropy and the AM function can be expressed as [54]:

$$M_{an} = M_s \frac{\sum_{n=0}^{\infty} \frac{h_e^{2n+1}}{(n+1)! 2^{2n+1}}}{1 + \sum_{n=0}^{\infty} \frac{h_e^{2n+1}}{(n+1)! 2^{2(n+1)}}}. \quad (2.25)$$

When anisotropy is zero, the crystal has no preferred direction. This case has a three-dimensional solution for isotropic materials. The AM function is expressed as Langevin's function [54],

$$M_{an} = M_s \left[\coth(h_e) - \frac{1}{h_e} \right] = M_s \mathcal{L}(h_e). \quad (2.26)$$

The AM curves calculated for various values of anisotropy constants and in different anisotropic directions are shown in Fig. 2.15. When $k_u > 0$, $\gamma = 0$, AM curves represent uniaxial anisotropy with magnetic field along the easy axis; when $k_u < 0$, $\gamma = \pi/2$, AM curves represent planar anisotropy with magnetic field in the easy plane; when $k_u = 0$, AM curves represent isotropy, and when $k_u > 0$, $\gamma = \pi/2$, AM curves represent the hard direction when the magnetic field is perpendicular to the uniaxial easy axis [54].

When the magnetic material is demagnetised under the action of a constant magnetic field, AM can be observed through experiments. However, since the magnetic flux meter must maintain the accuracy of integration during the demagnetisation process, the

measurement of AM is very complicated. As a result, it is possible to experimentally verify the AM model only for materials with negligible hysteresis loops [55].

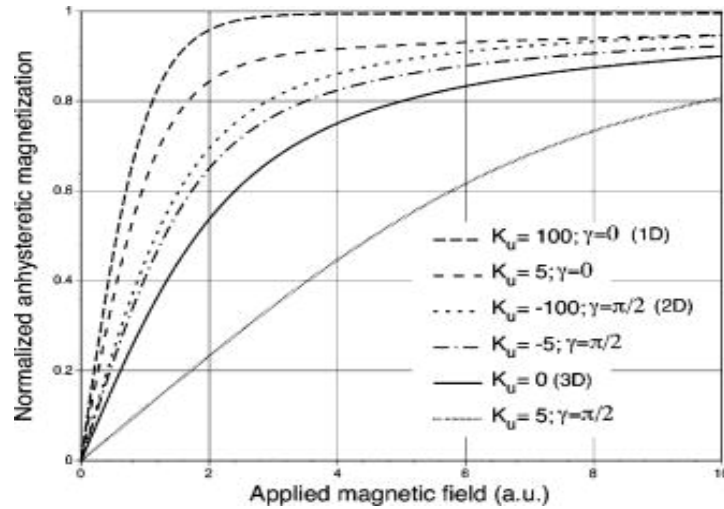


Fig. 2.15 Anhysteretic magnetisation curves calculated for various values of anisotropy constants and in different anisotropic directions [54].

The Langevin equation was developed for describing the magnetisation of a paramagnet [56]. Nonetheless, the modified Langevin equation does not give such a good performance for describing the magnetic properties of a ferromagnet because the model was developed without considering the possibility of impedance during magnetisation processes, such as domain wall movement being impeded by pinning sites [2].

The J-A model was derived by considering the energy needed to overcome the pinning site effect. The impedance energy considerations are based on two factors, the nature of the pinning site effect and the relative direction of magnetic moments in the domains on either side of the wall. It was assumed that the pinning sites are uniformly distributed in the materials. Each pinning site is regarded as having the mean pinning energy, then, the total energy needed to overcome the pinning site effect is proportional to the change of magnetisation. Then, the initial J-A model can be derived treating the AM function is isotropic material. The magnetisation can be obtained and expressed as [2]:

$$M = \mathcal{L}\left(\frac{H_{ef}}{a}\right) - \delta k \frac{dM}{dH_{ef}}, \quad (2.27)$$

where δ is the direction parameter, it takes the value +1 when $dH/dt > 0$, and -1 when $dH/dt < 0$. The pinning site effect is always opposite to the magnetisation direction. The coefficient k is not a constant and it is a function of M , H , M_{max} , and H_{max} . k is explained as the average energy required to overcome pinning site in the magnetic material [3].

2.4.2 Hysteresis Modelling

The magnetisation process is supposed to have two components, an irreversible component and a reversible component, corresponding to the irreversible or reversible

phenomena that occur in the magnetic material during the magnetisation process. For example, domain walls passing through the pinning site arouse irreversible displacement, and their movement between two consecutive pinning sites or rotation of the magnetic domain leads to a reduction in magnetisation when the field is reversed after reaching saturation, which is a reversible phenomenon [3]. Therefore, the total magnetisation is the sum of the two components:

$$M = M_{irr} + M_{rev}. \quad (2.28)$$

The irreversible magnetisation M_{irr} can be derived from the energy lost when domain walls pass over the pinning sites and is given as below expression [45]:

$$M_{irr} = M_{an} - k\delta \frac{dM_{irr}}{dH_{ef}}. \quad (2.29)$$

The differential irreversible susceptibility can be derived from equation (2.29), providing $k \neq 0$ and $k\delta - \alpha(M_{an} - M_{irr}) \neq 0$, namely:

$$\frac{dM_{irr}}{dH} = \frac{M_{an} - M_{irr}}{k\delta - \alpha(M_{an} - M_{irr})}. \quad (2.30)$$

At a given magnetic field strength, the component of the reversible magnetisation reduces the difference between the main irreversible magnetisation M_{irr} and M_{an} . This can be expressed as [3]:

$$M_{rev} = c(M_{an} - M_{irr}), \quad (2.31)$$

where c is a parameter representing magnetisation reversibility. Since the bending amount of the domain wall depends on the difference between the AM and the irreversible magnetisation, the differential reversible susceptibility is obtained [3]:

$$\frac{dM_{rev}}{dH} = c \left(\frac{dM_{an}}{dH} - \frac{dM_{irr}}{dH} \right). \quad (2.32)$$

The sum of the reversible and irreversible components of the differential susceptibility results in the total differential susceptibility as below [57]:

$$\frac{dM}{dH} = (1 - c) \frac{M_{an} - M_{irr}}{k\delta - \alpha(M_{an} - M_{irr})} + c \frac{dM_{an}}{dH}, \quad (2.34)$$

This is the final differential equation of the J-A model, which correlates the magnetisation and the magnetic field for the magnetic material sample.

The convenient method from the viewpoint of numerical solutions for hysteresis modelling is to solve (2.30) first for the irreversible component of magnetisation according to the chosen M_{an} , and then to solve (2.31) to obtain the reversible component. Some initial magnetisation curves and hysteresis loops shown in Fig. 2.16 – Fig. 2.19 are examples created by solving the model equations for various values of the model

parameters. These results revealed that the model is applicable to soft magnetic materials and can also be used for hard magnetic materials. For instance, the coercivity shown in Fig. 2.19 is 0.41×10^6 A/m [57].

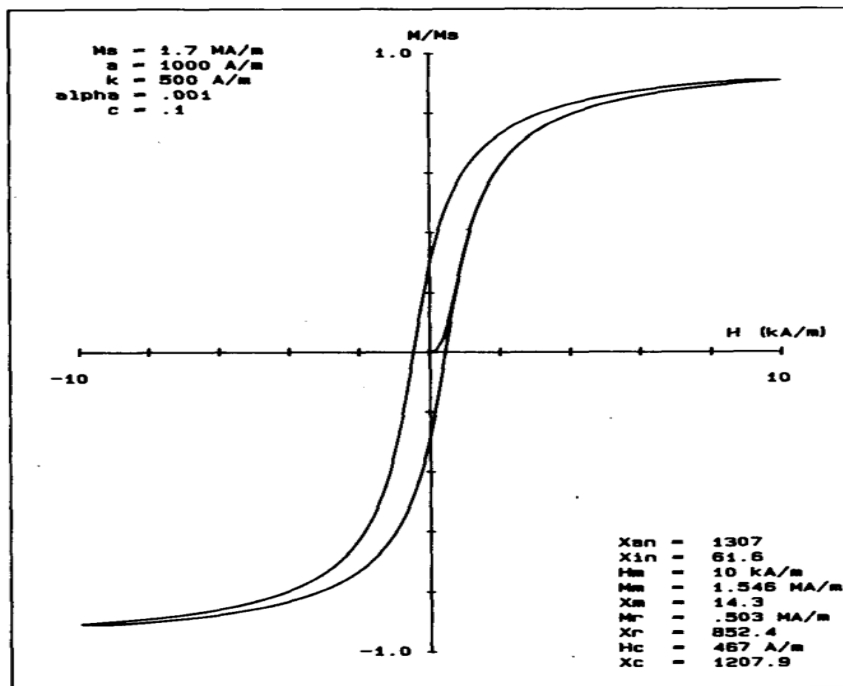


Fig. 2.16 The hysteresis loop calculated from solution of the J-A model equations with $M_s = 1.7 \times 10^6$ A/m, $a = 1000$ A/m, $k = 500$ A/m, $\alpha = 0.001$, $c = 0.1$ [57].

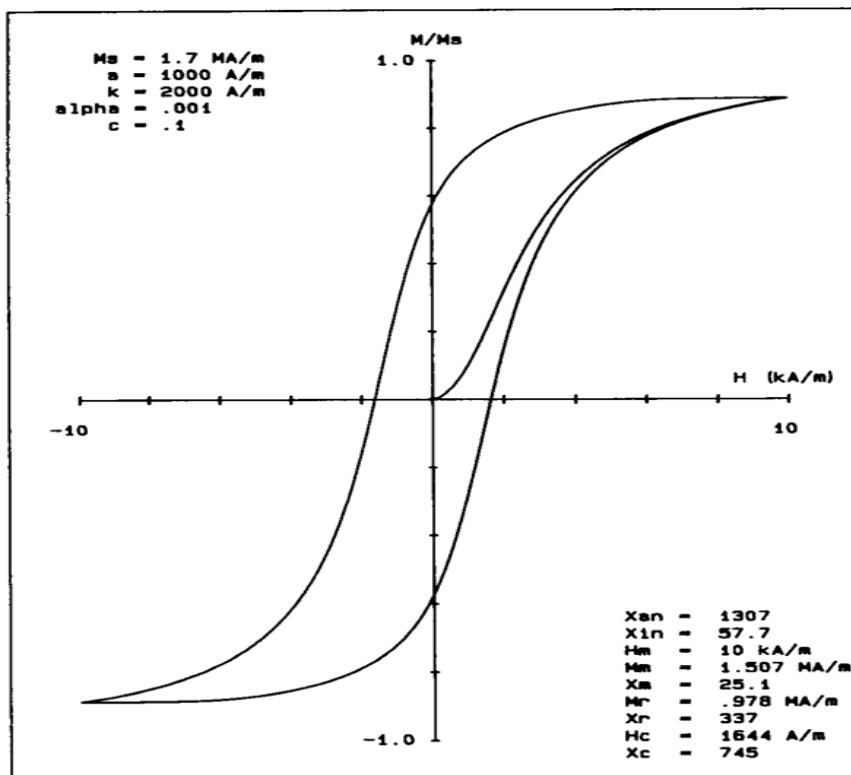


Fig. 2.17 The hysteresis loop calculated from solution of the J-A model equations with $M_s = 1.7 \times 10^6$ A/m, $a = 1000$ A/m, $k = 2000$ A/m, $\alpha = 0.001$, $c = 0.1$ [57].

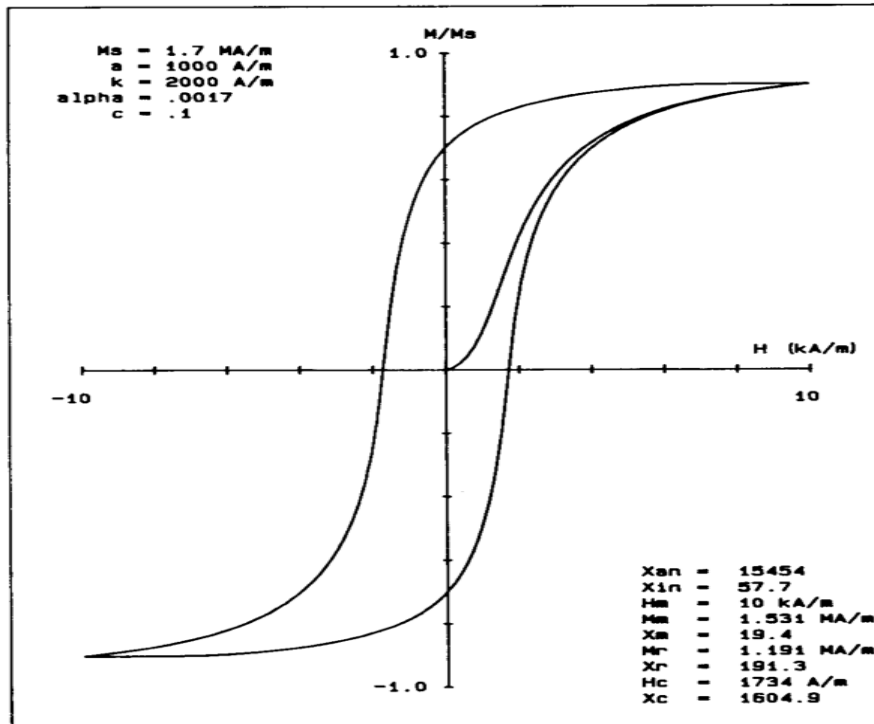


Fig. 2.18 The hysteresis loop calculated from solution of the J-A model equations with $M_s = 1.7 \times 10^6 \text{ A/m}$, $a = 1000 \text{ A/m}$, $k = 2000 \text{ A/m}$, $\alpha = 0.0017$, $c = 0.1$ [57].

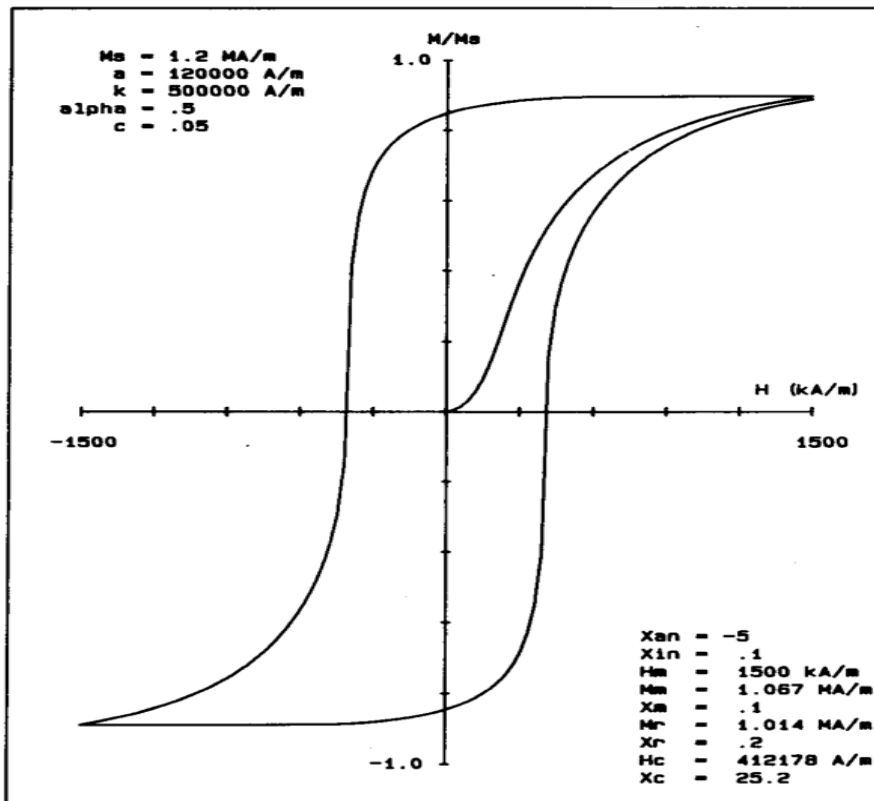


Fig. 2.19 The hysteresis loop calculated from solution of the J-A model equations with $M_s = 1.2 \times 10^6 \text{ A/m}$, $a = 1.2 \times 10^5 \text{ A/m}$, $k = 5 \times 10^5 \text{ A/m}$, $\alpha = 0.5$, $c = 0.05$ [57].

It is worth noting that the above figures were generated, treating the AM function as isotropic materials. When the grains in a material are preferentially oriented in a certain direction, the material has an anisotropic texture. In this case, the anisotropy of these grains plays an essential role in the magnetisation behaviour of the material.

Therefore, it can be considered that the magnetisation of the material is composed of isotropic and anisotropic components. In this case, the “fibre” texture is considered, which means that only a portion of the grains with easy directions is in line with the magnetic field direction, and the rest of the grains and domains are randomly oriented. The anisotropy and texture in polycrystalline magnetic materials was described by modifying the AM function to consider these anisotropic structures [55].

The AM function of typical magnetic materials can be expressed as a weighted sum of isotropic and anisotropic components [55]:

$$M_{an} = (1 - t)M_{an}^{iso} + tM_{an}^{aniso}, \quad (2.35)$$

where M_{an}^{iso} and M_{an}^{aniso} are isotropic and anisotropic components of AM, respectively. The t is the texture coefficient and represents the proportion of the anisotropic texture in the magnetic material [55].

The isotropic M_{an}^{iso} is determined according to the Boltzmann distribution. In the case of isotropic magnetic materials, the Boltzmann distribution can be simplified to a Langevin function that relates the isotropic AM to the effective magnetic field H_{ef} . Then, M_{an}^{iso} is expressed as [46]:

$$M_{an}^{iso} = M_s \left(\coth \left(\frac{H_{ef}}{a} \right) - \frac{a}{H_{ef}} \right) = M_s \mathcal{L} \left(\frac{H_{ef}}{a} \right), \quad (2.36)$$

where a is determined by domain walls density in the magnetic material, and $\mathcal{L}(x)$ is the Langevin function, M_s is the saturation magnetisation [2].

The anisotropic M_{an}^{aniso} is also determined based on the Boltzmann distribution [58]. However, in this case, the Boltzmann distribution function has no anti-derivative [59]. Therefore, it is necessary to integrate (2.36) numerically. The anisotropic M_{an}^{aniso} was initially proposed by Ramesh et al. [58] and corrected by Szewczyk [59]. M_{an}^{aniso} is given by the following equation:

$$M_{an}^{aniso} = M_s \frac{\int_0^\pi e^{0.5(E(1)+E(2))} \sin \theta \cos \theta d\theta}{\int_0^\pi e^{0.5(E(1)+E(2))} \sin \theta d\theta}, \quad (2.37)$$

where

$$E(1) = \frac{H_{ef}}{a} \cos \theta + \frac{K_{an}}{M_s \mu_0 a} \sin^2(\Psi - \theta), \quad (2.38)$$

and

$$E(2) = \frac{H_{ef}}{a} \cos \theta + \frac{K_{an}}{M_s \mu_0 a} \sin^2(\Psi + \theta). \quad (2.39)$$

K_{an} is the average energy density related to uniaxial anisotropy in the magnetic material, Ψ is the angle between the direction of the magnetic field and the easy magnetisation axis due to the anisotropy, and θ is the angle between the direction of atomic magnetic moment m and the direction of magnetic field H [59].

The parameters described in the J-A model are listed in Table 2.1 and Table 2.2. The parameters in Table 2.1 are initially used in the J-A model for isotropic characteristics [2] and the parameters in Table 2.2 are used in the extension considering uniaxial anisotropy introduced by Ramesh et al. and corrected by Szewczyk [58, 59].

Table 2.1 Parameters in the J-A model.

Parameter	Units	Definitions
α		Quantifies interdomain coupling
a	A/m	Quantifies domain walls density
k	A/m	Quantifies average energy to break pinning site
M_s	A/m	Saturation magnetisation
c		Magnetization reversibility

Table 2.2 Parameters in the J-A model extension.

Parameter	Units	Definitions
k_{an}	J/m^3	Average anisotropy energy density
θ	rad	Angle between atomic magnetic moment and magnetic field
ψ	rad	Angle between magnetic field and anisotropic direction

These parameters can easily be determined numerically by using experimental measurements and the data on the datasheet from the manufacturers. Since this model has a firm physical grounding according to the assumption of overcoming the impedance pinning sites of domain wall motion, the J-A model has been intensively developed to model the frequency dependence of magnetic hysteresis loop in conductive magnetic materials.

The AM curves can be modelled using (2.37) by the determination of hysteresis parameters for the modelling of magnetic properties. Fig. 2.20 and 2.21 present the

modelled AM curve and hysteresis loops for an anisotropic material [59]. Modelling was implemented with the magnetisation being parallel to the easy axis shown in Fig. 2.20 and perpendicular to the easy axis shown in Fig. 2.21. As can be seen, in both cases, the AM curves are located within the magnetic hysteresis loops for the anisotropic material. However, a significant anisotropic property of the AM curve within the hysteresis loop occurs with the magnetic field H parallel to the easy axis. Nonetheless, the AM curve shows a somewhat isotropic property occurs with the magnetic field H perpendicular to the easy axis.

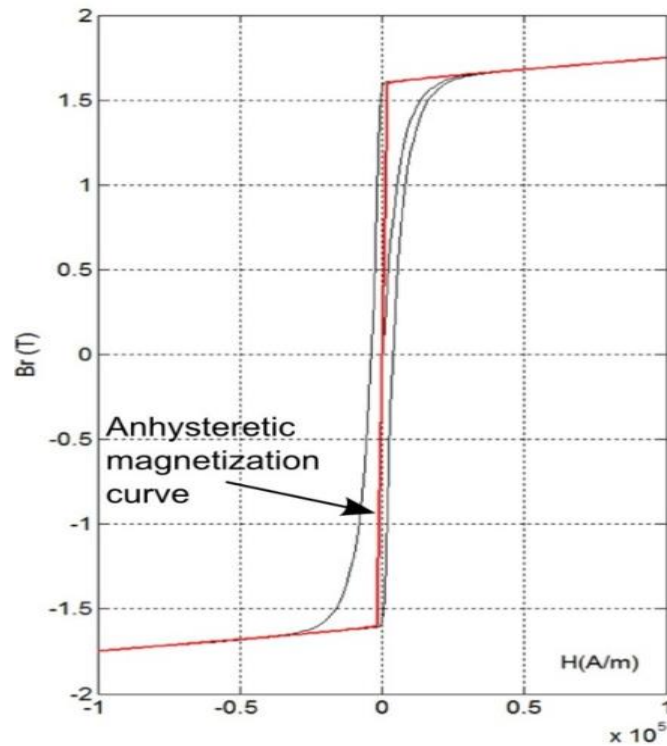


Fig. 2.20 The AM curve and hysteresis loops of the anisotropic magnetic material calculated with the J - A model's parameters: $M_s = 1.3 \times 10^6$ A/m, $a = 1000$ A/m, $k = 5000$ A/m, $\alpha = 0.001$. $c = 0.05$. The magnetisation is parallel to the easy axis ($\psi = 0$) [59].

The J-A model is also used to calculate the quasistatic hysteresis loop when modelling hysteresis loops using the energy loss separation model with equation (2.2). The application of the J-A model for numerical modelling of the measured quasi-static hysteresis loops of NOES was investigated in [60]. In this work a new variable parameter related to the mathematical description of the AM function was introduced. The quasi-static hysteresis loop was measured for a sample of 0.5 mm and Fe-Si 3% NOES. Comparisons of the hysteresis loop, measured and calculated using the original and improved J-A model, are shown in Fig. 2.22 [60].

Whether it is used independently or coupled with a classical eddy current model, the J-A model has found broad applications taking the hysteresis characteristic into account, when tracking the magnetic hysteresis loops or predicting the magnetic energy losses in ferromagnetic materials.

Since its introduction, the J-A model has gained widespread acceptance as the most popular approach for simulating magnetic hysteresis. Intensive research has been undertaken to enhance the performance of the J-A model. In a study conducted by [61], the magnetic hysteresis loops of raw 22MnB5 steel were measured using an Epstein frame from Brockhaus, following DIN-EN 10252 and DIN-EN 60404-2 standards. To improve the modelling accuracy, [61] adopted an enhanced arctangent model, which extends from the J-A model (representing the static component of the magnetisation processes) incorporating the Bertotti approach (representing the dynamic component of the magnetisation processes). The identification process involved the application of the Levenberg-Marquardt algorithm to both hysteresis models. The resulting dynamic hysteresis loops were calculated for both the extended J-A and Bertotti models. Fig. 2.23 illustrates a comparison between the improved arctangent model, the original J-A model, and the experimental data [61].

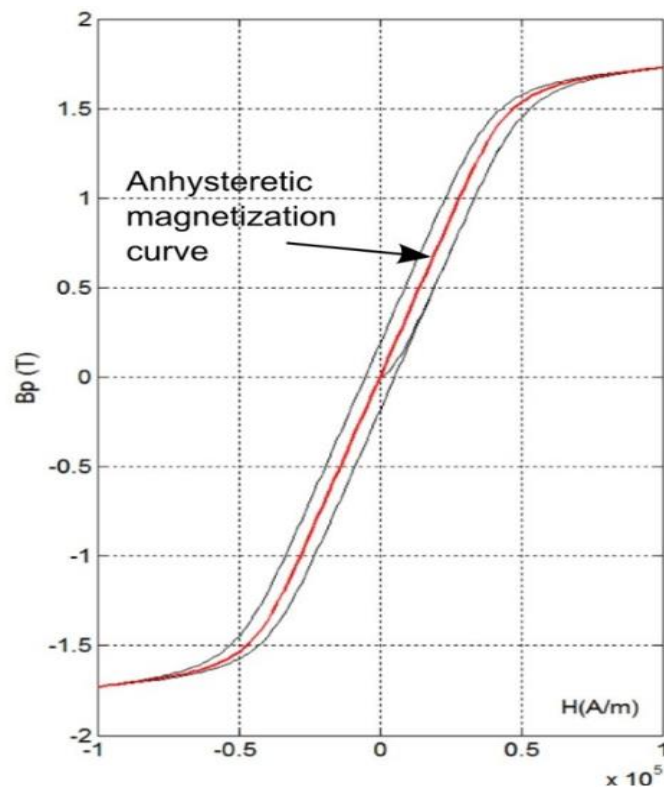


Fig. 2.21 The AM curve and hysteresis loops of the anisotropic magnetic material calculated with the J-A model's parameters: $M_s = 1.3 \times 10^6$ A/m, $a = 1000$ A/m, $k = 5000$ A/m, $\alpha = 0.001$. $c = 0.05$. The magnetisation is parallel to the easy axis ($\psi = 90^\circ$) [59].

In a study conducted by [62], the magnetic hysteresis loops of a cylindrical FeCrCo sample were experimentally measured using a Superconducting Quantum Interference Device (SQUID). To enhance the accuracy of the modelling process, [62] employed a modified J-A model specifically designed for simulating permanent magnet materials. In this modification, two correction coefficients related to the maximum magnetic flux density were introduced to improve the precision of the J-A model, particularly in simulating the minor hysteresis loops. To determine the appropriate values for the

introduced correction coefficients in the modified J-A model, the Hook-Jeeves algorithm was utilized. Fig. 2.24 provides a visual comparison between the results obtained from the modified J-A model, the original J-A model, and the measured curves [62].

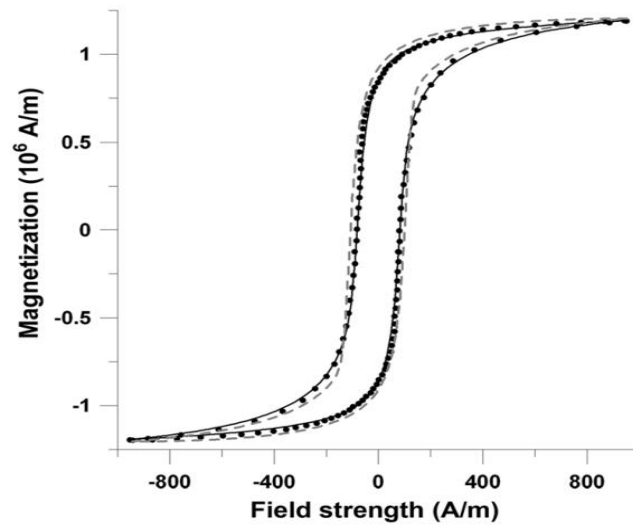


Fig. 2.22 Comparison of hysteresis loops between measured (points), calculated with improved J-A model (solid line) and original J-A model (dashed line) [60].

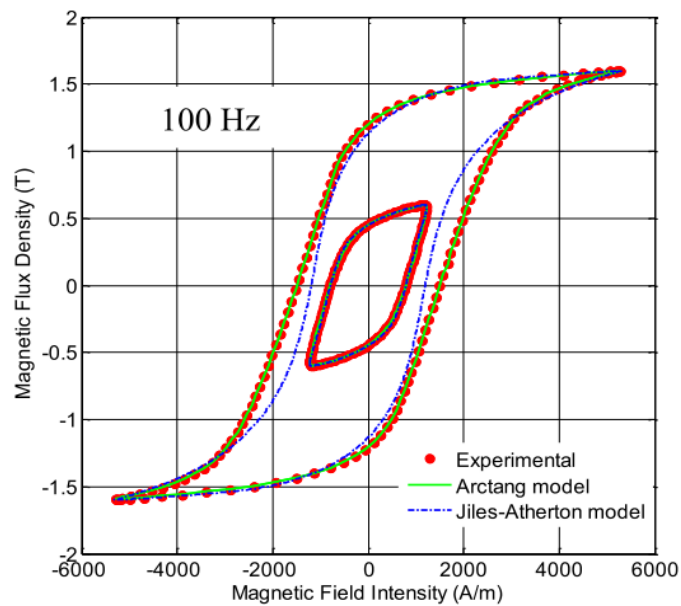


Fig. 2.23 Comparison of hysteresis loops between measured, calculated with improved arctangent model and original J-A model [61].

To enhance the accuracy of the modelling process for simulating GOESs, [63] introduced an improved J-A model with variable parameters. This proposed method is rooted in the magnetic domain theory and incorporates variable damping, variable pinning, and variable domain wall bending parameters to enhance the traditional J-A model. Fig. 2.25 illustrates a visual comparison between the results obtained from the measured curves and the modified J-A model [63], showcasing the effectiveness of the proposed approach in better simulating the behaviour of GOESs.

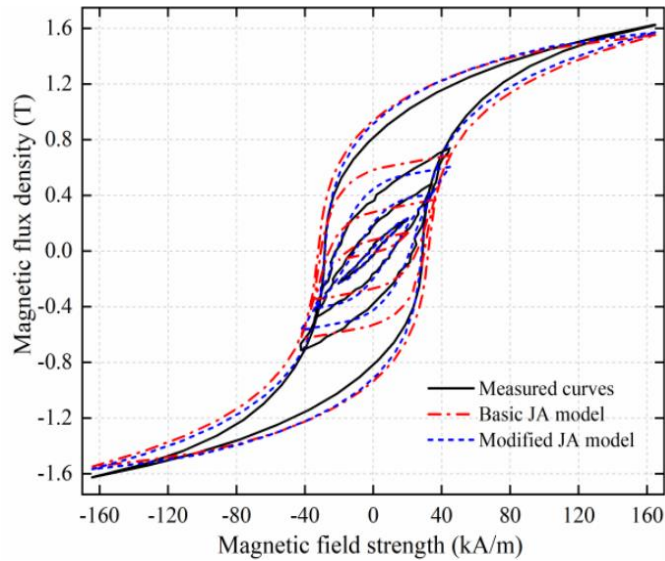


Fig. 2.24 Comparison of hysteresis loops between measured, calculated with modified and original J–A model [62].

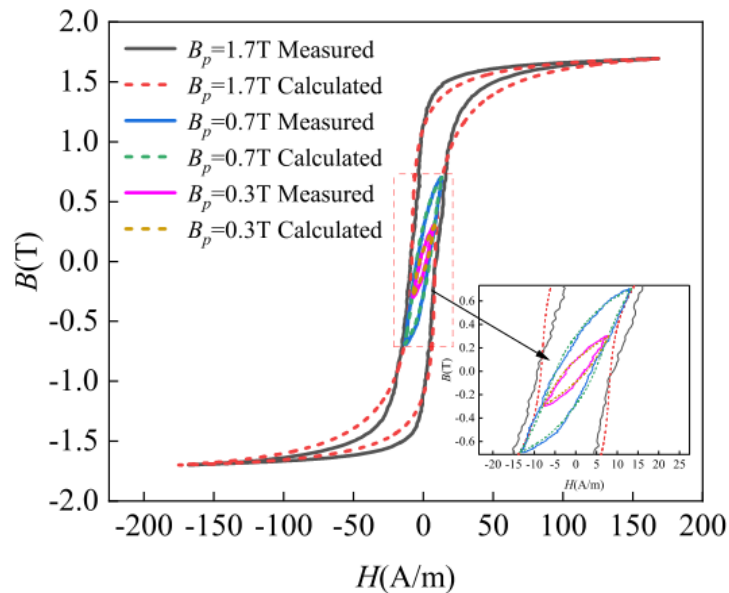


Fig. 2.25 Comparison of hysteresis loops between measured and calculated hysteresis loops using the improved J-A model [63].

2.5 Preisach model

The Preisach model of hysteresis, initially proposed by Ferenc (Franz) Preisach in 1935, generalizes magnetic hysteresis by describing the relationship between the magnetic field and magnetization of a magnetic material as a parallel connection of independent relay hysterons. In the context of ferromagnetism, the Preisach model is often used to depict a ferromagnetic material as a network of small, individually acting domains, each with a magnetization value of either m or $-m$. For instance, a sample of ferromagnetic material

may have magnetic domains evenly distributed, leading to a net magnetic moment of zero under an unmagnetised condition [4, 64].

The Preisach model is constructed using an infinite set of simple hysteresis relay operators, illustrated in Fig. 2.26 [65]. Each operator is represented as a rectangular loop on the input-output diagram. The numbers α and β correspond to the switching values of the input, indicating the "on" and "off" states, respectively. When the input signal surpasses a certain value, the operator causes the output signal to change in a stepwise manner. Usually, this change occurs between two values: a high one (turn on) and a low one (turn off). When the input signal $u(t)$ is smaller than α , the output signal $\gamma_{\alpha\beta}[u(t)]$ is low, indicating that the operator is in the "off" state. As $u(t)$ increases, the output remains low until $u(t)$ reaches the value of β , at which point the relay turns on. Further increases in $u(t)$ do not cause any additional changes. On the other hand, when $u(t)$ decreases, the output μ does not go low until $u(t)$ reaches α again. The behaviour of the relay operator $\gamma_{\alpha\beta}[u(t)]$ follows a loop path, and its future state depends on its past state, indicating a hysteresis effect [65].

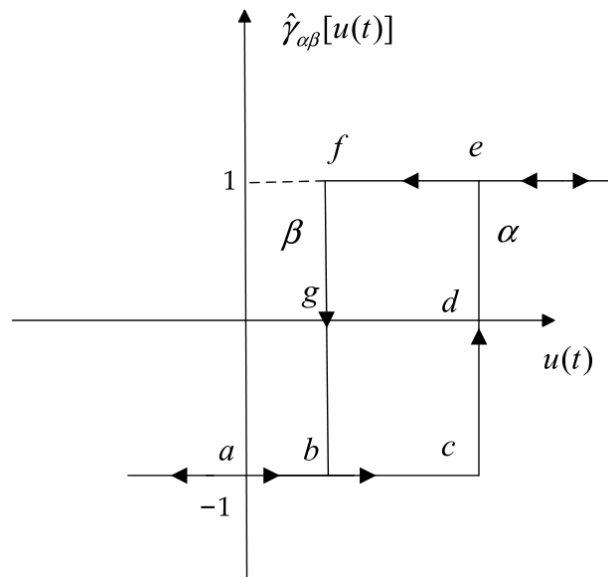


Fig. 2.26 Preisach relay operator [65].

The output $\gamma_{\alpha\beta}[u(t)]$ can be expressed mathematically as [65]:

$$\gamma_{\alpha\beta}[u(t)] = \begin{cases} 1 & \text{if } u(t) \geq \beta \\ -1 & \text{if } u(t) \leq \alpha \\ k & \text{if } \alpha < u(t) < \beta \end{cases} \quad (2.40)$$

The parameter k is defined as follows: if the last time the input variable v was outside the boundaries $\alpha < u(t) < \beta$, and it was in the region of $u(t) \leq \alpha$, then k is equal to -1; whereas if the last time v was outside the boundaries $\alpha < u(t) < \beta$, and it was in the region of $u(t) \geq \beta$, then k is equal to 1. This definition of the hysteron illustrates that the current value μ of the complete hysteresis loop is influenced by the historical behavior of

the input variable v . In other words, the hysteron's output depends on the past state of the input, reflecting the hysteresis effect [65].

The Preisach model is comprised of multiple relay hysterons that are connected in parallel and assigned specific weights, which are then combined through summation. This structure can be represented graphically with a block diagram shown in Fig. 2.27 [66]. Then, the Preisach model can be represented in a summation form using a finite number of rectangular elemental operators, which can be expressed as follows [66]:

$$f(t) = \sum_{j=1}^N \sum_{i=1}^N \mu(\alpha_i, \beta_j) \gamma_{\alpha_i \beta_j} [u(t)], \quad (2.41)$$

in which

$$\alpha_i = \beta_j = \alpha_i - 2 \frac{i-1}{N-1} \alpha_i.$$

Each of these relays is characterized by different α and β thresholds, and they are scaled by a factor, $u(t)$. Fig. 2.28 illustrates the hysteresis curves generated using Preisach model with different numbers of hysterons. As can be seen that the number of relay hysterons increases, the approximation of the modelled hysteresis curve improves [67].

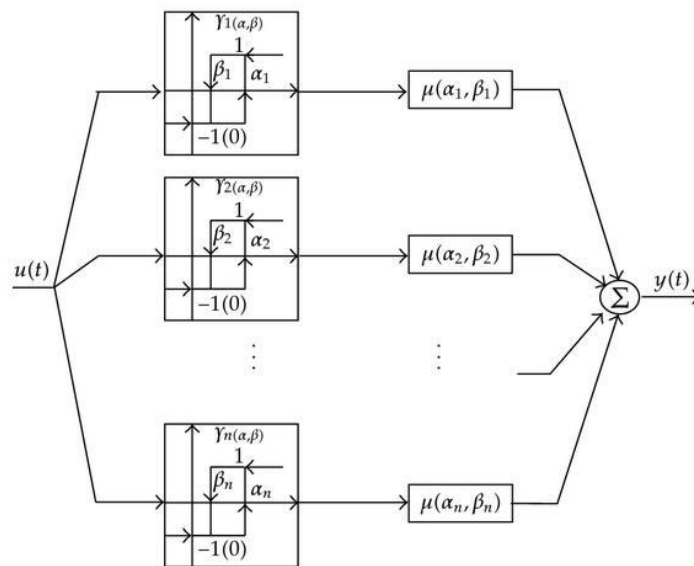


Fig. 2.27 Preisach model block diagram [66].

As the number of hysterons approaches infinity, the output function can be conceptualized as a continuous analogy of a system with parallel-connected two-position relays. These two-position relays take the input $u(t)$ and produce an output value of either +1 or -1. Each individual relay output is then multiplied by the corresponding weighted function $\mu(\alpha, \beta)$. To obtain the overall output, the products of the operator

outputs and weighted functions are integrated across all values of α and β . By following this process, the continuous Preisach model is derived [4, 66, 68]:

$$f(t) = \iint_{\alpha \geq \beta} \mu(\alpha, \beta) \gamma_{\alpha\beta}[u(t)] d\alpha d\beta. \quad (2.42)$$

The above discussion makes it evident that the Preisach model is constructed through the superposition of simple hysteresis operators, denoted as $\gamma_{\alpha\beta}[u(t)]$.

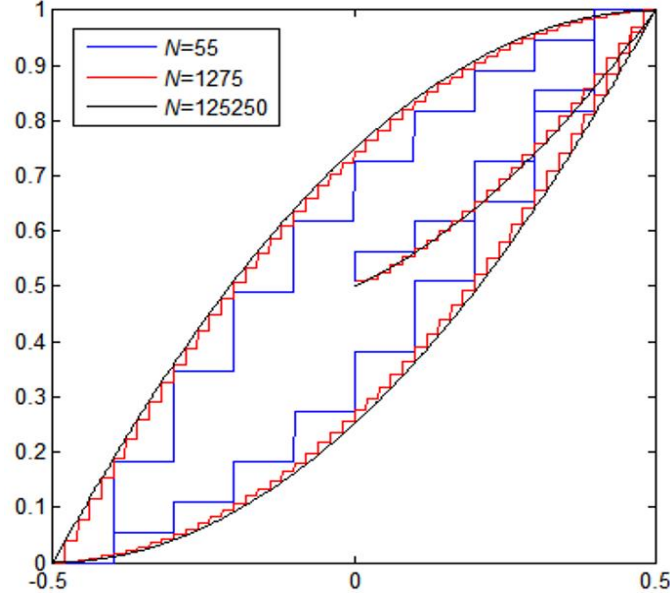


Fig. 2.28 Hysteresis curves generated using Preisach model with different numbers of hysterons [67].

2.5.1 Hybrid model combining J-A and Preisach models

In reference to [69], a hybrid model of dynamic hysteresis is proposed, which combines the J-A and Preisach models to effectively incorporate both domain wall motion and domain rotation, as well as account for the effects of eddy currents. To couple the J-A and Preisach models, a backpropagation neural network (BPNN) is employed. The validity of the proposed hybrid model of dynamic hysteresis is demonstrated through a comparison of the calculated and measured dynamic hysteresis loops and core losses in single sheet samples of GOESs and NOESs. Due to its consideration of full physical mechanisms, the proposed hybrid model exhibits enhanced accuracy and engineering applicability in simulating the magnetisation processes under both sinusoidal and non-sinusoidal excitations.

As mentioned in chapter 1, magnetisation can be influenced by both domain wall motion and domain rotation, and these phenomena occur simultaneously during the magnetisation process. The extent to which the magnetization changes due to either wall motion or rotation depends on both the applied field intensity and the current magnetisation state. To characterise the relationship between domain wall motion and

rotation mechanisms during the magnetization process, [69] introduced a dynamic proportion parameter K . Consequently, the total magnetisation of the material can be expressed as follows:

$$M = KM_P + (1 - K)M_J. \quad (2.43)$$

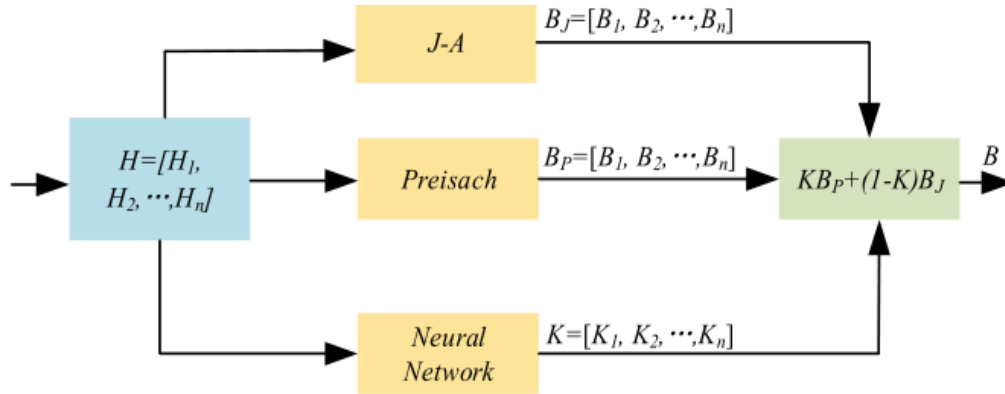


Fig. 2.29 Hybrid hysteresis model construction [69].

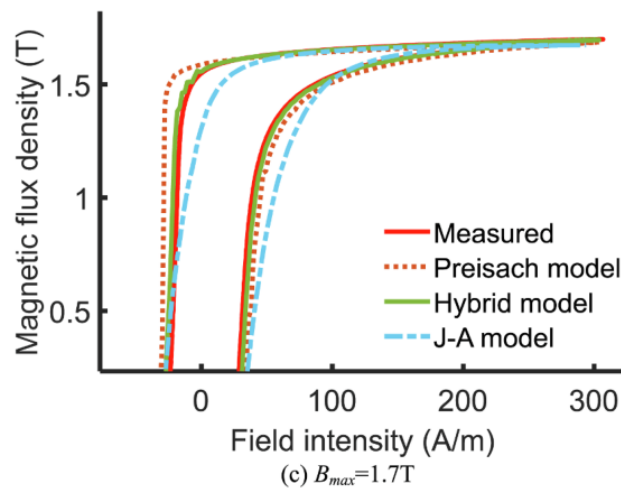


Fig. 2.30 Comparison of calculated and measured $B - H$ loops of GOES at excitation frequency $f = 50$ Hz [69].

In the context of the proposed hybrid hysteresis model [69], the magnetisation (M_P) attributed to domain rotation is better calculated using the Preisach model, whereas the magnetisation (M_J) associated with domain wall motion is better predicted by the J-A model. Since the domain distribution is complex, determining the dynamic proportion parameter K analytically is challenging. To accurately determine the proportion K for different magnetisation processes, a BPNN is employed. By considering the magnetisation mechanisms and their respective modelling approaches, the hybrid hysteresis model is constructed, as illustrated in Fig. 29. To evaluate the performance of the hybrid model, a comparison is made between the Traditional and Hybrid Models using hysteresis loops of GOES and NOES. Fig. 30 and 31 depict the comparison between the

hysteresis loops calculated by the J-A, Preisach, and proposed hybrid models against the measured results for GOESs and NOESs, respectively.

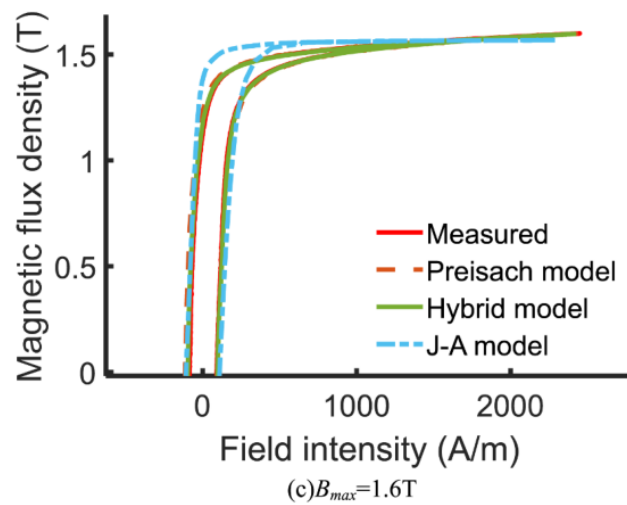


Fig. 2.31 Comparison of calculated and measured $B - H$ loops of NOES at excitation frequency $f = 50$ Hz [69].

2.6 Summary

Electrical steels are characterised by magnetic hysteresis under a controlled sinusoidal flux density. This phenomenon is linked to the microstructures of the materials and is involved in a complicated physical mechanism related to the magnetic domain theory. When the magnetic field changes direction, domains in the material are reoriented, tending to align themselves with the field. A time lag between magnetic flux density and magnetic field occurs due to the intertwined field interactions. The modelling of magnetic cores is mainly focused on tracking hysteresis loops and predicting energy losses. The models and theories have been continuously improved and enriched through the ongoing efforts of physicists and engineers for decades.

Direct modelling of hysteresis loops must overcome the obstacle of their nonlinearity, which arises during the magnetisation processes. The area of the hysteresis loop represents the energy loss per cycle, so tracking hysteresis loops and predicting energy losses are often linked. Nonetheless, energy loss was initially deemed as the sum of static hysteresis loss and classical eddy-current loss (Steinmetz). Experimental work indicated that the addition of these two components was always somewhat lower than the measured total loss. This difference between modelling results and measurement was defined as an anomalous loss. This led to the consideration of a third component (excess loss) in core loss analysis.

The ELSM of three components was developed by Bertotti, who proposed a statistical approach to calculate the components empirically. The static hysteresis loss was

evaluated using the Steinmetz equation, the classical eddy-current loss was calculated using the equation derived from Maxwell equations in one dimension, and the excess loss was described using a statistical equation according to the assumption of the domain structure. Zirka developed the ELSM based on the Bertotti model and adopted the magnetic field separation principle, which can be used to track hysteresis loops and provide a relatively high-level match compared to the corresponding measurements. As a result of tracking hysteresis loops in a wide range of frequencies and flux densities, the J-A model has proved to be the most popular and convenient model, which can be used to model major and minor loops with remarkable performance.

Many different models of magnetic hysteresis have been proposed from different perspectives of physics or mathematics over the years. Among the most widespread models, the J-A model revealed significant advantages. Compared to the previous models, the J-A model has several attractive features: it can be used with five parameters for isotropic materials and three more parameters for anisotropic materials. However, the parameter identification process is intricate. The non-physical behaviour of the original model occurs near the tip of the loop, forming an unclosed loop. If the initial parameters are not selected correctly, some convergence problems may occur. Nevertheless, the J-A model has been continuously developed and modified to describe the magnetic properties of diverse ferromagnetic materials. The Preisach model of hysteresis extends the concept of magnetic hysteresis by representing the relationship between the magnetic field and magnetic flux density of a magnetic material as a parallel connection of independent relay hysterons. Widely utilised, the Preisach model effectively captures both static and dynamic hysteresis loops. As a testament to the significance of both models, a hybrid approach combining the J-A model and the Preisach model is introduced. This hybrid model serves to emphasize the complementary strengths of each approach in hysteresis modelling.

Chapter 3 Magnetisation and Measurement Systems

This chapter provides details of the two standard methods of characterising electrical steel laminations. Steel samples of GOESs and NOESs can be characterised using a single sheet tester (SST) or an Epstein frame to determine magnetic properties, such as hysteresis loops, coercivities, permeability, and power losses under sinusoidal and non-sinusoidal excitations. In this chapter the SST and Epstein frame are introduced, and the experimental setups examined for different configurations and to investigate their effectiveness for determining the magnetic properties of laminated magnetic cores.

3.1 Single Sheet Tester

Single Sheet Tester (SST) is a standard measuring system to magnetise Epstein size laminations of electrical steel samples according to the BS EN 10280:2001 + A1:2007 [70, 71]. Fig. 3.1 illustrates an SST featuring a double yoke measuring coil system, constructed in accordance with IEC 60404-3A. This system ensures stringent quality control for strips, sheets, and slit strips across all processing widths. Construction schematic of an SST sensor with a test sample of steel sheet is provided in Fig. 3.2. The primary and secondary windings are uniformly distributed and surround the sample on a former. The magnetic field strength based on Ampere's law is measured from the input magnetisation current, and the magnetic path length is assumed as a fixed value [72]. An SST is designed to test electrical sheets and strips of any quality. The magnetic characteristics are investigated under sinusoidal and non-sinusoidal excitation for a wide range of flux densities and magnetisation frequencies.

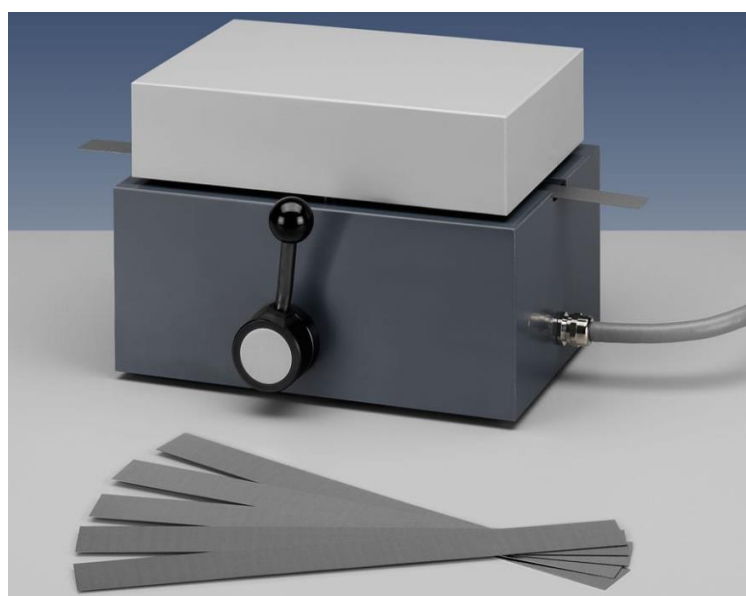


Fig. 3.1 SST with double yoke measuring coil system.

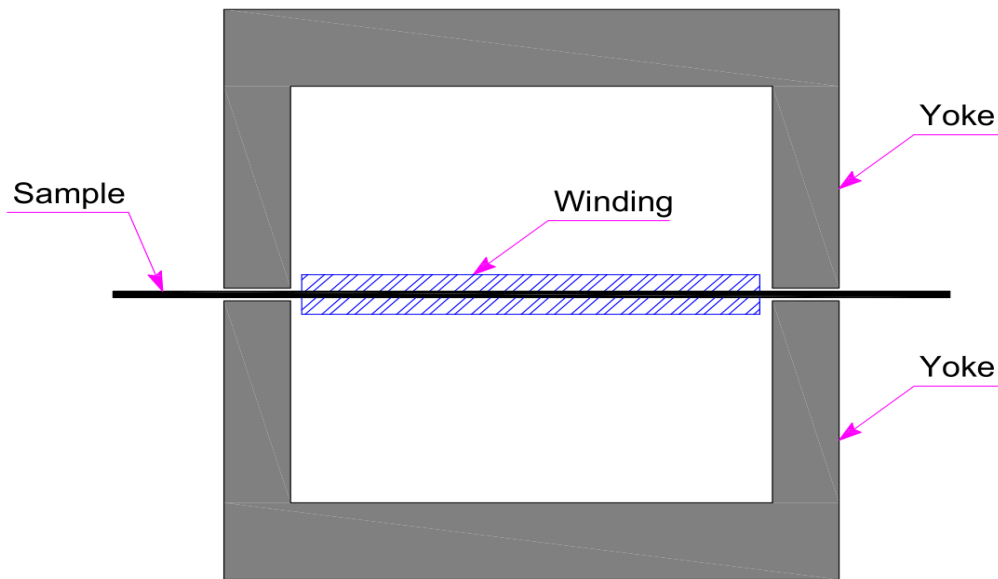


Fig. 3.2 Schematic of Single sheet tester with sample.

The principles of loss measurement, magnetic field, and magnetic flux density are based on the British standard described in [71]. In these experiments, the test samples are subjected to an alternating magnetic field of an excitation waveform; the magnetic field is deliberately controlled to achieve a sinusoidal magnetic flux density or with harmonic components.

A circuit diagram of this measuring system is shown in Fig 3.3, in which V_1 is used to measure the average rectified voltage and V_2 to measure the root mean square (RMS) voltage. M represents the air flux compensation mutual inductor, whereas T is the test frame. Mutual inductance is a circuit parameter that characterizes the relationship between two magnetically coupled windings, defining the ratio of the time-varying magnetic flux generated by one winding and induced into an adjacent second winding. To ensure precise measurement and reduce mutual inductance in the second winding, the primary winding of the mutual inductor should be connected in series with the primary winding of the test apparatus. Simultaneously, the secondary winding of the mutual inductor must be connected to the secondary winding of the test apparatus in series opposition. The mutual inductance value requires adjustment to ensure that, while passing an alternating current through the primary windings without the specimen in the apparatus, the voltage measured between the non-common terminals of the secondary winding remains below 0.1% of the voltage across the secondary winding of the test apparatus alone. Consequently, the average value of the rectified voltage induced in the combined secondary windings will be directly proportional to the peak value of the magnetic polarization in the test specimen [71].

The circuit is used to measure the total loss and magnetic flux density. The SST with the test sample represents an unloaded transformer. The total loss of the test sample is measured by the circuit. According to [71], the frequency meter has an accuracy of $\pm 0.1\%$, and the power measured by a wattmeter having an accuracy of $\pm 0.5\%$ or better under the power factor and crest factor conditions encountered during this type of measurements. The power supply is of low internal impedance and highly stable in terms of voltage and frequency. During the measurement, the voltage and the frequency is maintained constant within $\pm 0.2\%$. In addition, the waveform of the secondary induced voltage for sinusoidal excitation is maintained as sinusoidal as possible, which is normally achieved using a PID feedback controller or an electronic feedback amplifier [72]. It is preferable to maintain the form factor of the secondary voltage to within $1.111 \pm 1\%$. The secondary rectified voltage of the test apparatus is measured by an average type of voltmeter, which is used to determine the magnetic flux density shown in Fig. 3.4. The preferred instrument is a digital voltmeter having an accuracy of $\pm 0.2\%$. Meanwhile, a digital voltmeter with an accuracy of $\pm 0.2\%$ is used to measure the RMS values. The magnetic field strength is measured from the current of the primary winding as shown in Fig. 3.4. The peak value of the magnetic field strength is determined by measuring the voltage drop across a known precision resistor R_n with an accuracy of 0.1% using a voltmeter as shown in Fig. 3.4.

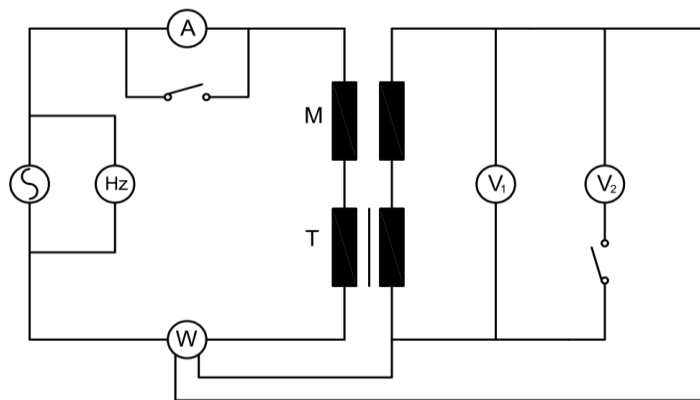


Fig. 3.3 Circuit for determining the total loss and magnetic flux density [71].

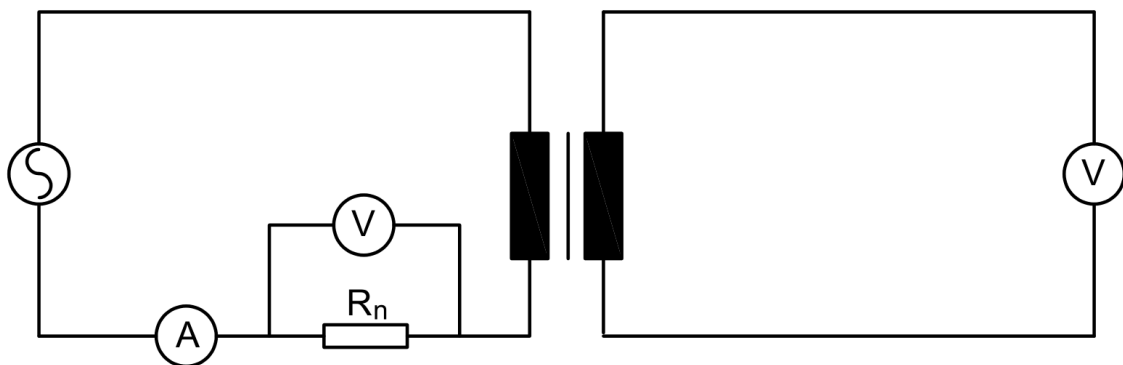


Fig. 3.4 Circuit for measuring the excitation current and magnetic field strength [71].

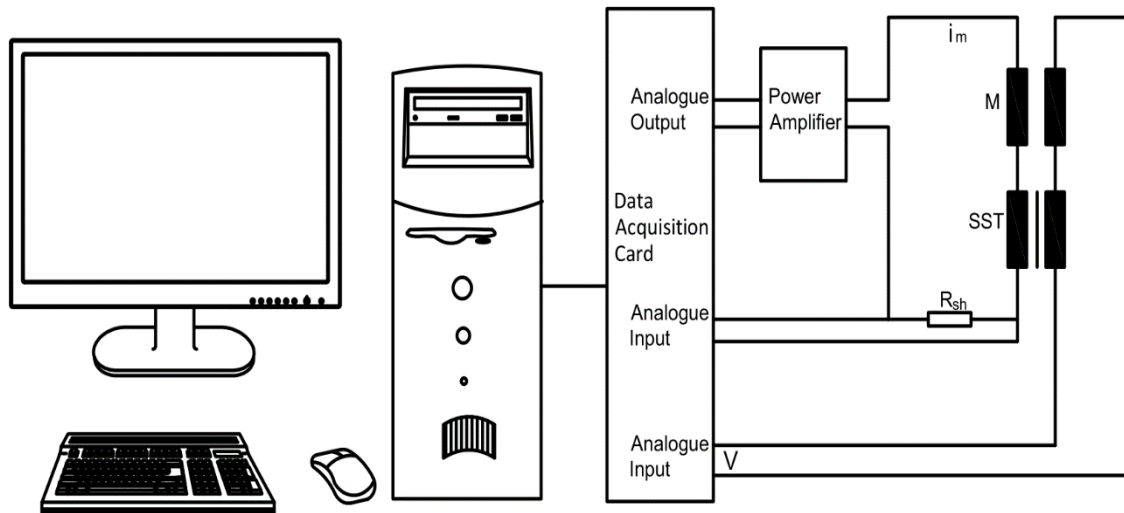


Fig. 3.5 Schematic diagram of computer-controlled SST measurement system.

Fig. 3.5 illustrates the measuring system, which is computer-controlled to monitor the measuring processes. These processes are controlled and monitored using reliable software, e.g. LabVIEW. The computer system is linked to the SST through a data acquisition Card (DAC). A power amplifier is used to supply the excitation current to the primary winding, a $1\ \Omega$ shunt resistor (R_{sh}) is used to measure the voltage drop, and an air flux compensated inductor is linked to the SST. A double vertical yokes magnetic sensor is used, both of which are made of grain-oriented silicon steel, as recommended by [71]. The magnetic sensor consists of two windings. This type of arrangement offers a low reluctance path to achieve accurate measurement data of the magnetic properties of GO steels.

3.2 Epstein Frame

Another standard measuring and characterising electrical steels is based on Epstein frame. Like the SST, with an Epstein frame the specific power losses, permeability and magnetic hysteresis loops of the test samples can be measured over a wide range of peak flux densities and magnetisation frequencies.

Measuring systems based on an Epstein frame are designed according to the British standard BS EN 60404-2:1998+A1:2008 [73] to characterise the magnetic properties of electrical steels. With this measuring system electrical steels can be characterised under sinusoidal and non-sinusoidal excitation with arbitrary harmonic components.

Fig. 3.6 depicts an Epstein frame with a squared coil arrangement, designed and constructed in accordance with IEC 60404-2. This specialized setup is utilized for conducting quality control assessments of electrical steel and other soft magnetic materials. A schematic diagram of an Epstein frame sensor and the test samples are shown in Fig. 3.7. There are four fixed windings connected in a series, the primary winding is connected to the power source to provide the magnetisation current, and the

secondary winding is connected to a voltmeter to measure the magnetic flux density. The primary winding, secondary winding, and specimen, which are tested as a core, form an unloaded transformer.

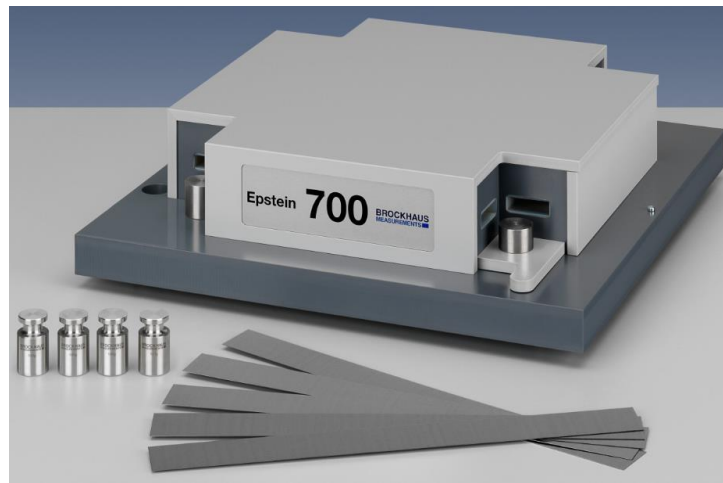


Fig. 3.6 Epstein Frame with squared coil arrangement.

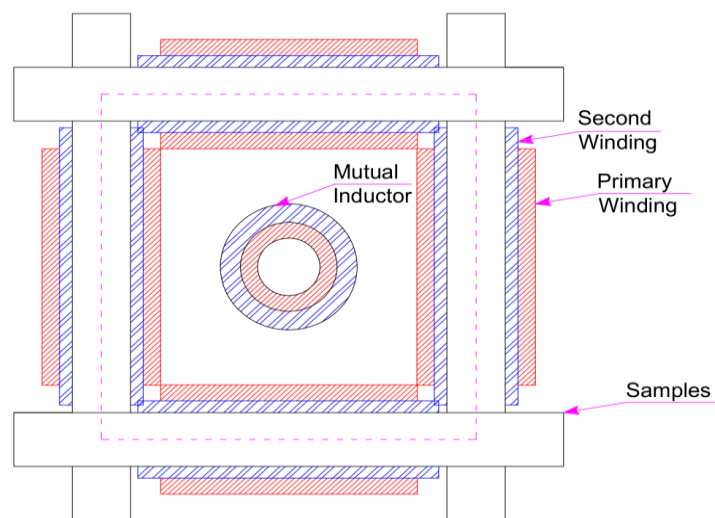


Fig. 3.7 Schematic of an Epstein frame and samples.

The total loss of the test sample is measured by the circuit, as shown schematically in Fig. 3.8. A wattmeter having an accuracy of $\pm 0.5\%$ or better under the power factor and crest factor conditions is used to measure the power W_m , which includes the power consumed by the instruments in the secondary circuit. A mutual inductor is used to compensate for the effect of the air flux. the mutual inductor for air flux compensation should be positioned at the centre of the space enclosed by the four coils, with its axis perpendicular to the plane of these coils' axes. The primary winding of the mutual inductor must be connected in series with the primary winding of the Epstein frame, while the secondary winding of the mutual inductor should be connected in series opposition to the secondary winding of the Epstein frame. The mutual inductance's value needs to be adjusted in a way that, when an alternating current passes through the primary

windings without the specimen in the apparatus, the voltage measured between the non-common terminals of the secondary windings does not exceed 0.1% of the voltage across the secondary winding of the test apparatus alone. Consequently, the average value of the rectified voltage induced in the combined secondary windings is directly proportional to the peak value of the magnetic polarization in the test specimen [73].

The total loss W_t of the test steel sheets is calculated using the following equation [73]:

$$W_t = \frac{N_1}{N_2} W_m - \frac{(1.111U_2)^2}{R_i}, \quad (3.1)$$

where N_1 is the total number of turns of the primary winding, N_2 is the total number of turns of the secondary winding, R_i is the total resistance of the instruments in the secondary circuit, and U_2 is the average value of the rectified voltage induced in the secondary winding [73].

With reference to [73], the internal impedance of the power supply should be low, and the voltage and frequency highly stable. During the measurement, the voltage and the frequency are maintained constant to within $\pm 0.2\%$. When measuring the secondary induced voltage with sinusoidal excitations, it is necessary to maintain a sinusoidal voltage. A digital controller was designed to achieve this task [74]. It is preferable to maintain the form factor of the secondary voltage to within $1.111 \pm 1\%$. The secondary rectified voltage of the Epstein frame is measured with a voltmeter, which is used to determine the magnetic flux density shown in Fig. 3.9. The preferred instrument is a digital voltmeter having an accuracy of $\pm 0.2\%$. The magnetic field strength can be calculated from the current of the primary winding measured using the circuit shown in Fig. 3.9 and the peak value of the magnetic field strength can be calculated from the peak magnetisation current measured using a voltmeter through the voltage drop across a known precision resistor R of the accuracy of 0.1% , the circuit is shown in Fig. 3.9.

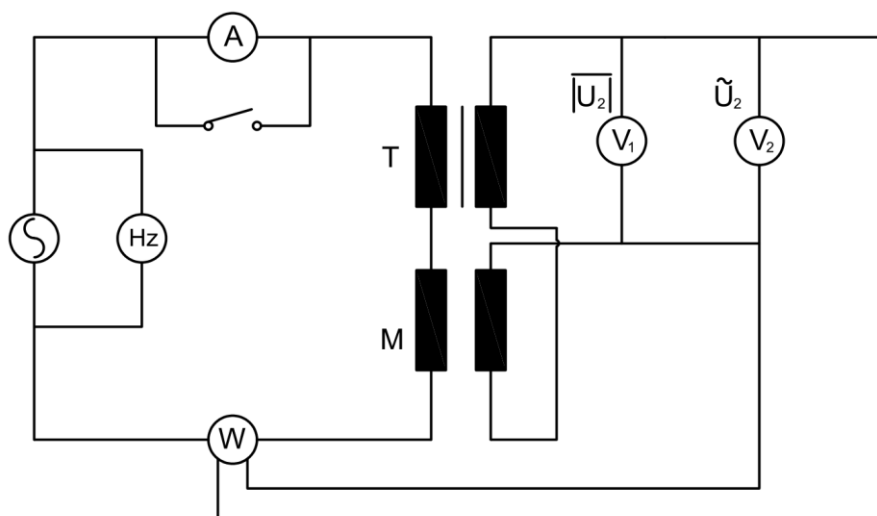


Fig. 3.8 Circuit for the core loss measurement [73].

The magnetic field $H(t)$ generated by the electrical current $i(t)$ of the primary winding are related via Ampere's law, expressed as follows:

$$H(t) = -\frac{N_1 i(t)}{l_m}, \quad (3.2)$$

where l_m is the magnetic path length, which is 0.94 m for a standard Epstein frame as specified in [73].

The magnetic flux densities $B(t)$ are derived according to Faraday's law and Lenz's law, and related as follows:

$$B(t) = -\frac{\int v(t) dt}{AN_2}, \quad (3.3)$$

where A is the lamination cross-sectional area, and $v(t)$ is the voltage measured across the secondary winding.

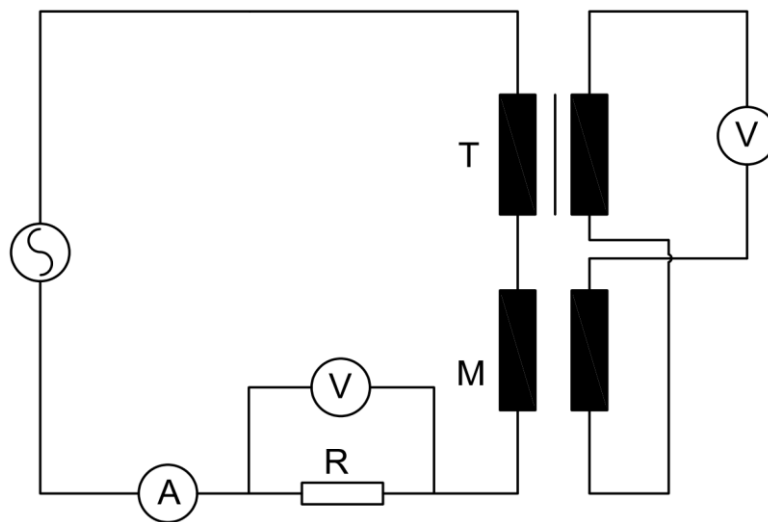


Fig. 3.9 Circuit for measuring the magnetising current and peak magnetic field strength using a voltmeter [73].

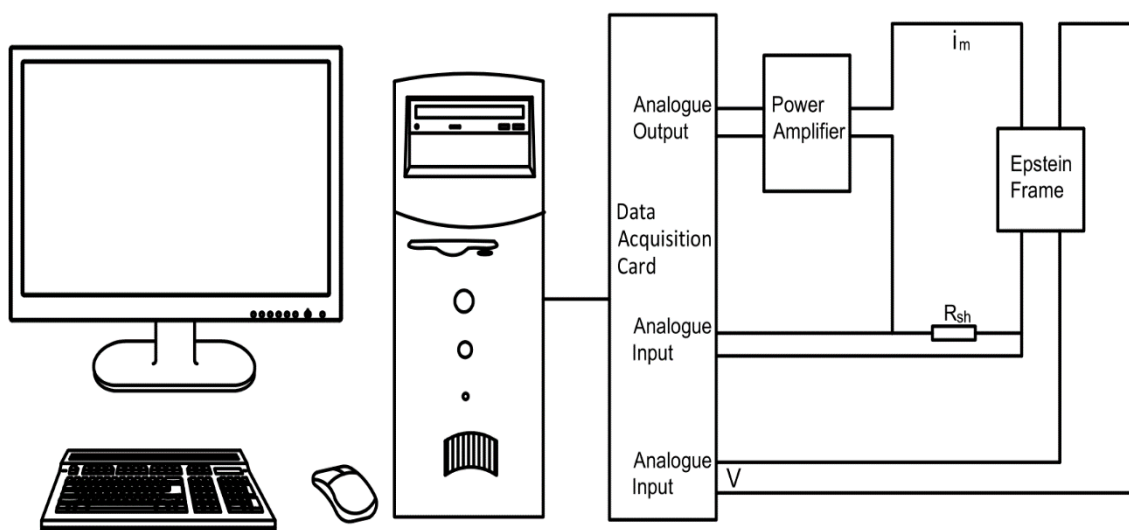


Fig. 3.10 Computer-controlled measurement system of Epstein frame [74].

The computer-controlled measurement system of the Epstein frame is shown schematically in Fig. 3.10. In this setup, the steel sheets are placed between the yokes of the standard Epstein, and the flux continuity at the square corners is ensured by double-lapped joints. In addition, a force of 1N is placed at each corner joint and provides a good and reproducible flux enclosure. This measurement arrangement consists of a computer-controlled system, a data acquisition card (DAC), a power amplifier, and a $1\ \Omega$ shunt resistor R_{sh} . Software is implemented to display the expected output in real-time according to a mathematical analysis of the process measurements. The software employed can save measurement data instantaneously.

3.3 Comparison of SST and Epstein Frame

The SST and the Epstein Frame are internationally accepted standards for measuring the magnetic hysteresis and energy losses of electrical steels. In this study, the magnetic hysteresis and energy losses of NOES was measured using both the Epstein-square and SST. The SST demonstrated standard S-shape hysteresis loops in isotropic characteristics, which were not detected using the Epstein Frame in the standard manner. Moreover, it was observed that the Epstein standard method of measurement could lead to a poor quality of certain NOES samples with serious distorted hysteresis loops. To address this issue, improved test procedures are suggested.

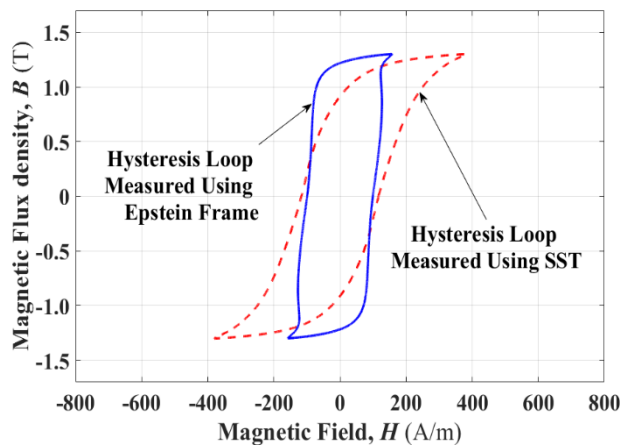


Fig. 3.11 Hysteresis loops for NOESs at 50 Hz and 1.3 T measured using SST and Epstein Frame.

When considering hysteresis loops and energy losses, assessing the advantages and disadvantages of the two measurement methods, namely SST and the Epstein frame, can be challenging. In recent times, SST have gained popularity for investigating the magnetic properties of electrical steel. One key advantage of using an SST is the significantly lower probe mass requirement compared to the Epstein frame. This makes the SST more suitable for observing variations in properties resulting from any treatment between two

measurements. On the other hand, the standardized Epstein frame offers the benefit of averaging, providing a more representative result for larger sheets of material.

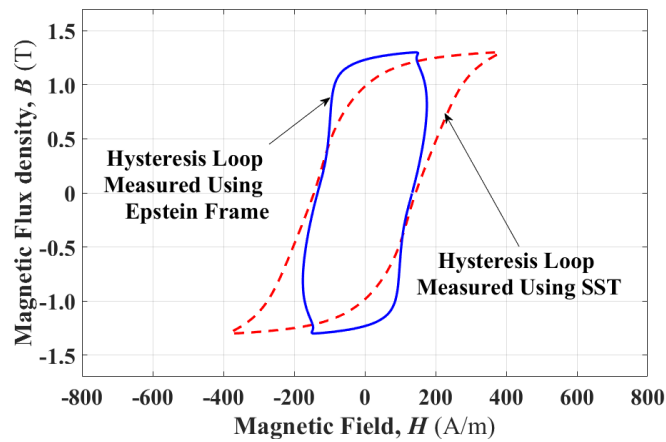


Fig. 3.12 Hysteresis loops for NOESs at 100 Hz and 1.3 T measured using SST and Epstein Frame.

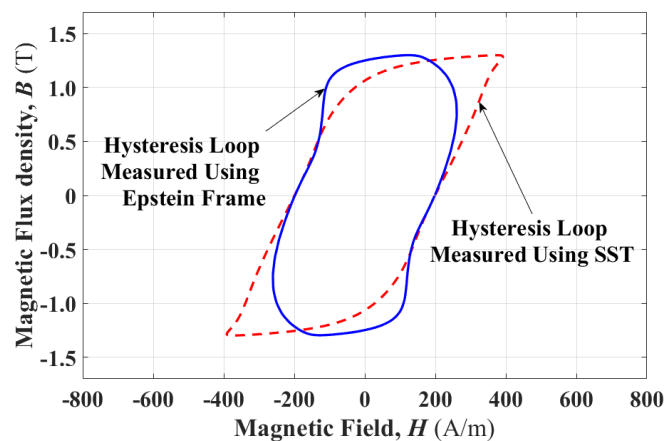


Fig. 3.13 Hysteresis loops for NOESs at 200 Hz and 1.3 T measured using SST and Epstein Frame.

Noticeable discrepancies exist between the measured hysteresis loops and energy losses obtained through the SST and Epstein frame methods. The primary objective of this study is to simulate the magnetic hysteresis loops and accurately evaluate the energy losses. However, the observed measurement deviations can introduce errors and potentially render some models inadequate. Particularly, the parameters and accuracy of the J-A model and Preisach model heavily rely on the measured hysteresis loops and data.

Before simulating the hysteresis loops, a comparison of the magnetic hysteresis loops measured using both the SST and Epstein-square methods is conducted to identify and develop the appropriate modelling methodology. Fig. 3.11 illustrates a comparative schematic diagram of Hysteresis loops for NOESs at 50 Hz and 1.3 T, as measured using SST and Epstein Frame. Clearly, the hysteresis loop obtained from the SST exhibits a

standard sigmoidal shape, while the one from the Epstein Frame shows some distortion. Additionally, the Epstein Frame captures anisotropic characteristics that the SST does not. Surprisingly, even though both sets of samples were from the same batch, the Epstein Frame magnetization results in the samples reaching peak flux density with significantly less magnetic field, indicating higher permeability. However, it remains challenging to determine definitively which method is superior.

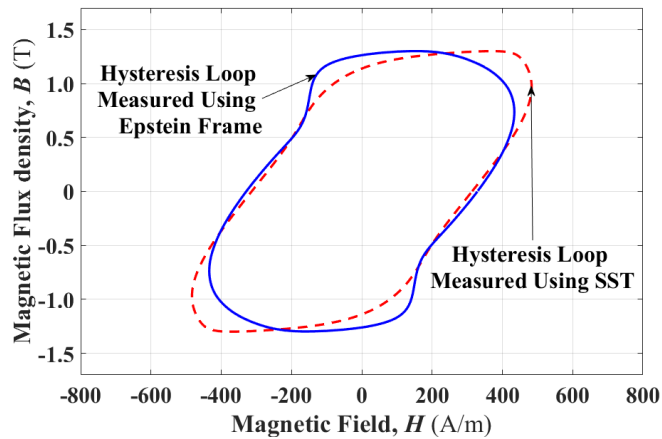


Fig. 3.14 Hysteresis loops for NOEs at 400 Hz and 1.3 T measured using SST and Epstein Frame.

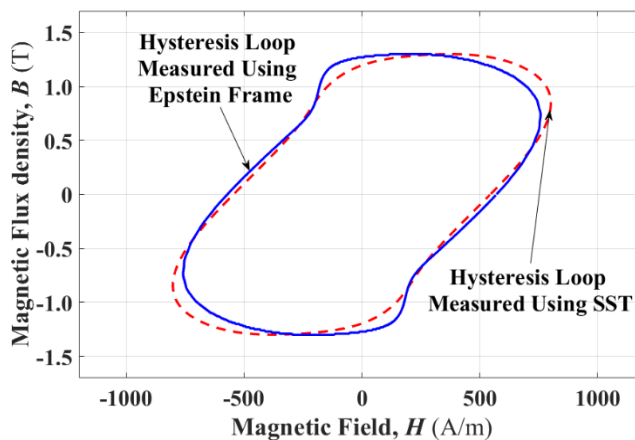


Fig. 3.15 Hysteresis loops for NOEs at 800 Hz and 1.3 T measured using SST and Epstein Frame.

The hysteresis loops of NOEs are also measured using both the SST and Epstein square test setups at frequencies of 100 Hz, 200 Hz, 400 Hz, and 800 Hz, with a magnetic flux density of 1.3 T. The results are shown in Fig. 12 to 15. It is evident that as the magnetisation frequencies increase, both SST and Epstein Frame methods produce distorted magnetic loops. This indicates that at higher frequencies, the magnetic properties become more complex, making energy loss evaluation intricate. However, there are notable similarities in the hysteresis loops obtained from the SST and Epstein frame at 400 Hz and 800 Hz as shown in Fig. 14 and 15. At these frequencies, both

measurement techniques exhibit anti-hysteresis features, wherein the magnetic flux density leads the magnetic field even as the field starts reducing from its maximum value. The magnetic flux density continues to increase until a certain maximum value is reached.

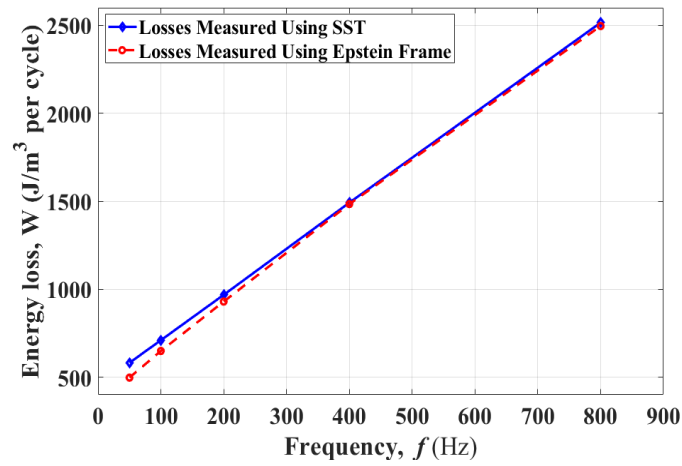


Fig. 3.16 Energy losses per cycle for NOESs at 50 - 800 Hz and 1.3 T measured using SST and Epstein Frame.

Table 3.1 Energy losses for NOESs at 50 - 800 Hz and 1.3 T measured using SST and Epstein Frame.

Magnetisation Frequency	50 Hz	100 Hz	200 Hz	400 Hz	800 Hz
Losses Using SST J/m ³	581.57	710.03	967.98	1491.8	2515.5
Losses Using Epstein Frame J/m ³	497.48	648.96	929.76	1483.9	2496.0
Differences J/m ³	84.09	61.07	38.22	7.90	19.50
Diff. percentage	16.9%	9.41%	4.11%	0.53%	0.78%

The measured energy losses of NOESs are compared in Fig. 3.16 using both the SST and Epstein square test setups. The measurements were taken at frequencies of 50 Hz, 100 Hz, 200 Hz, 400 Hz, and 800 Hz, with a magnetic flux density of 1.3 T. The results reveal a significant disparity between 50 Hz and 100 Hz measurements. Table 3.1 illustrates the differences for SST and Epstein Frame methods at 50 Hz and 100 Hz, which are 84.09 J/m³ and 61.07 J/m³, respectively. The corresponding percentage differences are 16.9% and 9.41%, indicating a high level of disagreement between the measured energy losses at low frequencies. However, at 200 Hz, 400 Hz, and 800 Hz, the differences between the measured energy losses for SST and Epstein Frame methods are found to be acceptable,

with percentage differences of 4.11%, 0.53%, and 0.78%, respectively. The primary focus of this study is to simulate the magnetic hysteresis loops and model the energy losses. Therefore, a discussion of the feasibility of the measurement setup will not be included in this thesis.

3.4 Research on Accurate Measurements

The above-mentioned standardised measurement methods, based on the use of an Epstein Frame or SST, provide good reproducibility, as verified by many researchers [75, 76]. As such, these two measurement systems have been widely used in industrial and academic research. Nonetheless, both Epstein Frame and SST methods can systematically contribute to the measurement uncertainty [77] and the measured power losses can be evidently different from the authentic loss values provided by accurate measurements of the effective magnetic field strength and the magnetic flux density [78, 79].

A great deal of efforts has been conducted to improve the accuracy of the measurement of the magnetic properties in laminations by using extended Epstein Frame and SST methods. [80] proposed a simplified structure of the SST using the compact cross-yoke with the new arm-slotted specimen and the integrated $2 - D B - H$ sensor to minimize the influence of the planar eddy currents to obtain accurate measurements. Some modifications of Epstein Frame have been made to improve the accuracy of measured magnetic hysteresis loops, magnetisation curves, and specific power losses [81, 82]. [83] used an extended Epstein Frame with different lengths to test the magnetic properties of GOESs in the rolling direction to check that the power losses are effectively proportional to the frame dimensions.

Although improving the accuracy of the measurement using different measurement methods is not the objectives of this study, it is important to be aware that measured data can be influenced by multiple elements. The accuracy of the measurements depends highly on the accuracy of the components in the measurement systems. Meanwhile, different measurement methods can acquire different characteristics of the magnetic materials. So, the development of the advanced measurement systems is critical to explore the effective properties of the magnetic materials.

The intension at the outset of the research undertaken in the production of this thesis, was for the author to undertake their own experimental work in order to collect complementary validation data. Unfortunately, due to the impact of Covid-19 this did not prove possible; despite, in March 2022 a window of a few days presenting the opportunity to undertake limited experimental measurements following a kind offer from the electronic and magnetic group at the National Physical Laboratory (NPL) to use their equipment. Disappointingly, the data gathered proved to be of insufficient quality for comparison purposes. Accordingly, the only feasible fallback position was to resort to

using existing reliable experimental data and cite that source. To this end raw data, including instantaneous waveforms of magnetic field and magnetic flux density for both GO and NO electrical steels, were taken from [84 - 87]. It is these data that are used for modelling validation purposes throughout the remainder of this thesis. Sources [84 - 87] provide an overview of the related experiment methodology and techniques behind the collection of this data.

Chapter 4 Novel magnetisation theory of ferromagnetic materials

A novel theory of magnetic hysteresis in ferromagnetic materials is presented based on the concepts of hysteresis, excitation, and magnetisation fields. This new theory utilises magnetic domain theory, including domain wall movement, domain annihilation, domain rotation, and domain nucleation. Magnetic hysteresis is a phenomenon of magnetisation lagging the magnetic field when a magnetic material is under external excitation. The cause of magnetic hysteresis is assumed to be the coupling effect of the magnetisation at any order reversal turning point. In this respect, the hysteresis and excitation fields are adopted to address the physical grounds of coercivity to enhance the new theory. A plot of the relationship between the input magnetic field and output magnetic flux density is generated based on a history-independent hysteresis model (J-A model) to analyse the magnetisation processes. This is sufficient to explain the new terms of the excitation and hysteresis fields. The excitation field drives the magnetisation processes, while the hysteresis field contributes to the magnetic flux density falling behind the magnetic field. In addition, the eddy current counter field is also considered as a means of describing the magnetic core loss. The new theory is suitable for describing the magnetisation processes of GOES and NOES laminations. The differences in the magnetisation processes of both samples are described in the context of future work to derive a general physical model that attempts to show all the features of magnetic hysteresis and predict the energy loss of magnetic cores in electromagnetic machines.

4.1 Introduction

Magnetic hysteresis usually occurs during the magnetisation processes in magnetic materials applied in electromagnetic devices as magnetic cores, i.e. transformers, motors, and generators. When the magnetic field is reversed from certain values to zero, the corresponding magnetisation cannot decrease to zero simultaneously. The magnetisation at zero magnetic field in the hysteresis loop is called remanent magnetisation M_r , and it is usually interpreted as the visible manifestation of magnetic hysteresis. This mysterious phenomenon is also revealed in the coercive field (coercivity) H_c , which brings the magnetisation to zero value along the descending branch of the major loop as though H_c is overcoming the lagging force to bring the magnetisation down to zero value. The coercivity provides an indicator to assess the magnetic hardness of the magnetic material and is related to the energy losses in the material when electromagnetic devices are in operation.

Typically, hysteresis loops can be obtained experimentally by measuring magnetic materials under sinusoidal excitation waveforms or theoretically by modelling specific magnetic materials by evaluating the effect of relevant parameters. The application of different magnetic materials in electromagnetic devices depend on the specific properties needed. The magnetic properties of GOES and NOES strips and sheets are investigated employing an Epstein frame and an SST. The samples are characterised by measuring the total energy losses and hysteresis loops under sinusoidal excitations of different frequencies and peak flux densities. In such experiments, the magnetic samples are subjected to an alternating field of a controlled excitation waveform, resulting in a sinusoidal magnetic flux density of the form:

$$B(t) = B_{pk} \sin(\omega t), \quad (4.1)$$

where B_{pk} is the peak flux density. Ideally, the magnetic field should be described, assuming magnetic linearity, by the function:

$$H(t) = H_{pk} \sin(\omega t + \theta), \quad (4.2)$$

due to the lagging in time behind the magnetic field of the magnetic flux density [88]. Unfortunately, the hysteretic mechanism is far more complicated than a simple linear relationship between $B(t)$ and $H(t)$ so that the $H(t)$ manifests unpredictable features during one cycle.

Ewing's theory, described in his treatise [89], is one of the earliest systematic theories for magnetic induction; he attempted to explain hysteresis phenomena in ferromagnetic material in terms of the forces between atoms. He regarded each atom as a micro permanent magnet free to rotate in any direction around its centre. The orientations of the various magnets are influenced by the magnetic forces and the mutual coupling between the magnets. The experiment was conducted using as many as 130 magnets sited at the points of a plane square lattice equally spaced. The magnetisation curve and hysteresis loop were calculated from the model by considering the magnetic potential energy of a magnet moment and the distance between the magnets [90]. Although limited by the differences between micro-scale reality and macro-scale assumption, Ewing's Theory provided a meaningful guideline for modern physicists and engineers.

Weiss's theory concerning the assumption of the molecular(atomic) field and domains of the ferromagnetic properties was proposed by Pierre Weiss in 1906 [5]; these far-reaching hypotheses were proved by the observation of magnetic domain imaging first made by Francis Bitter through Bitter patterns imaging technique [91]. Based on Weiss's postulation, it is generally accepted that the Weiss mean field (WMF) in a ferromagnetic sample below its Curie temperature is strong enough to magnetise the sample to saturation even in the absence of an applied external field. The ferromagnetic sample in the demagnetised state comprises many small magnetic domains. Each domain is

magnetised by the atomic field to the saturation value M_s , and the magnetisations of the different domains are oriented to cancel out each other so that the vector sum of the domain magnetisations has no magnetic manifestation. Many models were established based on the concept of magnetostatic energy proposed by Landau and Lifshitz [92], which accounts for the formation of domains. The domain structure in a single crystal ferromagnet with cubic symmetry is varied during a balance between four energy terms: exchange, magnetostatic, anisotropic, and magnetoelastic [93].

When a sample under demagnetised conditions is excited with a magnetic field H , the external field will break the magnetostatic energy balance by introducing an additional Zeeman energy [8]. The magnetic domain structure varies according to the new conditions to minimise the energy. Namely, the domains with M_s oriented approximately parallel to H become larger at the expense of those oriented antiparallel to H through domain wall motion [94]. When increasing H to a large enough value, domain walls will be removed entirely. A single domain parallel to the easy crystallographic direction nearest the direction of H is left to balance the magnetostatic and anisotropy energy.

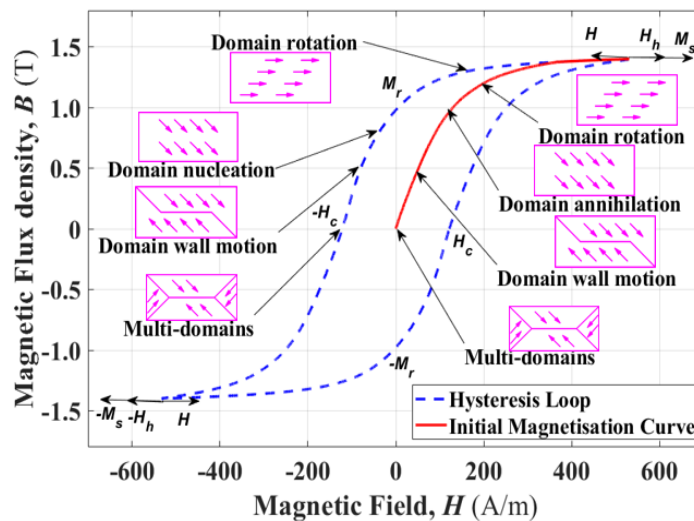


Fig. 4.1 Domain variations in NOES during the magnetisation procedure.

Further increasing H , the Zeeman energy will overcome the anisotropy energy, and rotate the domain direction to align with H , then magnetisation arrives at its technical saturation. Goodenough [94] investigated the possible mechanisms of domain nucleation when magnetisation is reversed from saturation, and he asserted that domains of reversal magnetisation are created in several regions at lattice imperfections. The processes of magnetic annihilation and nucleation are shown in Fig. 4.1 and Fig. 4.2 for NOES and GOES, respectively. By comparing the two figures, a sharp turning point of nucleation can be observed in Fig. 4.2. This is because, for GOES, the grains are oriented along the rolling direction so that the anisotropic direction is close to the direction of the magnetic field,

then the anisotropic energy needed to turn the single domain direction is less than that of NOES.

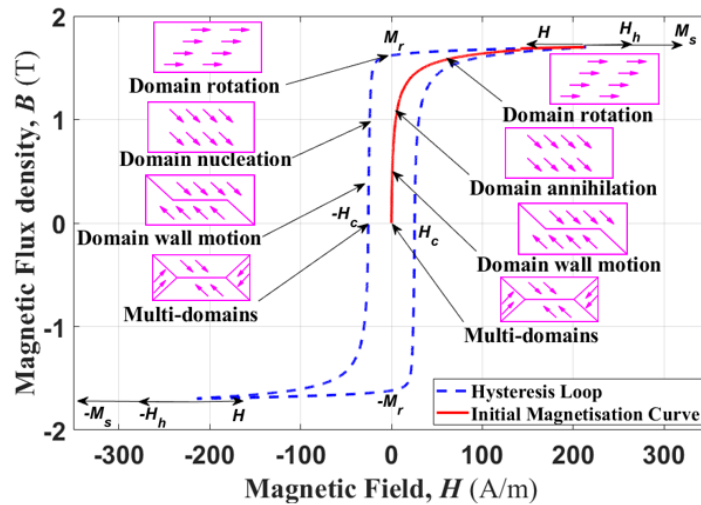


Fig. 4.2 Domain variations in GOES during the magnetisation procedure.

It is universally acknowledged that a single domain in a ferromagnetic material with many atomic magnetic moments (typically 10^{12} - 10^{18}) aligned parallel can be deemed as a micro magnet [56]. The directions of the domain vary randomly so that no magnetic feature manifests without an external magnetic field, but how to explain the phenomenon of hysteresis using the domain theory is still absent. Although extensive research has been conducted for decades, magnetic hysteresis is still a matter of intense debate between physicists and engineers. This study would like to propose one assumption for interpreting hysteresis. As shown in Fig. 4.1 and Fig. 4.2, the assumption is made according to the coupling effects between domains and atomic dipoles resembling the mutual reaction between the magnets in Ewing's theory or WMF in Weiss's theory. This study assumes that there exists a coupling field aligned with the direction of the previous magnetisation when the time rate of change of the magnetisation changing directions; it is this coupling field that accounts for the hysteresis field, which contributes mainly to the genuine reason for magnetic hysteresis. In other words, this coupling field can also be deemed as the WMF at the reversal turning point.

This chapter provides an in-depth analysis regarding the above hypothesis to tackle the protracted existing conundrum concerning magnetic hysteresis in ferromagnetic materials under external excitation sources. The hysteresis field is encountered at any order tuning point when magnetic flux density undergoes opposite direction-changing excitation. The contribution of the hysteresis field is due, theoretically, to the coupling effect of the previous magnetisation, and the coupling effect is determined based on the micro-structures of magnetic materials. The sum of the excitation field and hysteresis field establish the magnetic field, which triggers the magnetisation processes effectively.

4.2 Measurement System and Hysteresis Mechanism

Conventionally, the magnetisation of GOESs and NOESs has been analysed from the perspective of the hysteresis phenomenon [95, 96], the physical mechanism of magnetic hysteresis having been of interest to scientists for more than a century since the term hysteresis was first coined by Sir James Alfred Ewing in 1900 [97]. Because the eddy current will generate the counter field when the steel laminate is magnetised, an assumption was proposed by Arimatea and Jacquet in 2001 that magnetic hysteresis is attributed to eddy currents [98]. Another more widely accepted assumption was made according to the imperfect microstructures of the magnetic material. It was assumed that the hysteresis is caused by the pinning site effect, which impedes domain wall movement and results in the magnetisation lag behind the magnetic field [99 - 101]. The interpretation of magnetic hysteresis was described using a friction force due to the pinning effect of Bloch walls by Henrotte and Hameyer in 2006 [102]. Harrison proposed a positive feedback theory to explain the origin of magnetic hysteresis in 2009 [103]; this physical mechanism of hysteresis was established based on the WMF effect due to the interaction of atomic dipoles [8]. The theories in [99 - 102] and [103] are contradictory because pinning site effects or dry-friction force always produces negative feedback effects, whereas the WMF effect is described as positive feedback.

Apart from the analytical and numerical modelling, measuring systems based on the SST and Epstein frame are standardised, as described in chapter 3. These measuring systems are used to characterise Epstein size laminations of GOES and NOES in line with the national and international standards [71, 73]. Reliable computer software is used to measure, monitor, and control the magnetisation processes. During the measurement, the magnetic field $H(t)$ is produced by the excitation electrical current $i(t)$ of the primary winding. The secondary induced voltage for sinusoidal excitation is controlled using a PID feedback controller so that the waveform is maintained as sinusoidal as possible [72]. Then, the magnetic flux densities $B(t)$ are obtained based on Faraday's law and Lenz's law.

Fig. 4.3 illustrates the control loop of the measurement system; the relevant field separation is also schematically analysed. The error between the set point and measured magnetic flux density is input to the PID controller, and the controller's output signal is used to control the power amplifier so that the input current is regulated to achieve the sinusoidal waveform of magnetic flux density. The waveforms of magnetic flux density and magnetic field are obtained for a typical NO electrical steel at the magnetisation frequency of 50 Hz and peak flux density of 1.4 T; the waveforms of the magnetic flux density and magnetic field are shown in Fig. 4.4. Apparently, the magnetic flux density lag behind the magnetic field due to the hysteresis effects.

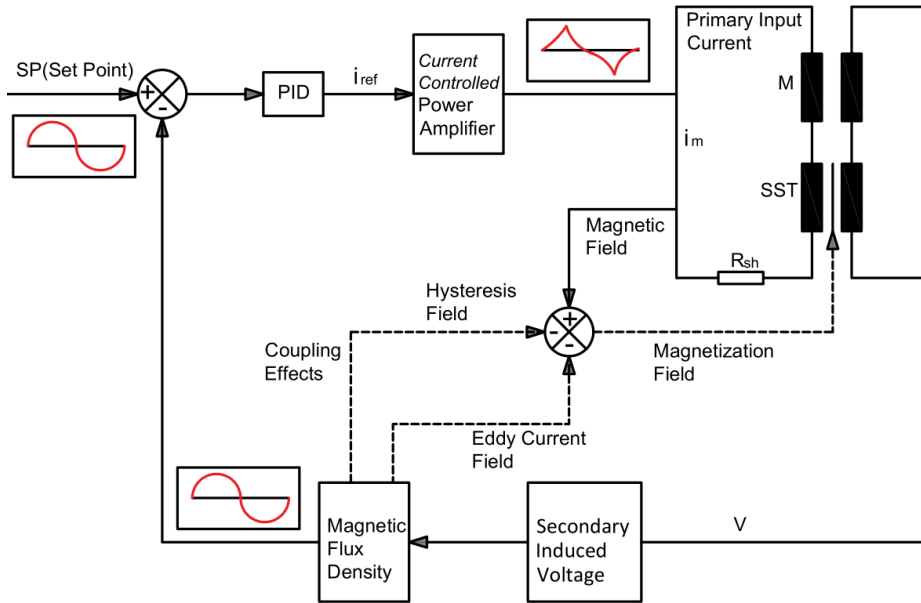


Fig. 4.3 Control loop of the measurement system with field separation components.

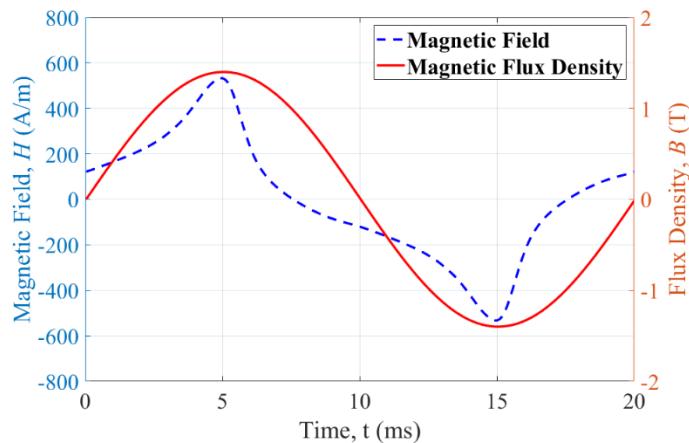


Fig. 4.4 Waveforms of magnetic field and magnetic flux density.

As shown in Fig. 4.4, the magnetisation processes change directions between magnetisation and demagnetisation in a cycle (usually many cycles per second). In the first and third quadrants of the magnetic flux density, the time rate of change of the magnetic flux density is positive and aligned in the magnetisation direction ($dB/dt > 0$). So, the process is the magnetisation process because the magnetisation is increasing. Nevertheless, the time rate of change of the magnetic flux density in the second and fourth quadrants is negative and opposite to the magnetisation direction ($dB/dt < 0$). During the demagnetisation process, the magnetisation decreases in amplitude. So, the output of the PID controller is a positive value in the first and fourth quadrants and a negative value in the second and third quadrants. The WMF [8] of magnetisation coupling effects of individual atomic dipoles is always in line with the magnetisation direction. Then, the WMF is positive in the first and second quadrants and negative in the third and fourth quadrants.

The hysteresis field is attributed to the WMF effects described in [4.19]. The eddy current field is generated by the varying magnetic flux based on Faraday's law and Lenz's law, so the eddy current field is always opposite to the magnetisation directions. As shown in Fig. 4.3, the magnetisation field is the vector sum of the three fields and expressed as the following:

$$H_m = H - H_h - H_e, \quad (4.x)$$

where the hysteresis field H_h and eddy current field H_e are opposite to the magnetic field H , so, the magnetisation field is a proportion of the magnetic field.

The direction of change of the magnetic field is the same as that of magnetic flux density, and the direction of the WMF is the same as that of magnetisation. So, the WMF effects and the output of the PID controller are oriented in the same direction in the first and third quadrants of the magnetic flux density and the opposite direction in the second and fourth quadrants. Then, the WMF exerts the positive feedback effects during the magnetisation process and the negative feedback effects during the demagnetisation process. The feedback effects are summarised according to the analysis of the WMF effects and PID controller outputs at different quadrants in the magnetic flux density sinusoidal waveform for one cycle and demonstrated in Table 4.1.

Table 4.1 Comparison of WMF Feedback effects and PID controller outputs.

Magnetic Flux Density	First quadrant	Second quadrant	Third quadrant	Fourth quadrant
PID output	+	-	-	+
Weiss field	+	+	-	-
Feedback effect	Positive	Negative	Positive	Negative

The energy created by the WMF effect can be estimated using the Zeeman energy between the WMF and magnetic flux density. The energy generated by the WMF in the first and third quadrants of the magnetic flux density boosts the magnetisation processes. Nonetheless, the WMF in the second and fourth quadrants depletes the energy from the excitation source. The energy consumed during the demagnetisation processes equals the energy produced by WMF during the magnetisation processes. So, the WMF positive and negative feedback effects cancel out each other except for the magnetisation tips ($dB/dt = 0$). The WMF reaches the maximum value at the tips because the maximum magnetisation has been obtained. Then the WMF feedback effect transits from positive to negative, and this maximum value contributes to the hysteresis effects if considering the counteraction between the WMF positive and negative feedback effects in the half cycle of the magnetic flux density.

According to Weiss's theory [8], the WMF can be expressed as the following equation:

$$H_w = \alpha M, \quad (4.3)$$

where α is the mean field constant. Then, the WMF feedback energy based on Zeeman energy can be described as:

$$W_w = \alpha \iint MBdMdB. \quad (4.4)$$

At the saturation tips, all the atomic dipoles in the steel sheets are oriented in the magnetic field direction. All the alignments of the dipoles will exert a strong coupling effect on the magnetic field, this interaction of individual atomic dipoles results in the WMF. Therefore, this study assumed that a magnetic force generated from the coupling effect of the magnetisation at the reversal turning point needed to be overwhelmed to continue the reversal demagnetisation process. This field is named hysteresis field H_h , and this field is the WMF at the magnetisation tips, then,

$$H_h = H_{wp} = \alpha M_{pk}. \quad (4.5)$$

Where M_{pk} is the magnetisation at the reversal turning point, and H_{wp} is the WMF linked to the M_{pk} . According to the definition of coercive force or coercivity H_c , it is the magnetic field required to demagnetise the material from certain magnetisation status or saturation. This means that the coercivity is the magnetic field needed to offset the WMF at tips so that the magnetic flux density can be demagnetised to zero. Then, H_h is equal to the coercivity H_c , which decreases B down to zero. Because the direction of the hysteresis field H_h is opposite to the reversed magnetic field H . So, the hysteresis field at the positive tip is expressed as:

$$H_h = H_c. \quad (4.6)$$

Nonetheless, the hysteresis field at the negative tip is expressed as:

$$H_h = -H_c. \quad (4.7)$$

Then, an astounding conclusion can be reached that the WMF feedback effects at the magnetisation tip are the physical origin of the magnetic hysteresis effect.

When the processes change the directions from magnetisation to demagnetisation at the reversal turning point, the excitation source must contribute more energy to compensate for the coupling effect of the magnetisation at the tips. This extra energy consumed at the tips is the hysteresis loss, which is a component of magnetic core loss.

4.3 Separation of the Magnetic Field

It is assumed that the electrical steel sheet is initially demagnetised. As shown in Fig. 4.5, the input magnetic field H is increased from the origin under a controlled excitation waveform; the corresponding magnetisation processes will change accordingly as shown

in Fig. 4.6. When H arrives at H_1 , the first local maximum point, the corresponding local maximum magnetisation M_1 is induced along the initial magnetising direction. Then, H attempts to reverse its direction, and it must surmount the hysteresis field H_h^1 , which is triggered by M_1 according to the coupling effect. Inside the magnetic lamination, there is a vector combination between the magnetic field H and H_h^1 . In this study, this vector combination is defined as excitation field h , then:

$$H = h + H_h^1. \quad (4.8)$$

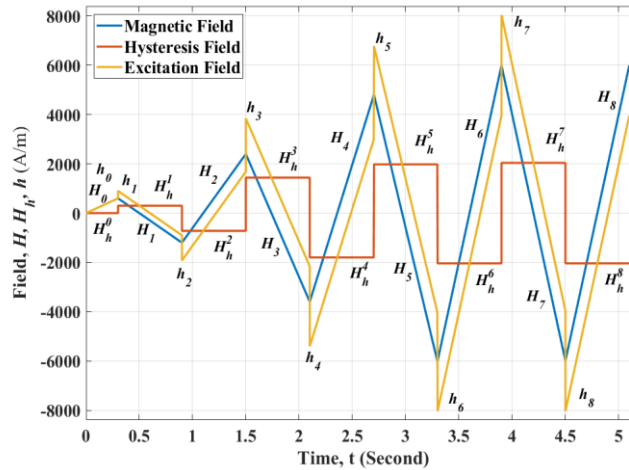


Fig. 4.5 Magnetic field, hysteresis field and excitation field in a spiral up magnetisation process.

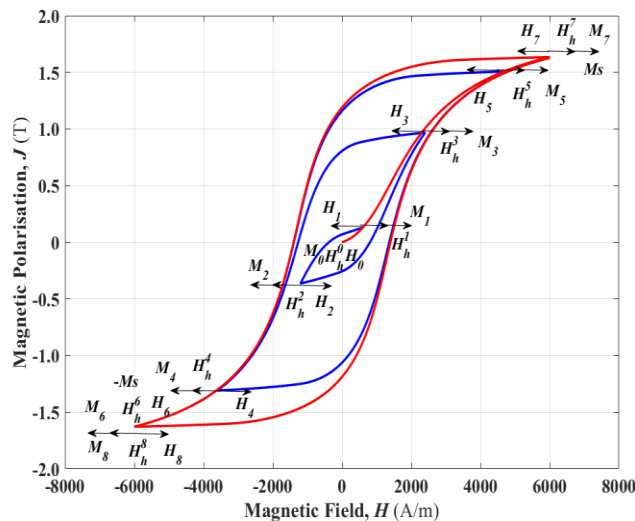


Fig. 4.6 Corresponding hysteresis field of magnetisation processes.

While H needs to make more effort to ensure that M is decreased smoothly in the sense of reversing direction, i.e., the time rate of magnetisation dM/dt changes from $+$ to $-$. It seems that H directly determines M as soon as it is formed when H changes its direction. It is worth noting that the magnetic field H_0 , the magnetisation M_0 and hysteresis field H_h^0

are zero at the origin; they are listed as a particular condition of the demagnetised state. Since H_h^0 is zero, the h between H_0 and H_1 is identical to H . Another notable phenomenon is that the hysteresis field H_h is far smaller than M because it has the same dimension as its counterpart $-H$.

From the viewpoint of magnetic domains, at the origin, the magnetic domains in the sample are in an energy balance condition so that the vectors of magnetic moments in all domains cancel out each other, manifesting no magnetic features. A similar postulated interacting field between domains analogous to the WMF in the domains is proposed here to analyse the process of magnetisation. The interacting field is, in effect, the inter-domain interaction, which causes the directions of the neighbouring domain to align antiparallel because the closure structure is favourable to the arrangement of domains to eliminate free poles. The interacting field is supposed to be proportional to the bulk magnetisation M which is the product of the magnetic moment of the unit magnetic domain m and domain number v . So, the hysteresis field resulting from the coupling effect of the magnetisation is obtained:

$$H_h^i = \alpha M, \quad (4.9)$$

where $M = vm$ and α is the interacting field coefficient and a function of frequency and peak flux density. This can be proved to be equivalent to assuming that each magnetic domain interacts with other magnetic domains within the sample according to the numbers of the domain. So, the interacting field is responsible for ordering domains through domain wall motion and domain rotation during magnetising and demagnetising processes. So, when H gets to H_1 , the volume of the domains oriented close to the magnetising direction becomes larger, and those facing an opposite direction of the excitation field dwindle in the same volume size. Then, the corresponding magnetisation M_1 represents the vector difference of the moments between domains parallel and antiparallel with the magnetic field. Then, the instant interacting field H_h^1 is triggered by M_1 and points in the direction of the previous magnetic field and magnetisation.

When H reverses direction, the domain walls of the magnetic domains in M_1 status will not shift backwards immediately because both M_1 and H_h^1 hold the domain walls in a fixed position. Since it is acknowledged conventionally that it is H_1 that induced M_1 , the value of h at the turning point of M_1 must be taken from the vector sum of H_1 and H_h^1 which makes M lag behind H . The effort of h to prevail the effect of H_h^1 on the magnetic field and magnetisation is made instantly which has been overlooked and never mentioned by the previous researchers. However, it exists undoubtedly due to the existence of interacting or coupling of inter-atoms and inter-domains, this interacting or coupling is equal to WMF at M_1 ; analogously, there is no doubt that two magnets close to each other will interact. This sudden leap in the value of h is unnoticed because it happens

instantaneously, so its impact on magnetisation cannot be observed by the instruments adopted in the experiment setup.

If H is continually decreased in the reversal direction, the corresponding h will decrease simultaneously according to equation (4.8). The induced M will decrease gradually until its value reaches zero when H arrives at coercive force, and h arrives at zero. This means that M lags H , but M is synchronised with h . It seems that M is induced by h directly. h can be obtained from H by removing the hysteresis proportion, and H measured is the external manifestation of the combination of h and H_h . Demagnetising from h_1 to zero is the reversal of magnetising from h_0 to h_1 , where the domain walls will move back to their original positions and ending up with the net magnetisation disappearing instantly. These processes of magnetising and demagnetising happen in the scope of multi-domains by moving domain walls forwards and backwards. The magnetic hysteresis loops are observed since the magnetisation features are revealed on $M - H$ and $B - H$ curves. If the magnetisation features are represented on $M - h$ or $B - h$ curves, a curve of a single point-to-point relationship will be seen.

Then, H continues to decrease along the reversal direction. This pushes the domain walls of the domains whose directions are aligned favourably to the reverse direction to move so that these domains expand at the expense of diminishing the size of other domains. When H compasses H_2 the first local minimum point of the magnetic field, h arrives at h_2 , and M_2 is created along the opposite initial magnetising direction, as shown in Fig. 4.6. When the time rate of H (dH/dt) switches its direction from - to +, M_2 leads to the creation of the hysteresis field H_h^2 . This counter field reduces the effectiveness of H to the magnetising process because H_h^2 offsets the action of H , which makes the magnetisation appear to be postponed by H , and H is obtained from a new expression by considering of H_h^2 :

$$H = h + H_h^2. \quad (4.10)$$

By overcoming H_h^2 , H takes over the magnetisation process and pushes forward M along the direction of initial magnetisation. Another consideration that should be mentioned here is that the diagram of Fig. 4.6 is created using the J-A model. It is a history-independent hysteresis model (HIHM) model, which means the third order reversal curve will not close the minor loop. Instead, it will tend to arrive directly at the saturation magnetisation tips. It is acceptable for observing magnetisation and its coupling effect, although it will underestimate the relevant energy losses in real materials. It is understandable that the domain walls are pushed back to the original position and move forward until reaching the next local maximum magnetisation.

The magnetising and demagnetising processes are repeated for four cycles, and every time the maximum values of H are higher than the previous ones, and the minimum values are lower until the magnetisation finally reaches saturation in both directions.

Every new cycle enlarges the magnetisation curve to form a spiral shaped curve inside the major hysteresis loop because the hysteresis model adopted is HIHM. If an HDHM is applied, the minor loops will be closed when the magnetic field returns to the previous turning point. By observing Fig. 4.1 and Fig 4.2, it is confirmed that, for the first and second cycles, the domain wall motions undergo the regime of multi-domains, and the magnetisations of the third and last cycles will encounter domain wall motion, domain annihilation, domain rotation, and domain nucleation repeatedly.

It is observed that when H_6 , H_7 and H_8 arrive at $-H_s$, H_s and $-H_s$, namely, the maximum magnetic field, the magnetisation arrives at the saturation magnetisation. H_s and $-H_s$ are the values when the sample is subjected to saturation magnetisation from the last demagnetised condition. Correspondingly, M_6 , M_7 and M_8 are identical to $-M_s$, M_s and $-M_s$, which are saturation magnetisation in two directions. If magnetisation reaches its saturation, the corresponding H_h^{-s} and H_h^s will reach their minimum and maximum value, which are a feature of the ferromagnetic materials and named saturation hysteresis field in this thesis. At these extrema tips, the maximum H is needed to prevail over the effectiveness of the H_h^{-s} and H_h^s . From Fig. 4.5, one can observe that the value of h is always higher than that of H for the descending curve and less than that of H for the ascending curve (except for the initial magnetisation, where h equals H) because H_h is always in the opposite direction to H . So, M lags H for a H_h distance seen in Fig. 4.5. The above analysis accounts for the hysteresis in an $M - H$ or $B - H$ loops.

After a few cycles of magnetisation, the major hysteresis loop, as shown in Fig. 4.6, is closed between the tips of $(-H_s, -M_s)$ and (H_s, M_s) , which consists of an ascending curve and a descending curve surrounding all other minor loops and any order reversal curves. As far as the ascending curve is concerned, the turning point starting from the tip of $(-H_s, -M_s)$, the magnetic field H is expressed as:

$$H = h + H_h^{-s}, \quad (4.11)$$

Contrastingly, the magnetic field of the descending curve is expressed as:

$$H = h + H_h^{+s}. \quad (4.12)$$

The ascending and descending curves cross the magnetic field coordinate at coercivity H_c and $-H_c$, respectively, which have a natural relationship with H_h^{-s} and H_h^{+s} . The ascending curve is split into two parts by the point $(H_c, 0)$, the section curve above the point is the magnetising part, and that below is the demagnetising part; the magnetic domain processes of these two parts are opposed to each other although they are connected seamlessly. The descending curve is separated by the point $(-H_c, 0)$, the section curve above the point is the demagnetising part, and below the point is the magnetising part; these two section curves are exactly the opposite of the counterpart of the ascending curve.

4.4 Coercive Force and Coercivity

As far as the major loop is concerned, for both ascending and descending curves, the magnetising procedures traverse from H_c or $-H_c$ to the saturation tips to form the magnetising curves, and the demagnetising curves are generated from the saturation tips to H_c or $-H_c$. These two conditions are opposite in terms of domain configurations and patterns. At both $(H_c, 0)$ and $(-H_c, 0)$ points, the magnetic domains are ordered in the demagnetised state in the sample in an instant time. At the tips of $(-H_s, -B_s)$ and (H_s, B_s) , the magnetisation reaches its saturation state, which means all atomic magnetic moments are aligned along the magnetic field direction.

Since the points of $(0, 0)$, $(H_c, 0)$, and $(-H_c, 0)$ stay in the demagnetised state, the domain structures should be arranged in a similar way even though they may not be the same. For both magnetising and demagnetising, the partial magnetisation from coercivities to saturation tips always points in the direction of the saturation tips. It means that the sum of the volumes of the domains aligned favourably in the direction of saturation is higher than that in the opposite direction of saturation. Nevertheless, the partial magnetisation during demagnetising processes is in line with the excitation field h , and the decreasing excitation field violates the magnetisation and brings down the magnetisation from saturation to partial magnetisation and then to zero when H arrives at coercivities.

The domain configurations for both processes can be inspected in Fig. 4.1 and Fig 4.2. The multi-domains in the demagnetised state are formed in closure structures that provide return paths for the magnetic flux within the solid so that no magnetisation or induction manifest on the surface of the sample. Here, the author would like to introduce a contradiction existing in classical magnetisation theory, which is never mentioned by previous researchers. At the demagnetised state of the origin, either B or M are considered equal to zero. But for both $(H_c, 0)$ and $(-H_c, 0)$ points at $M = 0$, the values are inserted in the equation (4.13) defined for magnetic induction, respectively:

$$B = \mu_0(H + M). \quad (4.13)$$

Then, two equations are obtained:

$$B_{-H_c} = \mu_0(-H_c + 0), \quad (4.14)$$

and

$$B_{H_c} = \mu_0(H_c + 0). \quad (4.15)$$

Contrastively, equation (4.13) can be substituted by both values of $(H_c, 0)$ and $(-H_c, 0)$ points for $B = 0$. Two result equations are gained as following:

$$0 = \mu_0(-H_c + M_{-H_c}), \quad (4.16)$$

and

$$0 = \mu_0(H_c + M_{H_c}). \quad (4.17)$$

This means that magnetic induction has a non-zero value when magnetisation is zero and vice versa. These results defy the common sense of the relationship between magnetic induction and magnetisation.

Another contradiction concerning domain patterns and configurations at both $(H_c, 0)$ and $(-H_c, 0)$ points arouses extra attention and discussion because the multi-domains encounter a complicated situation. If the demagnetised state is defined as $M = 0$ where magnetic domains are arranged in patterns without net magnetisation, then where does the magnetic induction in (4.14) and (4.15) come from? If the demagnetised state is defined as $B = 0$ where magnetic domains are arranged in patterns with net magnetisation, how will the net magnetisations in (4.16) and (4.17) impact the domain configurations? The coercivities at the $(H_c, 0)$ and $(-H_c, 0)$ points can be expressed as:

$$H_c = h_{H_c} + H_h^{-s}, \quad (4.18)$$

and

$$-H_c = h_{-H_c} + H_h^{+s}. \quad (4.19)$$

These equations are derived according to (4.11) and (4.12); two equations are attained by substituting H with H_c and $-H_c$ shown in (4.18) and (4.19). This study made one hypothesis for the physical ground of coercivity: an inner coupling field between domains cancels out the effectiveness of coercivities, and this counteraction brings the magnetisation to zero and forms the multi-domain patterns simultaneously.

It is assumed that the components of H induce magnetisation M separately, and then the corresponding magnetisations accounting for (4.18) and (4.19) are expressed as:

$$M_{H_c} = M_{h_c} + M_{H_h^{-s}}, \quad (4.20)$$

and

$$M_{-H_c} = M_{-h_c} + M_{H_h^{+s}}. \quad (4.21)$$

If M_{h_c} and M_{-h_c} are set to zero, then two equations are acquired,

$$M_{H_c} = -M_{H_h^{-s}}, \quad (4.22)$$

and

$$M_{-H_c} = -M_{H_h^{+s}}. \quad (4.23)$$

For both magnetising and demagnetising processes, the excitation fields are always in charge of the magnetisations by overcoming the counter effects of the hysteresis field.

Hence, the following results can also be reached:

$$H_c = -H_h^{-s}, \quad (4.24)$$

and

$$-H_c = -H_h^{+s}. \quad (4.25)$$

From the above analysis, a number of conclusions can be reached. At first, the coercivity and the hysteresis field are identical to one another. The magnetisations excited by the coercivity, and hysteresis field are counteracted because they are oriented in opposite directions. Secondly, at both the $(H_c, 0)$ and $(-H_c, 0)$ points, h dominates the magnetisations and results in the demagnetised state happening for both magnetic induction and magnetisation equal to zero when h is zero. Therefore, the author suggests that H in (4.13) should be replaced by h after the first order reversal curve whenever and wherever the first turning point occurs, (4.13) is then satisfied when h , M and B are zero simultaneously at coercivity points. Finally, M and B can be regarded as synchronised with h as they both become zero when h arrives at zero. Besides, in a $M - H$ curve, hysteresis happens when H goes ahead of h by the value of H_h^{-s} or H_h^{+s} for ascending or descending curves, respectively.

4.5 Analysis on Hysteresis Loops of GOES and NOES

It is conventional to plot M or B of the sample as a function of H since H is the externally measured field, which is deemed as driving the whole magnetisation process. However, due to the differences mentioned above between H and h , the curves of B vs h are investigated to reveal the applications of the novel theory for NOESs and GOESs.

Consequently, another important equation for the ascending curve of the major hysteresis loops is determined based on the above analysis:

$$h = H - H_h. \quad (4.26)$$

The hysteresis field is the same as the coercivity or coercive force of the magnetic material, then:

$$h = H - H_c. \quad (4.27)$$

This equation is the cornerstone for developing a new model of magnetic hysteresis loops.

Magnetic hysteresis is usually expressed as $B - H$ loops; H is measured simultaneously with B . h , as the defined driven force of the magnetisation process, is adopted here to explore the magnetic properties of ferromagnetic materials. The function of h can be observed in Fig. 4.7 and Fig. 4.9, respectively. These two figures show the magnetic field, excitation field and magnetic flux density in the NOES and GOES samples. It is observed that B synchronises with h , and lags H ; since h and B cross at the abscissa, and H goes in advance of h and B .

As shown in Fig. 4.8 and 4.10, the $B - H$ loops show hysteretic features for the NOES and GOES samples, respectively. The $B - h$ curves consist of two sigmoidal curves intersecting at the origin. These two curves are different from anhysteretic magnetisation curves, which are entirely reversible and measured experimentally by demagnetisation of the magnetic material under the influence of a constant biasing magnetising field [3].

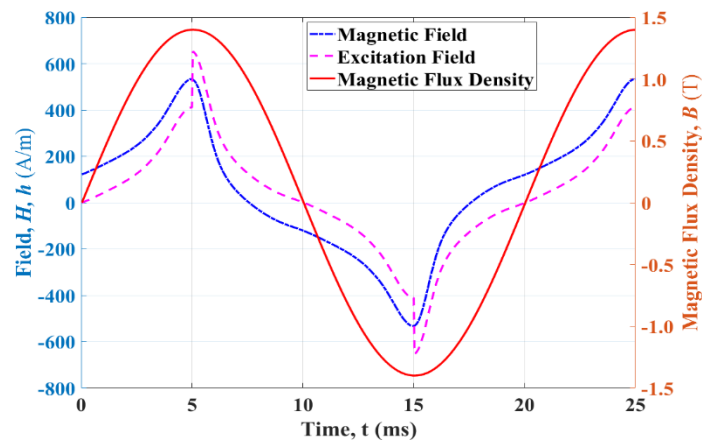


Fig. 4.7 Magnetic field, excitation field, and magnetic flux density for NOES at 50 Hz and 1.4 T.

The $B - h$ curves are obtained by removing the hysteretic effect from the $B - H$ loop, which can be deemed a hysteresis removal procedure via (4.27). Then H is determined to contain two components: hysteretic and nonhysteretic parts. The non-hysteretic part is the input excitation field, and the hysteretic part is the result of the counter field aroused by the magnetisation coupling at the turning points when magnetisation reverses its directions.

The hysteresis field will be parallel with the previous magnetisation and keep a consistent value unless it changes its direction again; then, the magnetisation at the new reversal point will determine another hysteresis field. That is why the coercivity or coercive force is identical to the last hysteresis field when it crosses with the magnetic field coordinate and converts the direction-changing of magnetisation. This assertion is correct and can be observed in the above figures.

Another important conclusion has been determined that the input excitation field incites the magnetisation, and magnetisation triggers the hysteresis field. Therefore, the combination of excitation field and hysteresis field leads to the magnetic field so that it lags the magnetisation due to the hysteresis field and need to be overcome.

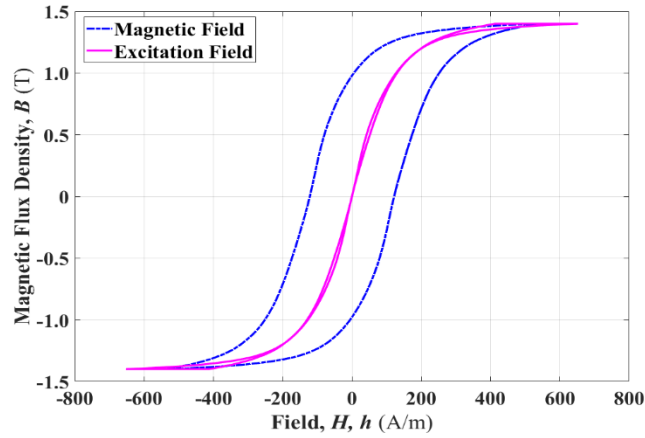


Fig. 4.8 Hysteresis loop and single curves for NO steel at 50 Hz and 1.4 T.

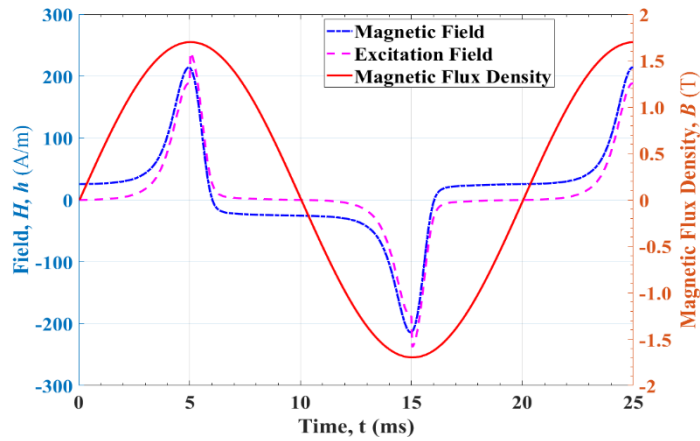


Fig. 4.9 Magnetic field, excitation field, and magnetic flux density for GOESs at 50 Hz and 1.7 T.

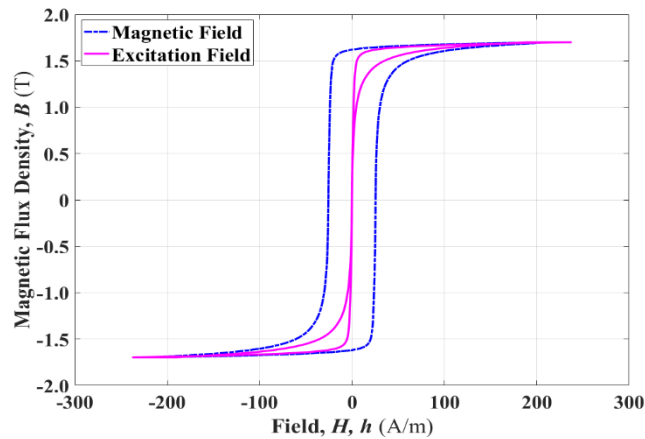


Fig. 4.10 Hysteresis loop and single curves for GOESs at 50 Hz and 1.7 T.

It is observed from Fig. 4.7 and Fig. 4.9 that the curve of h looks like a funnel between two peaks of B , and the relevant curves of B vs h are illustrated in 4.8 and 4.10. Since B is a sinusoidal curve, the functional nonlinearity of B vs h is determined so that the

magnetisation mechanism is separated accordingly into two parts. First, the demagnetising is processed from positive and negative peak flux density tips to zero, and magnetising undergoes from zero to positive and negative peak flux density tips.

In terms of domain configuration, demagnetising is divided into two steps. In the beginning, B is dominated by domain rotation from positive and negative peak flux density tips to the nucleation point; afterwards, B is controlled by further nucleating to multi-domains and domain wall motion. For magnetising, the first step of the process from demagnetised state to annihilation point is dominated by decreasing the number of domains through domain wall motion. The second step from annihilation point to positive and negative peak flux density tips involves domain rotation.

To keep B in a sinusoidal curve, H and h follow a controlled shape, and they change quickly due to domain rotation to form a sharp drop or rise from positive and negative peak flux density tips to the nucleation point. Afterwards, the time rates of H and h become flat and incline to the horizontal level, which indicates that the magnetic force needed to move the domain wall is far smaller than that required to rotate the domain to surmount anisotropic energy.

This novel theory of magnetisation applies to different ferromagnetic materials; the sample sheets of both NOES and GOES are considered in this thesis. There are no 100% isotropic materials in the world: even for a fine treated NOES lamination. Energy loss along with different magnetising directions in NOES and GOES sheets can vary significantly because the components of isotropic and anisotropic are different proportionally and affected by production procedures. GOESs present high permeability in the rolling direction of the sheets and suffer low power losses comparatively in the transverse direction due to enlarged grain size grown during hot annealing. Nevertheless, anisotropic energy for a NOES texture alters on a comparatively small scale which means it nearly presents a sense of similar magnetic properties in any lamination direction.

The ascending and descending $B - h$ curves in Fig. 4.8 are very close to each other because the energies to magnetise the NOES sheet to be in line with and opposite the rolling direction are approximately the same. Whereas it can be observed from Fig. 4.10 that there is a considerable gap between the two curves of $B - h$, because a large proportion of grains in the GOES sheet are aligned with the rolling direction.

To apply the novel theory and model to different magnetic materials, except for an appropriate method to observe the magnetic behaviour of various substances, the causation of the magnetic features should be investigated from the viewpoint of internal mechanisms. The magnetic characteristics we explored are due entirely to the electrons of the atom, which have a magnetic moment by virtue of their motion and spin. The magnetic hysteresis is affected strongly by the microstructures, such as grain orientation, grain size, domain configuration, domain size, crystallographic, lattice imperfections, and

impurities. These elements impact the hysteresis loop shape significantly. In addition, external elements, such as frequencies, peak flux density, and magnetising directions, should be considered when developing a new model to describe the magnetic properties. Fundamentally, both NOES and GOES materials are comprised of a similar amount of silicon mass contents, which means they have a lot in common, which provides an essential clue to the development of hysteresis models according to the magnetic nature of the substances.

4.6 Conclusions

This study proposes a novel magnetisation theory by explaining the differences between hysteresis field, excitation field, and magnetic field. In previous research, the excitation field and applied field are regarded as the same conceptions as the magnetic field; but in this thesis, they are entirely different representations with different functions in a magnetic loop. Whether from common sense or theoretical analysis, the magnetic field should have different components to magnetise the sample materials. Meanwhile, the counter field caused by the eddy current must be considered to prevent the magnetic field from changing.

The analyses show how the magnetic hysteresis can be determined in terms of how the excitation field overcomes the effectiveness of the counter field of magnetisation coupling effect. The magnetic field is formed by the excitation field and hysteresis field and is measured as an external combined field on a hysteresis loop. This represents a new development of the theory of ferromagnetic hysteresis, which makes it possible for the first time to describe a hysteresis loop with two synchronised curves passing through the origin point. Furthermore, it has been shown that hysteresis of both ascending and descending curves in a hysteresis loop can be removed when H is replaced by h , which makes it possible to develop a new model to interpret magnetic hysteresis loops.

The modelling of magnetic hysteresis has been of concern to physicists and engineers for decades, and it is deemed that it is impossible to develop a general physical model in the foreseeable future in terms of $B - H$ loop. Nevertheless, researchers have never ceased to find a general physical model for different magnetic materials describing hysteresis loops. Since B vs h is a synchronised injective function for the standard s-shape single curves, it is possible to develop a general physical model, which is in detail in the next chapter.

As far as NOESs and GOESs are concerned, their micro-structures are quite different, and these differences in micro-structure affect the magnetic hysteresis profoundly. However, domain structure and crystallographic texture are the main factors determining the hysteresis loops of magnetic materials, which makes it a potential eventuality to find their common characteristics to contribute an identical model to be suitable for both

magnetic materials. Therefore, the measurement data of magnetic features of NOES and GOES sheets is experimented with according to relevant British standards, and the measurement data used to test the model derived from the novel theory. The further contributions to hysteresis that need to be incorporated into the model are the calculation of parameters based on the data sheet from the manufacturer and experimental collections.

Finally, although the introduction of hysteresis field, excitation field, and magnetic field represent the underlying mechanism of magnetic hysteresis. The hysteresis loop has been adopted for more than a century and is effectively used to predict magnetic core losses of electromagnetic devices. The development of a new model should depend on understanding the materials chosen about grain texture, average grain size, and domain patterns. It is observed that both NOESs and GOESs are comprised of isotropic and anisotropic components [104 - 108]. The difference is that different materials have different proportions, which can vary the shape of the hysteresis loop and cause the power loss separation in different proportions. However, it will not change the hysteresis fundamentally. These commonalities can contribute to a general physical model, and a single equation for many magnetic materials is an ideal model.

Chapter 5 A novel hysteresis model of ferromagnetism based on domain theory

A novel analytical model of magnetic hysteresis in ferromagnetic materials is formulated utilising variations of the anisotropic and isotropic domain patterns in the presence of an external magnetic field excitation. The hysteresis field is generated by the coupling effect of magnetisation at the turning point where the magnetic field and magnetic induction reverse their directions. The excitation field is introduced to achieve a single magnetic curve derived from the hysteresis loop by counteracting the hysteresis force. A general physical model for the single curve is derived based on analysis of the domain patterns and excitation field coupling effect. The hysteresis properties are systematically analysed as a function of several important parameters: coercivity, peak flux density, and frequency of the magnetic field. The shape of the hysteresis loop is dependent on these parameters and the proportion of domain patterns in the ferromagnetic materials. The increase of frequency and peak flux density leads to an increase of the magnetisation coupling, which increases coercive force or coercivity. The hysteresis loop area increases accordingly. The new model is used to characterise the sheets of GOES and NOES, which exhibits all the features of hysteresis for both materials. The differences in magnetisation of both samples are described using the same single equation model for the generalisation of the physical model, which captures all the features of magnetic hysteresis of ferromagnetic materials. The results of hysteresis modelling and energy loss prediction reveal that all the features of hysteresis such as major hysteresis loops, minor hysteresis loops, and energy loss evaluations of loop area calculations are in excellent agreement with corresponding measurement data.

5.1 Introduction

Magnetic hysteresis modelling is essential to applying ferromagnetic materials used in electromagnetic devices as magnetic cores, such as transformers, motors, and generators. Conventionally, hysteresis loops can be acquired experimentally when ferromagnetic materials are subjected to a sinusoidal excitation waveform. The modelling of specific magnetic materials is carried out using measured data to evaluate the modelling results concerning calculating the relevant parameters in the models. The non-linear hysteresis loops are represented as a function of magnetic induction or magnetisation vs magnetic field. It is worth noting that the hysteresis loops obtained can be smooth regular loops or distorted irregular loops; the smooth regular loops are a one-to-two function, while the distorted irregular loops can be a function of one value mapping to multiple values. The applications of different magnetic materials in electromagnetic devices are determined by the specific magnetic properties needed to reduce losses and improve performance.

Unfortunately, the physical mechanism of hysteresis is far more complicated, so that there is still no satisfactory theory and model that can satisfactorily explain the phenomenon of hysteresis.

From the perspectives of physicists and engineers, a generalised physical model of a hysteresis loop or magnetisation curve for ferromagnetic materials, especially for GOES and NOES sheets, would be advantageous for the design, application, and development of electromagnetic devices. Despite decades of research, such a model has yet to be developed. Nevertheless, many existing hysteresis models exist to simulate hysteresis loops and for predicting magnetic core energy loss [1, 4, 88]. According to some references, the magnetic hysteresis phenomenon is assumed to be caused by the impedance of pinning sites due to the ingredient impurity. The domain wall motion under the influence of the magnetic field is impeded by the pinning sites, and the energy consumed by the impedance contributes to the hysteresis formation [2, 3]. It has long been noticed that increase of Silicon inclusions in the volume of ferromagnetic material will reduce the core losses [109], which in turn has raised curiosity as to why the impurity of Silicon in ferromagnetic materials has a contradiction regarding core losses which are calculated in terms of the area of the hysteresis. Normally, the impedance is caused by the impurity, and if the impedance results in hysteresis, why then does increase of Silicon ingredients in the magnetic materials lead to a decrease of the area of the hysteresis loops? The impurity is one of the factors that affect the hysteresis properties, but it is hard to say it is the cause of hysteresis, because even the pure iron can exhibit the hysteresis phenomenon [110]. There are so many models for tracing magnetic hysteresis loops; only the most widely acknowledged models are referred to here to facilitate the development of the novel model.

The wide-spread Preisach hysteresis model [4] proposed in 1935 by Ferenc Preisach is used to trace hysteresis loops using a network of small independently acting domains, each magnetised to a value of either M or $-M$. This model adopts equations for the summation of measurement data, which inevitably complicates the modelling procedures. It assumes that a sample of iron, for example, may have evenly distributed magnetic domains, resulting in a net magnetic moment of zero. The relationship between the magnetic field and magnetisation of a magnetic material as the parallel connection of independent relay hysterons is established according to this idealised assumption. As a matter of fact, the shapes of the magnetic domain in a ferromagnetic material are irregular, the sizes of the magnetic domain are not identical, and the directions of the magnetic domain moment are oriented arbitrarily [8, 111, 112]. These facts unavoidably limit the application of the Preisach model and have inspired many researchers to find alternative solutions based on reasonable assumptions.

The well-known 1-D diffusion (penetration) equation derived from the Ampere–Maxwell law and Faraday’s law can be used at power frequencies to model homogeneous materials in which grains are arbitrarily oriented [113 - 115]. However, it will produce an enormous error when used to model inhomogeneous structures such as GO steels [1, 5, 14]. The error between the modelling result and measurement is defined as excess loss [1, 116] because the physical mechanism was unclear. The modelling result of the 1-D diffusion equation consists of two components: static hysteresis and eddy-current effect. The static hysteresis component can be modelled using a Preisach-like model or J-A model. The quasi-static hysteresis loop can be measured from the Epstein frame connected to a permeameter with the period of sinusoidal induction of the order of 300 seconds and 5 Hz [1]. The three-component separation principle is deemed expedient to deal with the problem of modelling GO steels [1]. This method is beneficial to the study of the magnetisation mechanism of how the magnetic domains are processed when the magnetic material is subjected to an external magnetic field.

Measured hysteresis loops do not always have a standard sigmoid shape; in many cases, the loops obtained are distorted to form unexpected irregular hysteresis loops. At high frequencies above 200 Hz, for both GO and NO steels, the measured hysteresis loops are inevitably seriously disfigured due to the complicated conflict between hysteresis effect, eddy current counter field, and magnetic field. Even at a low frequency of 50 Hz, some materials can produce distorted irregular hysteresis loops. The deviations between modelling results using existing models and measured loops are often not acceptable because nearly all the models are used to trace smooth s-shape loops. Whereas the distorted hysteresis loops spoil the monotonicity of descending and ascending magnetic curves in hysteresis loops, which makes the modelling of hysteresis loops using existing models seem impossible.

The present work describes a model of magnetic hysteresis in the form of a single equation that generates both the standard smooth sigmoid hysteresis loops and distorted disfigured twisted hysteresis loops. It is derived according to the different domain patterns considering domain wall motion, domain nucleation, domain annihilation, and domain rotation due to the magnetisation processes under an external magnetic field. The existence of magnetic domains in ferromagnetism was first suggested by Pierre Weiss in 1907 [5]. Attempts to find a hysteresis model according to domain theory has never ceased, but the results are never good enough to be acceptable. To date, the novel model derived here is the most satisfactory in terms of the accuracy of the calculated losses compared to corresponding measured data.

5.2 Domain Patterns

In ferromagnetic materials, such as GOESs and NOESs, the magnetic properties are dominated by two domain patterns: anisotropic domain (Fig. 5.1(a)) and isotropic domain (Fig. 5.1(c)) [8]. In GOESs, the grains are mainly oriented along with the rolling direction, which determines a strong anisotropy if the sample is magnetised in line with the grain orientation, which is the easy axis of the crystallography. In NOESs, the grains are mainly oriented in an arbitrary direction which forms an isotropic structure since the magnetising direction has nearly identical effects on the grain orientation considering huge amount domains in the sheet. It is worth bearing in mind that there are both anisotropic and isotropic domains in GOESs and NOESs. The domains form the closure structures [104 - 107, 112, 117] to minimise the magnetostatic energy, but the domain size and orientation are different in different materials. So, the magnetic properties are determined by the proportion of the dominating domain structures in the materials.

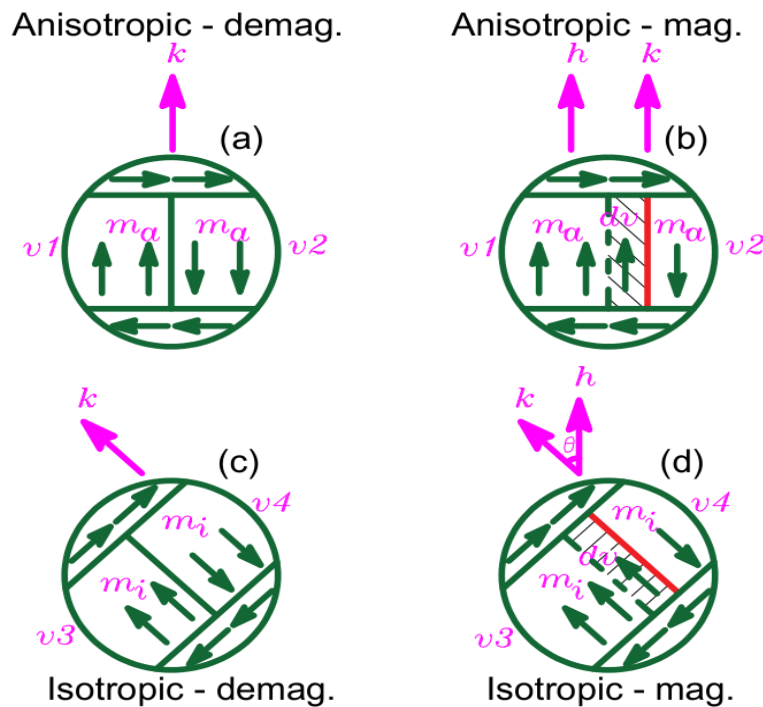


Fig. 5.1 Typical domain patterns for ferromagnetic materials. Top row anisotropic case: (a) demagnetised state; (b) in the presence of an excitation field. Bottom row isotropic case: (c) demagnetised state; (d) in the presence of an excitation field.

In this study, the magnetic field, applied field and excitation field are endowed with different definitions to differentiate two introduced physical conceptions. Conventionally, the magnetic field is regarded as the field generated directly from an exciting voltage or current source. Here, the magnetisation field H_m is introduced as the force to process the magnetisation procedures; and its functions are to push the domain wall motion, domain rotation, annihilation, and nucleation. It is universally accepted that magnetic

hysteresis loops are used to describe the relationship between magnetic flux density B or magnetisation M and magnetic field H . H_m must be lesser than magnetic field H measured manifestly because it contains another two components: eddy current counter field H_e and hysteresis field H_h . The eddy current counter field is an opposite field generated by the eddy current and against the changes of the magnetic induction and magnetic field. Whereas the hysteresis field is the coupling field created by the magnetisation coupling effect when the magnetic field and magnetic induction change their directions. Then, the magnetic field consists of three components, expressed as:

$$H(B) = H_h(B) + H_e(B) + H_m(B). \quad (5.1)$$

It is worth noting that the above equation is expressed in terms of vector quantities. The magnetic field $H(B)$ represents the measured field. At the initial magnetisation process, the magnetic field needs to surpass the counter field generated by eddy current, then at the turning point, it needs to exceed the hysteresis field created from magnetisation by coupling effect. These two opposite fields are hidden inside the magnetic core and not captured by instruments during the magnetisation measurement procedures. The magnetic field measured by instruments is an externally manifested field, which is used to establish the hysteresis loops conventionally.

The excitation field h is defined as the vector sum of the magnetic field H and the hysteresis field H_h , then:

$$h(B) = H_m(B) + H_e(B) = H(B) - H_h(B). \quad (5.2)$$

Unlike the conventional methods to describe $B - H$ loops, this novel model adopts a new form with $B - h$ curves, which can be deemed a hysteresis removal result from $B - H$ loops. Where h is the excitation field and expressed as:

$$h(B) = H(B) - H_c \quad (5.3)$$

The above equation is used for the ascending curve in a hysteresis loop, where H_c is the coercivity or coercive force. It is convenient for h to be derived from relevant measurement data. Then, the measured $B - h$ curves can be obtained simply from the measured $B - H$ loops through the hysteresis removal procedure.

To describe the magnetisation processes under the excitation field for anisotropic and isotropic domain patterns, it is assumed that a unit domain with a magnetic moment (in Fig. 5.1(a) is expressed as m_a and in Fig. 5.1(c) is m_i) is a typical domain with the magnetic moment per unit volume. According to Zeeman energy [110], the energies of magnetic moment per unit volume for anisotropic and isotropic domains under an excitation field h are expressed as:

$$E_a = -\mu_0 m_a \cdot h, \quad (5.4)$$

and

$$E_i = -\mu_0 m_i \cdot h, \quad (5.5)$$

respectively, where μ_0 is the permeability of the free space between the magnetic domains.

In Fig. 5.1(a), the magnetic moment m_a in the anisotropic domain is aligned with the excitation field h . When subjected to an excitation field, the domain wall between the domains in Fig. 5.1(b) will shift in a way that makes the domain aligned with the excitation field to enlarge at the expense of the domain opposite to the excitation field.

The direction alignment of m_i in isotropic domains in Fig. 5.1(c) varies from domain to domain randomly. In contrast, the domain directions can align to the anisotropic direction or not, which is decided if a particular crystallographic easy axis is preferred by the magnetic moments. In Fig. 5.1(d), the excitation field h is not in line with the anisotropic direction k , and there is an arbitrary angle θ between them. Therefore, the domain wall will move along with the vector perpendicular component of the excitation field to the magnetic domain moments. The novel model is derived from expressing the energy changes in these two domain patterns under the excitation field.

5.3 Model Derivation

As shown in Fig. 5.1, for a unit domain number v , the total magnetic moment of a typical anisotropic and isotropic domain can be expressed as:

$$M_a = m_a v, \quad (5.6)$$

and

$$M_i = m_i v, \quad (5.7)$$

respectively.

According to statistical thermodynamics, in a state of thermal equilibrium at temperature T , the probability of a unit domain having an energy E is proportional to the Boltzmann factor $\exp(-E/kT)$, where k is the Boltzmann constant [8]. The unit volume number in a domain is then given by the following expression:

$$v = c \exp\left(-\frac{E}{kT}\right), \quad (5.8)$$

where c is a constant of proportionality. With reference to Fig. 5.1(b), the number of the unit moment in the domain aligned with the excitation field can then be expressed as:

$$v_1 = c \exp\left(-\frac{E_1}{kT}\right), \quad (5.9)$$

while the number of the unit moment in the domain opposite to the excitation field is:

$$v_2 = c \exp\left(-\frac{E_2}{kT}\right). \quad (5.10)$$

As shown in Fig 5.1(b), the number of the unit moment in the domain aligned with the excitation field will increase due to the domain wall moving from the dashed line to the solid line position, and the number of the unit moment in the domain contrary to the field will decrease by the same amount. During the magnetising process, the increased dv number of the unit domain along with the excitation field is calculated as:

$$dv = v_1 - v_2, \quad (5.11)$$

and the total number unit moment in the anisotropic domain pattern is expressed as:

$$v = v_1 + v_2. \quad (5.12)$$

By replacing v with dv in (5.6), the magnetisation contributed by the anisotropic domain during the process of magnetisation is estimated to be:

$$M_a = m_a dv = m_a v \frac{v_1 - v_2}{v_1 + v_2}. \quad (5.13)$$

The magnetisation component of the anisotropic domain in the magnetisation process under the excitation field can then be expressed as:

$$M_a = M_{sa} \tanh(ah), \quad (5.14)$$

where,

$$a = \frac{\mu_0 m_a}{kT}, \quad (5.15)$$

is a balance coefficient for anisotropic components between the unit domain magnetic moment and the disordering effect of thermal agitation. M_a defined by (5.14), is the anisotropic component in the magnetising processes, which is derived from analysis of the anisotropic domain patten in ferromagnetic materials. $M_{sa} = m_a v$ is the saturation magnetisation of the anisotropic components when the anisotropic domain magnetic moments opposite to the excitation field are all wiped out to form a single domain in line with the excitation field.

Regarding the isotropic domains, the magnetic moments are oriented in an arbitrary direction to the excitation field direction. The domains are formed to achieve self-saturation spontaneously; they will be oriented randomly to form disordered structures with irregular shapes. Under the excitation field $h(B)$ having an angle θ with magnetic domain moment, the Zeeman energy for the unit domain volume can be expressed as follows:

$$E_i = -\mu_0 m_i h \cos\theta. \quad (5.16)$$

The number of the corresponding unit domain volume can then be expressed as:

$$v = c \exp\left(\frac{\mu_0 m_i h \cos\theta}{kT}\right) = c \exp(bh \cos\theta), \quad (5.17)$$

where,

$$b = \frac{\mu_0 m_i}{kT}, \quad (5.18)$$

is a balance coefficient for isotropic components.

During the magnetising process in Fig. 5.1(d), the increased dv number of the unit domain along with the excitation field is calculated as:

$$dv = v_3 - v_4. \quad (5.19)$$

When dv approaches 0, the increased dv number of the unit domain can also be expressed as the derivative of (5.17); then, the unit volume number differences due to domain wall motion caused by the excitation field in Fig. 1(d) is:

$$dv = -cbh \exp(bh \cos\theta) \sin\theta d\theta, \quad (5.20)$$

leading, on integration, to:

$$v = -cbh \int_0^\theta \exp(bh \cos\theta) \sin\theta d\theta. \quad (5.21)$$

According to (5.7), the magnetisation M_i of the isotropic component in the direction of the excitation field in Fig. 5.1(d) can be obtained from the contribution $m_i \cos\theta$ of the unit domain magnetic moment multiplied by the increased number of the unit volume domain dv integrated over the total number, giving:

$$M_i = \int_0^v m_i \cos\theta dv. \quad (5.22)$$

Combining (5.21) and (5.22), leads to:

$$\begin{aligned} M_i &= -cbhm_i \int_0^\pi \exp(bh \cos\theta) \sin\theta \cos\theta d\theta \\ &= m_i v \frac{\int_0^\pi \exp(bh \cos\theta) \sin\theta \cos\theta d\theta}{\int_0^\pi \exp(bh \cos\theta) \sin\theta d\theta}. \end{aligned} \quad (5.23)$$

To solve these integrals, assume $x = \cos\theta$, and $dx = -\sin\theta d\theta$. Then:

$$\begin{aligned} M_i &= m_i v \frac{\int_1^{-1} \exp(bh x) x dx}{\int_1^{-1} \exp(bh x) dx} \\ &= m_i v \left(\frac{\exp(bh) + \exp(-bh)}{\exp(bh) - \exp(-bh)} - \frac{1}{bh} \right). \end{aligned} \quad (5.24)$$

Following integration, the magnetisation process M_i of isotropic component, derived from the analysis of the isotropic domain pattern in ferromagnetic materials, in the direction of the excitation field is given by:

$$M_i = M_{si} \left(\coth(bh) - \frac{1}{bh} \right) = M_{si} L(bh), \quad (5.25)$$

where $M_{si} = m_i v$ is the saturation magnetisation of the isotropic component when the isotropic domain walls are all eliminated to form a unified domain approximate to the excitation field. Equation (5.25) is the well-known Langevin's function [56], which was

initially derived according to the microstructures in paramagnetic materials and represents the homogeneous structures in ferromagnetic materials.

The third component in the magnetisation processes is the coupling effect of the excitation field, which exists since the initial magnetisation but only weakly affects the magnetic induction B . When ferromagnetic material is subjected to an excitation field, the latter penetrates the material and leads to a coupling effect constituting a proportion of the magnetic induction, which is expressed as:

$$M_h = \alpha h, \quad (5.26)$$

where α is the coupling coefficient concerned with the microstructure of the ferromagnetic material. It can be calculated based on relevant measured data by using fitting tools. The magnetic induction comprised of the above three components is then acquired as a single generalized equation:

$$B = M_a + M_i + M_h, \quad (5.27)$$

or using equations (5.14), (5.25) to (5.27) as [118]:

$$B = M_{sa} \tanh(ah) + M_{si} L(bh) + \alpha h. \quad (5.28)$$

The right-hand side of equation (5.28) consists of three terms, representing anisotropic, isotropic and excitation field coupling components, respectively. As pointed out, h is obtained by removing the hysteresis portion from the magnetic field H .

It is worth noting that magnetisation is measured conventionally in ampere/meter, and the magnetic polarization is measured in tesla, the relationship between magnetic polarization and magnetisation can be expressed as follows:

$$J = \mu_0 M. \quad (5.29)$$

Magnetic flux density is measured in tesla, so, M_{sa} and M_{si} in (5.27) should be replaced by magnetic polarization. But M_{sa} and M_{si} in (5.27) are expressed as tesla for convenience of easy of understanding because both magnetic polarization and magnetisation represent the magnetic force generated by the microscopic current in the magnetic materials.

The above general physical model (5.27) is excellent for tracing sigmoid shape curves; however, magnetisation processes do not always result in standard smooth regular S-shape curves. When equation (5.27) is used to simulate distorted and irregular curves, the modelled results can reflect huge disparity compared to the measured curves. However, the excitation field coupling effect to the magnetic induction is weak in terms of the other two components. in such situations it can be considered negligible to a good approximation, and the hyperbolic tangent and the Langevin's function can be replaced by an exponential function. This results in a simplified expression for the magnetic induction as the follows [118]:

$$B = M_{sa} \exp(ah) + M_{si} \exp(bh). \quad (5.30)$$

Accordingly, equation (5.30) can be used to trace the segmented curves in a piecewise manner to achieve piecewise monotonicity when single curves arise with a distorted and irregular shape. Equation (5.28), and (5.30), differs from the traditional models used to trace magnetic hysteresis loops directly, in that they are used to track S-shaped single curves obtained from measured hysteresis loops. This new model can interpret the magnetic hysteresis and predict the energy loss of ferromagnetic materials under controlled sinusoidal and non-sinusoidal excitation. However, it is important to note that the piece-wise approach results in a set of parameters in (5.30) for each curve segment, which complicates the hysteresis modelling process. Furthermore, equation (5.30) is a purely mathematical approximation method employed to track the single curves within the piece-wise approach, causing it to lose the physical significance presented in (5.28).

5.4 Hysteresis Removal Procedure

Hysteresis loop phenomenon is the main hindrance to interpreting the magnetic characteristics of ferromagnetic materials in electromagnetic machines. The one-to-two relationship between H and B contributes a complicated nonlinearity, which is hard to model using regular mathematic formulas. In this study, a methodology is proposed to offset the hysteresis effects during the magnetisation processes. The hysteresis loop includes descending and ascending curves, and these two individual curves are one-to-one injective function. The method adopted here is to explore the relationship of descending and ascending curves to avoid simulating the hysteresis loops directly, which simplifies the modelling of magnetic curves.

The flowchart depicting the hysteresis modelling process using the recently developed hysteresis model is presented in Fig. 5.2. Not only does this procedure avoid having to model the hysteresis loop directly, but it is also intended to explore the genuine physical mechanism of magnetic hysteresis. Hysteresis loops are the phenomena that the magnetisation and magnetic induction lag the magnetic field. This hysteretic behaviour occurs at any order reversal point and results from the hysteresis field generated by magnetisation coupling effects. The hysteresis removal procedure counteracts the hysteresis effect using equation (5.3).

The first step illustrating the hysteresis removal procedure is to generate the hysteresis loop using the measured experimental data; here the case of controlled sinusoidal magnetic induction of a GOES is adopted at a magnetisation frequency of 50 Hz and peak flux density of 1.7 T; subsequent measurements for different frequencies and peak flux densities follow the same methodology. The corresponding hysteresis loop shown in Fig. 5.3 is comprised of two curves, descending and ascending ones. For the descending curve, the section from B_s to $-H_c$ represents demagnetisation; and that from $-H_c$ to

$-B_s$ is the magnetisation section. The inverse relationship applies for the ascending curve, which can be seen in Fig. 5.3. The single curves of B versus h are obtained by displacing the descending curve to the right and the ascending curve to the left a horizontal distance H_c , via equation (5.3), as shown in Fig. 5.4. It is worth noting that these single curves are disconnected at the saturation tips due to the parallel shift of the original descending and ascending sections together with the magnetic field coordinates to the origin.

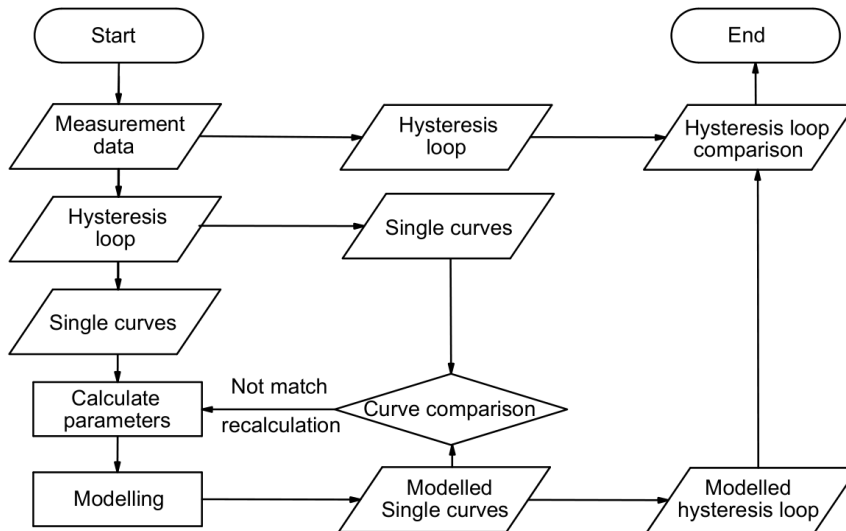


Fig. 5.2 Flowchart of hysteresis modelling using new hysteresis model.

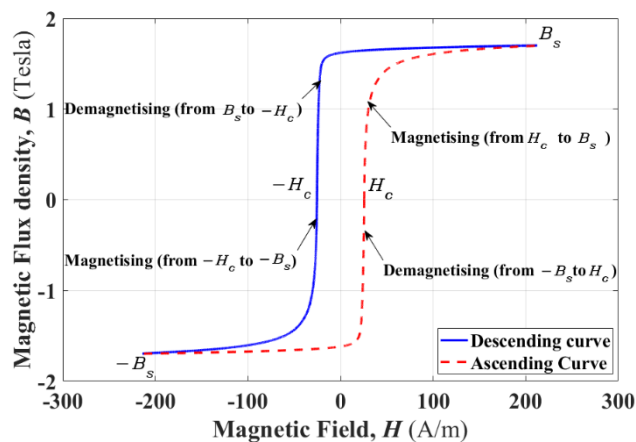


Fig. 5.3 Measured hysteresis loop for GOES at a magnetisation frequency of 50 Hz and peak flux density of 1.7 T.

Both single curves in Fig. 5.4 pass through the origin $(0, 0)$, which reveal a synchronised relationship of B versus h . The magnetic flux density and excitation field arrive at the origin at the same time, the nonlinear function between B and H is converted into two functions with a one-to-one relationship between B and h . The modelling of hysteresis loops can now be investigated through considering these single curves. The long overlapping sections close to the origin, represent the similar properties between the curves of being dominated by domain wall motion. The dissimilarity between them as they approach the saturation tips reveals characteristics dominated by the anisotropic domains.

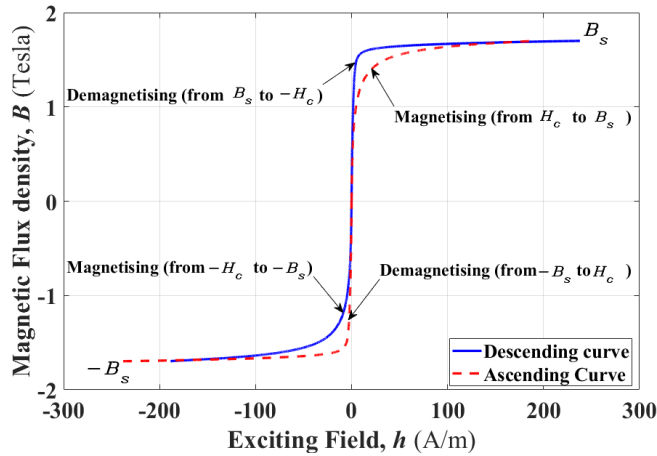


Fig. 5.4 Single curves for GOES at a frequency of 50 Hz and peak flux density of 1.7 T, obtained by displacing the measured ascending and descending curve of the hysteresis loop in Fig 5.3. an amount H_c to the left and right, respectively.

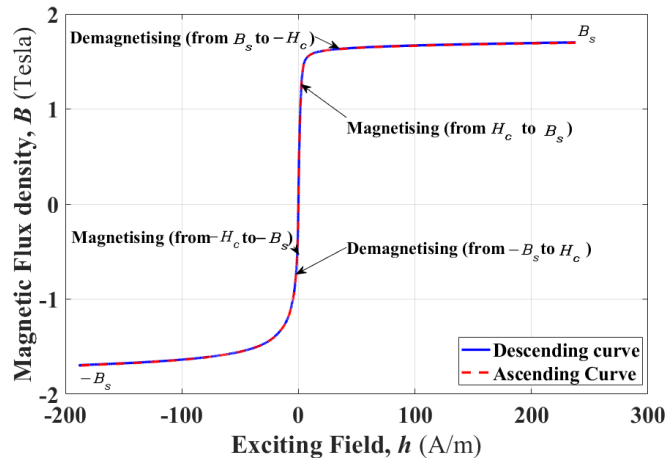


Fig. 5.5 Overlapping single curves for GOES at a frequency of 50 Hz and peak flux density of 1.7 T, obtained by rotating the ascending curve through 180° about both the B and h axis.

It has long been observed that the ascending and descending curves are symmetrical about the origin, this phenomenon is caused by the sinusoidal magnetic flux density under the controlled magnetic excitation. So, the next critical step in the processing of the single curves is to rotate the ascending single curve through 180° about both the B and h axes, the result is shown in Fig. 5.5. As expected, the descending and ascending curves are identical and lay on top of one another following rotation. The key feature of procedure in this way is that the modelling of hysteresis loops can be achieved by investigating just a single curve, which is a synchronized curve of B versus h given by equation (5.28), or (5.30). The modelled single curve in Fig. 5.6 is generated using (5.28) and is indistinguishable from its measured counterpart. The accompanying parameters are calculated separately for the magnetising and demagnetising sections of the curve. This is

because the domain pattern variations act in the opposite way for the two processes. The associated parameter values are provided in Table 5. 1.

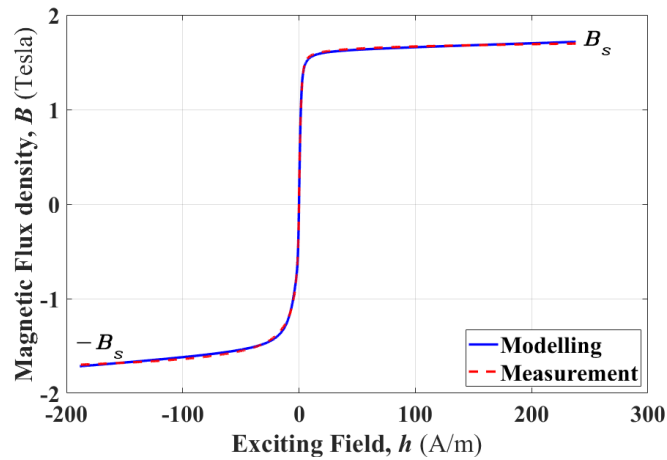


Fig. 5 6 Superimposed modelled and obtained single curves for GOES at a frequency of 50 Hz and peak flux density of 1.7 T.

While a key advantage of the proposed model is to describe the magnetising process, the main criterion for verifying the model is to now generate sigmoidal curves representing the corresponding hysteresis loop from the measurement data. Although the model was derived to describe single curves of B versus h , the relevant hysteresis loops of B versus H can be created by reversing the above processes, shifting the modelled curves to fit the experimental loops. Comparison between the modelled and measured hysteresis loop is provide in Fig. 5.7, demonstrating a remarkable degree of agreement.

Table 5.1 Parameters associated with equation (5.28) for obtaining the magnetising and demagnetising curve sections of Fig. 5.5 for GOES magnetised at a frequency of 50 Hz and peak flux density of 1.7 T.

Curve section	M_{sa} (T)	M_{si} (T)	a	b	α
Magnetising ($B < 0$)	0.555	1.007	84.18	23.83	0.072
Demagnetising ($B > 0$)	0.790	0.853	56.62	75.74	0.021

The most important requirement and test of the new model is its fit to measurement data relating to materials under different magnetisation frequencies and peak flux densities. Accordingly, calculating the modelling parameters involved requires processing

of the relevant measurement data for a particular range of magnetisation frequencies and peak flux densities. The modelling results for different frequencies and peak flux densities will be presented in the ongoing chapters.

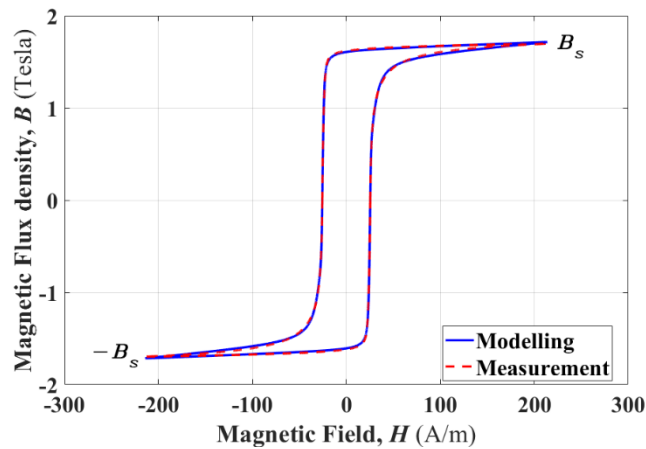


Fig. 5.7 Measured and modelled hysteresis loop for GOES at a frequency of 50 Hz and peak flux density of 1.7 T superimposed against the corresponding measured data.

Conveniently, the new model can be used to calculate the energy losses by simply integrating the single equation over the range of the excitation field. In contrast, the traditional method of evaluating the energy losses is by calculating the area of the hysteresis loops. For example, the percentage difference between measured and modelled energy losses is 0.6808 % for the sample case at the magnetisation frequency of 50 Hz and the peak flux density of 1.7 T. Based on analysing single curves, the new model provides an accurate and reliable methodology for creating the hysteresis loops and calculating the energy losses.

5.5 Conclusions

In this investigation, the aim was to derive a new model for describing the magnetisation processes in GOESs and NOESs, and the implementation of the general physical model to explore its accuracy in tracing the magnetisation processes under sinusoidal excitations. The measurement data were sampled at 50 Hz and the saturation magnetisation conditions for GOESs. The major loops were generated using MATLAB to process the relevant measurement data, and then the major loops were manipulated to achieve the single curves suitable for applying the single equation model. The fitting parameters were calculated separately for different curve sections to attain the best modelling results. The modelled hysteresis loops were created using the modelled single curves and MATLAB codes, which were compared to the measured hysteresis loops. These modelling results have significant implications for the understanding of the physical grounds of magnetisation processes dominated by the components of anisotropic and isotropic domain patterns by considering the coupling effect of the excitation field.

Chapter 6 Dynamic Modelling of Grain-Oriented Electrical Steels

This chapter uses the novel analytical model developed in chapter 5 to describe the magnetisation processes of GOESs. The model is derived based on the consideration of anisotropic and isotropic components, as well as the coupling effect of the excitation field in ferromagnetic materials. Intensive research has been conducted on the ability of the model to reproduce the magnetic hysteresis loops and evaluate the energy losses in GOESs under sinusoidal and non-sinusoidal magnetisation regimes. The model is validated for Epstein size laminations of 3 % SiFe GOESs at magnetisation frequencies ranging from 50 Hz to 1000 Hz and peak flux densities ranging from 1.0 T to 1.7 T. Close agreement, with a maximum difference of less than 2 %, was found between the calculations using the proposed model and measured energy losses.

6.1 Fitting the Model to the Measurement Data of GOESs

Although the single equation model is simple to implement, it should be noted that (5.28) is used to describe the relationship between B vs h , the excitation field. Conventionally, the hysteresis loop describes the relationship between B vs H , the magnetic field. The relevant standards of the experiment setup for measuring the magnetic properties of electrical steels were designed for this purpose, so the measurement data obtained experimentally is conveniently for B vs H . Once the measurement data is acquired, the excitation field is easy to calculate in accordance with (5.3). Then, the investigation of the hysteresis loop of B vs H becomes one of studying a single s-shaped curve of B vs h .

Parameters of the new model are linked to the microstructures of magnetic materials, which it is impossible to calculate from the data obtained from the manufacturer's data sheets. There is no measurement system able to detect the proportion of the anisotropic and isotropic components in a ferromagnetic material. Therefore, the most important investigation to appraise the general physical model is to fit the single equation to measurement data for different ferromagnetic materials under different magnetisation conditions. As the model derived is intended to describe the magnetisation process, the main criterion for verifying the model is to generate sigmoidal curves representing the hysteresis loop from the measurement data. The calculation of the modelling parameters is conducted in terms of processing the relevant measurement data, obtained for different frequencies and peak flux densities. The curve fitting tool in MATLAB is used to process the measurement data and calculate the parameters. The equations with

calculated parameters are then used to create the single curves of B vs h ; the hysteresis loops of B vs H can be generated by manipulating the single curves obtained. Finally, comparisons between the modelled and measured hysteresis loops are made to verify the general physical model.

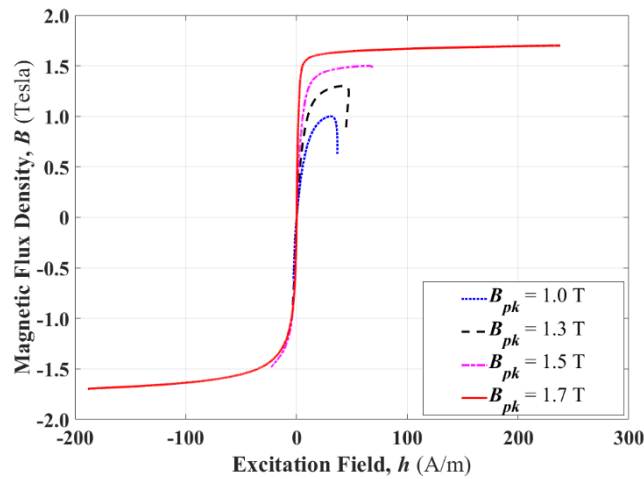


Fig. 6.1 Single curves of GOESs derived from the loops measured at a frequency of 50 Hz and peak flux densities ranging from 1.0 to 1.7 T under sinusoidal flux density.

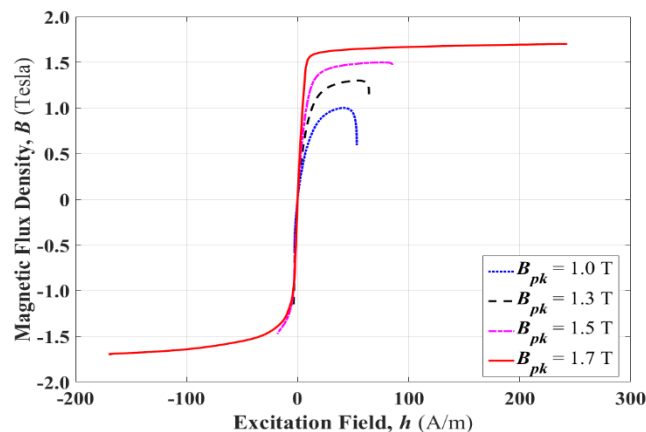


Fig. 6.2 Single curves of GOESs derived from the loops measured at a frequency of 100 Hz and peak flux densities ranging from 1.0 to 1.7 T under sinusoidal flux density.

It should be noted that the anisotropic components in GOESs dominate the magnetic properties, and the proportion of isotropic components is far less than that of anisotropic structures. Therefore, it is vital to obtain the best parameters for verifying the model suitable for specific materials, and the parameters may vary according to different exciting conditions, such as frequencies and peak flux densities.

The main advantage of this model is the fact that the parameters of the model represent the microstructure of the magnetic materials, which enables the modelling of minor and major hysteresis loops. The single curves of B vs h are derived from measured the major

and minor loops of GOESs. The curves are shown in Fig. 6.1 to Fig. 6.6, respectively, for magnetisation frequencies ranging from 50 Hz to 1000 Hz and peak flux densities ranging from 1.0 T to 1.7 T. These curves demonstrate the magnetisation processes for $h < 0$ and the demagnetisation processes for $h > 0$, respectively. Certainly, the parameters for these two processes are different, so the calculations need to be undertaken separately. It is worth noting that certain curve sections exhibit sharp bends, and in some cases, anti-hysteresis can be observed. As a result, these curve sections should be modelled by dividing them into smaller sections based on their bend features.

As shown in Fig. 6.1, the individual curves under magnetisation frequencies of 50 Hz, peak flux densities of 1.0 T and 1.3 T display sharp bends at the tips for $h > 0$. Therefore, the curve sections are divided into three and four sections, respectively. Subsequently, the parameters must be calculated separately to achieve the best modelling results. The individual curves, resulting from magnetisation frequencies of 100 Hz and peak flux densities of 1.0 T and 1.3 T, exhibit sharp bends displayed in Fig. 6.2. To accurately model these curves, the sections for these two single curves must be divided into three and four smaller sections, respectively. In Fig. 6.3, there are three single curves with sharp bends, derived from measurements magnetised at 200 Hz and flux densities of 1.0 T, 1.3 T, and 1.5 T. To achieve accurate modelling results, these single curves need to be separated into four smaller sections for $h > 0$. Additionally, the single curve shown in Fig. 6.4 at 200 Hz and 1.7 T must be divided into two sections for both magnetising and demagnetising sections to ensure the new model achieves the best similarity.

As demonstrated in Fig. 6.4 – 6.6, all the single curves exhibit some distortion, requiring a piecewise modelling approach for each curve. For the demagnetising sections of 1.0 T, 1.3 T, and 1.5 T under 400 Hz and 800 Hz, they must be divided into four sections. Similarly, both the magnetising and demagnetising sections of the single curve magnetised under a magnetic flux density of 1.7 T and frequencies of 400 Hz and 800 Hz need to be modelled with three separate sections, respectively. The most challenging scenario occurs with the curves magnetised at 1000 Hz, where all single curves experience severe distortion. To obtain ideal modelling results, the demagnetising sections at 1.0 T, 1.3 T, and 1.5 T must be divided into five sections. Moreover, the magnetising and demagnetising sections at 1.7 T have to be separated into three and five sections, respectively, in order to achieve satisfactory results with the model.

As a summary, it is observed that increasing the magnetisation frequencies leads to higher curve distortion, necessitating the division of the curves into more sections to achieve satisfactory modelling results. On the other hand, at low magnetic flux densities, such as 1.0 T and 1.3 T, all single curves experience distortion, requiring a piecewise modelling approach to accurately represent the measurement data.

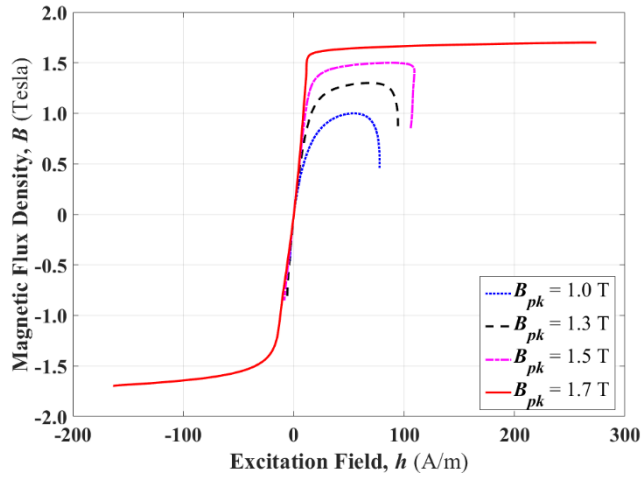


Fig. 6.3 Single curves of GOESs derived from the loops measured at a frequency of 200 Hz and peak flux densities ranging from 1.0 to 1.7 T under sinusoidal flux density.

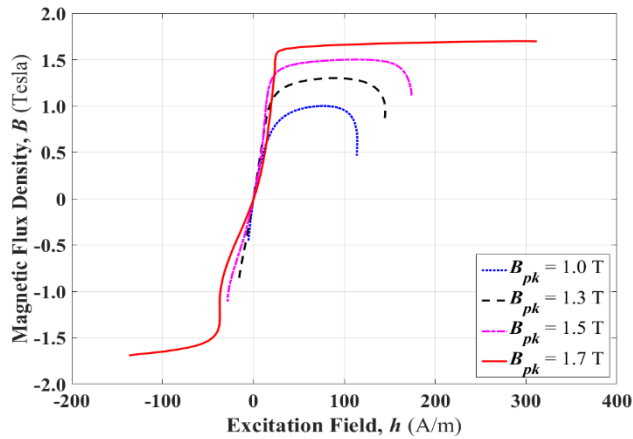


Fig. 6.4 Single curves of GOESs derived from the loops measured at a frequency of 400 Hz and peak flux densities ranging from 1.0 to 1.7 T under sinusoidal flux density.

As shown in Fig. 6.1, the tips of the single curves at the magnetisation frequency of 50 Hz and 1.0 T and 1.3 T, exhibit deviations due to the asynchronicity. As the frequency increases, the asynchronicity becomes more evident, which can be seen from the single curves displayed in Fig. 6.1 though to Fig. 6.6 for the magnetisation frequency ranging from 50 Hz to 1000 Hz. The curls at the single curve tip introduce an interesting phenomenon, the magnetic flux density leads the magnetic field. This phenomenon makes the calculation rather difficult, so the modelling of the single curves must be done using (5.30) by fitting piecewise curves. The resulting distortions of the single curve require the use of equation (5.30) to track them in a piecewise manner. The parameters for use in (5.30) must be determined for each piecewise section; the greater the number of piecewise sections employed, the greater the accuracy of the modelling results. Taking a magnetisation frequency of 800 Hz and peak flux density of 1.7 T as a typical example, the number of sections required is 6. The associated parameters for this case are provided in Table 6.1.

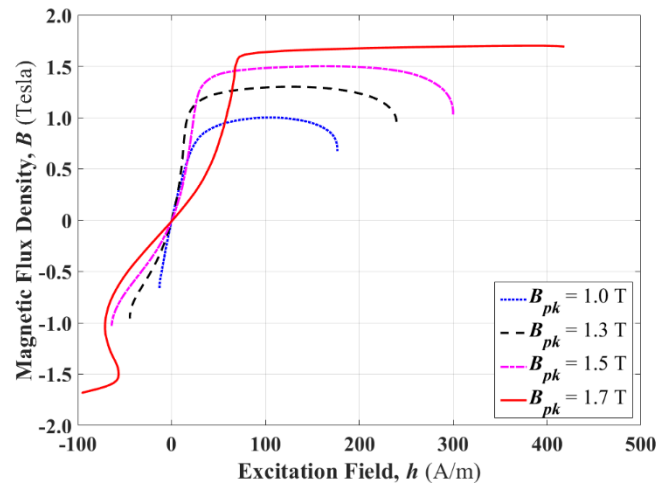


Fig. 6.5 Single curves of GOESs derived from the loops measured at a frequency of 800 Hz and peak flux densities ranging from 1.0 to 1.7 T under sinusoidal flux density.

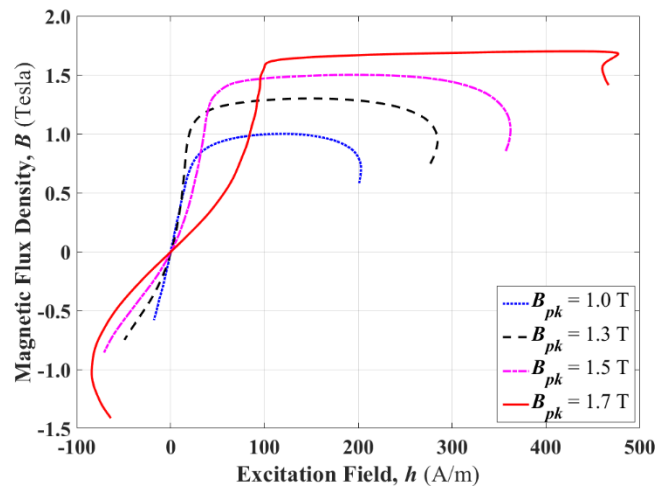


Fig. 6.6 Single curves of GOESs derived from the loops measured at a frequency of 1000 Hz and peak flux densities ranging from 1.0 to 1.7 T under sinusoidal flux density.

Although the hysteresis loops have different shapes for different frequencies and peak flux densities, the derived single curves display astounding similarities and pass through the origin. This means that the excitation field is partially synchronised with magnetic flux density, except for some tips where curls occur due to magnetisation coupling effects. So, this method of deriving single curves dramatically simplifies the investigation of the magnetic properties compared to studying $B - H$ loops directly. The single equation model is derived according to the magnetisation processes, so not only does this generalised single equation model give an excellent performance for the major hysteresis loop, but it is also suitable for modelling the minor loops as well.

The magnetic hysteresis loops of GOESs are generated using the proposed model for the range of magnetisation. The comparisons between measured and modelled hysteresis loops at magnetisation frequencies of 50 Hz to 1000 Hz and peak flux densities

of 1.0 T to 1.7 T are shown in Fig. 6.8 to Fig. 6.13, respectively. The result indicates that the modelled hysteresis loops are completely coincident with the measured loops for the range of magnetisation.

Table 6.1 Parameters associated with equation (5.30) used to obtain the contiguous magnetisation and demagnetisation curve sections, 6 in total, of Fig. 6.7 magnetised for GOES at a frequency of 800 Hz and peak flux density of 1.7 T.

Curve section	M_{sa} (T)	M_{si} (T)	a	b
Magnetisation Sections ($B < 0$)				
Section 1	-0.143	0.146	-5.757	2.093
Section 2	0	3.656	37.12	-1.279
Section 3	1.449	-4e+5	-0.127	-22.32
Demagnetisation Sections ($B > 0$)				
Section 4	0.306	-1.866	0.331	0.012
Section 5	4e+13	-1.554	39.14	-0.035
Section 6	0.144	-0.120	5.472	-2.910

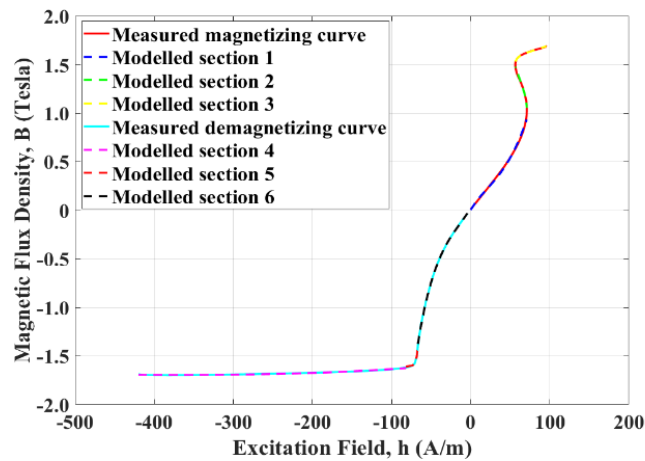


Fig. 6.7 Modelled contiguous curve sections, 6 in total, superimposed on the corresponding measured single curve for GOESs measured at a frequency of 800 Hz and peak flux density of 1.7 T under sinusoidal flux density.

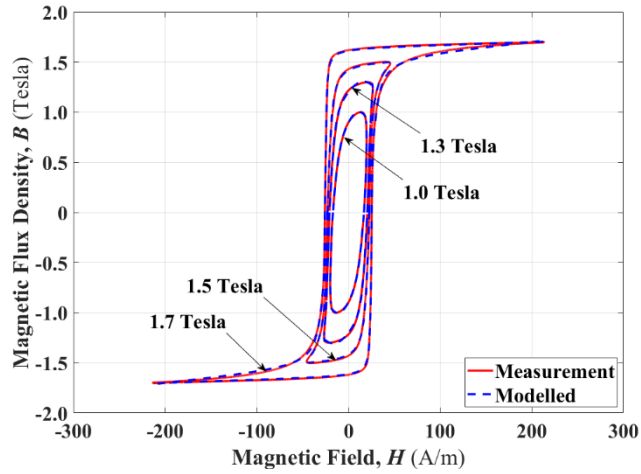


Fig. 6.8 Comparison between modelled and measured hysteresis loops for GOESs at 50 Hz and peak flux densities ranging from 1.0 T to 1.7 T under sinusoidal flux density.

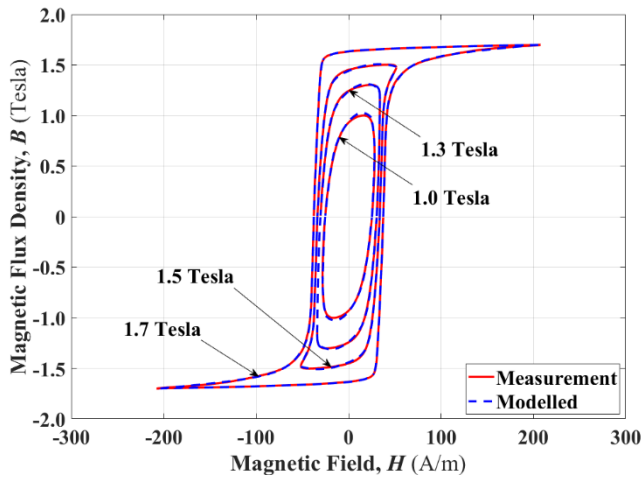


Fig. 6.9 Comparison between modelled and measured hysteresis loops for GOESs at 100 Hz and peak flux densities ranging from 1.0 T to 1.7 T under sinusoidal flux density.

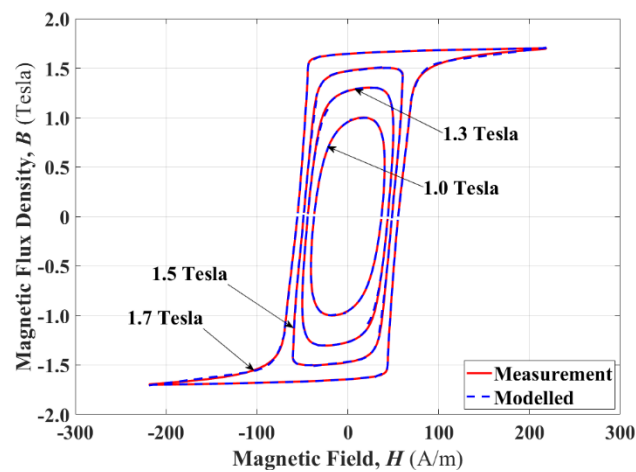


Fig. 6.10 Comparison between modelled and measured hysteresis loops for GOESs at 200 Hz and peak flux densities ranging from 1.0 T to 1.7 T under sinusoidal flux density.

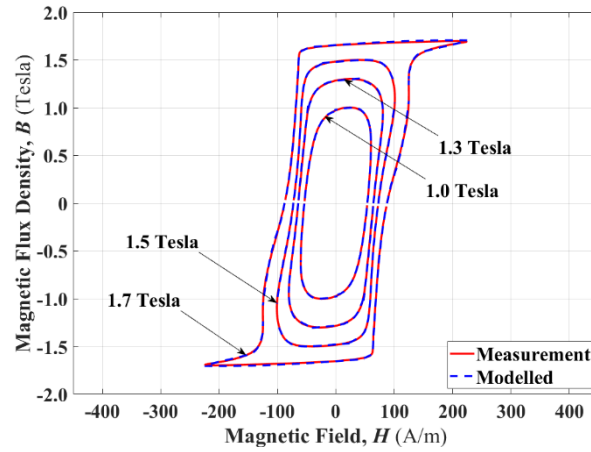


Fig. 6.11 Comparison between modelled and measured hysteresis loops for GOESs at 400 Hz and peak flux densities ranging from 1.0 T to 1.7 T under sinusoidal flux density.

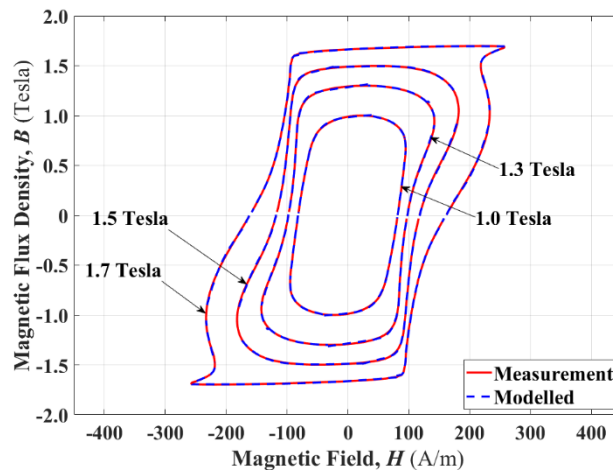


Fig. 6.12 Comparison between modelled and measured hysteresis loops for GOESs at 800 Hz and peak flux densities ranging from 1.0 T to 1.7 T under sinusoidal flux density.

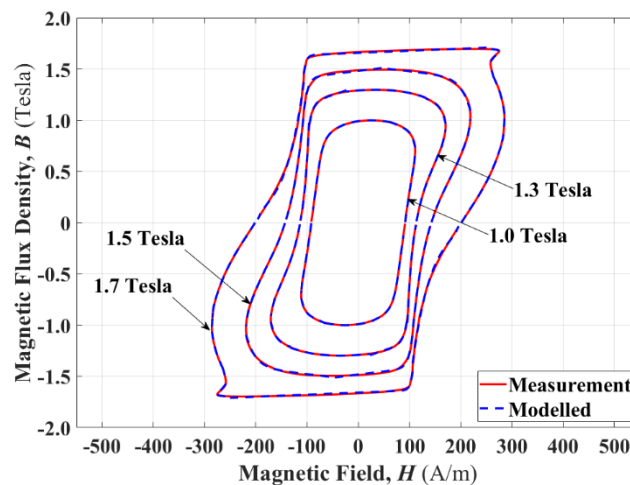


Fig. 6.13 Comparison between modelled and measured hysteresis loops for GOESs at 1000 Hz and peak flux densities ranging from 1.0 T to 1.7 T under sinusoidal flux density.

6.2 Evaluation of Energy Losses Using the Novel Model

Energy loss of ferromagnetic materials due to time-varying externally applied fields accounts for a large portion of the total loss of electromagnetic devices [16]. However, evaluation of the energy loss is still a challenging problem, usually addressed using the separation principle explained by Bertotti [7] and Zirka [1]. Theoretically, due to the hysteresis characteristics of ferromagnetic materials, this problem is highly nonlinear and rather complicated. So far, there is no exact model to fully describe this complex problem.

It is acknowledged that the energy loss separation model is so important in electromagnetic machine design that engineers can deal with loss mechanisms at different spatiotemporal scales. So far, engineers usually design machines based on phenomenological models, which are described by curve fitting equations verified by experimental results [7, 20].

Conventionally, the magnetic energy loss in the core materials can also be calculated based on Zeeman energy per cycle under sinusoidal excitation, which is equal to the area of the magnetic hysteresis loop [88]. After collecting the measurement data, the hysteresis loop of B vs H can be generated, and then energy loss of the magnetic core calculated using the following expression:

$$W = \int BdH. \quad (6.1)$$

There are two single curves of the B vs h , so that the energy loss can be evaluated according to the following expression:

$$W = 2 \int Bdh. \quad (6.2)$$

Then, the energy loss can be calculated by integrating (5.28) or (5.30), and the following simple equations for energy loss evaluation can be acquired:

$$W = 2 \int Bdh = 2 \int (M_{sa} \tanh(ah) + M_{si} L(bh) + ah) dh. \quad (6.3)$$

$$W = 2 \int Bdh = 2 \int (M_{sa} \exp(ah) + M_{si} \exp(bh)) dh. \quad (6.4)$$

So, the energy loss is also can be calculated based on the Zeeman energy of B vs h per cycle expressed as (6.3) and (6.4). After calculating the parameters of the single equation, the total energy loss per cycle is calculated by integrating the simple equation. The integration of (5.28) or (5.30) is implemented in the range of the excitation field. If (5.30) is used for piecewise section lines, the integration should be conducted in a piecewise manner.

The total energy losses were measured at different frequencies and peak flux densities to investigate the magnetic properties of GOESs under different magnetisation conditions.

A comparison between the measured energy losses and calculated losses using (6.3) or (6.4) is illustrated in Fig. 6.14 for magnetisation frequencies of 50 Hz to 1000 Hz and peak flux densities of 1.0 T to 1.7 T. It is evident that the single equation performs well in calculating the energy losses for GOESs under a wide range of magnetisation conditions.

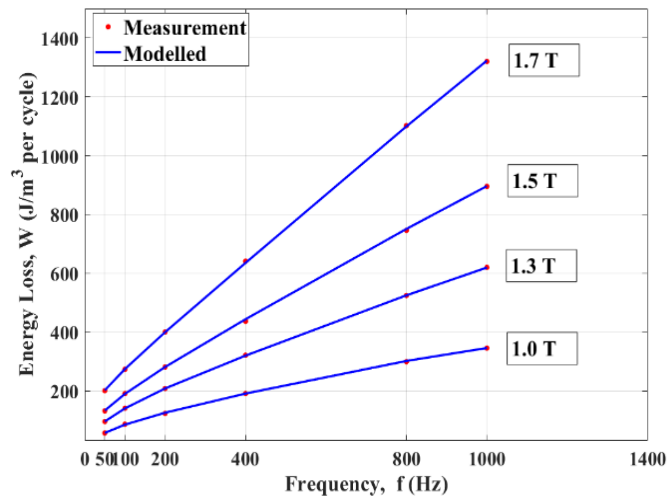


Fig. 6.14 Comparison between calculated and measured energy losses per cycle for GOESs at frequencies from 50 Hz to 1000 Hz and peak flux densities from 1.0 T to 1.7 T.

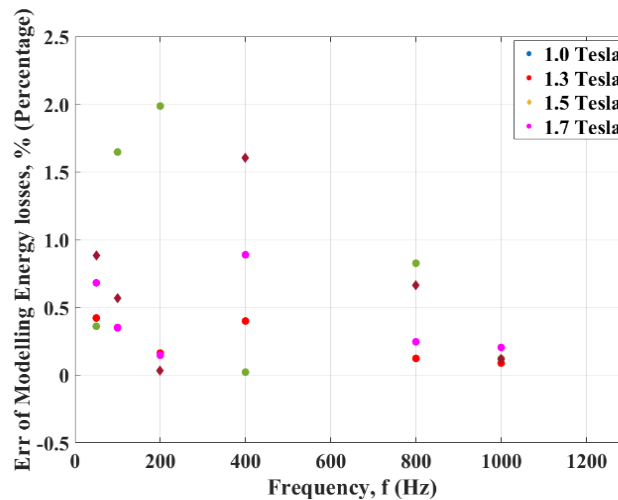


Fig. 6.15 Energy loss errors between the modelled and measured energy losses for GOESs at frequencies from 50 Hz to 1000 Hz and peak flux densities from 1.0 T to 1.7 T.

Fig. 6.15 reveals the errors between the modelled and measured energy losses for GOESs at magnetisation frequencies of 50 Hz to 1000 Hz and peak flux density ranging from 1.0 T to 1.7 T. Close agreement with a maximum difference of less than 2 % for the range of measurements is observed. Therefore, not only is the proposed single equation model an accurate and reliable technique for generating the magnetic hysteresis loops for GOESs, but it also provides excellent prediction for energy loss calculation purposes as well.

6.3 Investigation of Non-sinusoidal Excitation for GOESs

An SST measurement system is employed to measure the magnetic hysteresis loops and energy losses of GOESs under non-sinusoidal excitation, which contains fundamental frequency (50 Hz), 3rd, 7th, and 11th harmonics. In these measurements, the new model is employed to validate the modelling of non-sinusoidal excitations with arbitrary harmonics. The primary objective was to verify the modelling accuracy for non-sinusoidal magnetization regimes. Subsequent research will include more practical magnetization frequencies and peak flux densities by incorporating realistic non-sinusoidal excitation fields. Based on the proposed new model, the magnetic hysteresis and energy loss of the GOESs under harmonic excitation are investigated to explore the magnetic characteristics of GOESs under harmonic distorted magnetisation, e.g., in renewable energy applications. A comparison between the simulated results and the measurement data verifies the accuracy of the new model. Furthermore, application of the new model to GOESs under non-sinusoidal excitation for different peak flux densities ranging from 1.0 T to 1.7 T is analysed in detail to obtain a comprehensive understanding of non-sinusoidal induction on GOESs. So, the new model is potentially applicable to renewable energy systems where power electronic converters play an essential role.

6.3.1 Motivation based on emerging renewable energy

With the widespread application of power electronic converters in solar, wave and wind power generation systems, a wealth of harmonics and DC biases are generated in the power systems. These complex magnetic properties of magnetic materials can severely impair the safe operation of electrical equipment [119]. Magnetic cores of electromagnetic devices can be subjected to non-sinusoidal excitation, DC bias magnetisation, and distorted flux densities due to the presence of power electronic converters in renewable energy systems [121, 123].

In addition to all the advantages, power electronic converters are a potential source of unwanted harmonic emission, which may lead to complicated magnetic properties of the magnetisation processes and make energy loss analysis more complicated [121]. Energy losses increase rapidly with increasing magnetisation frequency and peak flux density, so the energy losses of the magnetic core under high-frequency and harmonic distorted magnetisation conditions become significantly higher [121]. Therefore, hysteresis modelling and energy loss evaluation of ferromagnetic materials is essential in the design and optimisation of power transformers and other electromagnetic devices in renewable energy systems.

Due to the existence of the harmonic excitation components, the waveforms of magnetic flux densities are distorted in the magnetic cores of power transformers, which make it intricate to model the nonlinear hysteresis and evaluate energy loss precisely [120]. Therefore, it is of great significance to model the magnetic properties of magnetic materials under the excitation of harmonics and DC bias [120].

The symmetrical hysteresis loops of ferromagnetic materials under sinusoidal excitation are investigated using Jiles-Atherton [2, 3] and Preisach [4] models. These models cannot be used directly to simulate the magnetic hysteresis and energy loss characteristics under non-sinusoidal excitation, such as harmonic and DC bias. The solution is either to improve the existing models or to propose a new effective model. One method to simulate the magnetic hysteresis loops under non-sinusoidal excitation is to incorporate the hysteresis model into the magnetic field separation method to estimate hysteresis, classical eddy current, and excess field components, respectively [20]. A dynamic Jiles-Atherton model was proposed to simulate the hysteresis loops and predict the energy losses of ferromagnetic materials under DC bias excitation [122]. The Preisach model was attempted to track the dynamic hysteresis loops and evaluate the energy losses under harmonic and DC Bias excitation [119, 120, 123].

Therefore, it is timely and beneficial to extend the new model of magnetisation processes derived in chapter 5 for the applications of renewable energy systems under arbitrary magnetisations. The main aim of this section is to simulate the hysteretic curves and evaluate the energy losses of GOESs under non-sinusoidal excitations. The study is based on measured magnetic hysteresis loops. The experimental results are compared to the modelled hysteretic curves and energy losses to show the effectiveness of the proposed new model.

The designed program codes based on this model can be used to process the experimental hysteresis loops, and the parameters of the equation for a specific material are calculated by the fitting programme. After obtaining the parameters, the hysteretic curves were regenerated, and the energy losses calculated for different frequencies and flux densities with harmonic components. The comparison between modelling results and measurement data indicates that this single equation model gives a good match for GOESs under non-sinusoidal excitation, revealing that the new model could be generalised to the application of renewable energy systems.

6.3.2 Fitting the Model to the Measurement Data of GOESs Under Non-sinusoidal Excitation

Applications of the new model for GOESs are investigated under non-sinusoidal excitation. The single equation model performs excellently in tracing the standard s-shape curves and distorted magnetic curves under sinusoidal excitation, as inferred from section

6.1. For the applications of GOESs under non-sinusoidal excitation, the hysteretic curves show more convoluted shapes than the distorted curves caused by high frequencies under sinusoidal excitation, because the 3rd, 7th, and 11th harmonics introduce three more hysteresis field components into the magnetic field. Therefore, the hysteresis field crossing the x-coordinate is considered when deriving the single curves of B vs h from the hysteretic curves of B vs H . The hysteresis field is deemed as the combined result of components triggered by the 3rd, 7th, and 11th harmonics with the fundamental frequency as well. Subsequently, the measured coercivity H_c is utilized to derive the single curve when subjected to non-sinusoidal excitation, and the same method in section 5.4 is applied so that the single curves obtained from the hysteretic curves under non-sinusoidal excitation can be tracked using the single equation model (5.30).

Parameters for the new model are determined based on the numbers of the separation of the single curves into section curves according to bends on the curves. The method to investigate the single curves obtained from the measurement data under non-sinusoidal excitation is the same as that to model the single curves acquired from sinusoidal excitation, and it is worth being aware that more section curves are divided to process the single curves to appraise the general physical model to fit the single equation with the measurement data under non-sinusoidal magnetisation conditions.

The curves displayed in Fig. 6.16 to 6.20 exhibit distinct characteristics when separated into two parts: the section where $h > 0$ is primarily influenced by demagnetising components, while the section where $h < 0$ is controlled by magnetising components. Both sections of the curves display significant distortions, necessitating a careful approach to divide them accurately by observing the points where the curves undergo changes in direction. In the case of the curve shown in Fig. 6.16 is magnetised under non-sinusoidal excitation at a frequency of 50 Hz and peak flux density of 1.0 T with 3rd, 7th, and 11th harmonics, the single curve is divided into 16 sections, with 7 sections corresponding to $h < 0$ and 9 sections for $h > 0$. Each of these individual sections requires separate calculations for all relevant parameters. It is essential to recognize that the harmonic components significantly affect the parameters of the model. Therefore, special attention must be given to accurately assess and account for these effects during the calculations.

As the peak flux density increases, modelling the single curves becomes more complex. Fig. 6.17 displays a single curve magnetized under non-sinusoidal excitation at a frequency of 50 Hz and a peak flux density of 1.1 T with 3rd, 7th, and 11th harmonics. The curve is divided into 31 sections, with 15 sections corresponding to $h < 0$ and 16 sections for $h > 0$. Similarly, in Fig. 6.18, the single curve is magnetized with a peak flux density of 1.3 T and divided into 35 sections, with 15 sections for $h < 0$ and 20 sections for $h > 0$. In Fig. 6.19, the single curve is magnetized with a peak flux density of 1.5 T and divided into

38 sections, with 18 sections for $h < 0$ and 20 sections for $h > 0$. Lastly, in Fig. 6.20, the single curve is magnetized with a peak flux density of 1.7 T and divided into 39 sections, with 20 sections for $h < 0$ and 19 sections for $h > 0$. Consequently, the calculation of parameters becomes an extremely tedious process due to the increased complexity. Additionally, the evaluation of energy using equations (6.3) and (6.4) becomes inaccurate because calculation errors are introduced by the connections between the separated curve sections. Hence, the energy evaluation under non-sinusoidal excitation is not discussed in this thesis. However, this topic will be the subject of future investigations, which will involve utilizing a new energy loss separation model to address the challenges posed by non-sinusoidal excitations.

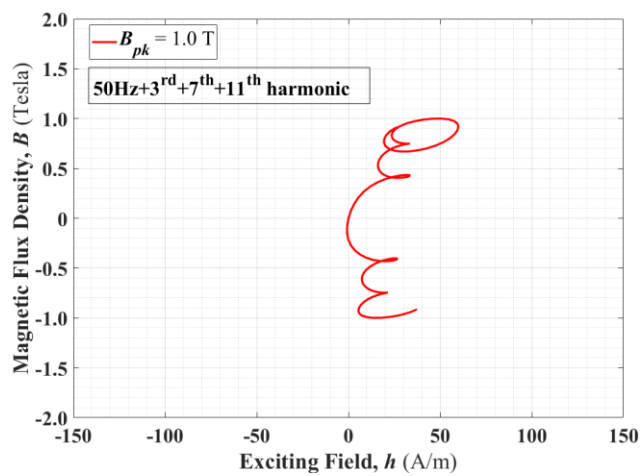


Fig. 6.16 Single Curves for GOESs under non-sinusoidal excitation at a frequency of 50 Hz and peak flux density of 1.0 T with 3rd, 7th, and 11th harmonics.

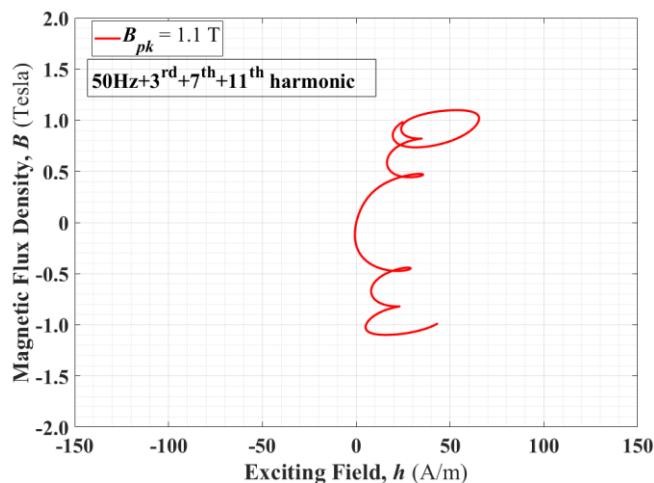


Fig. 6.17 Single Curves for GOESs under non-sinusoidal excitation at a frequency of 50 Hz and peak flux density of 1.1 T with 3rd, 7th, and 11th harmonics.

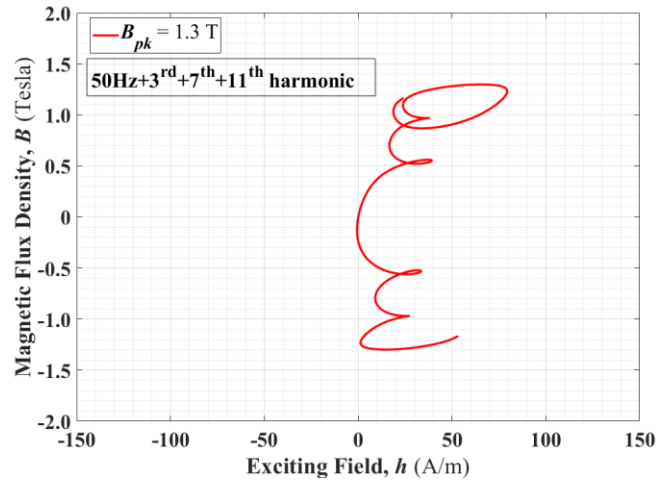


Fig. 6.18 Single Curves for GOESs under non-sinusoidal excitation at a frequency of 50 Hz and peak flux density of 1.3 T with 3rd, 7th, and 11th harmonics.

As the new model is intended to track the complicated single curves through the hysteresis removal procedure for magnetisation processes, the main criterion for verifying the model is to generate wiggling curves representing the hysteresis characteristics from the measurement data collected from non-sinusoidal excitation. The calculation of the modelling parameters is conducted by fitting the section curves, which represent the effectiveness under the different harmonic components.

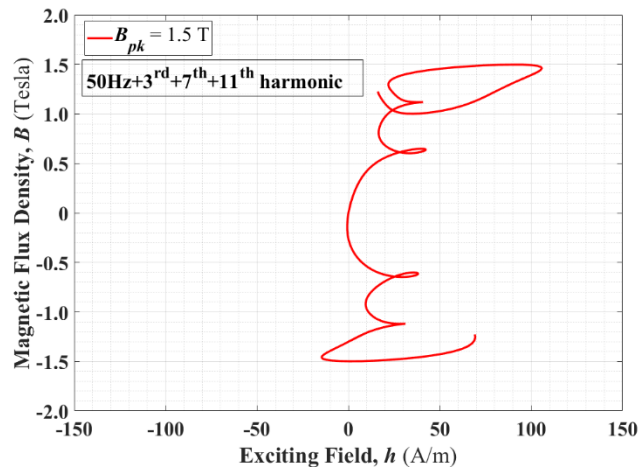


Fig. 6.19 Single Curves for GOESs under non-sinusoidal excitation at a frequency of 50 Hz and peak flux density of 1.5 T with 3rd, 7th, and 11th harmonics.

The curve fitting tool in MATLAB is used to process the measurement data of the section curves. The equation with calculated parameters is used to create the section curves of B vs h . Then the whole modelled single curves can be plotted by combining these section curves altogether. Afterwards, the modelled hysteresis loops of B vs H can be created by manipulating the single curves. Comparisons between modelled and measured data are

made to verify the application of the new model for tracking the hysteretic curves of non-sinusoidal excitation.

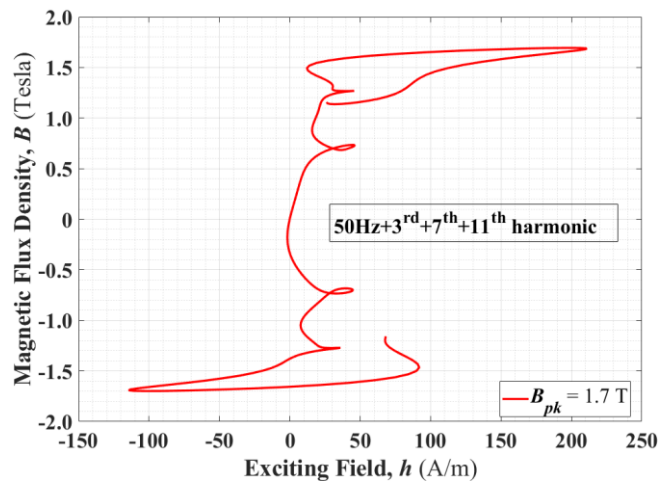


Fig. 6.20 Single Curves for GOESs under non-sinusoidal excitation at a frequency of 50 Hz and peak flux density of 1.7 T with 3rd, 7th, and 11th harmonics.

The single curves of B vs h derived from measured hysteresis loops for GOESs at the magnetisation frequency of 50 Hz and flux densities ranging from 1.0 T to 1.7 T with 3rd, 7th, and 11th harmonics are shown in Fig. 6.16 to Fig. 6.20, respectively. These curves show the magnetisation processes for $B < 0$ and demagnetisation processes for $B > 0$. Certainly, the parameters for the separated curve sections are different, and hence the calculations need to be done separately. Although the curves are significantly distorted, the single curves in Fig. 6.16 to Fig. 6.20 all pass through the origin, which means the hysteretic effects have been removed from the data processing procedure. So, the magnetic properties of B vs H can be investigated by studying the curves of B vs h .

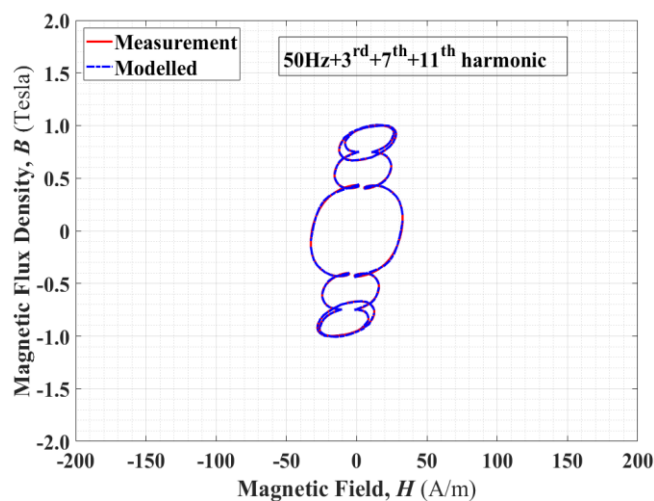


Fig. 6.21 Comparison of hysteresis loops for GOESs under non-sinusoidal excitation at a frequency of 50 Hz and peak flux density of 1.0 T with 3rd, 7th, and 11th harmonics.

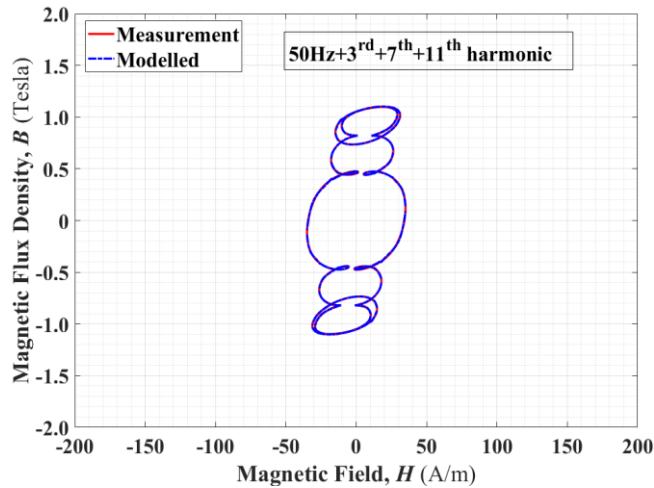


Fig. 6.22 Comparison of hysteresis loops for GOEs under non-sinusoidal excitation at a frequency of 50 Hz and peak flux density of 1.1 T with 3rd, 7th, and 11th harmonics.

It is apparent that the separated curve sections are synchronised between the B and h , so the curve sections can be simulated using the single equation model (5.30). The magnetic hysteresis loops of GOEs are generated using the proposed model for the range of magnetisation conditions. The measured and modelled hysteresis loops at the magnetisation frequency of 50 Hz and flux densities ranging from 1.0 T to 1.7 T with 3rd, 7th, and 11th harmonics are shown in Fig. 6.21 to Fig. 6.25, respectively.

The comparison of results between the modelled and measured hysteresis loops indicate that the calculated hysteresis loops have striking similarities with the measured loops for the range of magnetisation conditions. Apparently, this simple equation model can be used to model the complex magnetic properties of ferromagnetic materials under non-sinusoidal excitation with remarkable accuracy.

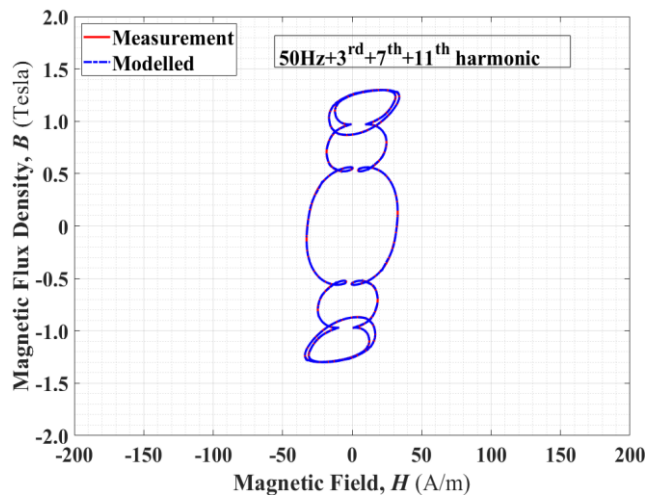


Fig. 6.23 Comparison of hysteresis loops for GOEs under non-sinusoidal excitation at a frequency of 50 Hz and peak flux density of 1.3 T with 3rd, 7th, and 11th harmonics.

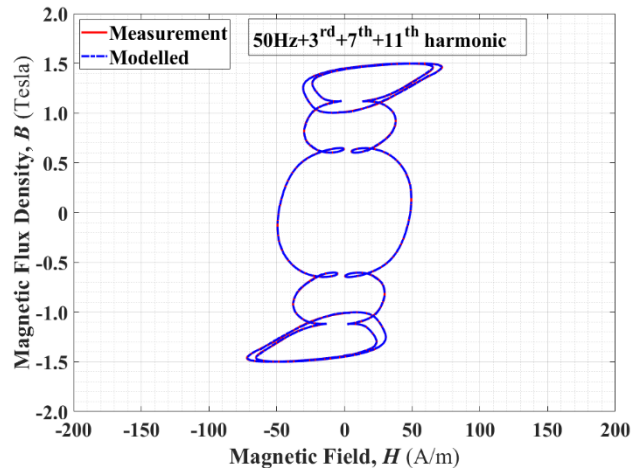


Fig. 6.24 Comparison of hysteresis loops for GOESs under non-sinusoidal excitation at a frequency of 50 Hz and peak flux density of 1.5 T with 3rd, 7th, and 11th harmonics.

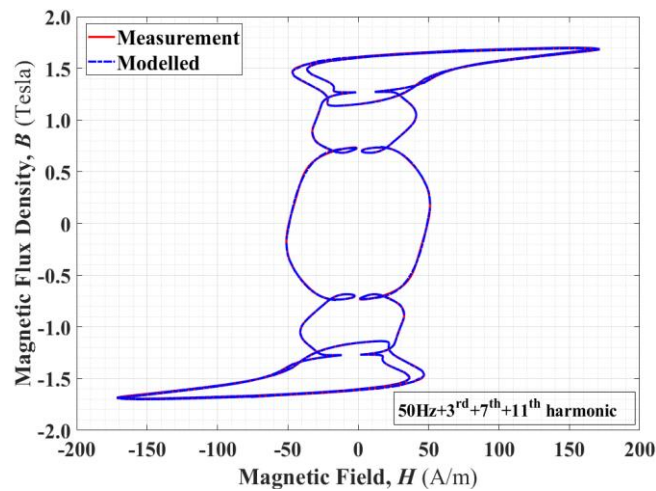


Fig. 6.25 Comparison of hysteresis loops for GOESs under non-sinusoidal excitation at a frequency of 50 Hz and peak flux density of 1.7 T with 3rd, 7th, and 11th harmonics.

6.4 Conclusions

In this chapter, the single equation model has been applied to calculate $B - h$ and $B - H$ curves under sinusoidal and non-sinusoidal excitation. This single equation was derived according to the magnetisation processes of different domain patterns in magnetic materials under sinusoidal excitation. The purpose of the derivation of this general physical model is to fill a technology gap for the modelling of the magnetisation of ferromagnetic materials. Compared to previous models for describing magnetic hysteresis loops, this single equation model is simple to implement and needs less calculation.

Normally, the application of a model is constrained by certain conditions, such as microstructures, magnetisation frequencies, and peak flux densities. This single equation

model is derived considering both anisotropic and isotropic structures; in addition, it is not limited by external conditions. So, it is suitable for modelling a variety of materials under a wide range of magnetisation conditions. The simulation of the magnetic properties of GOESs under non-sinusoidal excitation has proved that this new model is applicable in renewable energy systems for modelling the magnetic cores of transformers or other electromagnetic devices under non-sinusoidal excitation, such as harmonic and DC Bias excitation.

Chapter 7 Dynamic Modelling of Non-Oriented Electrical Steels

The magnetic properties of NOESs are almost the same in any magnetisation direction in the plane of the material because of the arbitrarily oriented grain directions. Nevertheless, just like GOESs, NOESs also contain anisotropic and isotropic domain patterns, so the novel analytical model introduced in Chapter 5 can also be applied to describe the magnetisation processes of NOESs. Intensive research has been conducted on the ability of the new model to simulate magnetic hysteresis loops and evaluate the energy losses in NOESs under sinusoidal magnetisation regimes. The new model is validated for Epstein size laminations of NOESs (3% SiFe) over a wide range of magnetisation frequencies and peak flux densities. Comparison between the modelling results and measurement data show that close agreement between them is reached with a maximum difference of less than 1.2 % between the calculated energy losses and experimental measurements. The new model is shown to be a generalised physical model based on its application to GOESs and NOESs.

7.1 Fitting the Model to the Measurement Data of NOESs collected using an SST

For both GOESs and NOESs, low energy loss and high permeability are the magnetic properties needed for machine design. These magnetic properties are determined by the microstructure, crystallographic structure, chemical composition, and mechanical conditions of the laminations in the magnetic core. The crystallographic structure is an essential factor in determining the magnetic properties of electrical steel because the magnetic permeability of ferromagnetic materials is closely linked to the orientation. GOESs have the best magnetic properties when magnetised in the rolling direction because the grains are oriented in the rolling direction, so the properties of GOES are dominated by the anisotropic components. Nonetheless, NOESs reveal identical magnetic properties regarding the magnetisation directions because the grains in NOES are randomly oriented rather than the rolling direction. So, the properties of NOESs are decided by the isotropic components. But there are anisotropic and isotropic structures in both GOESs and NOESs [104 - 107]. Both structures determine the magnetic properties in GOES and NOES laminates, so the model developed in chapter 5 can be applied to GOESs and NOESs in the same way.

First, the magnetic properties of NOESs were investigated using an SST measurement system. The measurement data of magnetic hysteresis and energy losses were collected at magnetisation frequencies ranging from 50 Hz to 800 Hz and peak flux densities ranging

from 1.0 T to 1.4 T. Choosing the appropriate equation is essential to simulate the hysteresis loops and calculate the energy losses fitting the model with the measurement data of the test materials according to the features of the hysteresis loops. The main advantage of equation (5.28) is it can be used to describe standard smooth sigmoidal curves. Nonetheless, the hysteresis loops measured at 400 Hz and 800 Hz using SST reveal somewhat distorted features. There are no existing models used directly to track the distorted curves, and it is a conundrum to generate distorted curves representing the hysteresis loop from the measurement data. Equation (5.30) is used to model the hysteresis loops at 400 Hz and 800 Hz through a piecewise method to tackle the issue caused by the figure distortion. Although it is intricate to process measurement data in a piecewise way, the relevant hysteresis loops can be created by connecting the section curves altogether to acquire the entire hysteresis loops to fit the experimental loops. The modelled energy loss can also be calculated by computing the integrals of the piecewise curves.

7.1.1 Modelling Results of NOESs for measurement data collected using an SST

The most important part of the new model is to fit the single equation with the measurement data of the test materials under different magnetisation conditions. As the main feature of the model is to describe the magnetisation processes, the main criterion to verify the model is to generate sigmoidal curves representing the hysteresis loop from measurement data. Although the model was derived to describe single curves of B versus h , the relevant hysteresis loops of B versus H can be obtained by manipulating the single curves to fit the experimental loops. These results can be achieved following the procedures described in chapter 5.

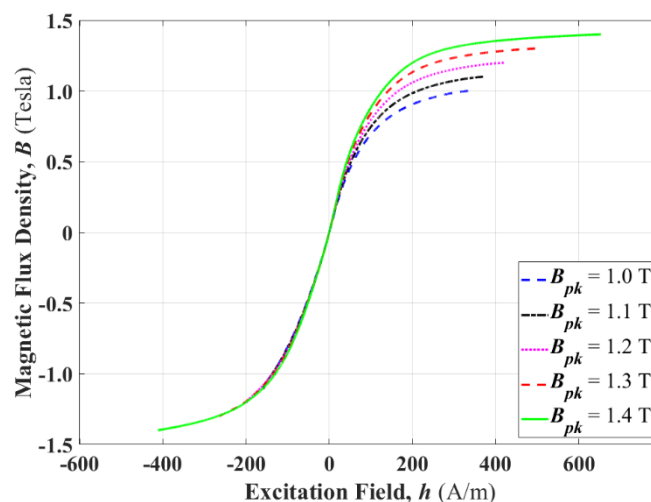


Fig. 7.1 Single Curves for NOESs under sinusoidal excitation at a frequency of 50 Hz and peak flux densities ranging from 1.0 T to 1.4 T.

Modelling the hysteresis loops with the new model comprises three main steps. In the first step, the curves of B versus h are derived from the measured hysteresis loops of B versus H . Then, the parameters of the single equation are calculated using MATLAB curve fitting tools to process the measurement data. Finally, the modelling results for the single curve and hysteresis loop are used for verification.

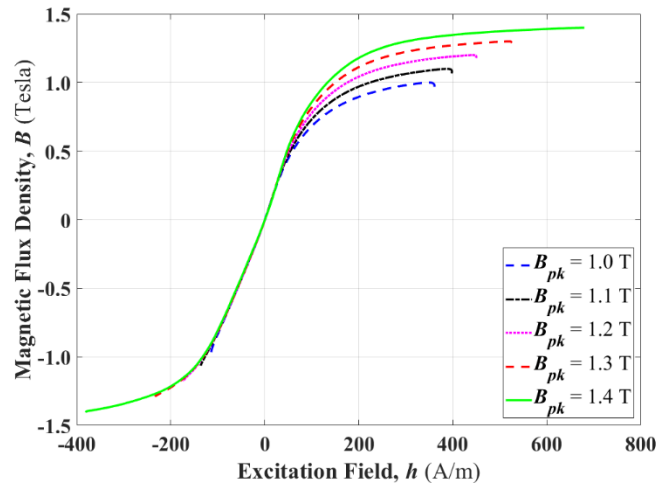


Fig. 7.2 Single Curves for NOESs under sinusoidal excitation at a frequency of 100 Hz and peak flux densities ranging from 1.0 T to 1.4 T.

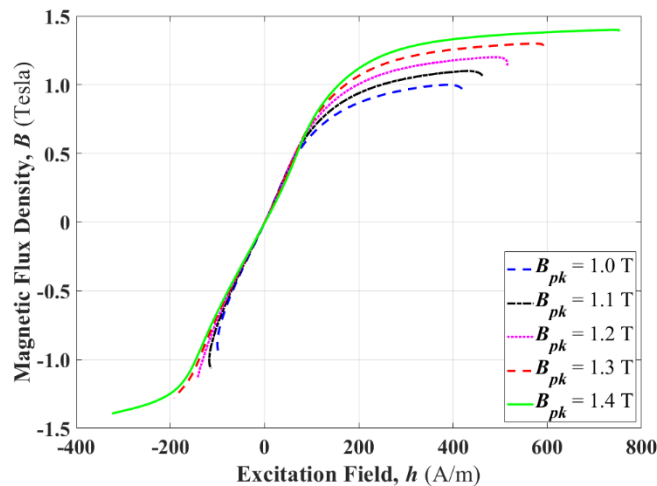


Fig. 7.3 Single Curves for NOESs under sinusoidal excitation at a frequency of 200 Hz and peak flux densities ranging from 1.0 T to 1.4 T.

As a first step, single curves of B versus h for NOESs were extracted from the measured magnetic hysteresis loops. The results for magnetisation frequencies from 50 Hz to 800 Hz and peak flux densities from 1.0 T to 1.4 T are shown in Figs. 7.1 to 7.5, respectively. For these curves, the sections with $h < 0$ represent the magnetisation processes, and the sections with $h > 0$ represent the demagnetisation processes. The parameters of these two curve sections need to be calculated separately due to the different magnetisation mechanisms.

One interesting finding from the single curves shown in Figs. 7.1 to 7.3 is that these single curves have similar shapes and pass through the origin. It is evident from the above figures that the new model can reproduce remarkably similar single curves. Next, the hysteresis loops of the test sample can be created using the new model for the range of magnetisation.

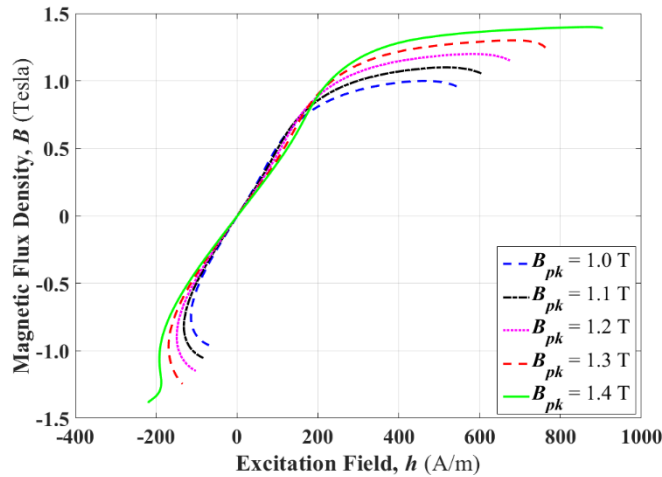


Fig. 7.4 Single Curves for NOESs under sinusoidal excitation at a frequency of 400 Hz and peak flux densities ranging from 1.0 T to 1.4 T.

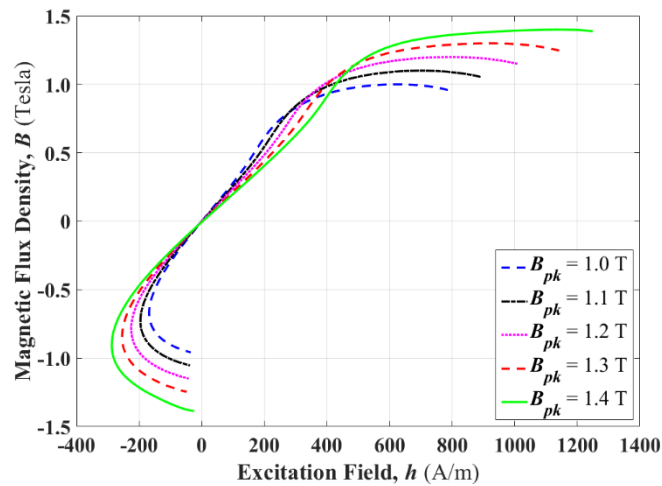


Fig. 7.5 Single Curves for NO steel under sinusoidal excitation at a frequency of 800 Hz and peak flux densities ranging from 1.0 T to 1.4 T.

As shown in Figs. 7.4 and 7.5, the single curves at 400 Hz and 800 Hz reveal somewhat curled tip sections, which reveals the asynchronous phenomena introduced by high frequencies with increased magnetic flux density and reduced magnetic field simultaneously. The enhancement of the magnetic flux density at the tips is supposed to be induced by the WMF when the magnetic field declines. When the excitation fields reach maximum values and start to reverse their directions, the magnetic flux densities are still increasing. It gives a sense that the flux densities go ahead of the excitation field.

These asynchronous phenomena caused by high frequencies make the calculation of parameters rather intricate, so the modelling of the single curves must be performed by fitting piecewise curves using equation (5.30). The parameters used in (5.30) must be calculated for each segment separately; the more segments used, the higher the accuracy of the model.

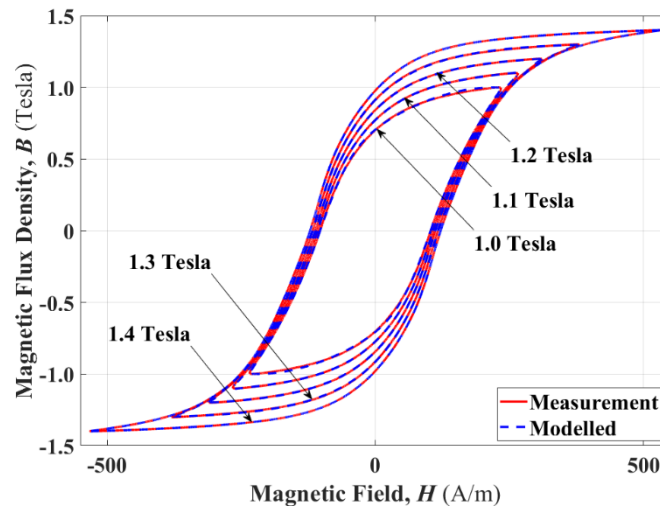


Fig. 7.6 Comparison of hysteresis loops for NOESs under sinusoidal excitation at 50 Hz and peak flux densities ranging from 1.0 T to 1.4 T.

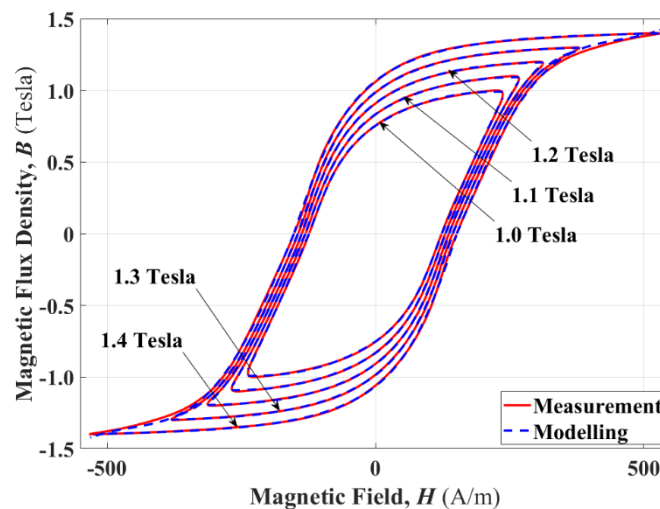


Fig. 7.7 Comparison of hysteresis loops for NOESs under sinusoidal excitation at 100 Hz and peak flux densities ranging from 1.0 T to 1.4 T.

Fig. 7.4 and 7.5 demonstrate the impact of sinusoidal excitation on single curves at various peak flux densities ranging from 1.0 T to 1.4 T and frequencies (400 Hz and 800 Hz). To obtain the best modelling results, for peak flux densities at 1.0 T, 1.1 T, 1.2 T, and 1.3 T, it is crucial to divide the demagnetising curve section into three sections and the magnetising curve section into six sections for the 400 Hz case. Similarly, for the 800 Hz scenario, dividing the demagnetising curve section into four sections and the magnetising curve section into six sections yields the best results. However, when dealing with a peak

flux density of 1.4 T, the approach needs to be adjusted. For the 400 Hz case, the demagnetising curve section should be divided into ten sections, and the magnetising curve section into five sections to achieve optimal results. On the other hand, for the 800 Hz case, even with the best efforts, the demagnetising curve section should be divided into three sections, and the magnetising curve section into three sections to attain the most accurate modelling results.

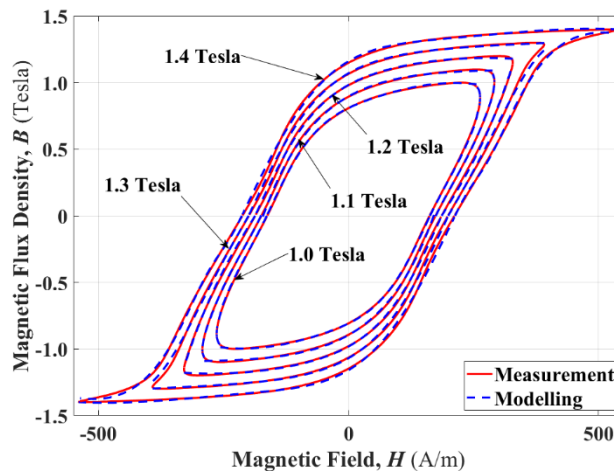


Fig. 7.8 Comparison of hysteresis loops for NOESs under sinusoidal excitation at 200 Hz and peak flux densities ranging from 1.0 T to 1.4 T.

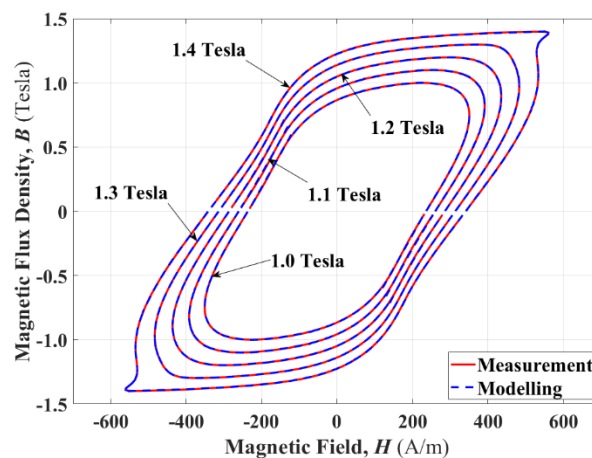


Fig. 7.9 Comparison of hysteresis loops for NOESs under sinusoidal excitation at 400 Hz and peak flux densities ranging from 1.0 T to 1.4 T.

The measured and calculated hysteresis loops at magnetisation frequencies of 50 Hz to 800 Hz and peak flux densities of 1.0 T to 1.4 T are shown in Figs. 7.6 to 7.10, respectively. The results indicate that the calculated loops are consistent with the measured hysteresis loops over the range of measurement frequency and magnetic flux density. The simple equation model links the macroscale features of the magnetic material with the microscale description of domain theories and validates the generalised physical model in this study. The new model is derived according to the magnetisation processes of the anisotropic and isotropic structures under external excitation, and all ferromagnetic

materials consist of anisotropic and isotropic components, so this new model is proven to be a general physical model suitable for interpreting the magnetic properties of all magnetic materials without needing to consider improvement and extension.

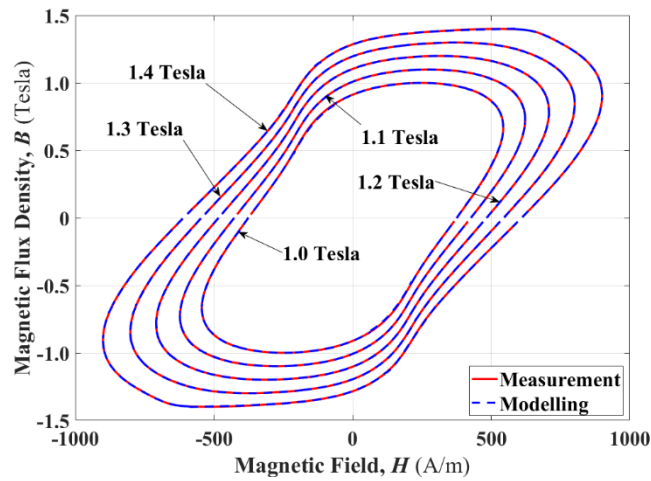


Fig. 7.10 Comparison of hysteresis loops for NOESs under sinusoidal excitation at 800 Hz and peak flux densities ranging from 1.0 T to 1.4 T.

7.1.2 Energy Losses Evaluation of NOESs

The new model can create the magnetic hysteresis loops of NOESs with remarkable accuracy. This model is also convenient for evaluating the energy losses using equations (6.3) and (6.4), which calculate the Zeeman energy between the excitation field and flux density.

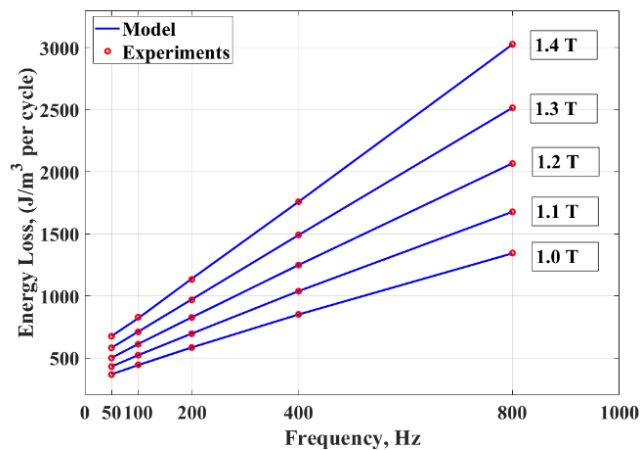


Fig. 7.11 Comparison between the calculated and measured energy losses per cycle for NOESs at frequencies from 50 Hz to 800 Hz and peak flux densities from 1.0 T to 1.4 T.

After the calculation of the parameters of the single equation, the total energy losses per cycle can be calculated by integrating the simple equation for a range of excitation fields. A comparison between calculated and measured results at magnetisation frequencies from 50 Hz to 800 Hz and the peak flux density of 1.0 T to 1.4 T is provided in

Fig. 7.11. Fig. 7.12 reveals a close agreement between the calculated and measured losses, with a maximum difference of less than 1 % for the range of magnetisation conditions.

Therefore, based on the single curves, the proposed new model provides an accurate and reliable means of generating hysteresis loops and calculating energy losses in the magnetic core of electromagnetic devices.

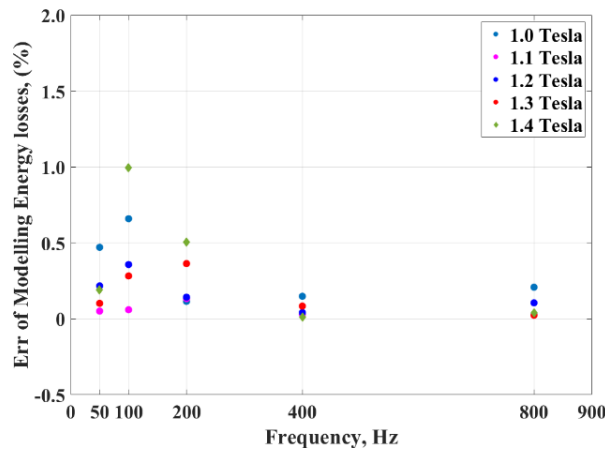


Fig. 7.12 Energy loss errors for NOESs under sinusoidal excitation at frequencies from 50 Hz to 800 Hz and peak flux densities from 1.0 T to 1.4 T.

7.2 Fitting the Model to the Measurement Data of NOESs collected using an Epstein Frame

The measurements were conducted using an Epstein frame for NOESs, covering magnetisation frequencies ranging from 50 Hz to 800 Hz and peak flux densities ranging from 1.0 T to 1.5 T. The collected measurement data of magnetic hysteresis and energy loss aimed to investigate the magnetic properties of the materials. Selecting the appropriate equation is crucial to effectively model the measurement data based on the characteristics of the hysteresis loops. The hysteresis loops measured at magnetisation frequencies from 50 Hz to 800 Hz using an Epstein frame exhibit somewhat distorted features. No existing models directly track these distorted curves, presenting a challenge in representing the hysteresis loops accurately from the measurement data. To address this, Equation (5.30) was employed to model the distorted hysteresis loops through a piecewise method. Though processing the measurement data in a piecewise manner can be intricate, connecting the section curves together allows us to reconstruct the entire hysteresis loops and fit them to the experimental loops. Additionally, using Equation (5.30), the energy losses can be calculated by computing the integrals of the piecewise curves.

7.2.1 Modelling Results of NOESs for measurement data collected using an Epstein Frame

The most important part of the new model is the fitting of the single equation (5.28) and (5.30) to the measurement data for the test materials under different magnetisation frequencies and peak flux densities. While a critical feature of the proposed model is to describe the magnetisation process, the main criterion for verifying the model is the generation of sigmoidal curves representing the hysteresis loop from the measurement data. Although the model was derived to yield single curves of B versus h , the relevant hysteresis loops of B versus H can be created by manipulating the curves to fit the experimental loops.

The procedures for obtaining hysteresis loops with the new model follow the method described in section 5.4. The parameters of the equation (5.28) and (5.30) are calculated using the MATLAB fitting tool to process the measurement data. Finally, the modelling results for the single curves and hysteresis loops are generated for comparison with experimental results.

The single curves for B versus h of NOESs are derived from the magnetic hysteresis loops measured using an Epstein frame. The single curves for the magnetisation frequencies of 50 Hz to 800 Hz and peak flux densities of 1.0 T to 1.5 T are shown in Figs. 7.13 to 7.17, respectively. These single curves are separated at zero flux density. The magnetisation processes occur for $h < 0$, and demagnetising processes happen for $h > 0$. The corresponding parameters of the model for the two processes are different, and hence the calculations must be performed separately. As shown in the figures, the single curves exhibit some distortion features, which makes the calculation difficult, so the modelling of the single curves must be done by fitting piecewise curves.

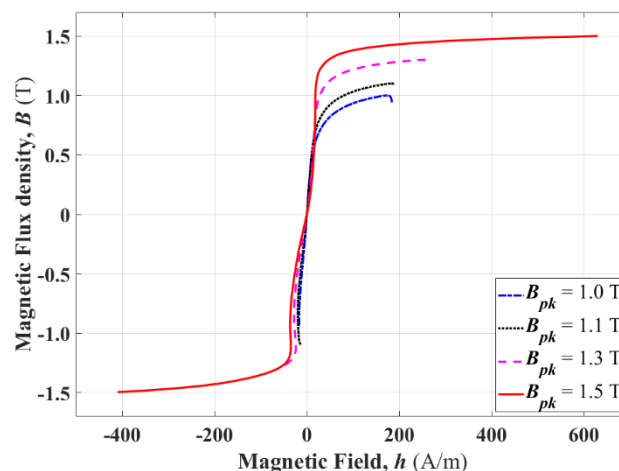


Fig. 7.13 Single Curves for NOESs under sinusoidal excitation at a frequency of 50 Hz and peak flux densities ranging from 1.0 T to 1.5 T.

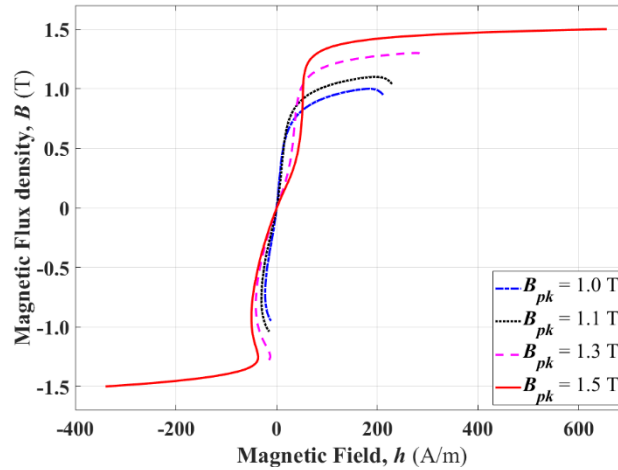


Fig. 7.14 Single Curves for NOESs under sinusoidal excitation at a frequency of 100 Hz and peak flux densities ranging from 1.0 T to 1.5 T.

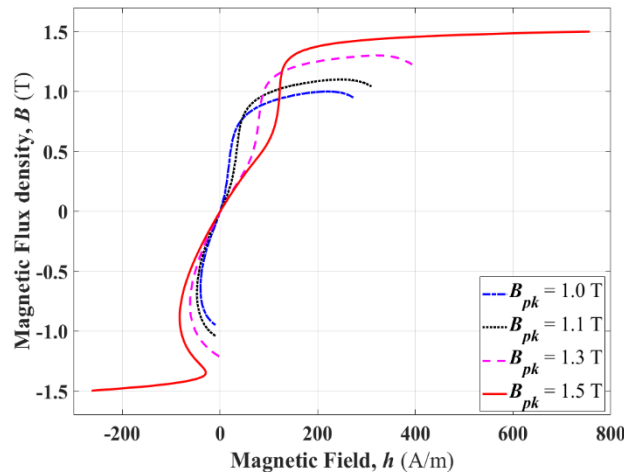


Fig. 7.15 Single Curves for NOESs under sinusoidal excitation at a frequency of 200 Hz and peak flux densities ranging from 1.0 T to 1.5 T.

One interesting finding from the single curves is that they have a similar shape and pass through the origin, which means that the excitation field is synchronised with the magnetic flux density. This model dramatically simplifies the investigation of magnetic properties compared to the studying of the $B - H$ loops directly. It is noticed that some single curves have curled tips caused by high frequency and low magnetic flux density. This phenomenon can be addressed using the piecewise method to achieve a one-to-one correspondence relationship.

Fig. 7.13 to 7.17 illustrate the impact of sinusoidal excitation on single curves at various peak flux densities ranging from 1.0 T to 1.5 T, and frequencies ranging from 50 Hz - 800 Hz. To achieve the best modelling results, it is essential to adopt different approaches for each scenario. For the 50 Hz and 100 Hz cases, as shown in Fig. 7.13 and 7.14, respectively, dividing both the demagnetising curve section and the magnetising curve section into

three sections is the optimal choice. In the 200 Hz scenario, depicted in Fig. 7.15, the best results are obtained by dividing both the demagnetising curve section and the magnetising curve section into four sections. However, when dealing with 400 Hz, as shown in Fig. 7.16, the approach needs to be adjusted based on the peak flux densities. For 400 Hz and peak flux densities at 1.0 T, 1.1 T, and 1.3 T, the demagnetising curve section should be divided into four sections, while the magnetising curve section can be modelled directly without further division. For 400 Hz and peak flux densities at 1.5 T, the demagnetising curve section should be divided into six sections, and the magnetising curve section can be separated into three sections. In the case of 800 Hz and peak flux densities at 1.5 T, as presented in Fig. 7.17, the demagnetising curve section should be divided into six sections, and the magnetising curve section should be divided into three sections. For the remaining single curves, the demagnetising curve section can be divided into four sections, while the magnetising curve section can be modelled directly without further division.

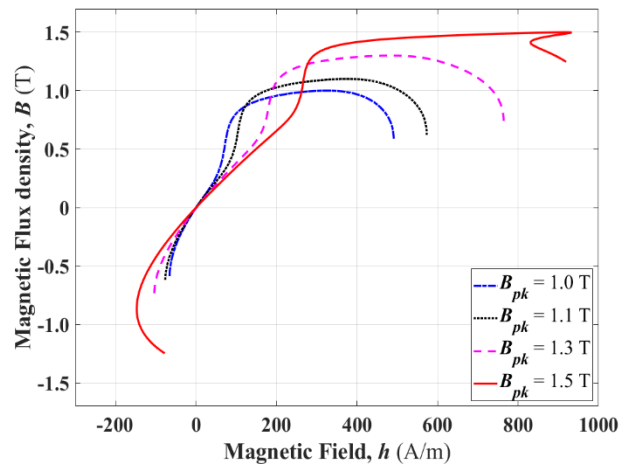


Fig. 7.16 Single Curves for NOESs under sinusoidal excitation at a frequency of 400 Hz and peak flux densities ranging from 1.0 T to 1.5 T.

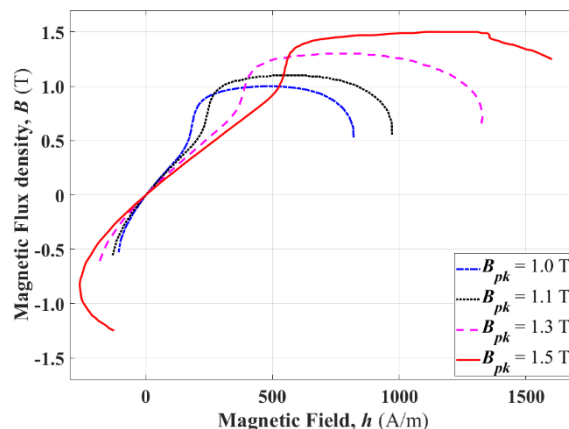


Fig. 7.17 Single Curves for NOESs under sinusoidal excitation at a frequency of 800 Hz and peak flux densities ranging from 1.0 T to 1.5 T.

Based on the provided description, it becomes evident that modelling single curves measured from the Epstein frame is significantly more complex compared to those measured using SST. For instance, at frequencies like 50 Hz and 100 Hz, single curves from SST can be modelled with just magnetizing and demagnetizing curve sections. In contrast, single curves from the Epstein frame require division into three distinct sections for both magnetizing and demagnetizing processes. However, at higher magnetization frequencies, both the single curves from the Epstein frame and SST necessitate more divisions when employing the single equation model for modelling.

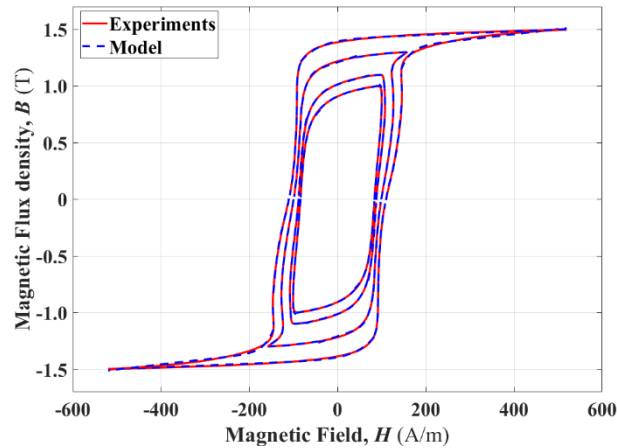


Fig. 7.18 Comparison of hysteresis loops for NOESs under sinusoidal excitation at 50 Hz and peak flux densities ranging from 1.0 T to 1.5 T.

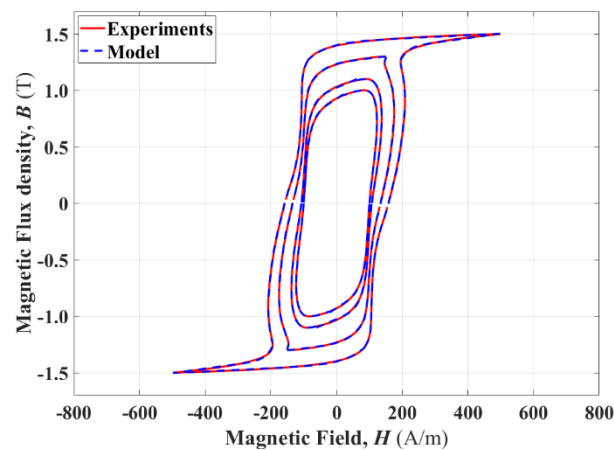


Fig. 7.19 Comparison of hysteresis loops for NOESs under sinusoidal excitation at 100 Hz and peak flux densities ranging from 1.0 T to 1.5 T.

The simplified equation (5.30) can be regarded as the representation of numerous magnetic domains. The parameters calculated for piecewise curves are different, and hence the calculations need to be performed individually. The segmented curves are separated according to the distortion extent of the curve to achieve piecewise monotonicity so that the segmented curves are all one-to-one functions in terms of excitation field versus magnetic flux density. Then, the parameters of each segmented

curve can be obtained by fitting the relevant measurement data with the simplified equation (5.30).

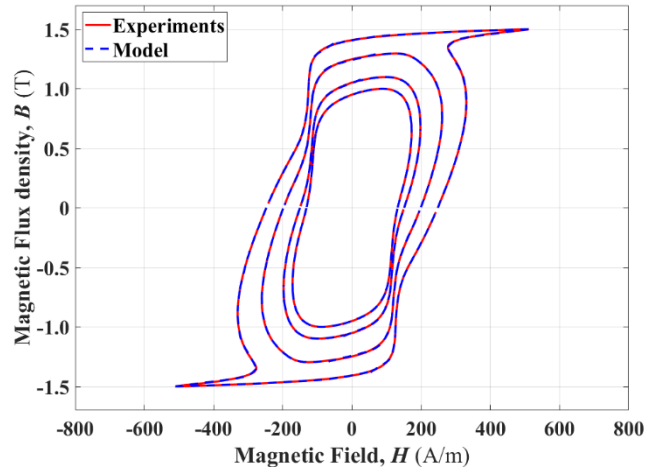


Fig. 7.20 Comparison of hysteresis loops for NOESs under sinusoidal excitation at 200 Hz and peak flux densities ranging from 1.0 T to 1.5 T.

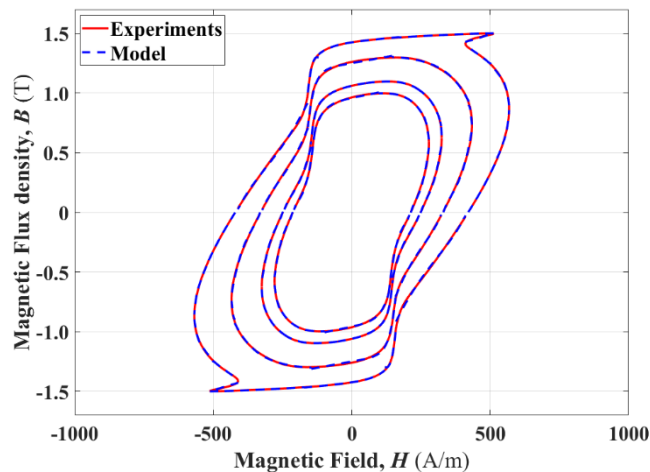


Fig. 7.21 Comparison of hysteresis loops for NOESs under sinusoidal excitation at 400 Hz and peak flux densities ranging from 1.0 T to 1.5 T.

The magnetic hysteresis loops of NOESs are modelled by combining all piecewise curves produced using the simplified equation for the range of magnetisation. The measured and calculated magnetic hysteresis loops at magnetisation frequencies of 50 Hz to 800 Hz and peak flux densities of 1.0 T to 1.5 T are shown in Figs. 7.18 to 7.22, respectively. The result reveals that the modelled magnetic hysteresis loops show remarkably good agreement with the measured loops for the range of measured frequency and magnetic flux density.

The simple equations (5.28) and (5.30), derived based on domain theories, have been shown to model the magnetic hysteresis loops of NOESs measured using an Epstein frame. This investigation of magnetic hysteresis loops validates the generalised physical

model for ferromagnetic materials. Hence, this new model can be potentially used to model other types of magnetic materials under a variety of magnetisation conditions.

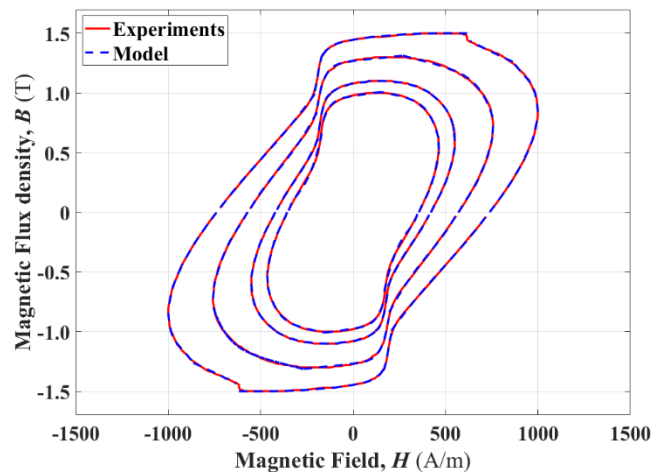


Fig. 7.22 Comparison of hysteresis loops for NOESs under sinusoidal excitation at 800 Hz and peak flux densities ranging from 1.0 T to 1.5 T.

7.2.2 Energy Losses Evaluation of NOESs

The total energy losses per cycle can be calculated using equations (6.3) and (6.4) with the calculated parameters in the range of the excitation field. A comparison between the calculated and measured energy losses at the magnetisation frequencies of 50 Hz to 800 Hz and the peak flux density from 1.0 T to 1.5 T is provided in Fig. 7.23. The error of calculated vs measured energy losses is shown in Fig. 7.24.

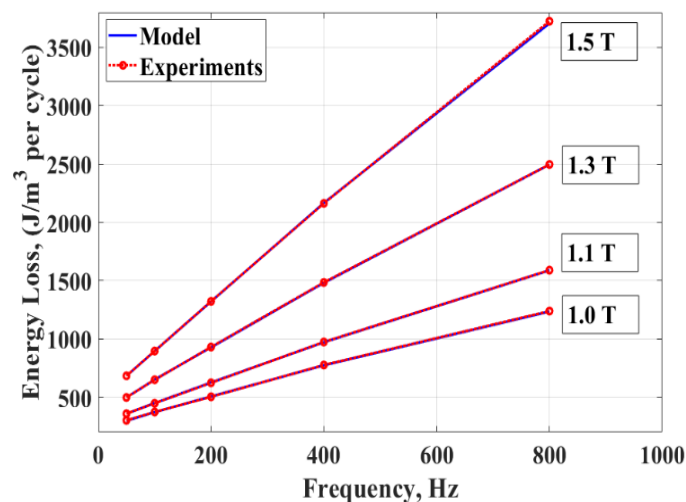


Fig. 7.23 Comparison between calculated and measured energy losses per cycle for NOESs under sinusoidal excitation at frequencies of 50 Hz to 800 Hz and peak flux densities ranging from 1.0 T to 1.5 T.

It is evident from Fig. 7.23 that the calculated energy losses using (6.3) and (6.4) provide a striking similarity compared to the measured energy losses using the Epstein frame. Fig. 7.24 shows close agreement between the calculated and measured losses, with an average error of less than 1.2 % for the range of measurement. Therefore, not only does the new model provide an accurate and reliable technique for generating magnetic hysteresis loops of NOESs, but it can calculate the energy losses with remarkable accuracy as well.

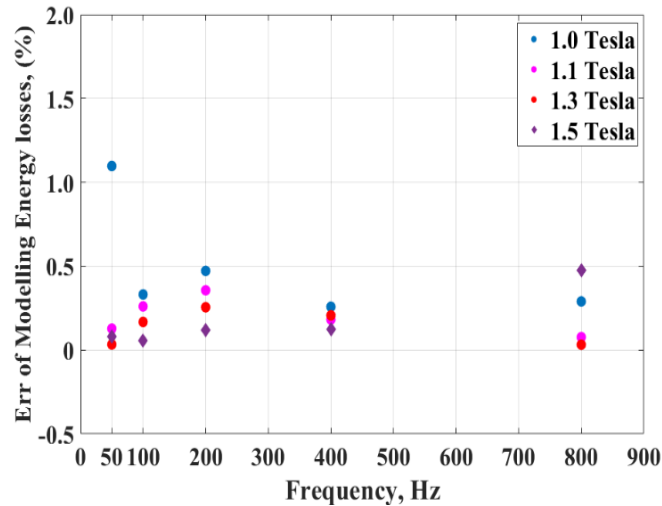


Fig. 7.24 Energy loss errors for NOESs under sinusoidal excitation at frequencies of 50 Hz to 800 Hz and peak flux densities ranging from 1.0 T to 1.5 T.

7.3 Conclusions

In this chapter, the single equation model has been utilized to calculate $B - h$ curves and then convert them to the $B - H$ loops. The purpose of the derivation of this general physical model is to fill a technology gap for the modelling of magnetisation processes of ferromagnetic materials for both GOESs and NOESs. Previous models for describing magnetic hysteresis loops are complicated regarding their application, and there are no other single equation models available with a robust physical underpinning to deal with both magnetic materials.

The simulation of experimental results for the magnetic hysteresis and energy losses in NOESs presented in this chapter shows that the proposed general physical model provides a reliable tool for exploring the connection between the magnetic hysteresis loops and the microstructure of NOESs. The single equation model was derived according to the domain patterns in GOESs, which represent the different microstructures, i.e., isotropic and anisotropic domains. NOESs consist of these two microstructures, too, so the hysteresis loops and loss curves at different frequencies and peak flux densities can be modelled with excellent agreement using equations (5.28), (5.30), (6.3), and (6.4).

Chapter 8 A novel energy loss separation model of ferromagnetism

Energy loss evaluation is essential to understand the energy loss mechanisms associated with the magnetisation of GOESs and NOESs, which in turn facilitates improvement of the quality and efficiency of power transformers, generators, and motors. In this chapter, a novel separation principle of energy loss in GOES and NOES is proposed, based on analysing the magnetisation processes from the perspective of microscopic structures. Unlike previous energy loss separation models (ELSMs), the magnetisation process is described as a physical mechanism intertwined with the magnetic field, hysteresis field, and eddy current counter field. The magnetisation field is the compound field of the above three fields generated during magnetisation. The new ELSM is developed in line with Maxwell's equations and the Zeeman effect. Calculations of energy loss using the model reveal the ratio of the calculated energy loss components. The model is analysed for Epstein size laminations of 3 % SiFe GOES at magnetisation frequencies 50 Hz and 100 Hz and peak flux densities ranging from 1.0 T to 1.7 T, and for 3 % SiFe NOES at magnetisation frequencies 50 Hz and 100 Hz and peak flux densities ranging from 1.0 T to 1.4 T. Furthermore, the energy loss components calculated using the model are visualised to reveal their features.

The original contribution made here is to introduce a new separation principle to estimate the energy loss components for GOESs and NOESs by seeking the individual physical meaning for the components by analysing the microscopic structure variation under external magnetic excitation. The model encapsulates the fundamental physics of magnetics and micromagnetics concerning electron motion, atomic magnetic moment, domain wall movement, domain rotation, domain nucleation, and domain annihilation.

8.1 New Energy loss Separation Model derivation

Magnetic hysteresis occurs during the magnetisation of ferromagnetic materials under external magnetic excitation. The magnetisation of a typical GOES, at magnetisation frequency of 50 Hz and peak flux density of 1.7 T, is shown in Fig. 8.1, and that of a typical NOES, for the same frequency with a peak flux density of 1.4 T, is shown in Fig. 8.2. Suppose the materials are magnetised from a demagnetised state, where the samples are in multi-domain status having the most domain walls. When an increasing magnetic field is applied, the magnetisation begins with a corresponding change in the domain structure. The introduced time-varying magnetic flux density generates an eddy current which creates an eddy current field opposite to the magnetic field direction to counteract the magnetisation process.

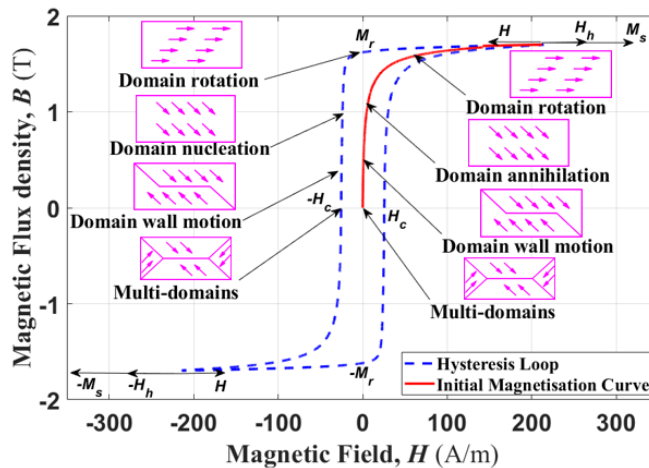


Fig. 8.1 The magnetisation of GOES.

The magnetisation force is the field remaining once the magnetic field has overcome the eddy current field. The magnetisation field pushes the domain walls so that the domains aligned with the magnetic field become bigger, and those in the opposite direction grow smaller. When the domain walls are removed, the whole steel sheet becomes a single domain aligned with the crystallographic axes [8]. Increasing the magnetic field finally prevails over the anisotropic energy and turns the single domain toward the magnetic field direction. This domain rotation raises the material to saturation level in the direction of the magnetic field. No hysteresis occurs during this initial magnetisation, but domain wall movement and domain rotation are fully engaged.

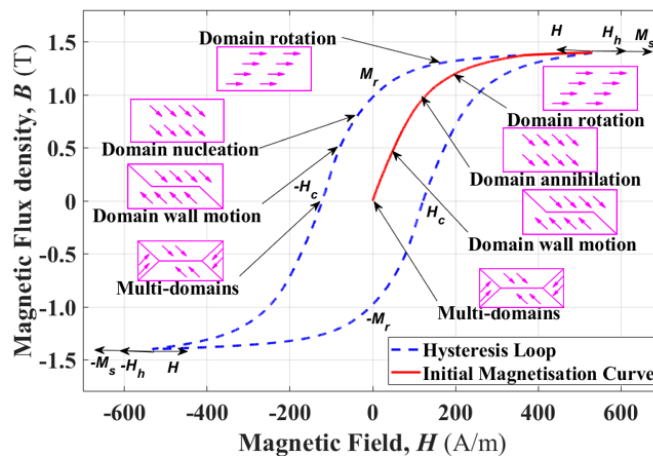


Fig. 8.2 The magnetisation of NOES.

At the saturation tip, all the atomic dipoles are paralleled to the magnetisation direction, so that magnetisation reaches a maximum. If the excitation field is switched off, the atomic dipoles will be partially aligned in the magnetisation direction; the material will stay in a magnetised state, and the remaining magnetisation is called remanence. However, if the magnetic field direction is reversed, the magnetic flux density undergoes demagnetisation. When the magnetic field decreases to zero, the magnetic flux density has a positive value named remanent magnetisation or retentivity B_r . The magnetic field is named coercivity or coercive force H_c when the magnetic flux density is zero. Magnetic

hysteresis occurs from the saturation tip to the coercivity. Demagnetisation is the opposite of the initial magnetisation process, so domain wall motion, domain rotation, eddy current, pinning site effect, and impurity influence act oppositely but under the exact same physical mechanism.

At the saturation tip, all the atomic dipoles in the samples are aligned with the magnetic field direction, exerting a strong effect on the magnetic field. It is for this reason the author assumed in Chapter 4, see also [118], that there is a magnetic force generated from the coupling effect of the magnetisation at the reversal turning point that needs to be overcome for the reversal magnetisation process to continue. This force is named the hysteresis field H_h , and is equal to the coercivity H_c , which reduces B to zero. Accordingly, the hysteresis field can be considered as a DC component during magnetisation, which generates a magnetic field with a coercivity value to counteract a part of the magnetic field from the excitation source when demagnetisation starts from the reversal turning point.

Because the direction of the hysteresis field H_h is opposite to the reversed magnetic field H , the hysteresis field at the positive tip can be expressed as:

$$H_h = H_c. \quad (8.5)$$

As illustrated in Fig. 8.3, magnetisation is governed by the atomic dipoles in ferromagnetic materials, with the moment of the atomic dipoles evaluated according to the microscopic eddy current due to electron motion around the atomic nucleus. Magnetisation results by changing the direction of the atomic moment changes through the domain wall movement and domain rotation. The force required to transfer the domain wall and rotate the domain moment is the magnetisation field, and another force required to move the electrons between atoms is the eddy current field. The magnetisation field can be calculated from the magnetic field by subtracting the hysteresis field and eddy current counter field as such the magnetisation process can be described via the following expression:

$$H = H_h + H_e + H_m \quad (8.6)$$

where H_e is the eddy current counter field, and H_m is the magnetisation field which is the main magnetisation force contributing to the magnetisation processes. At the origin, there is no coupling effect for the demagnetised condition, so, H_h is equal to zero; that is why there is no hysteresis on the initial magnetisation curve.

Equation (8.6) is a vector expression. The magnetic field, measured by instruments, from the excitation source is an externally manifested magnetic field, which is used to excite the steel sheets. So, the magnetic field represents the total field force from the excitation source required to undertake the magnetisation processes and cause the total magnetic core loss.

The fundamental physical interpretation of core loss is expressed as the Zeeman energy formed by the magnetic field and magnetic flux density. Hence, the energy loss per cycle in a thin sheet under sinusoidal excitation can be found by calculating the area of the hysteresis loop, which can be expressed as [88]:

$$W_t = \int B dH = \int H dB. \quad (8.7)$$

The magnetic loss in the core material is due to three field components on the left-hand side of (8.6). Substituting H from (8.7) into (8.6) yields:

$$W_t = \int H_h dB + \int H_e dB + \int H_m dB, \quad (8.8)$$

showing that the energy loss can be divided proportionately based on the Zeeman energy of three field components, namely hysteresis loss, eddy current loss, and magnetisation loss. Therefore, the total energy loss is described as:

$$W_t = W_h + W_e + W_m. \quad (8.9)$$

The magnetisation loss is caused by the magnetisation field pushing domain walls to implement the magnetisation process.

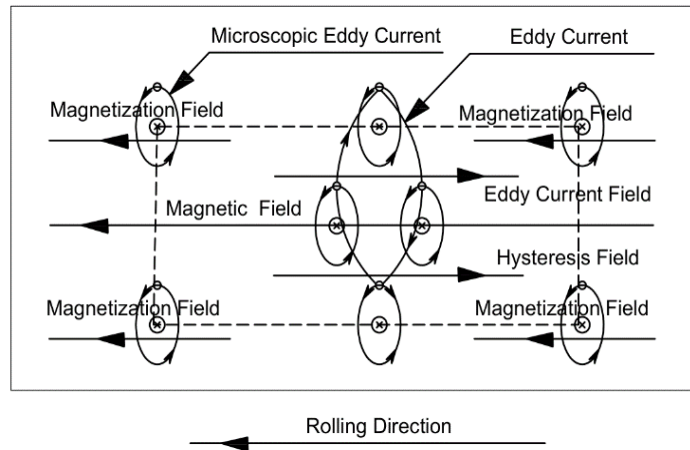


Fig. 8.3 Magnetisation process intertwined with the magnetic field, hysteresis field, magnetisation field and eddy current field.

As shown in Fig. 8.1 and 8.2, when the initial magnetisation curves approach the tip of magnetisation B_s , the magnetic field and magnetisation change direction at the reversal turning point. The excitation source must contribute more energy to compensate for the coupling effect of the magnetisation. The hysteresis field and the magnetisation will form Zeeman energy to determine the hysteresis energy needed to be compensated for to continue the reversal magnetisation process. In which case, the hysteresis energy can be expressed as:

$$W_h = 2H_h B_{pk} = 2H_c B_{pk}, \quad (8.10)$$

where B_{pk} is the peak flux density at any order reversal turning point, and B_{pk} is equal to B_s at saturation tips. The hysteresis energy loss can be deemed as the energy created by the DC component, which generates a magnetic field with a coercivity value.

After compensating for the hysteresis energy, the magnetic field reverses its direction and changes the status from magnetisation to demagnetisation. If the magnetisation tip is in saturated status, the magnetic field must release the anisotropy force to turn the atomic magnetic moments back to the easy direction. Afterwards, the single domain in the materials will encounter domain nucleation and form a multi-domain structure. Consequently, the energy consumed in these processes and the domain wall motions constitute another magnetisation energy part. The domain wall motions will then change the orbit of microscopic eddy currents so as to change the atomic moment directions. Accordingly, this part of magnetisation loss can be termed microscopic eddy current loss, which is the energy needed to move the domain walls and rotate the domain moments to achieve the Zeeman energy at the tips.

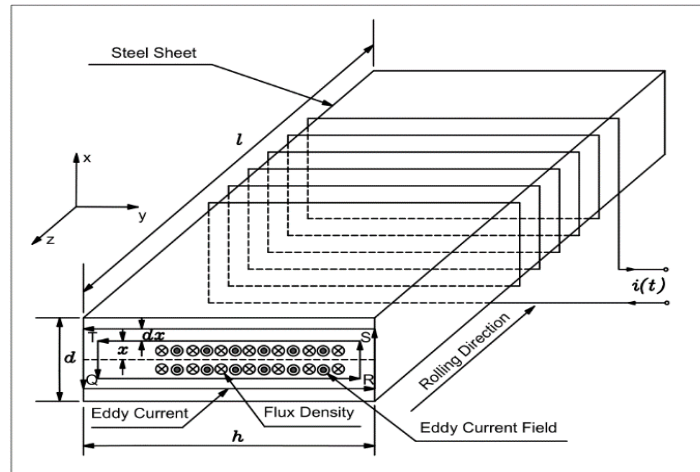


Fig. 8.4 Eddy current and related field.

As shown in Fig. 8.4, under an external sinusoidal excitation, the dynamic behaviour of an electrical steel sheet results from several interweaving phenomena: eddy current, saturation, remanence, and hysteresis. Under a controlled excitation waveform, the sinusoidal magnetic flux density is obtained and expressed via the following equation:

$$B(t) = B_{pk} \sin(\omega t). \quad (8.11)$$

A small, closed eddy current loop path QRSTQ is considered to derive the eddy current field, as shown in Fig. 8.4. The distance of the path from the origin is x , and the thickness of the path is dx . Voltage is induced in this closed loop by the varying magnetic flux density like the induced voltage in a single turn coil. Then, according to Faraday's law of induction and Lenz's law, the following equations are obtained:

$$E = -2\pi f B_{pk} A \cos(\omega t). \quad (8.12)$$

Since the height of the sheet is far greater than its thickness, the x dimension can be neglected, then the resistance of the eddy current path is given by:

$$R = \frac{2\rho h}{ldx}. \quad (8.13)$$

The eddy current of the closed path can be calculated from:

$$di_e = -\frac{2\pi f B_{pk} l \cos(\omega t) x dx}{\rho}. \quad (8.14)$$

then,

$$dH_e = -\frac{4\pi f B_{pk} l h \cos(\omega t) x^2 dx}{\rho}. \quad (8.15)$$

By considering the geometry of the sheets and the distribution of the field, the eddy current field can be calculated by integrating equation (8.15) from 0 to $d/2$, giving:

$$H_e = -\frac{4\pi f B_{pk} l h \cos(\omega t)}{\rho} \int_0^{d/2} x^2 dx, \quad (8.16)$$

and ultimately:

$$H_e = -\frac{\pi f B_{pk} d^2 \cos(\omega t)}{6\rho} (dhl). \quad (8.17)$$

In terms of the effective eddy current field energy per volume, this leads to:

$$\frac{H_e}{\pi f B_{pk} d^2 / 6\rho} = -\cos(\omega t). \quad (8.18)$$

Using the trigonometric identity $\sin^2 + \cos^2 = 1$, results in the following expression when equations (8.11) and (8.18) are combined:

$$\left(\frac{H_e}{\frac{\pi f B_{pk} d^2}{6\rho}} \right)^2 + \left(\frac{B}{B_{pk}} \right)^2 = 1, \quad (8.19)$$

revealing that the eddy current field has an elliptic form in terms of magnetic flux density with its centre located at the origin. The Zeeman energy of the eddy current field is obtained by calculating the area of the ellipse,

$$W_e = \int H_e dB = \frac{\pi^2 d^2 f B_{pk}^2}{6\rho}. \quad (8.20)$$

The eddy current loss per unit volume is a function of frequency and peak flux density, and the direction of the field caused by the eddy current is always opposite the direction of magnetic flux density and magnetisation field. It is worth noting that (8.20) is the well-known formula for the classical eddy current loss [29]. This equation is valid only for the case of low frequencies where magnetisation does not result in the skin effect.

As a summary of above analysis, we can conclude that:

- Magnetisation loss is the energy needed to move the domain walls and rotate the domain moments.

- The annihilation and nucleation of the magnetic domains during magnetisation results in a great proportion of magnetisation loss.
- Magnetisation loss is concerned with the microscopic eddy current loss, which is the energy consumed by the magnetic field rotating atomic dipoles to align them with the field.

The magnetisation field loop can be simulated using the new model proposed in [118] and expressed as follows:

$$B = M_{sa} \tanh(ah_m) + M_{si} L(bh_m) + \alpha h_m. \quad (8.21)$$

Then, the magnetisation loss can be calculated as follows:

$$W_m = 2 \int B dh_m = 2 \int (M_{sa} \tanh(ah_m) + M_{si} L(bh_m) + \alpha h_m) dh_m. \quad (8.22)$$

The methods for simulating the magnetization field hysteresis loop and calculating the magnetization loss component can utilize the same techniques employed in processing the measured hysteresis loop, as described in sections 5.4 and 6.2.

This ELSM is different from previous one [1, 7], which named the difference between the dynamic modelling and the measured loss as the anomalous excess loss, whose physical grounds have not been ascertained yet. The new separation model for magnetic core loss represents theoretically three effects: hysteresis, eddy current, and magnetisation process.

8.2 Energy loss modelling for GOESs

The new ELSM is applicable for low magnetisation frequencies in the absence of the skin effect. To verify the model, equations (8.10), (8.20), and (8.22) are used to calculate the loss components in GOESs for the magnetisation frequencies at 50 Hz and 100 Hz, and peak flux densities ranging from 1.0 T to 1.7 T; the loss components and their proportions are calculated accordingly. There are two ways to calculate the magnetisation loss. One way is to calculate the magnetisation field first according to (8.6), then to calculate the magnetisation loss based on (8.22); the other is to calculate the hysteresis loss and eddy current loss first, then to calculate the difference between the measured total loss and calculated loss components according to equation (8.9).

To explore the property of field components, the case of a controlled sinusoidal flux density of a GOES is considered at a magnetisation frequency of 50 Hz and peak flux density of 1.7 T. The magnetisation field is calculated by subtracting the hysteresis field and eddy current field from the measured magnetic field. The resulting magnetic field, magnetic flux density, and field components are shown in Fig. 8.5, with the corresponding measured loop and calculated component loops are provided in Fig. 8.6.

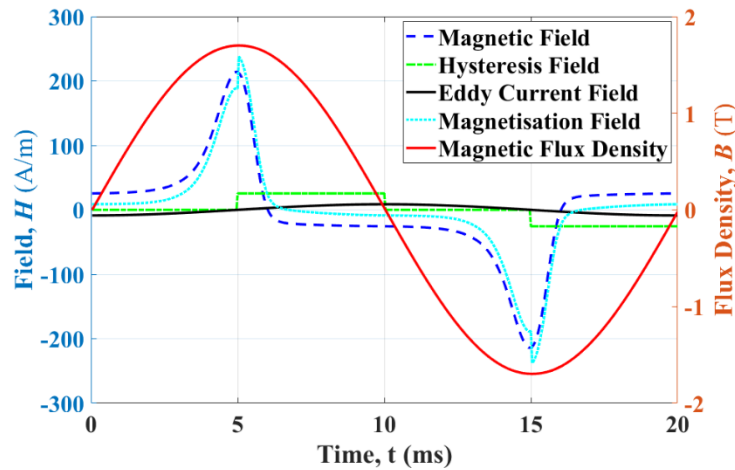


Fig. 8.5 Magnetic field components calculated for a GOES magnetised at a frequency of 50 Hz and peak flux density of 1.7 T.

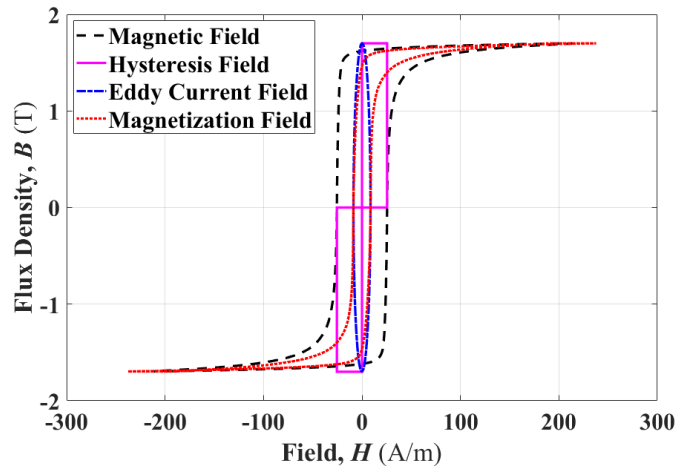


Fig. 8.6 Hysteresis loops based on magnetic field components calculated for a GOES at a frequency 50 Hz and peak flux density of 1.7 T.

The ellipse created by the eddy current field and magnetic flux density has the same transverse axis as the B -axis and its conjugate axis as the H -axis. The magnetisation field generates a narrow hysteresis loop with the coercivities located at the end vertices of the ellipse's minor axis created by the eddy current field. The H_c in the magnetisation field hysteresis loop is equal to its conjugate axis's eddy current counter field, which means the eddy current counter field has its maximum value when magnetic flux density is zero.

In accordance with the above analysis, prediction of the energy loss per cycle in the electrical steel takes the form of equation (8.9). The parameters required for equations (8.10) and (8.20) can be found in the manufacturer's datasheet and relevant measurement data, so it is very straightforward to calculate the relevant energy loss components. Nonetheless, the calculation of magnetisation loss based on (8.22) must be

done by processing the relevant measurement data, then with the magnetisation loss evaluated by calculating the area bounded by the magnetisation field loop.

Fig. 8.7 shows the energy loss components calculated for typical GOESs magnetised at 50 Hz and peak flux density ranging from 1.0 T to 1.7 T. The loss components percentages shown in Fig. 8.8 are calculated according to the results shown in Fig. 8.7. It can be seen that the total loss and individual components increase in tandem with an increase of the peak flux density; the magnetisation loss increases dramatically, which can also be seen from TAB. 8.1 in that the magnetisation loss increases from 6.94 J/m³ per cycle at 1.0 T to 68.92 J/m³ per cycle at 1.7 T, with the corresponding proportional loss increasing from 12.22% at 1.0 T to 34.13% at 1.7 T.

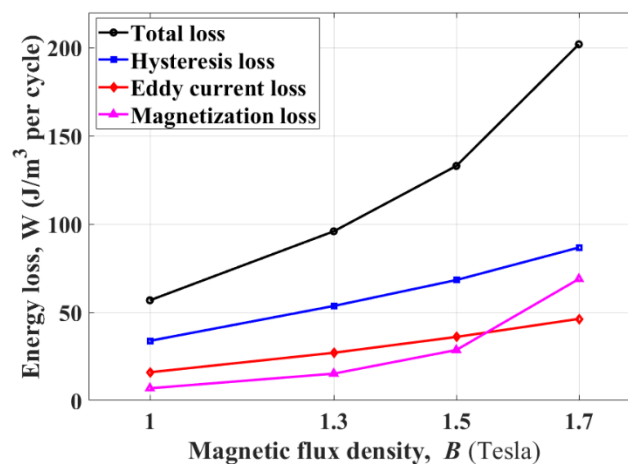


Fig. 8.7 Energy loss components per cycle calculated for GOESs magnetised at frequency 50 Hz and peak flux densities from 1.0 T to 1.7 T.

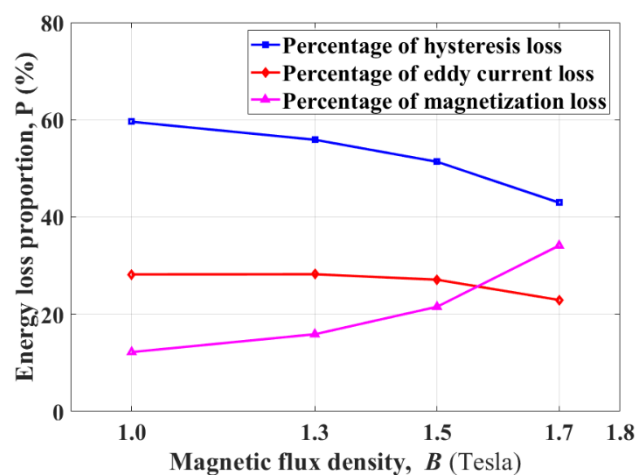


Fig. 8.8 Energy loss component per cycle proportions calculated for GOESs magnetised at frequency 50 Hz and peak flux densities from 1.0 T to 1.7 T.

The increasing magnetisation loss with peak flux density can be explained by domain theory, in that the higher the peak flux density the more domain wall movement is

needed, and more energy is needed to move the domain walls. Especially at 1.7 T, more energy is needed to rotate the domain moment to the magnetic field direction. The eddy current loss increases gradually, calculated according to (8.20), as can be seen in Fig. 8.7, but the proportions account for around 22% - 28%, as shown in TAB. 8.1.

Table 8.1 Energy loss components per cycle calculated for GOESs magnetised at frequency 50 Hz and peak flux densities from 1.0 T to 1.7 T.

B_{pk} (T)	W_t (J/m ³)	W_h (J/m ³)	W_e (J/m ³)	W_m (J/m ³)	P_h (%)	P_e (%)	P_m (%)
1.0	56.82	33.86	16.02	6.94	59.59	28.20	12.22
1.3	95.93	53.61	27.08	15.24	55.89	28.23	15.89
1.5	133.00	68.31	36.05	28.64	51.36	27.10	21.54
1.7	201.96	86.73	46.30	68.92	42.95	22.93	34.13

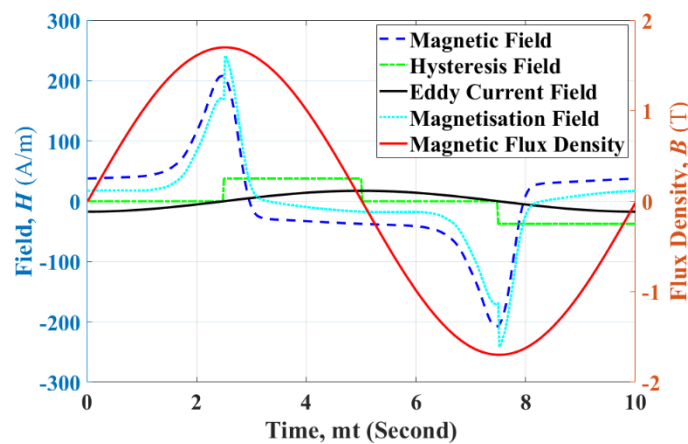


Fig. 8.9 Magnetic field components calculated for GOESs magnetised at frequency 100 Hz and peak flux density 1.7 T.

Fig. 8.9 shows the field components calculated from the measurements for GOESs at a magnetisation frequency of 100 Hz and peak flux density of 1.7 T. The corresponding measured loop and modelled component loops are shown in Fig. 8.10. Like the case of a magnetisation frequency of 50 Hz, the ellipse of the eddy current field and magnetic flux density has the transverse axis as the B -axis and its conjugate axis as the H -axis. The magnetisation field generates a narrow hysteresis loop, and the coercivity is identical to the minor radius of the ellipse created by the eddy current field. So, the H_c in the magnetisation field hysteresis loop is equal to its counterpart of eddy current counter field. From Fig. 8.9, the eddy current counter field has its maximum value when the

magnetic flux density is zero; at the magnetisation tips (maximum magnetisation) the eddy current counter fields are zero. Nonetheless, the hysteresis field is created at the magnetisation tips due to the magnetisation coupling effect.

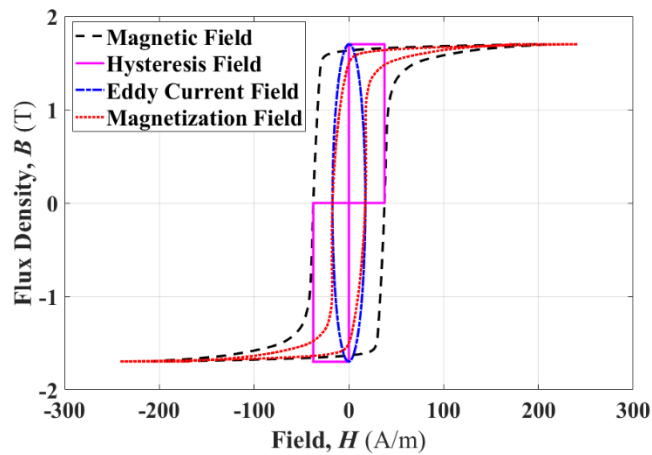


Fig. 8.10 Hysteresis loops based on magnetic field components calculated for GOESs at frequency 100 Hz and peak flux density 1.7 T.

Fig. 8.11 indicates the energy loss components calculated for the typical GOESs magnetised at 100 Hz and peak flux density ranging from 1.0 T to 1.7 T. The hysteresis loss and eddy current loss are calculated using the parameters from the manufacturer's datasheet and relevant measurement data. The magnetisation loss is obtained by calculating the difference between the measured total loss and calculated hysteresis and eddy current loss.

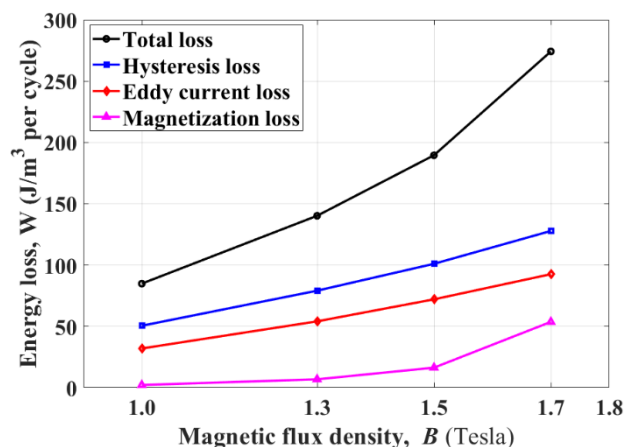


Fig. 8.11 Energy loss components per cycle calculated for GOESs magnetised at frequency 100 Hz and peak flux densities from 1.0 T to 1.7 T.

The energy loss components shown in Fig. 8.12 as a percentage, are calculated based on the results shown in Fig. 8.11. Fig. 8.11 reveals that the total loss and that of the individual components increase in tandem with an increase of the peak flux density, but

the magnetisation loss accounts for a very low percentage of total loss, because the eddy current loss, calculated using equation (8.20), without considering the skin effect is larger than real value.

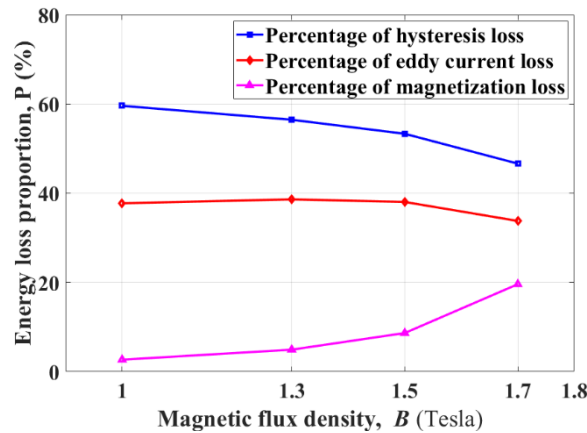


Fig. 8.12 Energy loss component proportions per cycle calculated for GOESs magnetised at frequency 100 Hz and peak flux densities from 1.0 T to 1.7 T.

Table 8.2 Energy loss components per cycle calculated for GOESs magnetised at frequency 100 Hz and peak flux densities from 1.0 T to 1.7 T.

B_{pk} (T)	W_t (J/m ³)	W_h (J/m ³)	W_e (J/m ³)	W_m (J/m ³)	P_h (%)	P_e (%)	P_m (%)
1.0	84.92	50.60	32.04	2.27	59.59	37.74	2.67
1.3	140.22	79.17	54.16	6.90	56.46	38.62	4.92
1.5	189.57	101.07	72.10	16.40	53.32	38.03	8.65
1.7	274.18	127.84	92.61	53.73	46.63	33.78	19.60

Interestingly, the proportions of hysteresis loss over total loss are around 50% for magnetisation frequencies of both 50 Hz and 100 Hz, as shown in TAB. 8.1 to 8.2. This phenomenon is related to the assumption that the hysteresis field is the coupling effect of the magnetisation at the reversal turning point and the peak flux densities are all the same for different frequencies. It is apparent from the above figures that magnetisation losses as a percentage decreases, while those for eddy current losses increases with increasing magnetisation frequency. It is because the greater eddy current results at higher frequencies.

8.3 Energy loss modelling for NOESs

The energy loss components for NOESs are now calculated in the same way for magnetisation frequencies at 50 Hz and 100 Hz and peak flux densities ranging from 1.0 T to 1.4 T. First, the components are investigated at a magnetisation frequency of 50 Hz and

peak flux density of 1.4 T. The eddy current counter field is obtained using (8.18), with the magnetisation field is found by subtracting the hysteresis field and eddy current field from the measured magnetic field. The magnetic field components are shown in Fig. 8.13, with the corresponding measured loop and calculated component are displayed in Fig. 8.14.

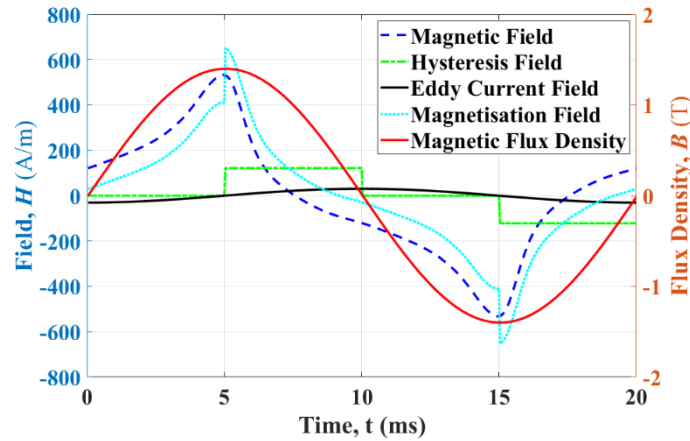


Fig. 8.13 Magnetic field components calculated for NOESs magnetised at frequency 50 Hz and a peak flux density of 1.4 T.

Fig. 8.13 reveals a clear abrupt increase in the magnetisation field when the magnetic flux density reaches a maximum value after 5 ms, and reversal of the magnetisation process begins. This is because all atomic dipoles in the samples are aligned in the previous magnetisation direction and exert a strong coupling effect on the hysteresis field, which the magnetisation field must overcome for demagnetisation to commence. The hysteresis effect only occurs during the demagnetisation when magnetic domains encounter nucleation and increase in number. The form of the magnetic flux density is that of a sine wave, while the eddy current counter field has a cosine waveform because it is generated by the variation in the magnetic flux density. The magnetic field has a regular waveform changing in a cyclical style, but it is not a sinusoidal curve because ferromagnetic material is non-linear material with apparent hysteresis effect under external magnetic excitation [124].

As can be seen in Fig. 8.14, the functional form of the eddy current field and magnetic flux density is a vertical ellipse with major axis orientated along the ordinate and the minor axis along the abscissa and centred at origin. The magnetisation field generates a narrow hysteresis loop with the coercivities located at the co-vertices of the ellipse's minor axis and created by the eddy current field. The H_c in the magnetisation field hysteresis loop is located at the co-vertices of the eddy current field loop. The hysteresis field loop represents the effects of the DC component at the positive and negative maximum tips. The combined area of both rectangles equals the hysteresis loss; the eddy current loss is obtained by evaluating the area of the ellipse, and the magnetisation loss by calculating the magnetisation field loop. The loops shown in Fig. 8.14 are the individual

loop representing the relevant effects. The sum of the areas of the three individual loops is equal to the area of the major loop formed by the magnetic field vs magnetic flux density, which is the total loss evaluated for one cycle.

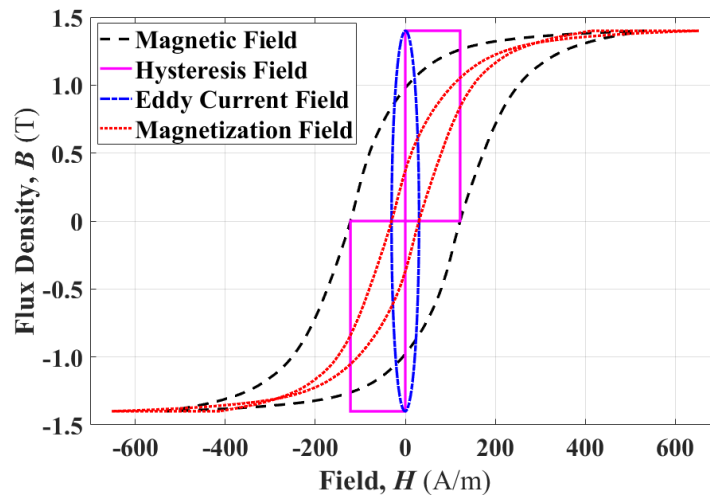


Fig. 8.14 Hysteresis loops based on magnetic field components calculated for NOESs at frequency 50 Hz and a peak flux density of 1.4 T.

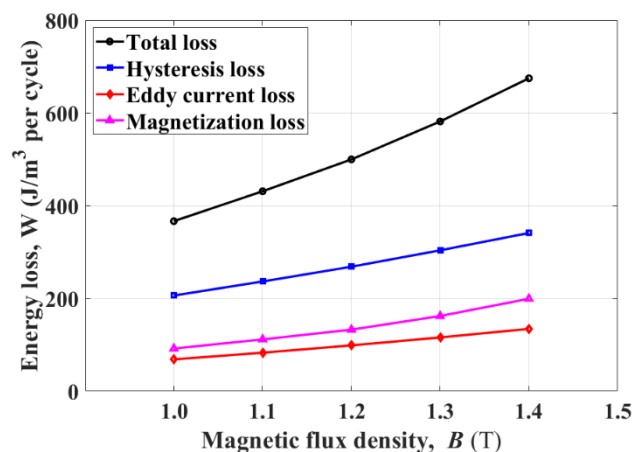


Fig. 8.15 Energy loss components per cycle calculated for NOESs magnetised at frequency 50 Hz and peak flux densities from 1.0 T to 1.4 T.

Fig. 8.15 shows the energy loss components calculated for NOESs magnetised at 50 Hz and peak flux density ranging from 1.0 T to 1.4 T. These are obtained by calculating the areas of the relevant loops created using equations (8.10), (8.20) and (8.22). The loss components shown as a percentage in Fig. 8.16 are based on the results of Fig. 8.15 which reveals that the total loss together with that of the individual components increase with increasing peak flux density, with the eddy current loss accounting for a very small proportion of the total loss. The data for the energy loss components and relevant percentages are shown in TAB. 8.3, from which the magnetisation loss grows from 91.86 J/m³ per cycle at 1.0 T to 199.32 J/m³ per cycle at 1.7 T, with the magnetisation loss as a

proportion increasing from 25.06% at 1.0 T to 29.54% at 1.7 T. From Fig. 8.16, the curves of hysteresis loss as a percentage, falls with increasing of the magnetic flux density, in contrast to the magnetisation loss as a percentage which increases.

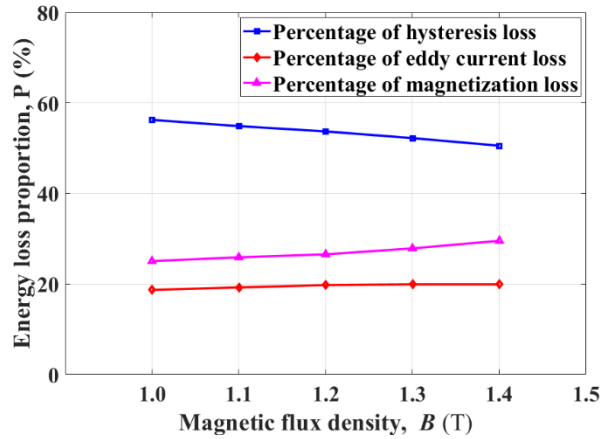


Fig. 8.16 Energy loss component per cycle proportions calculated for NOESs magnetised at frequency 50 Hz and peak flux densities from 1.0 T to 1.4 T.

Table 8.3 Energy loss components per cycle calculated for NOESs magnetised at frequency 50 Hz and peak flux densities from 1.0 T to 1.4 T.

B_{pk} (T)	W_t (J/m ³)	W_h (J/m ³)	W_e (J/m ³)	W_m (J/m ³)	P_h (%)	P_e (%)	P_m (%)
1.0	366.60	206.20	68.54	91.86	56.25	18.70	25.06
1.1	431.03	236.50	82.93	111.60	54.87	19.24	25.89
1.2	499.67	268.32	98.70	132.65	53.70	19.75	26.55
1.3	581.57	303.68	115.83	162.06	52.22	19.92	27.87
1.4	674.70	341.04	134.34	199.32	50.55	19.92	29.54

Compared to GOESs, NOESs suffer greater energy losses, which can be explained by domain theory and material microstructures. NOESs have smaller grains and more magnetic domains at demagnetised conditions. More domain wall movement is needed when NOESs are under external magnetic excitation, and more energy is needed to move them. In addition, the grain orientation also contributes to the performance along the rolling direction, in which case more energy is required for NOESs to achieve saturation and overcome anisotropic effects. The eddy current loss, calculated according to via (8.20) increases slightly in tandem with increasing magnetic flux density as can be seen in Fig. 8.16, with the proportions accounting for around 19% as shown in TAB. 8.4.

The Magnetic field components calculated for NOESs are presented in Fig. 8.17; the magnetic field and magnetic flux density relate to a frequency of 100 Hz and peak flux density of 1.4 T. The corresponding measured loop and calculated component loops are shown in Fig. 8.18. When compared with the case for a magnetisation frequency of 50 Hz, the hysteresis field and eddy current counter field at 100 Hz are seen to be increased significantly. Nevertheless, the field components have similar waveforms except that the extreme values are different. The increase in the hysteresis field and eddy current counter field inevitably increase the corresponding losses.

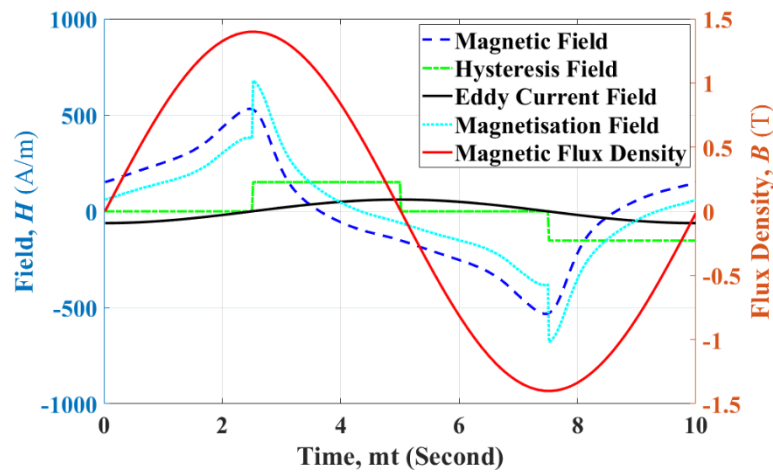


Fig. 8.17 Magnetic field components calculated for NOESs magnetised at frequency 100 Hz and peak flux density 1.4 T.

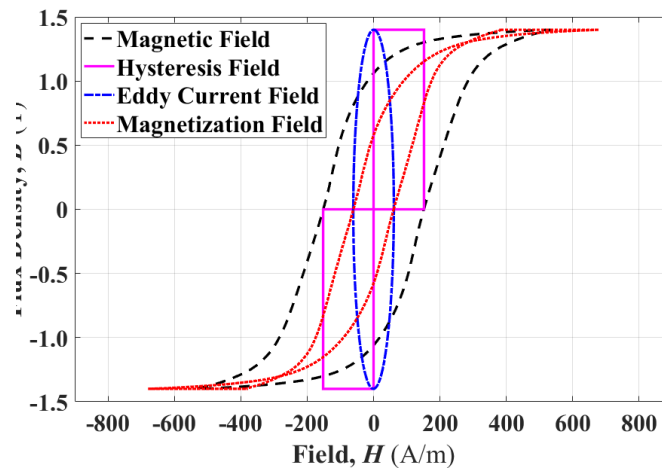


Fig. 8.18 Hysteresis loops based on magnetic field components calculated for NOESs at frequency 100 Hz and peak flux density 1.4 T.

The ellipse of the eddy current field and magnetic flux density has a wider conjugate axis (minor axis) compared to that when the magnetisation frequency is 50 Hz; the transverse axis (major axis) at the B -axis remains the same. The magnetisation field generates a

narrow hysteresis loop with twists at the tips because the hysteresis field is added to the magnetisation field used to compensate for the magnetisation coupling effect. The hysteresis field is identical to the coercivity, which is the amount of displacement of the hysteresis effect. So, the H_c in the magnetisation field hysteresis loop is equal to the maximum value of the eddy current counter field. From Fig. 8.17, the eddy current counter field has a maximum value when magnetic flux density is zero, and they are both zero at the magnetisation tips (maximum magnetisation). This is because the eddy current counter field is proportional to the time rate of the magnetic flux density.

The energy loss components calculated for the typical NOESs magnetised at 100 Hz and peak flux density ranging from 1.0 T to 1.7 T are displayed in Fig. 8.19. The magnetisation loss is gained by calculating the difference between the measured total loss and calculated hysteresis and eddy current field loss, or by calculating the area of the loop of the magnetisation field vs magnetic flux density. The curves in Fig. 8.19 reveal a clear trend of increasing total loss and relevant loss components with increasing peak flux density.

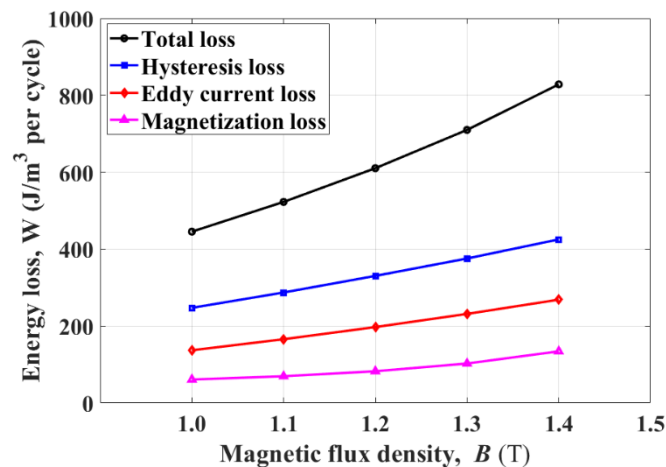


Fig. 8.19 Energy loss components per cycle calculated for NOESs magnetised at frequency 100 Hz and peak flux densities from 1.0 T to 1.4 T.

The percentage of loss components commensurate with the results shown in Fig. 8.19 are presented in Fig. 8.20. The hysteresis loss decreases gradually with increasing peak flux density. TAB 8.4 shows the percentage eddy current field loss increases from around 19% at a magnetisation frequency of 50 Hz to around 32% at 100 Hz. The percentage measures for all three components remains more-or-less the same for all peak flux densities. Closer inspection of TAB. 8.2 and 8.4 shows that the total measured loss for GOESs is 189.57 J/m³ per cycle at magnetisation frequency 100 Hz and peak flux density 1.5 T, whereas the same measure for NOESs is 828.36 J/m³ per cycle at magnetisation frequency 100 Hz and peak flux density 1.4 T. This is a significant difference between the two ferromagnetic materials. Under similar excitation conditions, the total loss for NOESs

can be as much as four times greater than that of GOESs; a phenomenon that carefully warrants consideration when using these materials in electromagnetic machines.

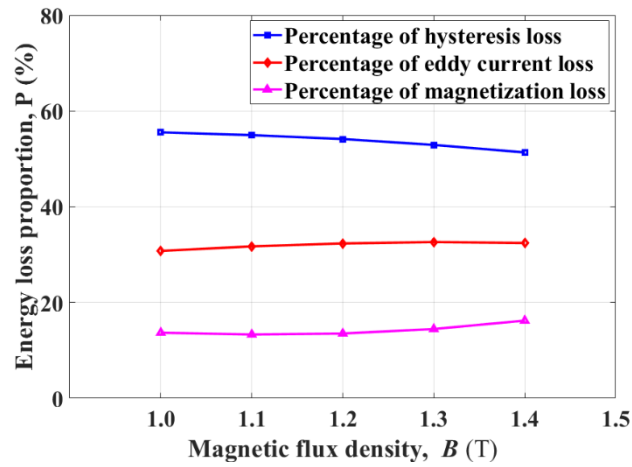


Fig. 8.20 Energy loss component per cycle expressed as a percentage for NOESs magnetised at frequency 100 Hz and peak flux densities from 1.0 T to 1.4 T.

Table 8.4 Energy loss components per cycle calculated for NOESs magnetised at frequency 100 Hz and peak flux densities from 1.0 T to 1.4 T.

B_{pk} (T)	W_t (J/m ³)	W_h (J/m ³)	W_e (J/m ³)	W_m (J/m ³)	P_h (%)	P_e (%)	P_m (%)
1.0	445.46	247.40	137.08	60.98	55.54	30.77	13.69
1.1	522.83	287.32	165.86	69.65	54.95	31.72	13.32
1.2	610.43	330.48	197.39	82.56	54.14	32.34	13.52
1.3	710.03	375.70	231.66	102.67	52.91	32.63	14.46
1.4	828.36	425.32	268.67	134.37	51.35	32.43	16.22

At 50 Hz, the magnetisation loss is close to the eddy current loss; but at 100 Hz, the magnetisation loss is a lot less than the eddy current loss, just 14%. This results from the fact that the energy needed to circulate the electrons inter-atoms increases phenomenally compared to the energy used to push the domain wall motion and domain rotation. Meanwhile, without considering skin effect, the eddy current losses, calculated using (8.20), loses any practical meaning along with increasing of the magnetisation frequencies. On closer inspection of tables TAB. 8.1 to TAB. 8.4 in this chapter the hysteresis loss percentage for GOESs and NOESS, for all measured categories, are all around 50% to 55%.

From the data presented in Tables 8.1 to 8.4, it is evident that the percentages of the three energy loss components (hysteresis losses, eddy current losses, and magnetization losses) in GOESs and NOESs exhibit significant differences, particularly with respect to the magnetization loss component. Although both categories are measured using SST, the energy loss components in NOESs remain quite stable, with hysteresis losses ranging from 50.55% to 56.25% at 50 Hz and from 51.35% to 55.54% at 100 Hz. At 50 Hz, eddy current losses account for approximately 18.70% to 19.92% for NOESs, while magnetization losses constitute 25.05% to 29.94% between 1.0 T and 1.4 T. However, at 100 Hz, the magnetization losses are significantly lower than the eddy current losses, representing only 13.32% to 16.66%, with eddy current losses accounting for around 30.77% to 32.63% for NOESs between 1.0 T and 1.4 T.

In contrast, the proportions of energy loss components in GOESs differ greatly. For the case of 50 Hz, as the magnetic flux density decreases from 1.7 T to 1.0 T, the percentages of hysteresis losses increase from 42.95% to 59.59%, the percentages of eddy current losses increase from 22.93% to 28.20%, while the magnetization losses decrease from 34.13% to 12.22%. Similarly, at 100 Hz, with decreasing magnetic flux density from 1.7 T to 1.0 T, the percentages of hysteresis losses increase from 46.63% to 59.59%, the percentages of eddy current losses increase from 33.78% to 37.74%, but the magnetization losses drop significantly from 19.60% to 2.67%. Clearly, as the magnetization frequencies increase, the separation between eddy current and magnetization losses becomes less feasible.

8.4 Summary

This chapter developed a new theory and model to describe the separation principle of energy loss for GOESs and NOESs. It differs considerably from what has done before, being based on a new magnetic theory of the hysteresis mechanism proposed in chapter 4 and reference [118]. This new separation model has clear physical underpinnings. The energy loss components are all modelled in accordance with the Zeeman effect because it is universally acknowledged that the energy loss per cycle is identical to the area enclosed by the hysteresis loop. In addition, the model is applicable to ferromagnetic materials at low magnetisation frequencies.

The modelling results suggest a significant advance in studying the separation principle of GOESs and NOESs and underpin a new theory for describing physical origin hysteresis associated with the magnetisation of GOESs and NOESs, which differs from conventional opinion. The change from excess loss to magnetisation loss is an attempt to provide the third part of the loss component with a precise physical meaning. The new ELSM is dedicated to contributing the core loss estimation of soft magnetic materials.

Chapter 9 Summary and Conclusion

An analytical hysteresis model has been proposed for describing the magnetisation processes of GOESs and NOESs. The proposed model is derived based on the analysis of different domain patterns, including anisotropic and isotropic components of the microstructure in the magnetic materials. Investigation of the magnetic properties of both materials is conducted in order to assess the model's ability to adequately generate magnetic hysteresis loops and calculate the energy losses under sinusoidal and non-sinusoidal magnetisation regimes. Validation is achieved for both electrical steel sheets for a wide range of magnetisation conditions, including excitations with harmonics.

The proposed energy loss separation model (ELSM) is another important method to evaluate the energy losses for both GOESs and NOESs to improve the performance of electrical machines. In the previous energy loss separation principle, the static hysteresis loss component is evaluated when the magnetisation frequency equals zero. The ELSM for both electrical steel sheets proposed in this thesis, was derived according to the analysis of magnetisation processes from the perspective of the new hysteresis theory. It evaluates the energy loss separation at the exact magnetisation frequencies by separating the magnetic field based on the physical mechanism of magnetisation processes. This means that the three field components coexist during the magnetisation processes. Furthermore, the modelling results of energy loss components can be calculated using the data from the datasheet provided by the manufacturers of the magnetic materials.

9.1 Summary

The fundamental magnetic definition, classical theory, and magnetic domain theory have been studied from the macroscale to the microscale from the critical perspective to achieve a comprehensive understanding of ferromagnetism. The magnetic induction B of a magnetic material is caused by a magnetic field H created by an external current. The hysteresis loop of $B - H$ is the plot which represents the bulk magnetic properties of a ferromagnetic material. The major loop is formed between the positive saturation tip and the negative saturation tip, and the minor loop is measured inside the major loop.

The theoretical underpinning of the proposed hysteresis model is based on analysis of the hysteresis field encountered at any order reversal turning point when the directions of the magnetic field strength H and magnetic flux density B are changed. Theoretically, the contribution of the hysteresis field is due to the coupling effect of magnetisation at the reversal point. The coupling effect is contributed to by WMF or the interaction of all atomic dipoles in the materials. The direction of the hysteresis field is aligned with the direction of the previous magnetisation and is the opposite of the reversed magnetic field.

Unlike the conventional methods used to describe the hysteresis phenomenon in terms of $B - H$ loops, the new model adopts the form with $B - h$ curves, which can be derived from $B - H$ loops. The excitation field h can be obtained from measured magnetic field values of H and coercivity or coercive force values. It is the $B - h$ curves that are used in the analysis of the new model.

In order to achieve the research objectives, the measurement data were processed using MATLAB codes to test the new models. The comparison between the modelling and measured results was made to ascertain the investigation of the project.

The achievements resulting from the above research activities enhance the current knowledge and understanding of the modelling of magnetisation processes. This theoretical development contributes to the derivation and realisation of an accurate mathematical model to explanation magnetisation processes and for the prediction of energy losses for both GOESs and NOESs.

In summary, the main achievements of this investigation are as follows:

1, A new theory concerning the explanation of magnetisation processes of ferromagnetic materials and the reason for magnetic hysteresis has been proposed with an accompanying detailed discussion and depiction.

2, A single equation model regarding the interpretation of magnetisation processes and the generation of magnetic hysteresis loops has been derived according to the new theory developed based on the domain patterns of anisotropic and isotropic components in both GOESs and NOESs.

3, A new ELSM pertaining to the description of the core loss mechanism for both GOESs and NOESs at low frequencies has been developed according to the analysis of magnetisation processes and the proposed hysteresis theory.

4, The hysteresis model and ELSM have been tested for GOESs and NOESs. The modelling results confirm the verification of the models by comparing the mathematical modelling results to experimental data.

9.2 Conclusion and future work

Research has been conducted involving intensive systematic investigation, with achievements made, that boost the prosperity of the electrical power industries. So far, the models proposed in this thesis have proved the convenience of interpreting the magnetisation processes for ferromagnetic materials under external excitation and verified to bring the simplest methods to simulate the magnetic hysteresis loops and calculate the energy losses.

The designed program codes based on these models can be used to process experimental data, and the parameters of the equation for a specific material are calculated by the fitting programme. After obtaining the parameters, the energy losses were calculated for different frequencies and flux densities. The comparison of results for modelling and measurement data indicate that this single equation model provides a good match for both GOESs and NOESs, for both major and minor loops, for both hysteresis loops and core losses, and under both sinusoidal and non-sinusoidal excitations.

The modelling results suggest an achievement in the investigation of domain patterns in ferromagnetic materials and underpin a new theory concerning magnetic hysteresis loops. The quantitative agreement of the modelling results for the magnetic hysteresis loops and energy losses represents a useful contribution to the modelling of the magnetisation processes of soft magnetic materials. The proposed model can be used to characterise electrical steels used as the core materials of electromagnetic components in renewable energy systems and modern electric motors. It could be also used an analytical tool to characterise electrical steel materials under high frequency and harmonic distorted excitations. The single equation approach presented here can be generalised to other soft magnetic materials, which is a challenging task to be addressed in future work.

Despite the above achievements a significant amount of research work remains to be done to investigate the application of the new models for other soft and hard magnetic materials, especially when the magnetic materials are used for renewable energy systems under harmonic operation conditions, such as power electronics converters and inverters for wind energy and solar power systems. It is therefore recommended that further research be undertaken in the following areas:

- 1, Application of the hysteresis models for interpreting the magnetic properties of manganese-zinc ferrite cores for use in converters in electric vehicles (EVs) under sinusoidal and non-sinusoidal excitations.

- 2, Application of the hysteresis models for interpreting the magnetic properties of nickel-zinc ferrite cores for use in converters in EVs under sinusoidal and non-sinusoidal excitation.

- 3, Application of the hysteresis models for interpreting nano core and powder core magnetic properties for use in advanced motors in EVs under sinusoidal and non-sinusoidal excitations.

- 4, Application of the hysteresis models for interpreting the magnetic properties of the magnetic core of power electronics converters and inverters for wind energy and solar power systems under sinusoidal and non-sinusoidal excitations.

5, Application of the hysteresis model to other materials and disciplines with hysteresis phenomena, such as smart materials, graphene, hysteresis controller, hysteresis motor, and piezoelectric actuator.

6, Modelling magnetic hysteresis of soft and hard magnetic materials under rotational magnetisations for EV applications.

Efficiency plays a crucial role in determining the battery life of EV motors, which, in turn, relies on the performance of stators and rotors. To optimize performance and efficiency and maximise battery life expectancy, magnetic cores are designed to cater to the specific requirements of EVs. Selecting appropriate magnetic materials for EV motors depends on the material characteristics. The main types of magnetic materials used in EV motors are ceramic (ferrite) magnets, AlNiCo (Aluminium Nickel Cobalt) magnets, SmCo (Samarium Cobalt) magnets, and NdFeB (Neodymium Iron Boron) magnets. These materials' magnetic properties significantly impact the performance of EV motors. To achieve high efficiency, an accurate model is essential to characterise the magnetic materials and advance motor design.

Generalising the new model to other soft magnetic materials presents challenges, primarily due to the necessity for collecting precise experimental data, a laborious task requiring substantial funding support. Additionally, the parameter calculation is complex due to the inherent intricacy of the magnetization processes of the magnetic materials. Moreover, there are plans to extend the model to simulate dynamic $B - H$ curves, necessary for truly transient simulations of electromagnetic components in power grids.

The current model is primarily used for static state operations, encompassing both standard and distorted curves. The parameters are calculated by separating the curves based on their natural bends. Future work aims to explore the use of machine learning and artificial neural networks to evaluate parameters and calculate them from instantaneously measured dynamic data. Consequently, the new model could be employed in power system or electromagnetic machine modelling during operations.

References

- [1] Zirka, S.E., Moroz, Y.I., Moses, A.J. and Arturi, C.M., 2011. Static and dynamic hysteresis models for studying transformer transients. *IEEE Transactions on Power Delivery*, 26(4), pp.2352-2362.
- [2] Jiles, D.C. and Atherton, D.L., 1984. Theory of ferromagnetic hysteresis. *Journal of applied physics*, 55(6), pp.2115-2120.
- [3] Jiles, D.C. and Atherton, D.L., 1986. Theory of ferromagnetic hysteresis. *Journal of magnetism and magnetic materials*, 61(1-2), pp.48-60.
- [4] Mayergoyz, I.D., 2003. *Mathematical models of hysteresis and their applications*. Academic Press.
- [5] Weiss, P., 1906. La variation du ferromagnétisme avec la température. *Comptes Rendus*, 143, pp.1136-1139.
- [6] Pry, R.H. and Bean, C.P., 1958. Calculation of the energy loss in magnetic sheet materials using a domain model. *Journal of Applied Physics*, 29(3), pp.532-533.
- [7] Bertotti, G., 1988. General properties of power losses in soft ferromagnetic materials. *IEEE Transactions on magnetics*, 24(1), pp.621-630.
- [8] Jiles, D., 2015. *Introduction to magnetism and magnetic materials*. CRC press.
- [9] Parker, R.H., Yu, C., Zhong, W., Estey, B. and Müller, H., 2018. Measurement of the fine-structure constant as a test of the Standard Model. *Science*, 360(6385), pp.191-195.
- [10] Davis, R.S., 2017. Determining the value of the fine-structure constant from a current balance: Getting acquainted with some upcoming changes to the SI. *American Journal of Physics*, 85(5), pp.364-368.
- [11] Weiss, P., 1907. L'hypothèse du champ moléculaire et la propriété ferromagnétique.
- [12] Hoshtanar, O., 2006. *Dynamic domain observation in grain-oriented electrical steel using magneto-optical techniques*. Cardiff University.
- [13] Chen, C.W., 2013. *Magnetism and metallurgy of soft magnetic materials*. Courier Corporation.
- [14] Brown, W.F., 1963. *Micromagnetics (No. 18)*. interscience publishers.
- [15] Tilley, R.J., 2020. *Crystals and crystal structures*. John Wiley & Sons.
- [16] Tumanski, S., 2016. *Handbook of magnetic measurements*. CRC press.
- [17] Rohaľ, V., Spiřák, E., Mulidrán, P. and Majerníková, J., 2020. Basic classification and processing of electrical steels. *The International Journal of Engineering and Science*, 9(07), pp. 01-06.
- [18] Bozorth, R.M., 1993. *Ferromagnetism (p. 992)*.

- [19] Steinmetz, C.P., 1984. On the law of hysteresis. Proceedings of the IEEE, 72(2), pp.197-221.
- [20] Zirka, S.E., Moroz, Y.I., Marketos, P., Moses, A.J., Jiles, D.C. and Matsuo, T., 2008. Generalization of the classical method for calculating dynamic hysteresis loops in grainoriented electrical steels. IEEE Transactions on Magnetics, 44(9), pp.2113-2126.
- [21] Bertotti, G., 1998. Hysteresis in magnetism: for physicists, materials scientists, and engineers. Academic press.
- [22] Petrun, M., Steentjes, S., Hameyer, K. and Dolinar, D., 2015. 1-D lamination models for calculating the magnetisation dynamics in non-oriented soft magnetic steel sheets. IEEE Transactions on Magnetics, 52(3), pp.1-4.
- [23] De Campos, M.F., Yonamine, T., Fukuhara, M., Landgraf, F.J., Achete, C.A. and Missell, F.P., 2006. Effect of frequency on the iron losses of 0.5% and 1.5% Si nonoriented electrical steels. IEEE Transactions on Magnetics, 42(10), pp.2812-2814.
- [24] Coleman, P., 2007. Handbook of magnetism and advanced magnetic materials.
- [25] Zirka, S.E., Moroz, Y.I., Marketos, P. and Moses, A.J., 2005. A viscous-type dynamic hysteresis model as a tool for loss separation in conducting ferromagnetic laminations. IEEE transactions on magnetics, 41(3), pp.1109-1111.
- [26] Najgebauer, M., 2010, October. Models for prediction of energy loss in soft magnetic materials. In XII International PhD Workshop OWD (pp. 23-26).
- [27] Hamzehbahmani, H., Anderson, P. and Preece, S., 2015. Application of an advanced eddy-current loss modelling to magnetic properties of electrical steel laminations in a wide range of measurements. IET Science, Measurement & Technology, 9(7), pp.807-816.
- [28] Zhang, Y., Cheng, M.C. and Pillay, P., 2011. A novel hysteresis core loss model for magnetic laminations. IEEE Transactions on Energy Conversion, 26(4), pp.993-999.
- [29] Zirka, S.E., Moroz, Y.I., Marketos, P. and Moses, A.J., 2010. Loss separation in nonoriented electrical steels. IEEE Transactions on Magnetics, 46(2), pp.286-289.
- [30] Chandrasena, W., McLaren, P.G., Annakkage, U.D. and Jayasinghe, R.P., 2004. An improved low-frequency transformer model for use in GIC studies. IEEE transactions on power delivery, 19(2), pp.643-651.
- [31] Goss, N.P., 1935. New development in electrical strip steels characterized by fine grain structure approaching the properties of a single crystal. Trans. Amer. Soc. Metals, 23(1), pp.511-531.
- [32] Zirka, S.E., Moroz, Y.I., Marketos, P. and Moses, A.J., 2004. Congruency-based hysteresis models for transient simulation. IEEE Transactions on Magnetics, 40(2), pp.390-399.
- [33] Akcay, H. and Ece, D.G., 2003. Modeling of hysteresis and power losses in transformer laminations. IEEE Transactions on Power Delivery, 18(2), pp.487-492.
- [34] Graham Jr, C.D., 1982. Physical origin of losses in conducting ferromagnetic materials. Journal of Applied Physics, 53(11), pp.8276-8280.
- [35] Lavers, J. and Biringer, P.P., 1976. Prediction of core losses for high flux densities and distorted flux waveforms. IEEE Transactions on Magnetics, 12(6), pp.1053-1055.

- [36] Lavers, J., Biringer, P.P. and Hollitscher, H., 1978. A simple method of estimating the minor loop hysteresis loss in thin laminations. *IEEE Transactions on magnetics*, 14(5), pp.386-388.
- [37] Bertotti, G., 1983. Space-time correlation properties of the magnetisation process and eddy current losses: Theory. *Journal of applied physics*, 54(9), pp.5293-5305.
- [38] Najgebauer, M., 2010, October. Models for prediction of energy loss in soft magnetic materials. In XII International PhD Workshop OWD (pp. 23-26).
- [39] Bertotti, G., 1984. A general statistical approach to the problem of eddy current losses. *Journal of magnetism and Magnetic Materials*, 41(1-3), pp.253-260.
- [40] Bertotti, G., 1986. Some considerations on the physical interpretation of eddy current losses in ferromagnetic materials. *Journal of magnetism and magnetic materials*, 54, pp.1556-1560.
- [41] Bertotti, G., 1985. Direct relation between hysteresis and dynamic losses in soft magnetic materials. *Le Journal de Physique Colloques*, 46(C6), pp.C6-389.
- [42] Bertotti, G., 1985. Physical interpretation of eddy current losses in ferromagnetic materials. I. Theoretical considerations. *Journal of applied Physics*, 57(6), pp.2110-2117.
- [43] Bertotti, G., 1985. Physical interpretation of eddy current losses in ferromagnetic materials. II. Analysis of experimental results. *Journal of Applied Physics*, 57(6), pp.2118-2126.
- [44] Thomson, J.J., 1892. On the heat produced by eddy currents in an iron plate exposed to an alternating magnetic field. *Electrician*, 28, pp.599-600.
- [45] Keer, R.V., Dupre, L.R., Melkebeek, J.A.A., Moroz, Y.I. and Zirka, S.E., 2001. On the evaluation of transients in conducting ferromagnetic cores. In *Scientific Computing in Electrical Engineering* (pp. 417-424). Springer, Berlin, Heidelberg.
- [46] Bottauscio, O., Manzin, A., Canova, A., Chiampi, M., Gruosso, G. and Repetto, M., 2004. Field and circuit approaches for diffusion phenomena in magnetic cores. *IEEE Transactions on Magnetics*, 40(2), pp.1322-1325.
- [47] Petrun, M., Steentjes, S., Hameyer, K. and Dolinar, D., 2015. 1-D lamination models for calculating the magnetisation dynamics in non-oriented soft magnetic steel sheets. *IEEE Transactions on Magnetics*, 52(3), pp.1-4.
- [48] Almeida, A.A., Rodrigues-Jr, D.L., Perassa, L.S., Leicht, J. and Landgraf, F.J., 2014. Anomalous loss hysteresis loop. *Materials Research*, 17, pp.494-497.
- [49] Landgraf, F.J.G., Teixeira, J.C., Emura, M., De Campos, M.F. and Muranaka, C.S., 1999, January. Separating components of the hysteresis loss of non-oriented electrical steels. In *Materials Science Forum* (Vol. 302, pp. 440-445). Trans Tech Publications Ltd.
- [50] Shilling, J. and Houze, G., 1974. Magnetic properties and domain structure in grain-oriented 3% Si-Fe. *IEEE Transactions on Magnetics*, 10(2), pp.195-223.
- [51] Shilling, J., Morris, W., Osborn, M. and Rao, P.R.A.K.A.S.H., 1978. Orientation dependence of domain wall spacing and losses in 3-percent Si-Fe single crystals. *IEEE Transactions on Magnetics*, 14(3), pp.104-111.

- [52] Ushigami, Y., Mizokami, M., Fujikura, M., Kubota, T., Fujii, H. and Murakami, K., 2003. Recent development of low-loss grain-oriented silicon steel. *Journal of magnetism and magnetic materials*, 254, pp.307-314.
- [53] Nowicki, M., 2018. An hysteretic magnetisation measurement methods for soft magnetic materials. *Materials*, 11(10), p.2021.
- [54] Raghunathan, A., Melikhov, Y., Snyder, J.E. and Jiles, D.C., 2009. Generalized form of an hysteretic magnetisation function for Jiles–Atherton theory of hysteresis. *Applied Physics Letters*, 95(17), p.172-510.
- [55] Jiles, D.C., Ramesh, A., Shi, Y. and Fang, X., 1997. Application of the anisotropic extension of the theory of hysteresis to the magnetisation curves of crystalline and textured magnetic materials. *IEEE Transactions on Magnetics*, 33(5), pp.3961-3963.
- [56] Cullity, B.D. and Graham, C.D., 2011. *Introduction to magnetic materials*. John Wiley & Sons.
- [57] Jiles, D.C., Thoenke, J.B. and Devine, M.K., 1992. Numerical determination of hysteresis parameters for the modeling of magnetic properties using the theory of ferromagnetic hysteresis. *IEEE Transactions on magnetics*, 28(1), pp.27-35.
- [58] Ramesh, A., Jiles, D.C. and Roderick, J.M., 1996. A model of anisotropic an hysteretic magnetisation. *IEEE Transactions on Magnetics*, 32(5), pp.4234-4236.
- [59] Szewczyk, R., 2014. Validation of the an hysteretic magnetisation model for soft magnetic materials with perpendicular anisotropy. *Materials*, 7(7), pp.5109-5116.
- [60] Gmyrek, Z., 2014. Numerical modeling of static hysteresis loop using variable parameters. *International Journal of Numerical Modelling: Electronic Networks, Devices and Fields*, 27(2), pp.199-212.
- [61] Hamel, M., Ouslimane, A.N. and Hocini, F., 2022. A study of Jiles-Atherton and the modified arctangent models for the description of dynamic hysteresis curves. *Physica B: Condensed Matter*, 638, p.413930.
- [62] Chen, J., Shang, H., Xia, D., Wang, S., Peng, T. and Zang, C., 2023. A Modified Vector Jiles-Atherton Hysteresis Model for the Design of Hysteresis Devices. *IEEE Transactions on Energy Conversion*.
- [63] Chen, L., Wen, X., Ben, T., Jing, L. and Liu, Q., 2023. Accurate calculation of global hysteresis properties of grain-oriented silicon steel based on an improved JA model with variable parameters. *AIP Advances*, 13(2).
- [64] Mörée, G. and Leijon, M., 2023. Review of Play and Preisach models for hysteresis in magnetic materials. *Materials*, 16(6), p.2422.

- [65] Yang, L., Ding, B., Liao, W. and Li, Y., 2022. Identification of preisach model parameters based on an improved particle swarm optimization method for piezoelectric actuators in micro-manufacturing stages. *Micromachines*, 13(5), p.698.
- [66] Zakerzadeh, M.R., Firouzi, M., Sayyaadi, H. and Shouraki, S.B., 2011. Hysteresis nonlinearity identification using new Preisach model-based artificial neural network approach. *Journal of Applied Mathematics*, 2011.
- [67] 'Preisach_model_of_hysteresis' (2023) Wikipedia. Available at: https://en.wikipedia.org/wiki/Preisach_model_of_hysteresis#External_links (This page was last edited on 10 July 2023, at 03:05 (UTC)).
- [68] Roussel, R., Edelen, A., Ratner, D., Dubey, K., Gonzalez-Aguilera, J.P., Kim, Y.K. and Kuklev, N., 2022. Differentiable preisach modeling for characterization and optimization of particle accelerator systems with hysteresis. *Physical Review Letters*, 128(20), p.204801.
- [69] Li, Y., Zhu, J., Li, Y. and Zhu, L., 2022. A hybrid Jiles–Atherton and Preisach model of dynamic magnetic hysteresis based on backpropagation neural networks. *Journal of Magnetism and Magnetic Materials*, 544, p.168655.
- [70] Hamzehbahmani, H., Anderson, P. and Preece, S., 2015. Application of an advanced eddy-current loss modelling to magnetic properties of electrical steel laminations in a wide range of measurements. *IET Science, Measurement & Technology*, 9(7), pp.807816.
- [71] BS EN 10280:2001 + A1:2007, Magnetic Materials - Methods of measurement of the magnetic properties of electrical sheet and strip by means of a single sheet tester, British Standard.
- [72] de la Barrière, O., Appino, C., Ragusa, C., Fiorillo, F., LoBue, M. and Mazaleyrat, F., 2018. 1-D and 2-D loss-measuring methods: Optimized setup design, advanced testing, and results. *IEEE Transactions on Magnetics*, 54(9), pp.1-15.
- [73] BS EN 60404-2:1998+A1:2008, Magnetic materials – Part 2: Methods of measurement of the magnetic properties of electrical steel strip and sheet by means of an Epstein frame, British Standard.
- [74] Mthombeni, T.L., Pillay, P. and Strnat, R.M., 2007. New Epstein frame for lamination core loss measurements under high frequencies and high flux densities. *IEEE Transactions on Energy Conversion*, 22(3), pp.614-620.
- [75] Sievert, J., Ahlers, H., Fiorillo, F., Rocchino, L., Hall, M.J. and Henderson, L.C.A., 2001. Magnetic measurements on electrical steels using Epstein and SST methods.
- [76] Appino, C., Ferrara, E., Fiorillo, F., Rocchino, L., Ragusa, C., Sievert, J., Belgrand, T., Wang, C., Denke, P., Siebert, S. and Norgren, Y., 2015. International comparison on SST and Epstein measurements in grain-oriented Fe-Si sheet steel. *International Journal of Applied Electromagnetics and Mechanics*, 48(2-3), pp.123-133.
- [77] Fiorillo, F., 2004. Characterization and measurement of magnetic materials. Academic Press.

- [78] Ferrara, E., Appino, C., Rocchino, L., Ragusa, C., de la Barrière, O. and Fiorillo, F., 2017. Effective versus standard Epstein loss figure in Fe-Si sheets. *International Journal of Applied Electromagnetics and Mechanics*, 55(S1), pp.105-112.
- [79] Sasaki, T., Imamura, M., Takada, S. and Suzuki, Y., 1985. Measurement of rotational power losses in silicon-iron sheets using wattmeter method. *IEEE Transactions on Magnetics*, 21(5), pp.1918-1920.
- [80] Dou, Y., Li, Y., Lin, Z., Yue, S. and Zhu, J., 2021. An Improved Cross-Yoke SST for Accurate 1-D and 2-D Magnetic Testing of Fe-Si Sheets. *IEEE Transactions on Instrumentation and Measurement*, 71, pp.1-10.
- [81] Koprivica, B., Milovanovic, A. and Brkovic, V., 2016, November. Electrical steel testing using modified Epstein frame. In *International Scientific Conference, Gabrovo* (pp. 18-19).
- [82] Su, W.M., Mao, S.H. and Wang, P.J., 2019. Estimation of the core losses of induction machines based on the corrected Epstein test method. *IEEE Transactions on Magnetics*, 55(3), pp.1-8.
- [83] Parent, G., Penin, R., Lecointe, J.P., Brudny, J.F. and Belgrand, T., 2016. Determination of specific losses in the limbs of an Epstein frame using a three Epstein frame methodology applied to grain oriented electrical steels. *Sensors*, 16(6), p.826.
- [84] Hamzehbahmani, H., 2021. Static hysteresis modeling for grain-oriented electrical steels based on the phenomenological concepts of energy loss mechanism. *Journal of Applied Physics*, 130(5), p.055102.
- [85] Hamzehbahmani, H., 2019. Development of a new approach to core quality assessment of modern electrical machines. *IET Electric Power Applications*, 13(6), pp.750-756.
- [86] Hamzehbahmani, H., Anderson, P. and Preece, S., 2015. An application of an advanced eddy current power loss modelling to electrical steel in a wide range of magnetising frequency. *IET Science, Measurement & Technology*, 9(7), pp.807-816.
- [87] Hamzeh Bahmani, H., 2014. Development of novel techniques for the assessment of inter-laminar resistance in transformer and reactor cores (Doctoral dissertation, Cardiff University).
- [88] Fiorillo, F., Appino, C., Pasquale, M. and Bertotti, G., 2006. Hysteresis in magnetic materials. *The Science of Hysteresis*, 3, pp.1-190.
- [89] Ewing, J.A., 1900. Magnetic induction in iron and other metals." *The Electrician*".
- [90] Bozorth, R.M., 1947. Magnetism. *Reviews of modern physics*, 19(1), p.29.
- [91] Bitter, F., 1931. On inhomogeneities in the magnetisation of ferromagnetic materials. *Physical review*, 38(10), p.1903.
- [92] Landau, L. and Lifshitz, E., 1935. On the theory of magnetic permeability in ferromagnetic bodies, *sPhysik. Z. Sowejtunion*, 8, p.153.
- [93] Kittel, C. and Galt, J.K., 1956. Ferromagnetic domain theory. In *Solid state physics* (Vol. 3, pp. 437-564). Academic Press.
- [94] Goodenough, J.B., 1954. A theory of domain creation and coercive force in polycrystalline ferromagnetics. *Physical Review*, 95(4), p.917.
- [95] Zhang, S., Ducharne, B., Takeda, S., Sebald, G. and Uchimoto, T., 2021. Low-frequency behavior of laminated electric steel sheet: investigation of ferromagnetic hysteresis loops

and incremental permeability. *Journal of Magnetism and Magnetic Materials*, 538, p.168278.

[96] Noori, M. and Altabey, W.A., 2022. Hysteresis in Engineering Systems. *Applied Sciences*, 12(19), p.9428.

[97] Ewing, J.A., 1900. *Effects of stress & magnetic induction in iron & other materials*. Van Norstrand, NY.

[98] Arimatea, C. and Jacquet, D., 2001. *Mesure de l'influence magnétique du cycle proton 450 GeV sur le cycle positron (No. SL-Note-2001-013-MD)*. CERN-SL-Note-2001-013-MD.

[99] Kersten, M., 1938. Zur deutung der koerzitivkraft. In *Probleme der Technischen Magnetisierungskurve* (pp. 42-72). Springer, Berlin, Heidelberg.

[100] Kersten, M., 1946. *Grundlagen einer Theorie der ferromagnetischen Hysterese und der Koerzitivkraft*. JW Edwards.

[101] Stoner, E.C., 1940. *Ferromagnetismus*. By R. Becker and W. Döring. *The Journal of Physical Chemistry*, 44(4), pp.531-531.

[102] Henrotte, F. and Hameyer, K., 2006. A dynamical vector hysteresis model based on an energy approach. *IEEE Transactions on Magnetics*, 42(4), pp.899-902.

[103] Harrison, R.G., 2009. Physical theory of ferromagnetic first-order return curves. *IEEE transactions on magnetics*, 45(4), pp.1922-1939.

[104] Birsan, M. and Szpunar, J.A., 1997. The influence of texture on power losses in nonoriented electrical steels. *Journal of applied physics*, 81(2), pp.821-823.

[105] Pirgazi, H., Petrov, R.H. and Kestens, L.A., 2016. Effect of Grain Boundary-Magnetic Domain Interaction on the Magnetisation Behavior of Non-Oriented Electrical Steels. *steel research international*, 87(2), pp.210-218.

[106] Shirkoohi, G.H. and Arikat, M.A.M., 1994. Anisotropic properties of high permeability grain-oriented 3.25% Si-Fe electrical steel. *IEEE transactions on magnetics*, 30(2), pp.928-930.

[107] Shirkoohi, G.H. and Liu, J., 1994. A finite element method for modelling of anisotropic grain-oriented steels. *IEEE transactions on magnetics*, 30(2), pp.1078-1080.

[108] Jiles, D.C., Ramesh, A., Shi, Y. and Fang, X., 1997. Application of the anisotropic extension of the theory of hysteresis to the magnetization curves of crystalline and textured magnetic materials. *IEEE Transactions on Magnetics*, 33(5), pp.3961-3963.

[109] Beckley, P., 2000. *Electrical steels: a handbook for producers and users*. European Electrical Steels.

[110] Satpute, N., Dhoka, P., Iwaniec, M., Jabade, S. and Karande, P., 2022. Manufacturing of Pure Iron by Cold Rolling and Investigation for Application in Magnetic Flux Shielding. *Materials*, 15(7), p.2630.

[111] McCord, J., 2015. Progress in magnetic domain observation by advanced magneto-optical microscopy. *Journal of Physics D: Applied Physics*, 48(33), p.333001.

[112] Takamiya, T., Hanazawa, K. and Suzuki, T., 2016. Recent development of grain-oriented electrical steel in JFE Steel. JFE Steel Corporation, Japan, JFE Technical Report.

[113] Dupre, L.R., Bottauscio, O., Chiampi, M., Repetto, M. and Melkebeek, J.A., 1999. Modeling of electromagnetic phenomena in soft magnetic materials under unidirectional time periodic flux excitations. *IEEE Transactions on Magnetics*, 35(5), pp.4171-4184.

- [114] Barranger, J.P., 1965. Hysteresis and eddy-current losses of a transformer lamination viewed as an application of the Poynting theorem. National Aeronautics and Space Administration.
- [115] Van Keer, R., Dupre, L.R. and Melkebeek, J.A.A., 2000. Numerical Methods for the Evaluation of Transients in the Conducting Ferromagnetic Core. In SCEE-2000, 3rd Int. Workshop, 20-23 August, Germany, Poster-CP-P3.
- [116] Zirka, S.E., Moroz, Y.I., Steentjes, S., Hameyer, K., Chwastek, K., Zurek, S. and Harrison, R.G., 2015. Dynamic magnetisation models for soft ferromagnetic materials with coarse and fine domain structures. *Journal of Magnetism and Magnetic Materials*, 394, pp.229-236.
- [117] Takezawa, M., Wada, Y., Yamasaki, J., Honda, T. and Kaido, C., 2003. Effect of grain size on domain structure of thin nonoriented Si-Fe electrical sheets. *IEEE transactions on magnetics*, 39(5), pp.3208-3210.
- [118] Zhang, Z., Hamzehbahmani, H. and Gaskell, P.H., 2021. A Novel Dynamic Hysteresis Model for Grain-Oriented Electrical Steels Based on Magnetic Domain Theory. *IEEE Transactions on Magnetism*, 58(1), pp.1-9.
- [119] Zhao, X., Xu, H., Cheng, Z., Du, Z., Zheng, K. and Zhang, Y., 2020, October. Hysteresis and Loss Modelling of Silicon Steel Sheet under the Non-Sinusoidal Excitation. In 2020 IEEE International Conference on Applied Superconductivity and Electromagnetic Devices (ASEMD) (pp. 1-2). IEEE.
- [120] Zhao, X., Liu, X. and Li, L., 2019, August. Hysteretic and loss modelling of silicon steel sheet under the DC biased magnetisation based on the Preisach model. In 2019 22nd International Conference on Electrical Machines and Systems (ICEMS) (pp. 1-6). IEEE.
- [121] Hamzehbahmani, H., 2019. Inter-laminar fault analysis of magnetic cores with grain-oriented electrical steels under harmonic distortion magnetisations. *IET Science, Measurement & Technology*, 14(1), pp.26-31.
- [122] Wang, Y. and Liu, Z., 2016. Estimation model of core loss under DC bias. *IEEE Transactions on Applied Superconductivity*, 26(7), pp.1-5.
- [123] Zhao, X., Wang, R., Du, Z., Dong, L. and Liu, L., 2020. Study on Dynamic Hysteretic and Loss Properties of Silicon Steel Sheet Under Hybrid Harmonic and DC Bias Excitation. *IEEE Access*, 8, pp.187343-187352.
- [124] Vecchio, R.D., 1980. An efficient procedure for modeling complex hysteresis processes in ferromagnetic materials. *IEEE Transactions on Magnetism*, 16(5), pp.809-811.

Appendix I – Research Outcomes

Journal Papers:

1. Zhang, Z., Hamzehbahmani, H. and Gaskell, P.H., 2021. A Novel Dynamic Hysteresis Model for Grain-Oriented Electrical Steels Based on Magnetic Domain Theory. IEEE Transactions on Magnetics, 58(1), pp.1-9.
2. Zhang, Z., Hamzehbahmani, H. and Gaskell, P.H., 2023. A new hysteresis simulation method for interpreting the magnetic properties of non-oriented electrical steels. Journal of Magnetism and Magnetic Materials, 576, p.170763.

Conference Posters:

1. 24th Soft Magnetic Materials International Conference
Poster title: Characterisation of Non-Oriented Electrical Steels based on the Dynamic Hysteresis Loop (DHL).
2. 25th Soft Magnetic Materials International Conference
Poster title: A New Hysteresis Model for characterising Grain-Oriented Electrical Steels

Appendix II – Journal Paper

A Novel Dynamic Hysteresis Model for Grain-Oriented Electrical Steels Based on Magnetic Domain Theory

Zhi Zhang[✉], Hamed Hamzehbahmani[✉], and Philip H. Gaskell

Department of Engineering, Durham University, Durham DH1 3LE, U.K.

A novel approach is adopted to model the hysteresis phenomenon of grain-oriented electrical steels (GOESs), by incorporating a variation of the domain patterns associated with ferromagnetic materials during magnetization and demagnetization. The ensuing model treats the anisotropic and isotropic components separately, together with the coupling effect of the excitation field. Its ability to replicate experimentally obtained dynamic hysteresis loops (DHLs) for Epstein size laminations of GO 3% SiFe electrical steels, for different magnetizing frequencies and peak flux densities, and facilitate the straightforward evaluation of the energy loss in GOESs is demonstrated for the case of controlled sinusoidal magnetic induction. Close agreement is found to exist between the predicted energy loss and corresponding bulk measurements, with the maximum difference being less than 2%.

Index Terms—Dynamic modeling, energy loss, ferromagnetic materials, grain-oriented electrical steels (GOES), magnetic hysteresis.

I. INTRODUCTION

GRAIN-ORIENTED electrical steels (GOESs) are silicon steels in which strong magnetic properties exist in the rolling direction of production in the material's plane. Consequently, GOES laminations are widely used in industry for producing distribution and power transformers, reactors, and large turbo generators, where energy efficiency and high performance are essential [1]. As to the future, improved electrical machines and new infrastructure will prove essential in addressing the urgency surrounding the need for increased renewable energy integration into existing power systems, in which GOESs will continue to play a vital role. Accordingly, data analysis of magnetization measurements and accurate modeling of the magnetic properties of GOESs are critical to investigate the performance of the materials involved in the practice.

The magnetization of such materials can be analyzed by means of the hysteresis phenomenon. In this respect, the well-known 1-D diffusion equation, linking the magnetic field strength H and the magnetic flux density B through the material resistivity ρ , has been used for decades for the dynamic modeling of electrical steels [2]

$$\frac{\partial B}{\partial t} = \rho \frac{\partial^2 H}{\partial x^2}. \quad (1)$$

However, this equation was developed when the concept of magnetic domains had yet to be proposed [3]. It describes a homogeneous medium and, hence, is rarely used alone as a hysteresis model for magnetic materials. In practice, electrical steels are inhomogeneous, containing grains and magnetic domains [4], [5]; accordingly, the total energy loss calculated using (1) will invariably be lower than the corresponding measured value [2].

Manuscript received July 24, 2021; revised October 19, 2021; accepted November 13, 2021. Date of publication November 16, 2021; date of current version December 22, 2021. Corresponding author: Z. Zhang (e-mail: zhi.zhang@durham.ac.uk).

Color versions of one or more figures in this article are available at <https://doi.org/10.1109/TMAG.2021.3128765>.
Digital Object Identifier 10.1109/TMAG.2021.3128765

0018-9464 © 2021 IEEE. Personal use is permitted, but republication/redistribution requires IEEE permission.

See <https://www.ieee.org/publications/rights/index.html> for more information.

A widely adopted approach to characterize magnetic materials is the utilization of a static hysteresis model (SHM) coupled to an eddy current one to accurately predict the magnetic loss and magnetization behavior. An alternative approach for evaluating the magnetization process of electrical steels is based on the statistical energy loss separation principle proposed by Bertotti [6]. In this approach, the total energy loss of the material, P_t , is expressed as

$$P_t = P_{\text{hys}} + P_{\text{eddy}} + P_{\text{exc}} \quad (2)$$

where P_{hys} is the static hysteresis component, P_{eddy} is the classical eddy-current loss, and P_{exc} is the excess loss [2]. The latter, P_{exc} , is argued to be a result of the competition between the external magnetic field and the opposite field induced by eddy currents and microstructural interactions [6]. The physical basis of the energy loss separation principle is founded on the dynamic behavior of ferromagnetic cores in operation, which is due to a combination of hysteresis, classical eddy currents, domain wall motion, skin effect, and saturation [7].

The model proposed by Jiles and Atherton (J-A) [8], [9] assumes that hysteresis is caused by overcoming the impedance pinning of domain wall motion. It can be used as an SHM instead of the measured static hysteresis loop (SHL). Their model consists of two differential equations representing irreversible and reversible differential susceptibilities, whose combination results in the total differential susceptibility. In the J-A model, the basic an-hysteretic magnetization equation is derived for homogeneous isotropic materials. However, this idealistic magnetic material is not suitable for inhomogeneous anisotropic structures. Ramesh *et al.* [10] and Szweczyk [11] extended the J-A model for the case of anisotropic magnetic materials by introducing anisotropic energy to the an-hysteretic magnetization equation, making it possible to trace their magnetic hysteresis.

Other mathematical models, such as the scalar Preisach model and the vector Preisach model [12], or the stop and play models [13], are not linked to the physics of magnetic

materials: their implementation is cumbersome due to a large number of measurements or hysteresis needed to superpose the operators with a weighting or shape function [14]. Despite this, the Preisach model represents magnetic hysteresis with reasonable accuracy for the tracing of hysteresis loops, which has led to its subsequent wide use for the analysis of magnetization.

Zirka *et al.*'s [15] model uses experimentally established magnetization rules, i.e., flux density congruency of the reversal curves; the latter, to any arbitrary order, is constructed using the major hysteresis loop. Prior to this, Zirka *et al.* [16] proposed a model using the congruency property, present in the derivation of the Preisach model, to construct a history-dependent hysteresis model (HDHM). Their model is based on the internal segments of the first-order reversal curves. A history-independent hysteresis model (HIHM) is characterized in which any order reversal curves are determined by the current reversal point and generated directly leading to the major curves of the loop [17].

This article presents a new analytical model in the form of a single equation to describe the magnetic behavior and dynamic performance of GOESs. Its distinguishing feature is in embodying the microstructure of the magnetic material, i.e., the domain patterns, enabling the modeling of dynamic hysteresis loops (DHLs) with a high degree of accuracy. Another advantage is its simple implementation in tracking the DHL. It can also be used to characterize magnetizing processes and perform an energy loss analysis for GOESs.

II. PROBLEM FORMULATION

Derivation of the theoretical underpinning of the new model differs from previous work: it is based on the postulation that the hysteresis field occurs at any order reversal point when the directions of the magnetic field strength H and the magnetic flux density B are changed. On the assumption that the excitation field $h(t)$ is the vector summation of the hysteresis field H_h generated from the magnetization coupling effect at the turning point and the magnetic field $H(t)$ triggered from the excitation source, it leads to

$$h(t) = H(t) + H_h \quad (3)$$

The direction of H_h is aligned with that of the previous magnetization at the turning point and is opposite to the reversed magnetic field. H_h is used to remove the hysteresis effect from H during magnetization to obtain $h(t)$, and H_h is equal to the coercivity or coercive force H_c but acting in the opposite direction, $H_h = -H_c$. In that case, (3) becomes

$$h(t) = H(t) - H_c \quad (4)$$

Accordingly, unlike the conventional methods used to describe the hysteresis phenomenon in terms of $B - H$ loops, the approach adopted here utilizes in preference $B - h$ curves, which can conveniently be formed from experimentally measured $H(t)$ and H_c values.

GOESs consist of both anisotropic and isotropic domain patterns, which, in a demagnetized state, forms closed structures so that no external magnetic field is revealed. When magnetized, the magnetic properties are dominated by the

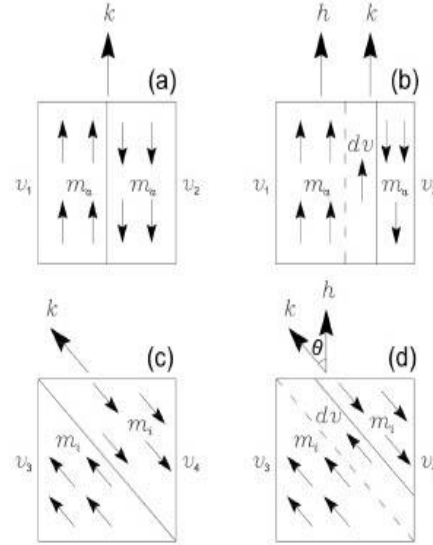


Fig. 1. Typical domain patterns for ferromagnetic materials. Top row anisotropic case: (a) demagnetized state and (b) in the presence of an excitation field. Bottom row isotropic case: (c) demagnetized state and (d) in the presence of an excitation field.

anisotropic components during magnetization because the grains are mainly aligned in the rolling direction, which forms a strong anisotropic structure leading to an easy magnetizing direction.

Fig. 1 shows a schematic of the demagnetized [(a) and (c)] and magnetized [(b) and (d)] domain states for ferromagnetic materials, representing anisotropic and isotropic domains, respectively. In order to describe the magnetizing processes in the presence of an excitation field $h(t)$ for both domain patterns, it is assumed that a unit domain with a magnetic moment per unit volume, which, in Fig. 1(a), is expressed as m_a and, in Fig. 1(c), as m_i , represents a typical domain.

The magnetic moment of the anisotropic domain in Fig. 1(a) is aligned with the rolling direction, coincidentally with the same direction as the anisotropic direction k_a , where v_1 and v_2 are the number of the unit domain moment m_a . For the corresponding isotropic domain, as shown in Fig. 1(c), v_3 and v_4 are the numbers of the unit domain moments m_i . In a demagnetized state, v_1 and v_2 are equal. However, when $h(t)$ is applied, the magnetic moment $M_1 = m_a v_1$ in the domain is aligned with the excitation field increases, while the domain moment $M_2 = m_a v_2$ opposite to $h(t)$ reduces due to the domain wall motion, as illustrated in Fig. 1(b). The alignment of the domain in Fig. 1(c) varies randomly from domain to domain, whereas the domain's direction could be aligned with the easy crystallographic axis direction, which depends on whether the crystallographic axis is preferred by the magnetic moments. In Fig. 1(d), the excitation field $h(t)$ does not align with the anisotropic direction k_a , and there is an arbitrary angle θ between them.

During magnetization for the domain pattern of Fig. 1(a), the domain wall only moves, along with the direction, to enlarge the volume of the domain aligned with the field

due to the strong uniaxial anisotropy. There is no domain rotation in Fig. 1(b) because both domain directions and anisotropic directions are aligned with the excitation field direction. By comparison, the domain in Fig. 1(d) encounters rotation before nucleation or after unification; in that case, the isotropic domain suffers more energy losses in order to rotate the domain direction pointing at the excitation field direction.

Allowing for the Zeeman effect [18], the energies due to the magnetic moment per unit volume for anisotropic and isotropic domains under an excitation field h are

$$E_a = -\mu_0 m_a \cdot h \quad (5)$$

and

$$E_i = -\mu_0 m_i \cdot h \quad (6)$$

respectively, where μ_0 is the permeability of the free space between the magnetic domains. The new model is based on expressing the energy changes in these two domain patterns in the presence of an excitation field. The total magnetic moments in a typical anisotropic and isotropic domain with unit domain number v can be expressed as

$$M_a = m_a v \quad (7)$$

and

$$M_i = m_i v \quad (8)$$

respectively.

According to statistical thermodynamics, in a state of thermal equilibrium at temperature T , the probability of a domain having energy E is proportional to the Boltzmann factor $\exp(-E/kT)$, where k is Boltzmann's constant. The unit volume number in a domain is then given by the following expression:

$$v = c \exp\left(-\frac{E}{kT}\right) \quad (9)$$

where c is a constant of proportionality. With reference to Fig. 1(b), the number of the unit moment in the domain aligned with the excitation field can then be expressed as

$$v_1 = c \exp\left(-\frac{E_1}{kT}\right) \quad (10)$$

while the number of the unit moment in the domain opposite to the excitation field is

$$v_2 = c \exp\left(-\frac{E_2}{kT}\right). \quad (11)$$

As shown in Fig. 1(b), the number of the unit moment parallel to the excitation field will increase due to the domain wall moving from the dashed line to the solid line position, and the number of the unit moment antiparallel to the field will decrease by the same amount. During the magnetizing process, the increased dv number of the unit domain along with the excitation field is calculated as

$$dv = v_1 - v_2 \quad (12)$$

and the total number of unit moments in the anisotropic domain pattern is expressed as

$$v = v_1 + v_2. \quad (13)$$

By replacing v with dv in (8), the magnetization contributed by the anisotropic domain during the process of magnetization is estimated to be

$$M_a = m_a dv = m_a v \frac{v_1 - v_2}{v_1 + v_2}. \quad (14)$$

The magnetization process in the anisotropic domain under the excitation field can then be expressed as

$$M_a = M_{sa} \tanh(ah) \quad (15)$$

where

$$a = \frac{\mu_0 m_a}{kT} \quad (16)$$

is a balance coefficient for anisotropic components between the unit domain magnetic moment and the disordering effect of thermal agitation. M_a , as defined by (15), is the anisotropic component in the magnetizing processes, which is derived from analysis of the anisotropic domain pattern in ferromagnetic materials. $M_{sa} = m_a v$ is the saturation magnetization of the anisotropic components when the anisotropic domain magnetic moments opposite to the excitation field are all canceled out to form a unified domain aligned with the excitation field.

Regarding the isotropic domains, the magnetic moments are oriented in an arbitrary direction to the excitation field direction. The domains are formed to achieve self-saturation; they will be aligned randomly to form disordered structures with irregular shapes. Under the excitation field $h(t)$, having an angle θ with magnetic domain moment, the Zeeman energy for the unit domain volume can be expressed as follows:

$$E_i = -\mu_0 m_i h \cos\theta. \quad (17)$$

The number of the corresponding unit domain volume can then be expressed as

$$\begin{aligned} v &= c \exp\left(\frac{\mu_0 m_i h \cos\theta}{kT}\right) \\ &= c \exp(bh \cos\theta) \end{aligned} \quad (18)$$

where

$$b = \frac{\mu_0 m_i}{kT} \quad (19)$$

is a balance coefficient for isotropic components.

During the magnetizing process in Fig. 1(d), the increased dv number of the unit domain along with the excitation field is calculated as

$$dv = v_3 - v_4. \quad (20)$$

When dv approaches 0, the increased dv number of the unit domain can also be expressed as the derivative of (18); then, the unit volume number differences due to domain wall motion caused by the excitation field in Fig. 1(d) is

$$dv = -cbh \exp(bh \cos\theta) \sin\theta d\theta \quad (21)$$

leading, on integration, to

$$v = -cbh \int_0^\pi \exp(bh \cos\theta) \sin\theta d\theta. \quad (22)$$

According to (9), the magnetization M_i in the direction of the excitation field in Fig. 1(d) can be obtained from the contribution $m_i \cos\theta$ of the unit domain magnetic moment multiplied by the number of the unit volume domain dv integrated over the total number, giving

$$M_i = \int_0^v m_i \cos\theta dv. \quad (23)$$

Combining (22) and (23) leads to

$$\begin{aligned} M_i &= -cbhm_i \int_0^\pi \exp(bh \cos\theta) \sin\theta \cos\theta d\theta \\ &= m_i v \frac{\int_0^\pi \exp(bh \cos\theta) \sin\theta \cos\theta d\theta}{\int_0^\pi \exp(bh \cos\theta) \sin\theta d\theta}. \end{aligned} \quad (24)$$

Following integration, the magnetization processes of isotropic component M_i , derived from the analysis of the isotropic domain pattern in ferromagnetic materials, in the direction of the excitation field are given by

$$\begin{aligned} M_i &= M_{si} \left(\coth(bh) - \frac{1}{bh} \right) \\ &= M_{si} L(bh) \end{aligned} \quad (25)$$

where $M_{si} = m_i v$ is the saturation magnetization of the isotropic components when the isotropic domain walls are all eliminated to form a unified domain aligned with the excitation field. The second line of (25) is the well-known Langevin's function [18], which was initially derived according to the microstructures in paramagnetic materials and represents the homogeneous structures in ferromagnetic materials.

The third component in the magnetization processes is the coupling effect of the excitation field, which exists since the initial magnetization but only weakly affects the magnetic induction B . When the ferromagnetic material is subjected to an excitation field, the latter penetrates the material and leads to a coupling effect constituting a proportion of the magnetic induction, which is expressed as

$$M_h = ah \quad (26)$$

where a is the coupling coefficient concerned with the microstructure of the ferromagnetic material; it can be calculated based on relevant measured data. The magnetic induction comprised of the above three components is then acquired as a single generalized equation:

$$B = M_a + M_i + M_h \quad (27)$$

or using (15), (25), and (26) as

$$B = M_{sa} \tanh(ah) + M_{si} L(bh) + ah. \quad (28)$$

The right-hand side of (28) consists of three terms, representing anisotropic, isotropic, and excitation field coupling components, respectively. As pointed out, h is obtained by removing the hysteresis portion from the magnetic field.

The above general physical model is excellent for tracing sigmoid shape curves; however, magnetization processes do not always result in standard smooth regular S-shape curves. When (28) is used to replicate distorted and irregular curves, the differences between modeled and measured curves can prove unacceptable. However, with the recognition that the excitation field coupling effect to the magnetic induction is weak compared to the other two components, in such situations, it can be considered negligible to a good approximation and the hyperbolic tangent together with Langevin's function replaced by an exponential function. This leads to the following simplified expression for the magnetic induction:

$$B = M_{sa} \exp(ah) + M_{si} \exp(bh). \quad (29)$$

Accordingly, (29) can be used to trace the segmented curves in a piecewise manner to achieve piecewise monotonicity when single curves arise with a distorted and irregular shape. Equations (28) and (29) differ from the traditional models used to trace magnetic hysteresis loops directly, in which they are used to track S-shaped single curves obtained from measured hysteresis loops. This new model can interpret the magnetic hysteresis and predict the energy loss of ferromagnetic materials under controlled sinusoidal excitation.

III. METHODOLOGY

The proposed model, based on a single equation, (28) or (29), describes the relationship between B and h , in the form of a single curve. Standard methods designed for determining the magnetic properties of electrical steels involve the construction of $B-H$ hysteresis loops via direct measurements, which cannot be used directly in the proposed model. Therefore, as a preliminary step, the excitation field h must be obtained from such experimental data using (4). Determination of the associated parameters, M_{sa} and M_{si} , for use in (28) or (29), based on the microstructures of the magnetic materials, cannot be calculated from the manufacturer's datasheets. Calculating them involves processing the relevant measurement data over the range of measured frequencies and peak flux densities of interest, which was done using MATLAB's curve fitting tool. Once the parameters have been determined, (28) or (29) can then be used to create the required modeled $B-H$ hysteresis loops.

Prior to modeling, experiments were undertaken to measure bulk energy loss and monitor the DHLs of the test samples. Epstein size laminations (30 mm × 305 mm) of GO 3% SiFe (thickness $d = 0.3$ mm and resistivity $\rho = 0.462 \mu\Omega\text{m}$) were provided by Cogent Power Ltd., and a standard Single Strip Tester (SST) was used to measure the magnetic properties of the test samples according to BS EN 10280:2001 + A1:2007 [19]. The SST with the test samples represents an unloaded transformer, and the specific energy loss and DHLs for the samples were measured at peak flux densities from 1.0 to 1.7 T, and magnetizing frequencies from 50 to 1000 Hz. In these experiments, the magnetic samples were subjected to an alternating field excitation waveform; a sinusoidal magnetic flux density was achieved by controlling the magnetic field. Uncertainty analysis of the measuring

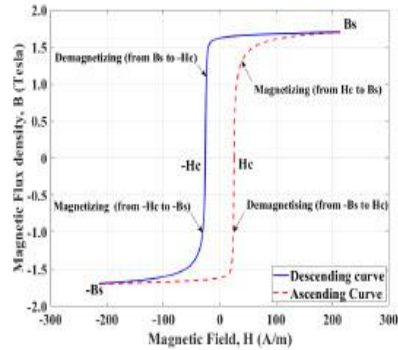


Fig. 2. Measured hysteresis loop for GOES at a frequency of 50 Hz and a peak flux density of 1.7 T.

system was performed based on the recommendations given in UKAS M3003 [20]. Type A uncertainty was estimated at $\pm 0.30\%$ and Type B uncertainty at $\pm 0.63\%$. Further details of the test setup can be found in [21].

IV. MODELING RESULTS

The complexity associated with the modeling of magnetic induction is due, in the main, to the associated hysteresis loop phenomenon, which contributes to a one-to-two relationship from H mapping to B . In the methodology proposed here, this relationship is overcome by treating the curves forming the hysteresis loop as individual descending and ascending sections to achieve a one-to-one injective function, making the tracing of magnetic curves simple. While this procedure avoids having to function the hysteresis loop directly, it is also aligned with exploring the genuine physical meaning of magnetic hysteresis. Hysteresis loops are regarded as lagging behind the phenomenon of magnetization and magnetic induction to the magnetic field. This hysteretic behavior starts at any order reversal point and is caused by the hysteresis field triggered by magnetization coupling effects. The procedure conducted cancels out the hysteresis effect using (4).

As the first step to both illustrate the above procedure and its efficacy, the case of the controlled sinusoidal magnetic induction of a GOES is considered at a magnetizing frequency of 50 Hz and a peak flux density of 1.7 T; subsequent measurements for different frequencies and peak flux densities follow the same methodology. The corresponding measured hysteresis loop shown in Fig. 2 is comprised of two sections: descending and ascending curves. For the descending one, sections B_s to $-H_c$ and $-H_c$ to $-B_s$ represent demagnetization and magnetization curves, respectively; the inverse applies for the ascending curve. Separate curves of B versus h are obtained by displacing the descending curve to the right and the ascending curve to the left a horizontal distance H_c , via (4), as shown in Fig. 3. Note that these now single curves are disconnected at the saturation tips due to the parallel shift of the original descending and ascending sections together with the magnetic field coordinates to the origin.

Both single curves in Fig. 3 pass through the origin (0, 0) establishing a synchronized relationship of B versus h . The modeling of hysteresis loops can now be explored by

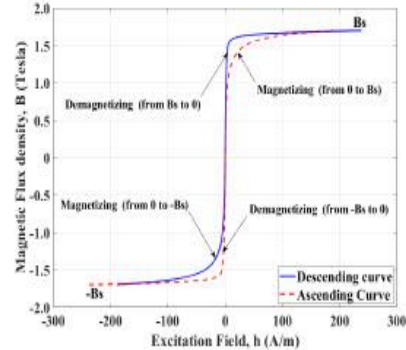


Fig. 3. Single curves for GOES at a frequency of 50 Hz and a peak flux density of 1.7 T, obtained by displacing the measured ascending and descending curve of the hysteresis loop in Fig. 2, an amount H_c to the left and right, respectively.

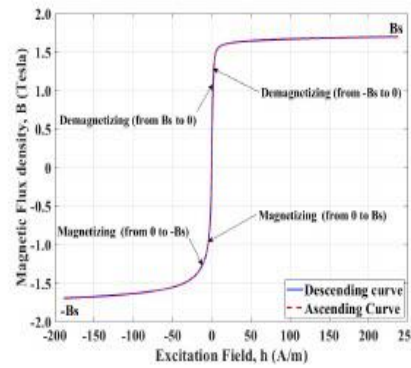


Fig. 4. Overlapping single curves for GOES at a frequency of 50 Hz and a peak flux density of 1.7 T, obtained by rotating the ascending curve through 180° about both the B - and h -axes.

considering these single curves. The long overlapping section close to the origin represents the similarity between the curves of being dominated by domain wall motion. The dissimilarity between them as they approach the saturation tips reveals the anisotropic characteristics of the steels.

It has long been observed that hysteresis loops are symmetrical about the origin, which makes sense because the magnetic flux density is a sine wave under the controlled magnetic excitation. The next critical step in the processing of the single curves is to rotate the ascending single curve through 180° about both the B - and h -axes, the result of which is shown in Fig. 4. As expected, the descending and ascending curves lay on top of one another following rotation. The key feature of proceeding in this way is that the modeling of hysteresis loops can be achieved by investigating just a single curve, which is a synchronized curve of B versus h given by (28) or (29). The modeled single curve in Fig. 5 is generated using (28) and is indistinguishable from its measured counterpart. The accompanying parameters are calculated separately for the magnetizing and demagnetizing sections of the curve. This is because the domain pattern variations act in the opposite way for the two processes. The associated parameter values are provided in Table I.

TABLE I
PARAMETERS ASSOCIATED WITH (28) FOR OBTAINING THE
MAGNETIZING AND DEMAGNETIZING CURVE SECTIONS OF FIG. 5 FOR
GOES MAGNETIZED AT A FREQUENCY OF 50 Hz AND A PEAK
FLUX DENSITY OF 1.7 T

Curve section	M_{sa} (T)	M_{dt} (T)	a	b	α
Magnetizing	0.555	1.007	84.18	23.83	0.072
Demagnetizing	0.790	0.853	56.62	75.74	0.021

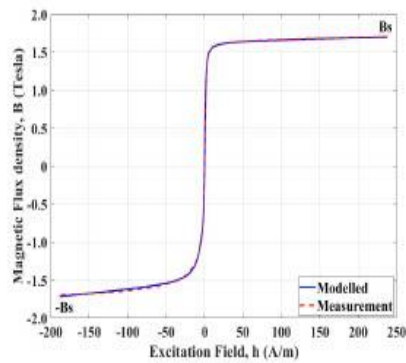


Fig. 5. Superimposed modeled and obtained single curves for GOES at a frequency of 50 Hz and a peak flux density of 1.7 T.

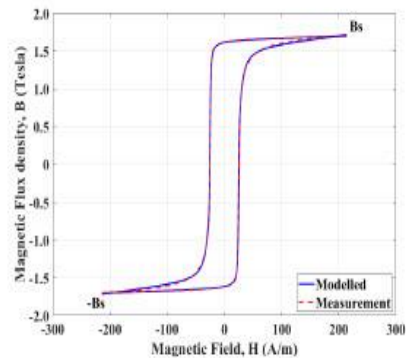


Fig. 6. Measured and modeled hysteresis loop for GOES at a frequency of 50 Hz and a peak flux density of 1.7 T superimposed against the corresponding measured data.

While a key feature of the proposed model is to describe the magnetizing process, the main criterion for verifying the model is to now generate sigmoidal curves representing the corresponding hysteresis loop from the measurement data. Although the model was derived to describe single curves of B versus h , the relevant hysteresis loops of B versus H can be created by reversing the above process, shifting the modeled curves to fit the experimental loops. Comparison between the modeled and measured hysteresis loop is provided in Fig. 6, demonstrating a remarkable degree of agreement.

The most important requirement and test of the new model are its fits to measurement data relating to materials under different magnetizing frequencies and peak flux densities. Accordingly, calculating the modeling parameters involved

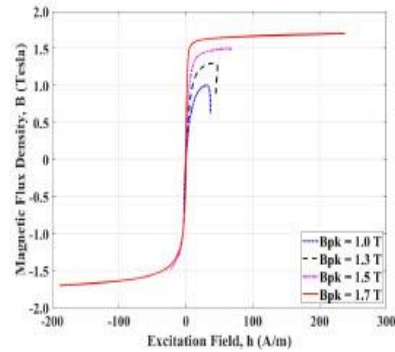


Fig. 7. Single curves obtained, following the same process as in Figs. 2–4, for GOES under sinusoidal excitation at a frequency of 50 Hz and peak flux densities ranging from 1.0 to 1.7 T.

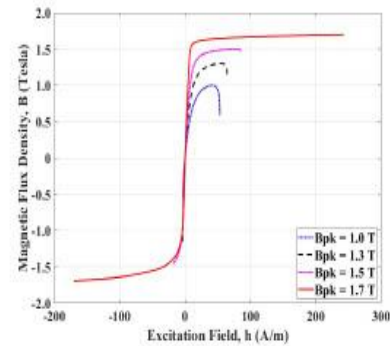


Fig. 8. Single curves obtained for GOES, following the same process as in Figs. 2–4, under sinusoidal excitation at a frequency of 100 Hz and peak flux densities ranging from 1.0 to 1.7 T.

requires the processing of the relevant measurement data for a particular range of magnetizing frequencies and peak flux densities.

The same procedure as explained for a magnetizing frequency of 50 Hz and a peak flux density of 1.7 T is applied for different frequencies and flux densities. First, single curves of B versus h for the test sample were extracted from the measured DHLs. The results for magnetizing frequencies ranging from 50 to 1000 Hz and peak flux densities from 1.0 to 1.7 T are shown in Figs. 7–12, respectively. These curves represent the magnetizing processes for $h < 0$ and demagnetizing processes for $h > 0$. The parameters for these two processes are different, and the calculations need to be performed separately. As shown in Fig. 7, tips of the single curves at a magnetizing frequency of 50 Hz at 1.0 and 1.3 T exhibit deviations due to the asynchronicity.

As the frequency increases, the effect of asynchronicity becomes more evident, which can be seen from the curves displayed in Figs. 8–12 for the different magnetizing frequencies. The resulting distortions of the single curve require the use of (29) to track them in a piecewise manner. The parameters for use in (29) must be determined for each piecewise section; the greater the number of piecewise sections employed, the greater the accuracy of the model. Taking a magnetizing frequency of 800 Hz and a peak flux density of 1.7 T, as a

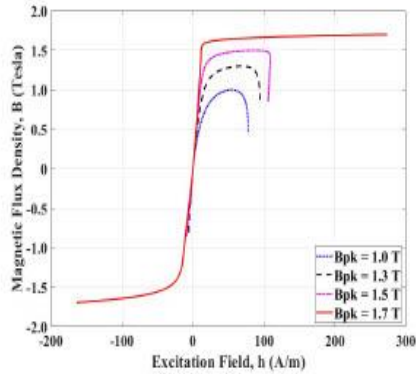


Fig. 9. Single curves obtained for GOES, following the same process as in Figs. 2–4, under sinusoidal excitation at a frequency of 200 Hz and peak flux densities ranging from 1.0 to 1.7 T.

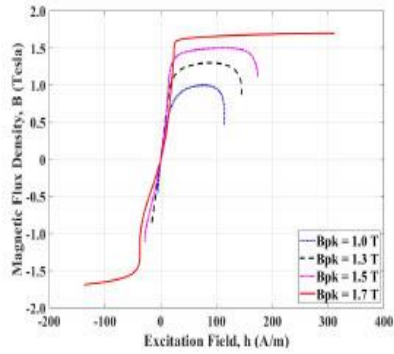


Fig. 10. Single curves obtained for GOES, following the same process as in Figs. 2–4, under sinusoidal excitation at a frequency of 400 Hz and peak flux densities ranging from 1.0 to 1.7 T.

TABLE II
PARAMETERS ASSOCIATED WITH (29) USED TO OBTAIN THE CONTIGUOUS MAGNETIZING AND DEMAGNETIZING CURVE SECTIONS, SIX IN TOTAL, OF FIG. 13 FOR GOES MAGNETIZED AT A FREQUENCY OF 800 Hz AND A PEAK FLUX DENSITY OF 1.7 T

Curve section	M_{sa} (T)	M_{st} (T)	a	b
Magnetizing				
Section 1	-0.143	0.146	-5.757	2.093
Section 2	0	3.656	37.12	-1.279
Section 3	1.449	-4e+5	-0.127	-22.32
Demagnetizing				
Section 4	0.306	-1.866	0.331	0.012
Section 5	4e+13	-1.554	39.14	-0.035
Section 6	0.144	-0.120	5.472	-2.910

typical example, the number of sections required is 6. The associated parameters for this case are provided in Table II.

The magnetizing and demagnetizing curves, and associated modeled sections of each, using (29), are plotted and shown in Fig. 13, while the corresponding parameters for the modeled sections are provided in Table II. Despite the considerable distortion at the tip of the magnetizing curve, the comparison of Fig. 13 confirms the accuracy of the modeling results.

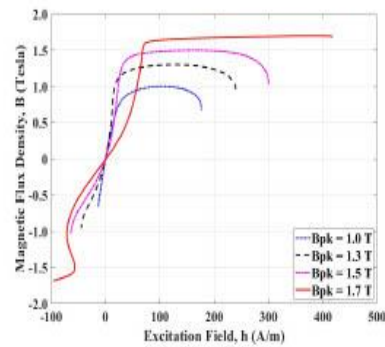


Fig. 11. Single curves obtained for GOES, following the same process as in Figs. 2–4, under sinusoidal excitation at a frequency of 800 Hz and peak flux densities ranging from 1.0 to 1.7 T.

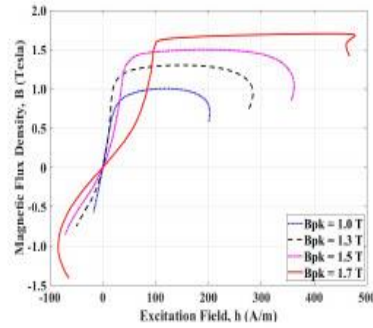


Fig. 12. Single curves obtained for GOES, following the same process as in Figs. 2–4, under sinusoidal excitation at a frequency of 1000 Hz and peak flux densities ranging from 1.0 to 1.7 T.

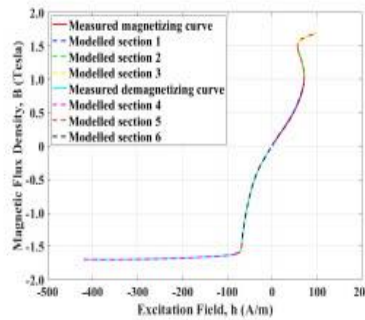


Fig. 13. Modeled contiguous curve sections, 6 in total, superimposed on the corresponding measured single curve for GOES, following the same process as in Figs. 2–5, under sinusoidal excitation at a frequency of 800 Hz and a peak flux density of 1.7 T.

All other such experimentally obtained distorted single curves are processed in the same way.

An interesting feature of the curves shown in Figs. 7–12 is that they have somewhat similar shapes and pass through the origin, which means that the excitation field is partially synchronized with magnetic induction, except for the tips where curl occurs, which dramatically simplifies the investigation of the magnetic properties compared to studying of the $B - H$ loops directly.

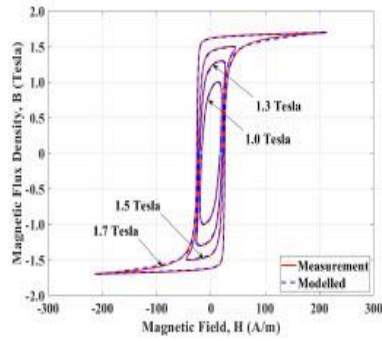


Fig. 14. Modeled hysteresis loops for GOES under sinusoidal excitation at 50 Hz and peak flux densities ranging from 1.0 to 1.7 T superimposed against the corresponding measured data.

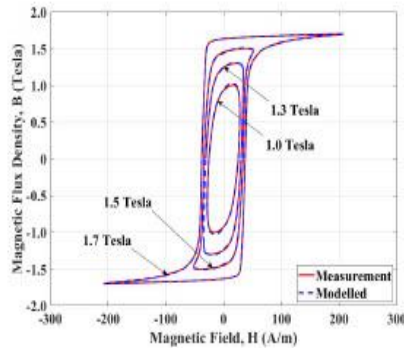


Fig. 15. Modeled hysteresis loops for GOES under sinusoidal excitation at 100 Hz and peak flux densities ranging from 1.0 to 1.7 T superimposed against the corresponding measured data.

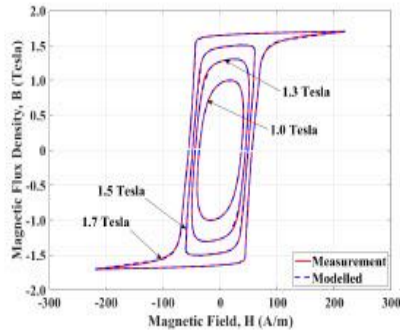


Fig. 16. Modeled hysteresis loops for GOES under sinusoidal excitation at 200 Hz and peak flux densities ranging from 1.0 to 1.7 T superimposed against the corresponding measured data.

The corresponding DHLs for the test sample produced by the model are shown in Figs. 14–19, showing that they coincide exactly with the measured loops for the range of measured frequencies and peak flux densities considered. Equation (28), linking the macroscale features of the magnetic material with the microscale description of domain theories, advances the confirmation of the generalized physical model used in this study.

Conveniently, (28) and (29) can be used to undertake an energy loss evaluation. Unlike the traditional method of

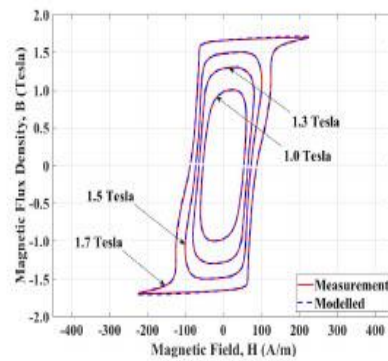


Fig. 17. Modeled hysteresis loops for GO steel under sinusoidal excitation at 400 Hz and peak flux densities ranging from 1.0 to 1.7 T superimposed against the corresponding measured data.

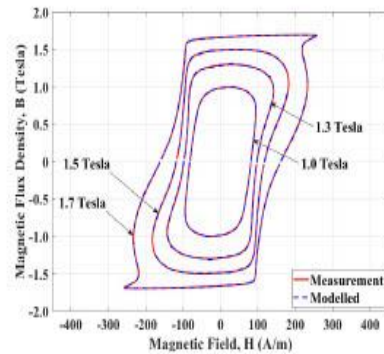


Fig. 18. Modeled hysteresis loops for GOES under sinusoidal excitation at 800 Hz and peak flux densities ranging from 1.0 to 1.7 T superimposed against the corresponding measured data.

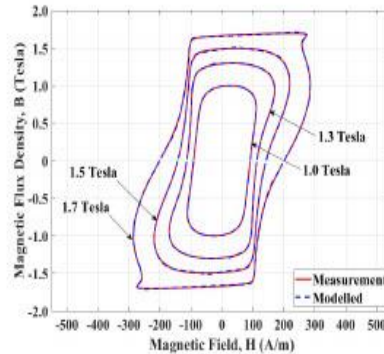


Fig. 19. Modeled hysteresis loops for GOES under sinusoidal excitation at 1000 Hz and peak flux densities ranging from 1.0 to 1.7 T superimposed against the corresponding measured data.

estimating the energy loss by calculating the area within the hysteresis loop, with the present methodology, the total energy loss per cycle can be calculated by simply integrating the model equation, over the range of the excitation field. A comparison between the calculated and measured results, and the percentage difference at the magnetizing frequencies of 50–1000 Hz and the peak flux density of 1.0–1.7 T is provided in Figs. 20 and 21, respectively.

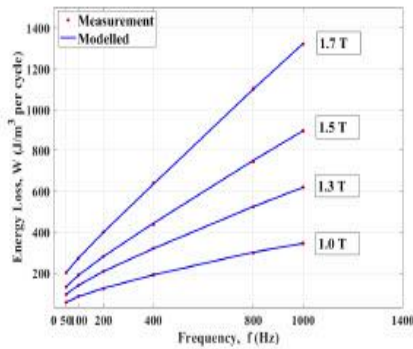


Fig. 20. Comparison between calculated and measured energy losses per cycle for GOESs under sinusoidal excitation at frequencies of 50–1000 Hz and peak flux densities from 1.0 to 1.7 T.

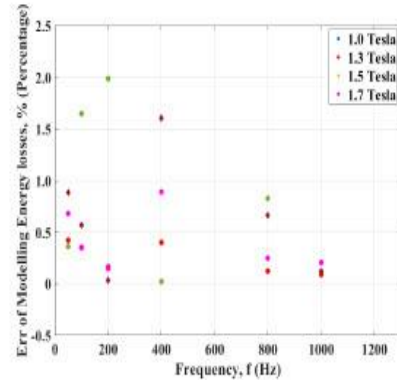


Fig. 21. Energy loss errors for GOESs under sinusoidal excitation at frequencies of 50–1000 Hz and peak flux densities from 1.0 to 1.7 T.

Close agreement with a maximum difference of less than 2% for the range of measurement is observed. It is clear that the new model, based on analyzing single curves, provides an accurate and reliable technique for reproducing the DHLs of GOESs and, hence, for energy loss calculations purposes.

V. CONCLUSION

A model based on incorporating variation in the domain patterns associated with ferromagnetic materials, treating the anisotropic and isotropic components separately, is derived in the form of a single (28) or (29) when the excitation field coupling effect is omitted. The proposed model is then shown to replicate extremely well experimentally obtained DHLs in the case of Epstein size laminations of GO 3% SiFe electrical steels. This assertion is reinforced via comparisons drawn with corresponding laboratory measurements for a range of magnetizing frequencies and peak flux densities. An additional feature of this single equation is that it enables the total energy loss per cycle to be readily calculated by simply integrating it over the range of the excitation field.

Besides suggesting a significant step forward in the modeling of the magnetization processes associated with soft magnetic materials, it is underpinned by a novel theoretical approach related to DHLs that differs from conventional

opinion. The model is equally applicable for the investigation of related magnetic materials, which is underway.

DATA AVAILABILITY

The data that support the findings of this study are available from the corresponding author upon reasonable request.

ACKNOWLEDGMENT

The authors are grateful to Cogent Power Ltd. for providing the electrical steel materials and Cardiff University for the experimental data.

REFERENCES

- [1] P. Beckley, *Electrical Steels: A Handbook for Producers and Users*, 1st ed. Newport, South Wales: European Electrical Steels, 2000.
- [2] S. E. Zirka, Y. I. Moroz, A. J. Moses, and C. M. Arturi, "Static and dynamic hysteresis models for studying transformer transients," *IEEE Trans. Power Del.*, vol. 26, no. 4, pp. 2352–2362, Oct. 2011.
- [3] J. J. Thomson, "On the heat produced by eddy currents in an iron plate exposed to an alternating magnetic field," *Electrician*, vol. 28, pp. 599–600, 1892.
- [4] M. Takezawa, Y. Wada, J. Yamasaki, T. Honda, and C. Kaido, "Effect of grain size on domain structure of thin nonoriented Si-Fe electrical sheets," *IEEE Trans. Magn.*, vol. 39, no. 5, pp. 3208–3210, Sep. 2003.
- [5] A. P. S. Baghel, B. S. Ram, K. Chwastek, L. Daniel, and S. V. Kulkarni, "Hysteresis modelling of GO laminations for arbitrary in-plane directions taking into account the dynamics of orthogonal domain walls," *J. Magn. Magn. Mater.*, vol. 418, pp. 14–20, Nov. 2016.
- [6] G. Bertotti, "General properties of power losses in soft ferromagnetic materials," *IEEE Trans. Magn.*, vol. MAG-24, no. 1, pp. 621–630, Jan. 1988.
- [7] M. Petrun, S. Steentjes, K. Hameyer, and D. Dolinar, "1-D lamination models for calculating the magnetization dynamics in non-oriented soft magnetic steel sheets," *IEEE Trans. Magn.*, vol. 52, no. 3, pp. 1–4, Mar. 2016.
- [8] D. C. Jiles and D. L. Atherton, "Theory of ferromagnetic hysteresis," *J. App. Phys.*, vol. 55, no. 6, pp. 2115–2120, 1984.
- [9] D. C. Jiles and D. L. Atherton, "Theory of ferromagnetic hysteresis," *J. Magn. Magn. Mater.*, vol. 61, nos. 1–2, pp. 48–60, Sep. 1986.
- [10] A. Ramesh, D. C. Jiles, and J. M. Roderick, "A model of anisotropic anhysteretic magnetization," *IEEE Trans. Magn.*, vol. 32, no. 5, pp. 4234–4236, Sep. 1996.
- [11] R. Szcwzyk, "Validation of the anhysteretic magnetization model for soft magnetic materials with perpendicular anisotropy," *Materials*, vol. 7, no. 7, pp. 5109–5116, Jul. 2014.
- [12] I. D. Mayergoyz, *Mathematical Models of Hysteresis and Their Applications*. New York, NY, USA: Academic, 2003.
- [13] S. Bobbio, G. Miano, C. Serpico, and C. Visone, "Models of magnetic hysteresis based on play and stop hysterons," *IEEE Trans. Magn.*, vol. 33, no. 6, pp. 4417–4426, Nov. 1997.
- [14] S. Steentjes, K. Hameyer, D. Dolinar, and M. Petrun, "Iron-loss and magnetic hysteresis under arbitrary waveforms in no. electrical steel: A comparative study of hysteresis models," *IEEE Trans. Ind. Electron.*, vol. 64, no. 3, pp. 2511–2521, Mar. 2016.
- [15] S. E. Zirka, Y. I. Moroz, R. G. Harrison, and N. Chiesa, "Inverse hysteresis models for transient simulation," *IEEE Trans. Power Del.*, vol. 29, no. 2, pp. 552–559, Apr. 2013.
- [16] S. E. Zirka, Y. I. Moroz, P. Markatos, and A. J. Moses, "Congruency-based hysteresis models for transient simulation," *IEEE Trans. Magn.*, vol. 40, no. 2, pp. 390–399, Mar. 2004.
- [17] L. Dupre, R. Van Keer, J. Melkebeek, Y. Moroz, and S. Zirka, "Hysteresis models for transient simulation," in *Scientific Computing in Electrical Engineering*. Berlin, Germany: Springer, 2001, pp. 105–112.
- [18] D. Jiles, *Introduction to Magnetism and Magnetic Materials*. Boca Raton, FL, USA: CRC Press, 2015.
- [19] *Magnetic Materials—Methods of Measurement of the Magnetic Properties of Electrical Sheet and Strip by Means of a Single Sheet Tester*, Standard BS EN 10280:2001+A1:2007, 2007.
- [20] *The Expression of Uncertainty and Confidence in Measurement*, 4th ed. U.K.: United Kingdom Accreditation Service, Oct. 2019.
- [21] H. Hamzehbahmani, P. Anderson, and K. Jenkins, "Interlaminar insulation faults detection and quality assessment of magnetic cores using flux injection probe," *IEEE Trans. Power Del.*, vol. 30, no. 5, pp. 2205–2214, Oct. 2015.



Contents lists available at ScienceDirect

Journal of Magnetism and Magnetic Materials

journal homepage: www.elsevier.com/locate/jmmm

Research article

A new hysteresis simulation method for interpreting the magnetic properties of non-oriented electrical steels

Z. Zhang^{*}, H. Hamzehbahmani, P.H. Gaskell

Department of Engineering, Durham University, Durham DH1 3LE, UK



ARTICLE INFO

Keywords:

Hysteresis simulation
Non-oriented electrical steels
Magnetic losses

ABSTRACT

The magnetic properties of non-oriented electrical steels (NOESs) are characterized using an analytical simulation method accounting for the microstructures in ferromagnetic materials. Complementary experimental data for thin sheet laminations, obtained using a standard single strip tester (SST), are employed with the hysteresis mechanism investigated in terms of the measurement system and Weiss Mean Field effects. It is shown that the magnetic hysteresis loops of NOESs of 3% SiFe can be generated with remarkable accuracy for a broad range of magnetization frequencies and peak flux densities. The simulation method is also suitable for performing an energy loss analysis with calculated energy losses, when compared to corresponding measured data, showing a strikingly accurate match with, in most cases, an error of less than 1%.

1. Introduction

Electrical steels are the most suitable ferromagnetic material for the manufacture of the magnetic cores of various electromagnetic devices. They can be divided into two categories based on their microscopic grain structures: non-oriented electrical steel (NOES) and grain-oriented electrical steel (GOES). The magnetic properties of NOES are roughly the same in any magnetization direction in the plane of the material because of the arbitrarily oriented grain directions [1]. NOES laminates are widely used in industry, from large motors and generators that require good isotropic magnetic properties to EI laminates for small transformers. Due to the accelerating electrification of the world and increasing emphasis on electrical motor performance, NOESs will play a vital role in future energy systems, especially in relation to electric vehicles in the race to achieve zero carbon emissions. Therefore, the accurate analysis and numerical modelling of the magnetic behavior of NOESs is crucial for studying the magnetization processes and performance of ferromagnetic materials within the magnetization range of practical interest.

The magnetization processes of ferromagnetic materials can be accurately analyzed using the hysteresis phenomenon [2,3]. The physical origin of hysteresis has been of interest to scientists for over a century since the term hysteresis was coined around 1900 by Sir James Alfred Ewing [4]. The attribution of magnetic hysteresis to eddy currents was proposed because of the counter field, which is opposite to the

magnetic induction, generated by the eddy currents when a steel laminate is magnetized [5]. The most widespread assumption of attribution of hysteresis is the pinning site effect, which impedes domain wall movement and causes the magnetization to be asynchronous to the magnetic field [6–8]. An assertion cited from [9] suggests that lattice defects and the eddy current effect result in the pinning effect, which dominates the irreversible domain wall displacement associated with hysteresis loops. The causation of magnetic hysteresis is also described in [10] using a friction force due to the pinning effect of Bloch walls. Positive feedback theory contributing to the origin of hysteresis is presented in [11]; this quantum mechanism of hysteresis was established based on the Weiss Mean Field (WMF) due to the coupling effect of atomic dipoles [12]. Because the pinning site effects or dry-friction force always exert negative feedback effects, the theories in [6–10] and [11] are contradictory. To date, which of the above theories is correct has yet to be definitively answered.

The Jiles-Atherton (J-A) model [13] was proposed based on the assumption of overcoming the impedance pinning of domain wall motion. It can be used to simulate the hysteresis loop independently for homogenous materials because the anhysteretic magnetization equation is derived for isotropic materials [14]. Two differential equations are used to represent irreversible and reversible differential susceptibilities, their combination resulting in the total differential susceptibility [14]. However, this model is not suitable for inhomogeneous anisotropic structures. Ramesh [15] and Szweczyk [16] extended the J-A model to

^{*} Corresponding author.

E-mail addresses: zz1v22@oton.ac.uk, zhi.zhang@durham.ac.uk (Z. Zhang).

<https://doi.org/10.1016/j.jmmm.2023.170763>

Received 21 December 2022; Received in revised form 19 April 2023; Accepted 19 April 2023

Available online 24 April 2023

0304-8853/© 2023 Elsevier B.V. All rights reserved.

include anisotropic magnetic materials by introducing anisotropic energy to the anhysteretic magnetization equation. The extension makes it possible to trace the magnetic hysteresis of anisotropic materials.

Mathematical models utilizing operators, such as the Preisach [17] and vector Preisach models [18], or the Stop and Play models [19], are not linked to the physics of magnetic materials. The Preisach model represents magnetic hysteresis with reasonable accuracy for tracing hysteresis loops, which has led to it being widely used for the analysis of magnetization. [20] proposes a hybrid model of dynamic magnetic hysteresis, which combines the dynamic J-A and Preisach models based on backpropagation neural networks.

The authors recently presented a new hysteresis simulation method [21] developed according to the assumption that the hysteresis field is the coupling effect of magnetization at the reversal turning point, which is the WMF at the magnetic flux density tips, which are the transition points from magnetization to demagnetization. The WMF executes a counterforce (negative feedback) to the magnetic field when it manages to reverse the direction of magnetic flux density. The simulation method derived was based on the microscopic variations in the ferromagnetic materials subjected to an external magnetic field and used to simulate hysteresis loops and evaluate energy loss.

This paper presents a new analytical simulation method in the form of a single equation to describe the magnetic behaviour of NOESs. Its main advantage is that the parameters involved represent the microstructure of the magnetic materials, i.e., the domain patterns, which enable the simulation of the hysteresis loops with high accuracy. The method can be used to both characterize the magnetization processes and enable an energy loss prediction for NOESs with remarkable accuracy.

2. Measurement system and hysteresis mechanism

A standard single strip tester (SST) was used to magnetize Epstein size laminations of NOES samples based on the BS EN 10290:2001 + A1:2007 [22,23]. Epstein size laminations (30 mm × 305 mm) of NO 3% SiFe with a thickness of $d = 0.5$ mm and resistivity $\rho = 0.3$ $\mu\Omega\cdot\text{m}$ were employed in this work. Fig. 1 illustrates the computer-controlled measuring system used to monitor the measuring processes. The magnetization processes were controlled and monitored using reliable software. The computer system is linked to the SST through a data acquisition Card (DAC). The excitation current was supplied by a power amplifier to the primary winding, and a 1 Ω shunt resistor (R_{sh}) used to measure the voltage drop. An inductor linked to the SST was used to compensate the air flux. The energy losses and hysteresis loops for the

samples were measured at peak flux densities ranging from 1.0 T to 1.4 T, and magnetizing frequencies ranging from 50 Hz to 800 Hz.

During the measurement, the magnetic field $H(t)$ is generated by the input electrical current $i(t)$ of the primary winding. Meanwhile, the waveform of the secondary induced voltage for sinusoidal excitation is maintained as sinusoidal as possible, achieved using a PID feedback controller [24]. Then, the magnetic flux densities $B(t)$ are derived according to Faraday's law and Lenz's law.

The control loop of the measurement system and field separation is illustrated in Fig. 2. The error between the set point and measured magnetic flux density is calculated by the PID controller, with the input current regulated by controlling the power amplifier. The sinusoidal waveform of magnetic flux density is obtained by maintaining a sinusoidal waveform of the secondary induced voltage. The instantaneous waveforms of the magnetic field and magnetic flux density obtained for a typical NOES at a magnetizing frequency of 50 Hz and peak flux density of 1.4 T, are shown in Fig. 3, from which it is evident that the magnetic flux density lags the magnetic field due to the hysteresis effects.

As shown in Fig. 3, the magnetization processes cycle between magnetization and demagnetization. Magnetization occurs in the first and third quadrants of the magnetic flux density, with demagnetization taking place in the second and fourth quadrants. The time rate of change of magnetization is aligned with the magnetization direction ($dB/dt > 0$), while the time rate of change of the demagnetization process is opposite to the magnetization direction ($dB/dt < 0$). So, the output of the PID controller is positive and negative for magnetization and demagnetization, respectively. The WMF [12] of the magnetization coupling effects of individual atomic dipoles is always oriented in the direction of the magnetization. Accordingly, the WMF is positive in the first and second quadrants and negative in the third and fourth quadrants.

The hysteresis field is contributed by the WMF effect described in [11], and the eddy current field generated by the magnetic flux is always opposite to the magnetization direction based on Faraday's law and Lenz's law. As illustrated in Fig. 2, the vector combined field, comprised of the magnetic field, hysteresis field and eddy current field, is the magnetization field driving the magnetization processes.

The time rate of change of the magnetic field is aligned with that of magnetic flux density. So, the WMF and the output of the PID controller are oriented in the same direction in the first and third quadrants of the magnetic flux density and the opposite direction in the second and fourth quadrants. Then, the WMF provides a positive or negative feedback effect during magnetization and demagnetization, respectively. The feedback effects are summarized, according to analysis of the WMF

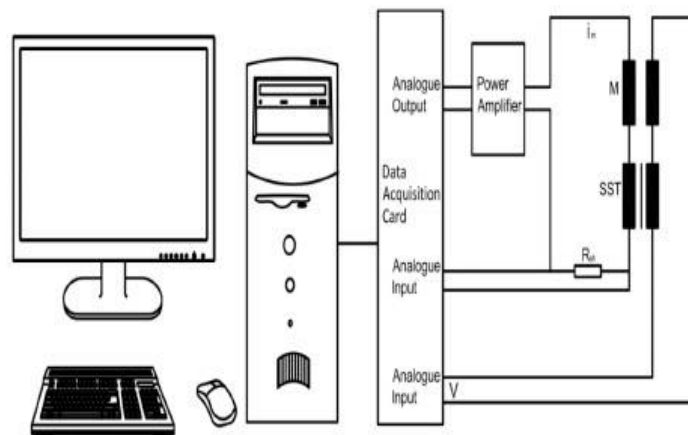


Fig. 1. Schematic diagram of SST measurement system.

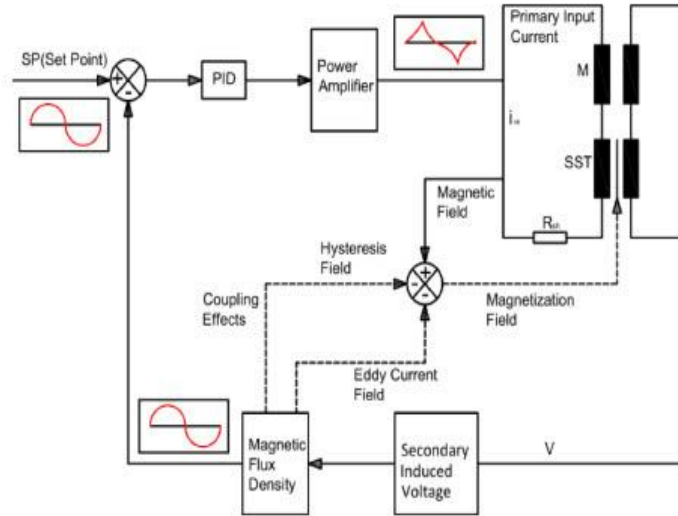


Fig. 2. Control loop and field separation theory.

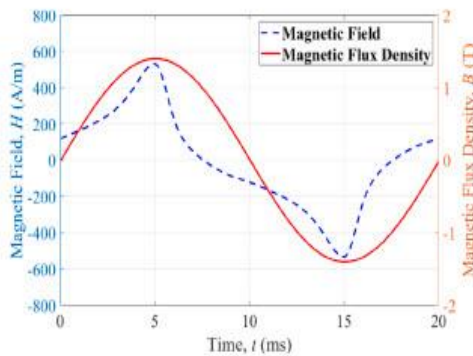


Fig. 3. Instantaneous waveforms of the magnetic field and magnetic flux density at magnetizing frequency of 50 Hz and peak flux density of 1.4 T.

and PID controller output for the different quadrants in the magnetic flux density sine waveform for one cycle, in Table 1.

The energy linked to the WMF effect can be described using the Zeeman energy between the WMF and magnetic flux density. The energy generated by the WMF in the first and third quadrants of the magnetic flux density enhances the magnetization processes; the energy linked to the WMF in the second and fourth quadrants has the opposite effect. The WMF feedback effects can be observed in the waveform of the magnetic field shown in Fig. 3, the slope of the magnetic field at the start of the second and fourth quadrants is far larger due to the energy needed to compensate for the WMF negative feedback effects during demagnetization.

In the first and third quadrants, the WMF provides energy to the

Table 1
Feedback effects based on WMF and PID controller output.

Magnetic Flux Density	First quadrant	Second quadrant	Third quadrant	Fourth quadrant
PID output	+	-	-	+
Weiss field	+	+	-	-
Feedback effect	Positive	Negative	Positive	Negative

system to boost the magnetization processes. In contrast, the WMF feeds off the energy from the system to constrain the demagnetization processes. The energy consumed during demagnetization equals the energy produced by the WMF during magnetization. So, the WMF positive and negative feedback effects offset each other except at the magnetization tips ($dB/dt = 0$). The WMF reaches a maximum value at the tips when the WMF feedback effect transitions from positive to negative, and this maximum value contributes only to the hysteresis losses if considering the counteraction between the WMF positive and negative feedback effects.

According to Weiss theory [12], the WMF, H_w , can be expressed in terms of the following equation:

$$H_w = aM, \tag{1}$$

where a is the mean field constant and M is the instantaneous magnetization. Then, the WMF feedback energy based on Zeeman energy against the magnetic induction B , W_w , can be expressed as:

$$W_w = a \int \int MBdMdB. \tag{2}$$

So, at the saturation tips, all the atomic dipoles in the samples are aligned with the magnetic field direction. All these alignments exert a strong coupling effect on the magnetic field, while this interaction of individual atomic dipoles results in the WMF. Therefore, this study assumed that a magnetic force generated from the coupling effect of the magnetization at the reversal turning point must be overcome to continue the reversal demagnetization process. This field, referred to as a hysteresis field H_h , which is the WMF at the magnetization tips, can be expressed as,

$$H_h = H_{wp} = aM_p, \tag{3}$$

where M_p is the magnetization at any order reversal point, and H_{wp} is the WMF created by M_p . According to the definition of coercivity, H_c is the magnetic field required to demagnetize the material. This means the magnetic field at coercivities needs to counteract the WMF at tips so that the magnetic flux density can be reduced to zero. Then, H_h is equal to the coercivity H_c , for magnetic flux density B to be zero. Because the direction of the hysteresis field H_h is opposite to the reversed magnetic field H , the hysteresis field at a positive tip is given by:

$$H_h = H_e, \quad (4)$$

and the hysteresis field at a negative tip by:

$$H_h = -H_e. \quad (5)$$

Then, the resulting conclusion reached is that the WMF feedback effects at magnetization tips are the physical origin of the magnetic hysteresis effect.

When the processes change directions from magnetization to demagnetization at the reversal turning point, the excitation source must contribute more energy to compensate for the coupling effect of the magnetization at the tips.

3. A simulation method of magnetic hysteresis

The theme of this paper is the simulation of the magnetization processes of ferromagnetic materials. A simulation method [21] was derived according to the domain patterns in ferromagnetic materials and the excitation field coupling effect. The simulation method is derived based on the assumption that the hysteresis field H_h is generated at the reversal turning point when the magnetic field strength H and the magnetic flux density B change their directions. Conventionally, the magnetic field $H(t)$ is produced by the excitation source. In [21], it is assumed that the excitation field $h(t)$ is the vector summation of the magnetic field $H(t)$ and the hysteresis field H_h , such that:

$$h(t) = H(t) + H_h \quad (6)$$

The excitation field for an ascending curve is then obtained as follows:

$$h(t) = H(t) - H_e, \quad (7)$$

and the excitation field for descending curve is obtained using the following equation:

$$h(t) = H(t) + H_e. \quad (8)$$

Therefore, the excitation field can be easily calculated using experimental data. Curves of $B-h$ are single curves of bijective function without hysteresis effects. It is far easier to explore a single curve than to study a hysteresis loop, which is represented by the one-to-two function with nonlinearity.

GOESs show the best magnetic properties along with the rolling direction because of the grains' orientation, so the properties are dominated by the anisotropic components. NOESs demonstrate identical magnetic properties as per the magnetizing directions because the grains in NOESs are randomly oriented other than in just the rolling direction. So, the properties of NOESs are decided by the isotropic components. Nonetheless, there are anisotropic and isotropic structures in both GOESs and NOESs [25–28]. Both anisotropic and isotropic structures determine the magnetic properties in GOES and NOES sheets, so the simulation method of GOES developed in [21] can also be applied to NOES in the same way.

The magnetization processes of the anisotropic structure can be described using a hyperbolic tangent function [21]:

$$M_a = M_a \tanh\left(\frac{\mu_0 m_a h}{kT}\right) = M_a \tanh(ah), \quad (9)$$

which was derived based on the variation of the anisotropic domain pattern under an excitation field.

In equation (9) m_a is the typical unit magnetic moment in the anisotropic domain, and

$$a = \frac{\mu_0 m_a}{kT}, \quad (10)$$

is a coefficient related to the unit moment of the anisotropic magnetic domain and the temperature T . μ_0 is the vacuum permeability, and k is

the Boltzmann constant [12]. M_a is the magnetization saturation of the anisotropic component when all the magnetic dipoles in the anisotropic domain are aligned with the excitation field [21].

The isotropic domain moment is randomly oriented in terms of the excitation field. Some moments may coincide with the crystallographic direction; however, most domains have irregular shapes and show a disoriented structure. Driven by the excitation field, the magnetization of the isotropic domain pattern can be expressed as the well-known Langevin function (11), which represents the homogeneous structure in the magnetic material [21]:

$$M_i = M_a \left(c \alpha h(bh) - \frac{1}{bh} \right) = M_i L(bh), \quad (11)$$

where,

$$b = \frac{\mu_0 m_i}{kT}, \quad (12)$$

is a coefficient related to the unit moment of the isotropic magnetic domain, and the temperature T . m_i is the typical unit magnetic moment in the isotropic domain, while M_i is the magnetization saturation of the isotropic components when all the magnetic dipoles in the isotropic domain are aligned with the excitation field [21].

The third component of the simulation method is the coupling effect of the excitation field, which provides a proportion of the magnetic induction B . When the excitation field is excited, the field will generate a part of the magnetic induction and can be expressed as:

$$M_h = ah(t), \quad (13)$$

where a is a coefficient linked to the material microstructure and magnetization conditions. The process of magnetic flux density B versus excitation field h can then be expressed via the following single equation:

$$B = M_a + M_i + M_h, \quad (14)$$

or instead, using the equations (9), (11), and (13), as:

$$B = M_a \tanh(ah) + M_i L(bh) + ah \quad (15)$$

The magnetization processes of GOESs can be analyzed using the single equation (15), which has proved to deliver an excellent performance [21]. The domain patterns in GOESs and NOESs are identical, although the domain size, grain size and grain orientation in both are different. Therefore, equation (15) is also suitable for describing the magnetization processes of NOESs. Nevertheless, the proportion of anisotropic and isotropic domain structures in GOESs and NOESs varies significantly due to different production procedures, so their magnetic properties show striking divergence. The above methodology is applied to simulate magnetic hysteresis loops and calculate the energy losses of NOESs under controlled sinusoidal excitation.

The simulation method is excellent for generating the sigmoid shape curve. Nonetheless, the measured magnetic hysteresis loops sometimes show irregular and distorted S-shaped curves. When using (15) to simulate such distorted and irregular curves, the third component can be omitted because the coupling effect of the excitation field is far smaller than the other two components in the ferromagnetic material. The hyperbolic tangent and Langevin functions can be replaced by exponential functions, and the magnetic induction expressed via the simplified expression [21]:

$$B = M_a \exp(ah) + M_i \exp(bh), \quad (16)$$

When a single curve is deformed and irregularly shaped, it can be sub-divided into several sections with one-to-one functions and equation (16) applied to simulate the segment curves. Accordingly, equations (15) and (16) can be conveniently used to simulate single curves converted from measured hysteresis loops, avoiding the need to simulate

the hysteresis loops directly.

Conventionally, the magnetic loss is evaluated by calculating the area of the magnetic hysteresis loop. So, the energy loss per cycle in a thin sheet under sinusoidal excitation can be expressed as [29]:

$$W_t = \int BdH. \tag{17}$$

Replacing H with h and considering there are two single curves, the energy loss can be calculated via the following expression:

$$W_t = 2 \int Bd h = 2 \int (M_{is} \tanh(ah) + M_{nl}(bh) + ah) dh. \tag{18}$$

The main advantage of this methodology is that the parameters are related to the microstructure of the magnetic material so that it can also be used to interpret the magnetization processes and analyze energy losses. Meanwhile, the magnetic hysteresis loop can be simulated with high accuracy. The main goal is to prove that the analytical simulation method is a general one concerning the magnetization processes of ferromagnetic materials. Below, it is used to describe the magnetic properties and dynamic behavior of NOESs by tracking hysteresis loops and calculating energy losses.

4. Simulation results

The key achievement of the simulations is that the methodology provides a new theory of magnetic hysteresis in relation to the magnetization processes of ferromagnetic materials. This theory, based on the WMP at the tips, justifies the cancelling out the hysteresis effect (coercive field) from the measured $B-H$ hysteresis loops to obtain a $B-h$ single curve, which is a curve passing through the origin representing a one-to-one injective function. The simulation of complicated hysteresis loops can then be achieved by tracking a single curve, which in turn can be used to generate the relevant hysteresis loop. The cancellation of the hysteresis effect is performed using equations (6) and (7).

Following the same data processing procedure as in [21], the first step is to consider the controlled sinusoidal magnetic induction of NOESs at a typical magnetization frequency of 50 Hz and a peak flux density (B_{pk}) of 1.4 T. The same method is used subsequently to process measurements at other frequencies and peak flux densities. As shown in Fig. 4, the measured hysteresis loop is comprised of two s-shape curves, a descending and an ascending one. The descending curve extends from B_s to $-B_s$. The single curves are separated by coercivities. On the descending curve, the segment from B_s to $-H_c$ is a demagnetizing section, and that from $-H_c$ to $-B_s$ represents a magnetizing section. The counterpart of the ascending curve extends from $-B_s$ to B_s , with the segments from $-B_s$ to H_c and H_c to B_s represent demagnetizing and

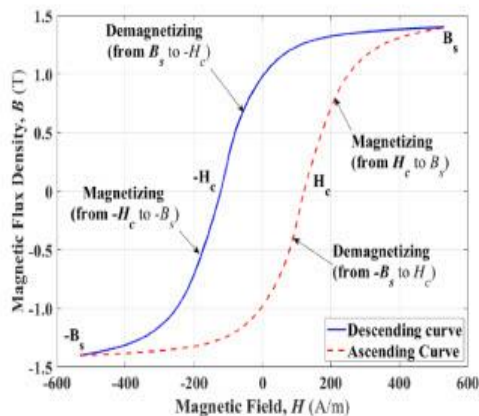


Fig. 4. Hysteresis loop of NOES Measured at 50 Hz and $B_{pk} = 1.4$ T.

magnetizing sections, respectively. The descending and ascending curves constitute a cycle of magnetization.

Equations (7) and (8) are used to offset the hysteresis effect to obtain two single curves without hysteresis. The single curves of B versus h acquired are shown in Fig. 5. After the procedure of cancelling out the hysteresis effect, the descending curve moves to the right a horizontal distance H_c , and the ascending curve shifts to the left the same distance. Both curves intersect at the origin and for both the descending and ascending curve, the magnetic flux density and excitation field are synchronized. Because of the parallel displacement of the descending and ascending curves to the origin, the two are disconnected at the peak flux density tips.

It is evident that both single curves in Fig. 5 are smooth s-shaped curves, and the relationship between B and h is a one-to-one function. The injective function of the single curves facilitates their simulation using the single equation (15). In this study, single curves are investigated first rather than simulating the hysteresis loops directly. The similarity of the two single curves reveals that the magnetic properties of NOES are dominated mainly by isotropic structures leading to similar magnetism regarding the magnetization direction. The gap between the peak flux density tips of the two single curves represents the extent of the hysteresis field, which is linked to the magnetization frequencies, peak flux densities, and material microstructures.

Magnetization under sinusoidal excitation is a cyclic process from magnetization to demagnetization and then magnetization again, and so on. So, the ascending and descending curves are symmetric with respect to the origin. The next step is to manipulate the single curves. The ascending curve is rotated through 180° about the origin. As shown in Fig. 6, the ascending and descending curves are identical after the rotation. Therefore, the descending curve is chosen to study the magnetic properties instead of tracing the hysteresis loop directly.

The s-shape descending curve of B versus h can be simulated using equation (15). During magnetization and demagnetization, the anisotropic and isotropic domain patterns act in opposite ways correspondingly. So, the magnetization and demagnetization curve sections need to be processed separately to calculate the relevant parameters in equation (15). The measurement data is processed using MATLAB curve fitting tools to conduct a regression analysis [30] using (15); the optimized solver parameters for the case 50 Hz and 1.4 T can be found in Table 2. The simulated single curve created is shown in Fig. 7 and shown to be identical to the measured descending curve. It is observed that the magnetization is dominated by isotropic structures during the magnetization process and is determined by anisotropic components during the

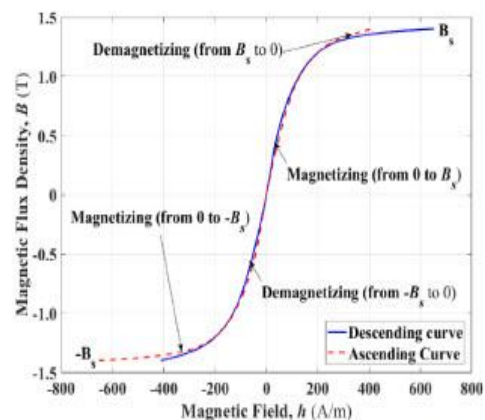


Fig. 5. Single curves of NOES obtained from the hysteresis loop in Fig. 1 by shifting the descending curve to the right at a horizontal distance H_c and ascending curve to the left at the same distance.

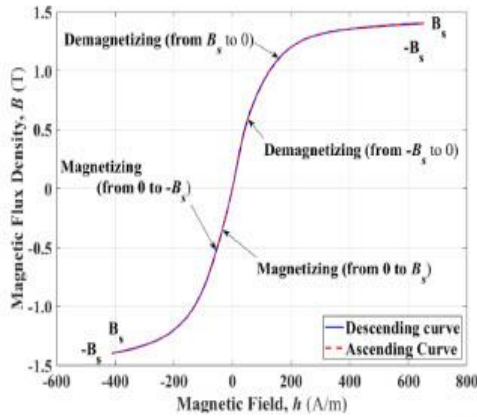


Fig. 6. Two identical single curves of NOES obtained from the curves in Fig. 5 by rotating the ascending curve 180° about the origin.

Table 2

Parameters of equation (15) for creating the magnetizing and demagnetizing curve sections for NOES magnetized at 50 Hz and B_{pk} from 1.0 T to 1.4 T.

Excitation	Curve section	$M_m(T)$	$M_d(T)$	a	b	α
50 Hz	Mag.	0.011	0.425	10.95	2.774	0.393
1.0 T	Demag.	0.468	0.580	1.361	0.961	0.030
50 Hz	Mag.	0.068	1.087	1.090	1.602	0.137
1.1 T	Demag.	0.663	0.375	0.583	4.333	0.019
50 Hz	Mag.	0.444	0.331	0.922	2.077	0.200
1.2 T	Demag.	0.726	0.428	0.549	4.051	0.013
50 Hz	Mag.	0.196	1.345	0.456	1.612	0.008
1.3 T	Demag.	0.768	0.506	0.512	3.691	0.008
50 Hz	Mag.	0.503	0.973	0.722	1.384	0.011
1.4 T	Demag.	0.846	0.508	0.508	3.658	0.008

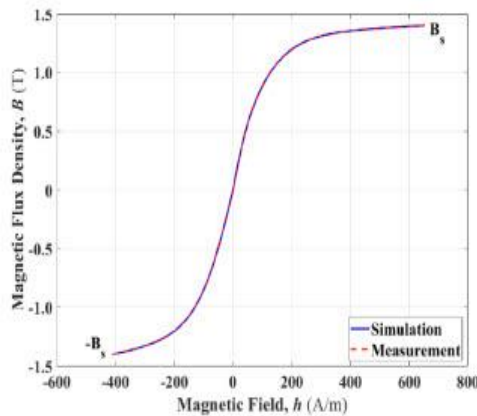


Fig. 7. Comparison of simulated and derived single curves for NOES at 50 Hz and $B_{pk} = 1.4$ T.

demagnetization process.

The simulation method describes the magnetization processes based on the reaction of the microstructures to the external excitation field, while measured hysteresis loops are plotted as a function of B versus H . The equivalent simulated hysteresis loop is achieved by manipulating the simulated single curve to fit the measured hysteresis loop. The simulated and measured hysteresis loops are shown in Fig. 8, from which it is evident that the simulation method performs very well at

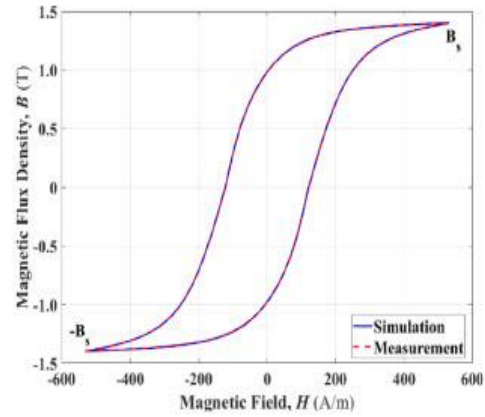


Fig. 8. Comparison of simulated and measured hysteresis loops for NOES at 50 Hz and $B_{pk} = 1.4$ T.

tracing the magnetic hysteresis loop.

The simulation of NOES for a variety of magnetization frequencies and peak flux densities is now undertaken using the same methodology as employed above. Single curves of B versus h are derived from the measured hysteresis loops for magnetization frequencies from 50 Hz to 300 Hz and peak flux densities from 1.0 T to 1.4 T. The obtained single curves are shown in Figs. 9 to 13. On these curves, the sections $h < 0$ and $h > 0$ represent magnetization and demagnetization, respectively. The parameters associated with these two curve sections need to be calculated separately due to the different magnetization mechanisms.

One interesting finding from the single curves shown in Figs. 9 to 11 is that they have similar shapes, and all pass the origin. They are the standard s-shape curves that can be simulated using (15); the associated optimized parameters of (15) magnetized at 50 Hz, and 1.0 T to 1.4 T are listed in Table 2, and the corresponding hysteresis loops are shown in Fig. 15. The parameters shown in Table 2 were obtained using regression analysis; however, the isotropic and anisotropic components in ferromagnetic materials are impossible to measure using current measurement technology. Accordingly, the parameters may contain unknowable errors, but it is still possible to distinguish that magnetization is mainly determined by the isotropic components, since M_{it} is greater the M_{id} , while demagnetization is mainly attributable to the anisotropic components because the M_{id} is greater than the M_{it} .

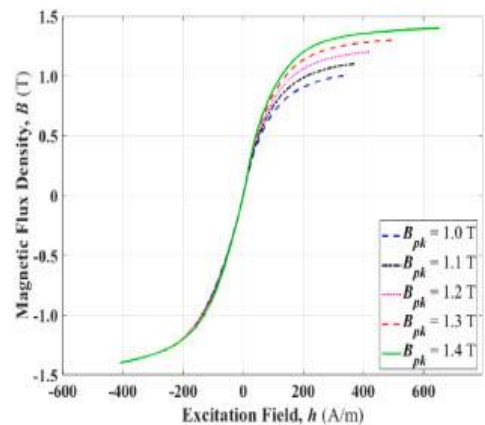


Fig. 9. Single Curves of NOES obtained from the hysteresis loops measured at 50 Hz and B_{pk} from 1.0 to 1.4 T.

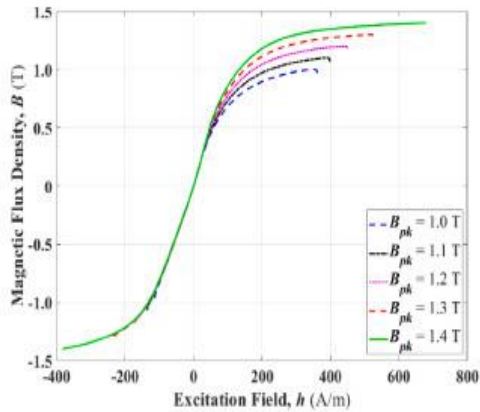


Fig. 10. Single Curves of NOES obtained from the hysteresis loops measured at 100 Hz and B_{pk} from 1.0 to 1.4 T.

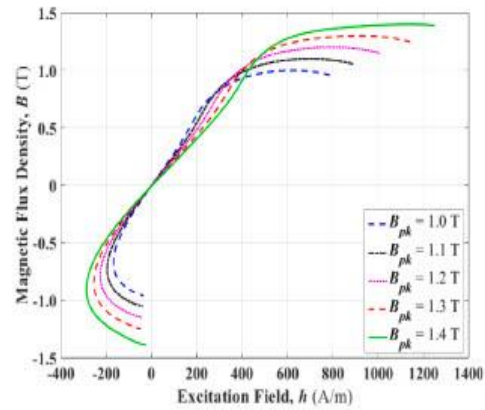


Fig. 13. Single Curves of NOES obtained from the hysteresis loops measured at 800 Hz and B_{pk} from 1.0 to 1.4 T.

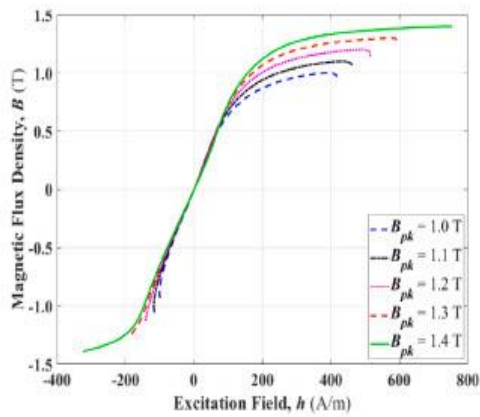


Fig. 11. Single Curves of NOES obtained from the hysteresis loops measured at 200 Hz and B_{pk} from 1.0 to 1.4 T.

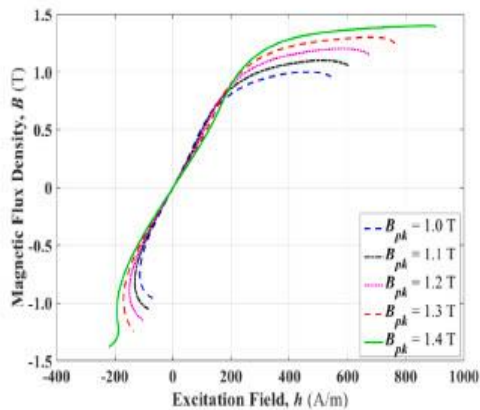


Fig. 12. Single Curves of NOES obtained from the hysteresis loops measured at 400 Hz and B_{pk} from 1.0 to 1.4 T.

Table 3

Parameters of equation (15) for creating the magnetizing and demagnetizing curve sections for NOES magnetized at frequencies from 50 Hz to 200 Hz and $B_{pk} = 1.4$ T.

Excitation	Curve section	$M_{sa}(T)$	$M_{sd}(T)$	a	b	α
50 Hz	Mag.	0.503	0.973	0.722	1.384	0.011
1.4 T	Demag.	0.846	0.508	0.508	3.658	0.008
100 Hz	Mag.	0.840	1.104	0.722	0.451	0.000
1.4 T	Demag.	0.626	0.875	0.885	1.097	0.000
200 Hz	Mag.	1.323	0.360	0.402	0.678	0.000
1.4 T	Demag.	0.904	0.564	0.510	0.957	0.000

Table 3 shows the optimized parameters for use with equation (15) for NOES magnetized at frequencies from 50 Hz to 200 Hz and peak flux density of 1.4 T. As above, the relevant single curves were simulated using (15) with these parameters and the corresponding hysteresis loops plotted. Physically, the sum of M_{sa} and M_{sd} should be around the peak flux density because the third component of (15) is very small. So, the parameters of magnetization at 50 Hz and 1.0 T lose their physical meaning. Theoretically, the proportionality of M_{sa} and M_{sd} is mainly determined by the materials and the magnetization directions with a much weaker link to the magnetization frequencies and peak flux densities. The dependency of the magnetic losses regarding the magnetization frequencies and peak flux densities will be explored in future work.

As shown in Figs. 12 and 13, the single curves at 400 Hz and 800 Hz reveal curl at magnetization section tips, which reveals the asynchronous phenomena introduced by high frequencies. When the excitation fields reach maximum values and start to reverse their directions, the flux densities are still increasing. It gives a sense that the flux densities go ahead of the excitation field. These asynchronous phenomena caused by high frequencies make the calculation of parameters rather intricate, so the simulation of the single curves must be performed by fitting the piecewise curves using (15) or (16). The parameters used in (15) or (16) must be calculated for each segment separately, the more segments used, the higher the accuracy of the simulation. The calculation of the segmented parameters is conducted separately for the magnetization and demagnetization sections.

For the case of 800 Hz and 1.4 T, the simulation of the $B-h$ curve is conducted in a piecewise fashion. The magnetizing section is separated into four segments and simulated using (16), whereas the demagnetizing section is divided into three segments and simulated using (15). The parameters calculated are listed in Table 4. The parameters obtained using the MATLAB fitting tool in the piecewise method cannot represent

Table 4. Parameters associated with equation (15) for magnetizing sections and (16) for demagnetizing sections used to obtain the contiguous magnetizing and demagnetizing curve sections of Fig. 14 for NOES magnetised at 800 Hz and 1.4 T.

Curve section	$M_m(T)$	$M_d(T)$	a	b	α
Magnetizing					
Section 1	0.249	-0.242	0.330	-0.352	
Section 2	0.148	0	0.464	9.766	
Section 3	1.642	0	-0.120	7.133	
Section 4	1.567	-0.176	-0.093	-0.859	
Demagnetizing					
Section 1	-0.800	1.4	-9.01	0.239	-0.028
Section 2	3.408	0.694	-2.406	0.694	-0.110
Section 3	14.91	-24.57	0.352	0.739	0.961

the authentic physical meaning of the magnetization processes. The simulated single curve is shown in Fig. 14. It is evident from the figure that equations (15) and (16) can reproduce the single curve with remarkable similarity. Then, the hysteresis loops of the test sample can be created using the simulation method for the range of magnetization.

The measured and calculated hysteresis loops at magnetization frequencies of 50 Hz to 800 Hz and peak flux densities of 1.0 T to 1.4 T are illustrated in Figs. 15 to 19, respectively. The results indicate that the calculated loops are consistent with the measured hysteresis loops in the range of measurement frequency and magnetic flux density. Evidently, the simulation method according to domain theory can reproduce the magnetic hysteresis loops of NOESs with remarkable accuracy. This simulation method is also convenient for evaluating the energy loss using equation (18), which is used to calculate the Zeeman energy between the excitation field and magnetic flux density.

Fig. 20 compares the calculated and measured energy losses at magnetization frequencies from 50 Hz to 800 Hz and peak flux densities from 1.0 T to 1.4 T. Fig. 21 demonstrates the errors between the calculated and measured energy losses. It is observed that the maximum difference with the measurement data is less than 1% and in very close agreement.

5. Conclusions and future work

In this study, a simulation method having a sound physical underpinning is used to reproduce the magnetic hysteresis loops of NOESs with isotropic characteristics. This single equation simulation has already been verified for GOESs with strong anisotropic characteristics [21]. Accordingly, the approach is applicable to both homogeneous and inhomogeneous materials. Meanwhile, the energy loss per cycle can be

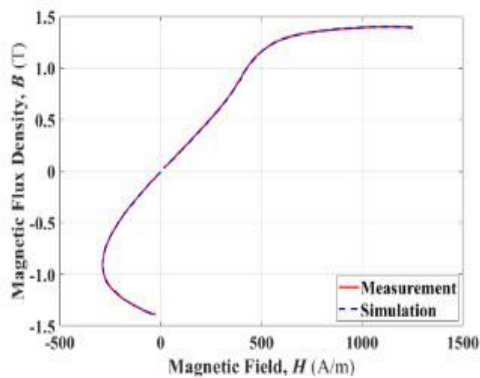


Fig. 14. Simulated contiguous curve sections, 4 in total for magnetizing section using (16), 3 in total for demagnetizing section using (15), superimposed on the corresponding measured single curve for NOES at 800 Hz and $B_{pk} = 1.4$ T.

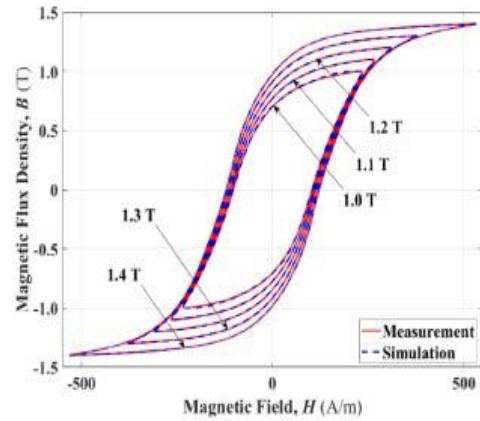


Fig. 15. Comparison between simulated and measured hysteresis loops for NOES at 50 Hz and B_{pk} from 1.0 T to 1.4 T.

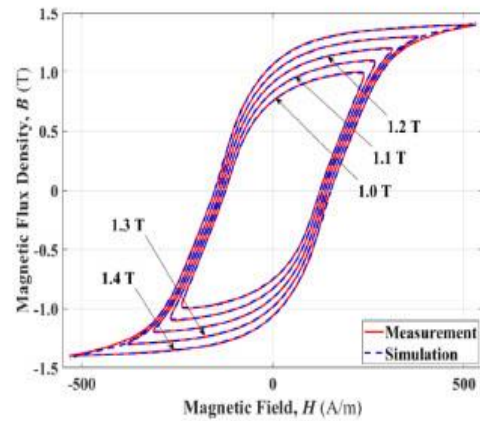


Fig. 16. Comparison between simulated and measured hysteresis loops for NOES at 100 Hz and B_{pk} from 1.0 T to 1.4 T.

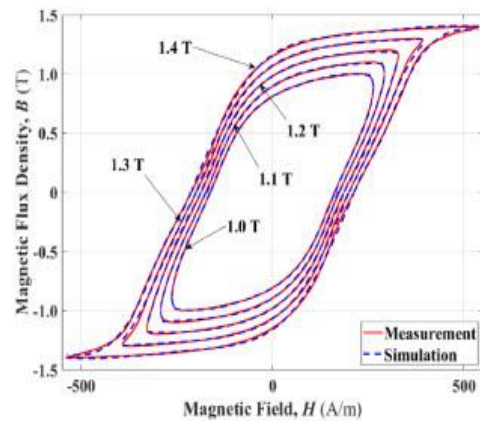


Fig. 17. Comparison between simulated and measured hysteresis loops for NOES at 200 Hz and B_{pk} from 1.0 T to 1.4 T.

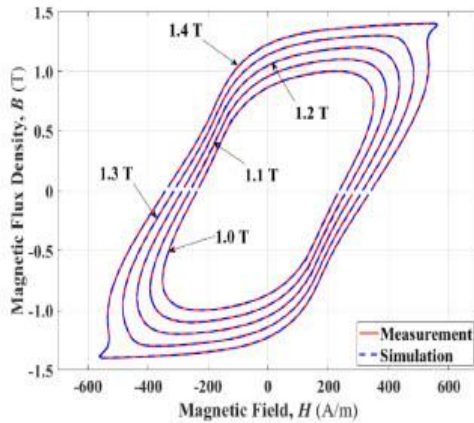


Fig. 18. Comparison between simulated and measured hysteresis loops for NOEs at 400 Hz and B_{pk} from 1.0 T to 1.4 T.

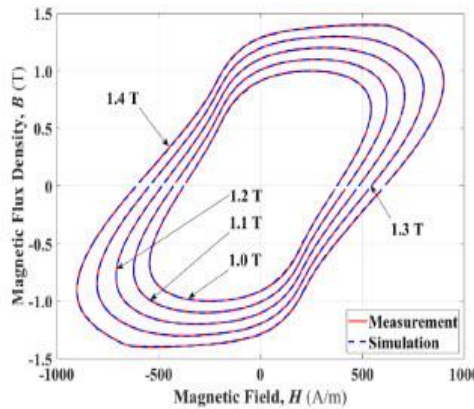


Fig. 19. Comparison between simulated and measured hysteresis loops for NOEs at 800 Hz and B_{pk} from 1.0 T to 1.4 T.

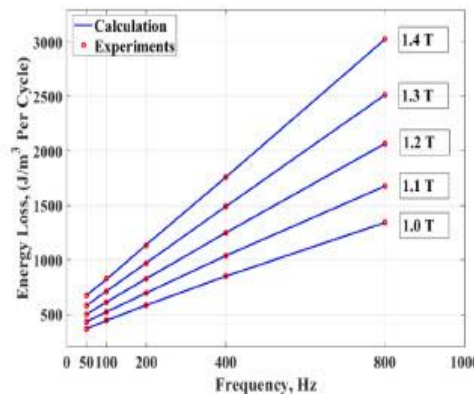


Fig. 20. Comparison between calculated and measured energy losses for NOEs magnetized at frequencies ranging from 50 to 800 Hz and B_{pk} from 1.0 to 1.4 T.

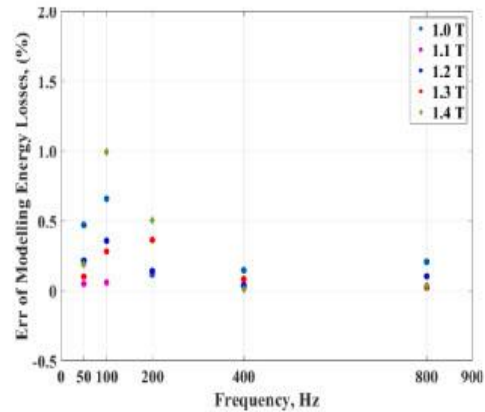


Fig. 21. Errors for NOEs between calculated and measured energy losses at frequencies ranging from 50 to 800 Hz and B_{pk} from 1.0 to 1.4 T.

calculated by simply integrating the single equation over the range of the excitation field. The energy losses are calculated for NOEs over a wide range of magnetization frequencies and flux densities. The results obtained show that this method performs very well for tracing the major and minor loops of NOEs. It is also the first-time energy loss has been calculated using a single equation with such a high level of accuracy.

The results of this study demonstrate the reliability of the simulation methodology in predicting the magnetic hysteresis behavior of NOEs for a range of magnetization. Despite the single equation being currently the simplest simulation method of magnetic hysteresis, it has a sound physical underpinning and fills a technology gap for interpreting the magnetization processes of ferromagnetic materials. Compared to previous simulation methods, the one described here is simple to implement and needs far fewer calculations.

In addition to showing a critical step forward in interpreting the magnetization process related to soft magnetic materials under sinusoidal excitation, the proposed simulation method is also capable of investigating magnetic behavior under non-sinusoidal excitation widely applied in renewable energy systems, which is currently under investigation. The insights might be of interest to the physicists and engineers that endeavour to improve the performance of magnetic components in power electronics.

CRedit authorship contribution statement

Z. Zhang: Conceptualization, Methodology, Visualization, Formal analysis, Writing - original draft. H. Hamzehbahman: Investigation, Supervision, Data curation, Writing - review & editing. P.H. Gaskell: Supervision, Writing - review & editing.

Declaration of Competing Interest

The authors declare that they have no known competing financial interests or personal relationships that could have appeared to influence the work reported in this paper.

Data availability

Data will be made available on request.

Acknowledgement

The authors are grateful to Cogent Power Ltd. for providing the electrical steel sheets, and Cardiff University for the experimental results.

References

- [1] P. Beckley, *Electrical Steels: A Handbook for Producers and Users*, first ed., European Electrical Steel, Newport, South Wales, 2000.
- [2] S. Zhang, B. Ducharme, S. Takeda, G. Sebald, T. Uchimoto, *J. Magn. Magn. Mater.* 538 (2021), 168278.
- [3] M. Noori, W.A. Altabey, *Appl. Sci.* 12 (19) (2022) 9428.
- [4] J.A. Ewing, *Magnetic induction in iron and other metals*, D. Van Nostrand Company (1900).
- [5] C. Arimatea and D. Jacquet, *Mesure de l'influence magnétique du cycle proton 450 GeV sur le cycle positron (No. SL-Note-2001-013-MD)*. CERN-SL-Note-2001-013-MD, 2001.
- [6] M. Kersten, Zur Deutung der Koerzitivkraft, in: R. Becker, K.J. Sixtus, W. Döring, M. Kersten, J.L. Snoek, G. Richter, H. Schulze, G. Masing, W. Gerlach, H. Lange, R. Becker (Eds.), *Probleme der Technischen Magnetisierungskurve*, Springer Berlin Heidelberg, Berlin, Heidelberg, 1938, pp. 42–72.
- [7] M. Kersten, *Grundlagen einer Theorie der ferromagnetischen Hysterese und der Koerzitivkraft*, JW Edwards (1946).
- [8] R. Becker, W. Döring, *Ferromagnetismus*, Springer, Berlin, 1939.
- [9] S. Takahashi, S. Kobayashi, *IEEE Trans. on Magn.* 44 (11) (2008) 3859–3862.
- [10] P. Henrotte, K. Hameyer, *IEEE Trans. on Magn.* 42 (4) (2006) 899–902.
- [11] R.G. Harrison, *IEEE trans. on Magn.* 45 (4) (2009) 1922–1939.
- [12] D.C. Jiles, *Introduction to Magnetism and Magnetic Materials*, Chapman & Hall, London, 1998.
- [13] D.C. Jiles, D.L. Atherton, *J. Appl. Phys.* 55 (6) (1984) 2115.
- [14] S. Zhang, B. Ducharme, S. Takeda, G. Sebald, T. Uchimoto, *J. Magn. Magn. Mater.* 531 (2021), 167971.
- [15] A. Ramesh, D. Jiles, J. Roderick, *IEEE Trans. on Magn.* 32 (5) (1996) 4234.
- [16] R. Szweczyk, *Materials* 7 (7) (2014) 5109.
- [17] I.D. Mayergoyz, *Mathematical models of hysteresis and their applications*, Academic Press, New York NY, 2003.
- [18] R. Zeinali, D. Krop, E. Lomonova, *IEEE Trans. on Magn.* 57 (6) (2021) 1–4.
- [19] S. Bobbio, G. Milano, C. Serpico, C. Visone, *IEEE Trans. on Magn.* 33 (6) (1997) 4417.
- [20] Y. Li, J. Zhu, Y. Li, L. Zhu, *J. Magn. Magn. Mater.* 544 (2022), 168655.
- [21] Z. Zhang, H. Hamzehbahmani, and P. H. Gaskell, *IEEE Trans. on Magn.*, 58(1), pp.1–9, 2021.
- [22] BS EN 10280:2001 + A1:2007, *Magnetic Materials - Methods of measurement of the magnetic properties of electrical sheet and strip by means of a single sheet tester*, British Standard.
- [23] H. Hamzehbahmani, *Development of novel techniques for the assessment of inter-laminar resistance in transformer and reactor cores*, Cardiff University, 2014. Doctoral dissertation.
- [24] O. de la Barrière, C. Appino, C. Ragusa, P. Fiorillo, M. LoBue, F. Mazaleyrat, *IEEE Trans. on Magn.* 54 (9) (2018) 1–15.
- [25] M. Birzan, J.A. Szpunar, *J. Appl. Phys.* 81 (2) (1997) 821–823.
- [26] H. Pirgazi, R.H. Petrov, L.A. Kerstens, *Steel Research International* 87 (2) (2016) 210–218.
- [27] G.H. Shirkoobi, M.A.M. Arikat, *IEEE Trans. on Magn.* 30 (2) (1994) 928–930.
- [28] G.H. Shirkoobi, J. Liu, *IEEE Trans. on Magn.* 30 (2) (1994) 1078–1080.
- [29] P. Fiorillo, C. Appino, M. Pasquale, G. Bertotti, *Hysteresis in magnetic materials, The Science of Hysteresis 3* (2006) 1–190.
- [30] L. The MathWorks, *Curve Fitting Toolbox*, Natick, Massachusetts, United State, 2020. Available at: <https://www.mathworks.com/products/curvefitting.html>.

Appendix III – Conference Posters

Characterisation of Non Oriented Electrical Steels based on the Dynamic Hysteresis Loop (DHL)

Hamed Hamzehbahmani, *Senior member, IEEE*, Zhi Zhang

Department of Engineering, Durham University, Durham, DH1 3LE, UK

Non-Oriented (NO) electrical steels are silicon steels in which magnetic properties are practically the same in any direction of magnetisation in the plane of the material. Due to the approximate homogeneous nature of NO steels, magnetisation process of the material can be evaluated by numerical solution of the 1-D diffusion equation [1]:

$$\frac{\partial B_z(x, t)}{\partial t} = \rho \frac{\partial^2 H_z(x, t)}{\partial x^2} \quad (1)$$

which link the flux density $B_z(x, t)$ and the field strength $H_z(x, t)$ directed in z-axis in a thin ferromagnetic lamination of resistivity ρ .

Hysteresis loops of the magnetic materials and magnetic cores may take many different shapes, which depend on the magnetising conditions, properties of the materials, and quality of the magnetic cores [2]. In this work Epstein size

lamination of 0.5 mm thick NO 3 % SiFe was characterised. DHL of the sample was measured under sinusoidal induction at peak flux densities of 1.1 T, 1.3 T and 1.5 T and frequencies of 50 Hz, 400 Hz and 800 Hz, the results are shown in Fig 1.

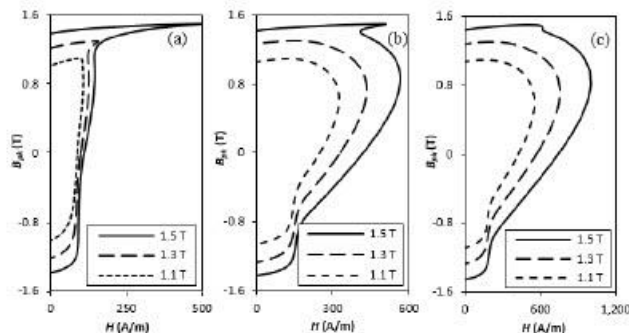


Figure 1 DHL of the sample at peak flux densities of $B_{pk}=1.5$ T, $B_{pk}=1.3$ T and $B_{pk}=1.1$ T and frequencies of (a) 50 Hz (b) 400 Hz and (c) 800 Hz

An approach was developed [3] to calculate the specific energy loss from the measured DHL. A close agreement with a maximum difference of less than 3 % was found between the measured and calculated energy losses.

References:

- [1] S. Zirka, et. al., *JMMM*, Vol. 394, Nov. 2015, pp 229-236
- [2] G. Bertotti and I. Mayergoyz “*The Science of Hysteresis*”, Academic Press 2005
- [3] H. Hamzehbahmani, *IET Electric Power Applications*, Accepted for publication, 2019

Electrical steels were provided by Cogent Power Ltd, and the experimental work were performed at Wolfson center for magnetics at Cardiff University.

A New Hysteresis Model for characterising Grain-Oriented Electrical Steels

Zhi Zhang^a, Hamed Hamzehbahmani^a, Philip H. Gaskell^a

^aDepartment of Engineering, Durham University, Durham DH1 3LE, UK

This paper presents a novel analytical model to describe the magnetization processes of Grain-oriented electrical steels (GOESs), based on analysing the variations of the different domain patterns during magnetization and demagnetization processes. The model was validated for Epstein size laminations of GO 3 % SiFe electrical steels, with close agreement, having a maximum difference of less than 2 %, found between the calculated energy loss predicted and bulk measurements.

Keywords: Hysteresis modelling, grain-oriented electrical steels, energy loss

1. Model

GOESs consist of both anisotropic and isotropic domain patterns at an unmagnetized condition to form the closed structures [1]. When magnetizing, the magnetic induction comprised of three components is expressed as a single generalized equation:

$$B = M_{sa} \tanh(ah) + M_{si} L(bh) + ah. \quad (1)$$

where a is a balance coefficient for anisotropic components between the unit domain magnetic moment and the disordering effect of thermal agitation, M_{sa} is the saturation magnetization of the anisotropic components. b is a balance coefficient for isotropic components and M_{si} is the saturation magnetization of the isotropic components. The third component is the coupling effect of the exciting field, a is the coupling coefficient, while h is the exciting field obtained from the magnetic field H through hysteresis displacement procedure.

2. Application

The new model is used to describe the relationship between B and h , which is a single curve. The proposed method avoids functioning the hysteresis loop directly. The hysteretic behaviour starts at any order reversal point and is caused by the hysteresis field triggered by the magnetization coupling effect. The relevant hysteresis loops of B versus H can be created by manipulating the curves to simulate the experimental loops.

2.1. Results

A standard Single Strip Tester was used to magnetise Epstein size laminations of GO electrical steel samples according to the BS EN 10280:2001 [2, 3] and dynamic hysteresis loops (DHLs) for the samples measured at peak flux densities ranging from 1.0 T to 1.7 T, and magnetizing frequencies ranging from 50 Hz to 1000 Hz.

DHLs of the test sample were reproduced using the

model for the range of magnetization. The measured and calculated DHLs at magnetizing frequencies of 50 Hz and peak flux densities of 1.0 T to 1.7 T are shown in Figure 1. The result indicates that the calculated DHLs coincide exactly with the measured loops.

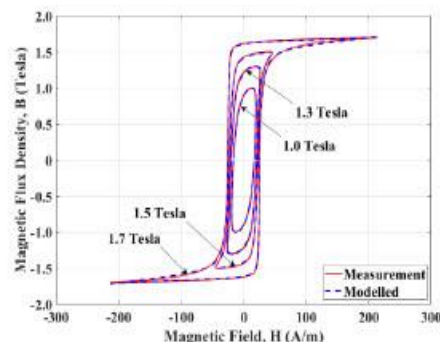


Figure 1 : Comparison of hysteresis loops for GO steel

The good quantitative agreement of the resulting dynamic hysteresis loops for GOESs with corresponding experimental data establishes the new model, the theory on which it is based and its applicability. It represents an essential contribution to the modelling of the magnetisation processes of soft magnetic materials.

References

- [1] D. Jiles, "Introduction to magnetism and magnetic materials," CRC press, 2015.
- [2] BS EN 10280:2001 + A1:2007, Magnetic Materials - Methods of measurement of the magnetic properties of electrical sheet and strip by means of a single sheet tester.
- [3] Hamzehbahmani, H., Anderson, P., and Preece, S., "Application of an advanced eddy-current loss modelling to magnetic properties of electrical steel laminations in a wide range of measurements", IET Science, Measurement & Technology, vol. 9, no. 7, pp.807-816, 2015.

* Corresponding author: zhi.zhang@durham.ac.uk